APPLIED
COMPUTATIONAL
ELECTROMAGNETICS
SOCIETY
JOURNAL

SPECIAL ISSUE

ON

INTERNATIONAL

COMPUTATIONAL

ELECTROMAGNETICS

GUEST EDITORS
JOAO PEDRO BASTOS,
ADALBERT KONRAD,
AND
JOHN BRAUER

1997
Vol. 12 No. 1

ISSN 1054-4887

19970226 020

The ACES Journal is abstracted in INSPEC, in Engineering Index, and in DTIC.

The second, third, fourth, and fifth illustrations on the front cover have been obtained from Lawrence Livermore National laboratory.

The first illustration on the front cover has been obtained from FLUX2D software, CEDRAT S.S. France, MAGSOFT Corporation, New York.

THE APPLIED COMPUTATIONAL ELECTROMAGNETICS SOCIETY

JOURNAL EDITORS

THE APPLIED COMPUTATIONAL ELECTROMAGNETICS SOCIETY

JOURNAL

INTERNATIONAL COMPUTATIONAL ELECTROMAGNETICS

TABLE OF CONTENTS

Announcements:

EDITORIAL

We are very pleased to present a special issue of the ACES Journal that showcases international research in computational electromagnetics. The papers published here have been especially selected from those presented at the Brazilian Conference on Electromagnetics. It was held May 1995 at Florianopolos, Santa Catarina, Brazil, at the "CBmag'95, Congresso Brasileiro de Eletromagnetismo" (Brazilian Conference on Electromagnetics).

A total of 26 papers appear in this special issue. Many of the authors of these papers reside in Brazil and are not well known in the northern hemisphere. Some of us in the United States, Europe, and Asia will be surprised by the high quality of the papers in this issue. They show that our neighbors to the south are truly an active part of the computational electromagnetics community.

With the increase in the popularity of the world wide web and other communications media, important advances in numerical computations will occur in all corners of the globe. We hope that this special issue is a forerunner to help foster further international activity and cooperation in computational electromagnetics.

Joao Pedro Bastos   Adalbert Konrad   John Brauer

3B-Splines in the Integral Equation Solution
for Scattering from Bodies of Revolution

F.L. Teixeira[1], J.R. Bergmann[2]

[1]EMBRATEL S.A., Satellite Transmission Department
[2]CETUC - Center for Telecommunication Studies, Catholic University of Rio de Janeiro

Abstract- The use of B-Spline functions is investigated in conjunction with the Method of Moments integral-equation solution to the problem of scattering from conducting bodies of revolution. Its computational performance in terms of relative accuracy and storage/CPU time requirements is evaluated against entire-domain and sampling-like basis functions. Particular attention is given to the description of currents near edges. Questions of time (space) and frequency (wavenumber) localization are also addressed. A simple scheme devised to enforce boundary conditions *a priori* is shown to be potentially capable to stabilize otherwise spurious solutions.

I. INTRODUCTION

The numerical treatment of open-boundary radiation or scattering problems in the frequency domain is usually done with the use of a linear integral equation (IE) formulation. The Method of Moments (MoM) is a general procedure to reduce an IE to a matrix equation [1] that is usually dense and computationally intensive to solve. In order to reduce the matrix dimensions, a crucial aspect of the MoM solution is the adequate choice of basis functions. Two major classes of basis functions commonly employed in the MoM can be identified: entire-domain functions [2-4] and local-domain (compact support) functions [4-6]. Entire-domain functions are more specialized, being used in specific problems to attain a fast convergence. Local-domain functions are geometrically flexible, being more practical to analyze complex geometries.

The fast rate of convergence achieved with the use of entire-domain functions for certain problems of scattering from perfect electric conductors (PECs) [2,3] is related to the spectral characteristic (in the spatial-frequency domain of the wave-number $\bar{k}$) of the induced electric currents. Of particular interest, because of its practical importance, is the class of smooth objects, i.e., with local radius of curvature greater than one wavelength. For these objects, a reasonable assumption is that the induced current has a bandlimited nature, i. e., can be well approximated by functions of confined wavenumber spectrum, $|\bar{k}| < k_m$ (moreover in the context of far-field scattering). Heuristic arguments in favor of this hypothesis were well posed by Hermann [7]. Entire-domain functions as Fourier trigonometric functions usually have a low-frequency spectrum and thus, are natural candidates for an efficient expansion for the unknown currents.

One attractive characteristic of the local-domain functions not shared by the entire-domain functions is local support. It permits a faster evaluation of integrals since only a small region of the scatterer needs to be integrated in the evaluation of each coefficient of the MoM linear system (impedance matrix). In addition, since the entire-domain functions are defined over the whole object, the CPU time for evaluating each coefficient is also dependent on the electric size of the object. As a consequence, it implies an even worse frequency-scaled dependency of the required CPU time to solve the problem.

The interest to develop a scheme combining the attractive aspects of local and entire-domain functions can be traced from the above observations. It would correspond to the use of basis functions having band-limited spectrum and, simultaneously, local support. Ideally speaking, this objective is not strictly possible, since the Fourier transform of any function with a finite spatial support has necessarily an infinite support. The objective to be sought is then an approximation to this ideal.

One scheme that proved successful in this direction was the use of the so-called quasi-localized bandlimited basis functions (sampling-like) [7,8]. In the examples considered there, the sampling rate associated with the MoM was reduced from the usual number of 10 basis functions per wavelength to an average rate of between 2.5 and 3 bandlimited basis functions per wavelength. At the same time these functions allowed a very rapid computation of the integrals involved due to their limited overlap. The basic limitation of this approach is that it does not provide special treatment for currents near the edge of the scatterer (in the case of open scatterers), where a singular behavior is expected in the induced currents (leading to spatially localized high-frequency components). Failure to incorporate the correct edge behavior can result in erroneous currents and anomalous behavior of the solution near the edge [9].
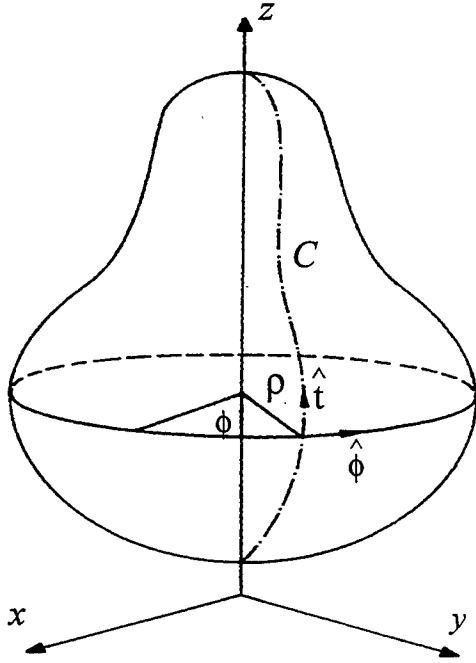
Fig. 1- Geometry and coordinates of a body of revolution

II. METHOD OF MOMENTS SOLUTION OF THE SCATTERING FROM BODIES OF REVOLUTION

In this section the basic formulation of the MoM analysis of conducting BoRs is briefly reviewed. For a more detailed discussion the reader is referred to [5].

Fig. 1 depicts a general BoR. It is generated by a rotation of the curve C about the z-axis. For numerical purposes, C is approximated by a sequence of linear segments ε_i. Any point on the BoR surface can be described by two coordinates: ϕ, the azimuth angle; and t, the arclength along C. Given an incident electric field $\vec{E}^{inc}$ the solution of the problem follows from the application of the pertinent boundary condition:

$$\hat{n} \times (\vec{E}^{inc} + \vec{E}^s) = 0 \qquad (1)$$

on the surface of the PEC scatterer, where $\vec{E}^S(\vec{r})$ is the scattered field due to surface currents $\vec{J}(\vec{r}')$ on the body and $\hat{n}$ is the unit normal vector to the surface. The scattered field can be expressed in terms of the induced current through the radiation integral, with an $e^{j\omega t}$ dependency assumed:

$$\vec{E}^s(\vec{r}) = -j\omega\mu \iint_s \vec{J}(\vec{r}')G(\vec{r},\vec{r}')ds' -$$

$$\frac{j}{\omega\varepsilon}\vec{\nabla}_s \iint_s (\vec{\nabla}'_s.\vec{J})G(\vec{r},\vec{r}')ds' \qquad (2)$$

here $G(\vec{r},\vec{r}')$ is the free space Green's function:

$$G(\vec{r},\vec{r}') = \frac{e^{-jk|\vec{r}-\vec{r}'|}}{4\pi|\vec{r}-\vec{r}'|} \qquad (3)$$

Combining (1) and (2) the Electric Field Integral Equation (EFIE) is obtained:

$$\vec{E}^{inc}_{tan} = L(\vec{J}) = j\omega\mu \iint_s \vec{J}(\vec{r}')G(\vec{r},\vec{r}')ds' +$$

$$\frac{j}{\omega\varepsilon}\vec{\nabla}_s \iint_s (\vec{\nabla}'_s.\vec{J})G(\vec{r},\vec{r}')ds' \qquad (4)$$

By decomposing the induced current and the incident tangential electric field in terms of its (orthogonal) components along the t and ϕ directions, a set of two coupled integro-differential equations is obtained. In a dyadic form they are written as:

To alleviate these problems, this work explores the use of B-splines in the context of scattering from PEC bodies of revolution (BoR). Among the advantages presented by these functions and herein investigated are: (i) Near-optimal localization on the spatial and spatial-frequency (or wavenumber) domains $(\vec{r},\vec{k})$ with asymptotic convergence to Gaussian functions, which have an optimal localization [10]; (ii) Ability to model the singular behavior near the edges through the use of multiple knots; (iii) Analytical simplicity that permits an exact analytic extraction of singularities arising in the kernel of the IE. Two specific examples are considered: the scattering from an infinitely thin, PEC circular disc, and the scattering from a finite, PEC hollow cylinder. For the second example it is also shown that a simple scheme devised to enforce *a priori* boundary conditions on the longitudinal current component can also solve the problem of instability in the azimuthal component when using the Electric Field Integral Equation (EFIE) [11].

This work is organized as follows. In section II the MoM solution of the electromagnetic scattering from conducting bodies of revolution is briefly reviewed. Section III contains a description of the basis functions used in this paper, with particular attention given to the interesting properties of B-splines. In section IV comparative results from the analysis of a circular disk and a finite hollow cylinder are presented. Finally, section V summarizes the most important conclusions.

$$(L^{tt}\hat{t}\hat{t} + L^{t\phi}\hat{t}\hat{\phi} + L^{\phi t}\hat{\phi}\hat{t} + L^{\phi\phi}\hat{\phi}\hat{\phi}) \cdot$$
$$(J_t\hat{t} + J_\phi\hat{\phi}) = E_t^{inc}\hat{t} + E_\phi^{inc}\hat{\phi} \qquad (5)$$

where L^{pq} are the integro-differential scalar operators (p and q stand for t and ϕ). The MoM is then applied to solve the above equations. We start by expressing the unknown currents in terms of a suitable set of basis functions:

$$\vec{J}(t,\phi) = \sum_{m=-M}^{N} \left[\sum_{i=1}^{Nt} I_{mi}^t \vec{b}_{mi}^t(t,\phi) + \sum_{i=1}^{N\phi} I_{mi}^\phi \vec{b}_{mi}^\phi(t,\phi) \right]$$

$$\vec{b}_{mi}^t(t,\phi) = \frac{f_i^t(t)}{\rho(t)} e^{jm\phi}\hat{t}$$

$$\vec{b}_{mi}^\phi(t,\phi) = f_i^\phi(t)e^{jm\phi}\hat{\phi} \qquad (6)$$

The factor $1/\rho(t)$ (radial distance to z-axis) in the t-component serves to cancel the $\rho(t)$ associated with the element of surface $dS' = \rho d\phi dt$. The coefficients in (6) are the unknowns of the problem. The above integro-differential equations in a Hilbert space are transformed (projected) into a matrix equation by inserting (6) in (5) and performing an inner product of the resultant equations with a set of test functions defined as complex conjugates of the basis functions (Galerkin method). The inner product is operationally defined to be the integral over S of the dot product of the basis and test functions. From the choice of harmonic dependence on ϕ, there follows, in view of the rotational symmetry of there problem, a natural decoupling among different modes (index m). The resultant linear system matrix (impedance matrix) exhibits a block diagonal form and each mode can be treated separately, greatly reducing the computational effort to solve the overall problem. The impedance matrix equation for the m-th mode is expressed as:

$$\begin{bmatrix} Z_m^{tt} & Z_m^{t\phi} \\ Z_m^{\phi t} & Z_m^{\phi\phi} \end{bmatrix} \begin{bmatrix} I_m^t \\ I_m^\phi \end{bmatrix} = \begin{bmatrix} V_m^t \\ V_m^\phi \end{bmatrix} \qquad (7)$$

$$\left(Z_m^{pq}\right)_{ij} = \left\langle L(\vec{b}_{mj}^q), \vec{b}_{mi}^{p*} \right\rangle$$

$$\left(V_m^p\right)_i = \left\langle \vec{E}^{inc}, \vec{b}_{mi}^{p*} \right\rangle$$

where $\langle \, , \, \rangle$ denotes inner product. The right-hand side vector in (7) is called the excitation vector. Explicit expressions for the impedance matrix and excitation vector (plane-wave excitation) elements and can be found in [5]. The solution of the above matrix equation (7) determines the induced electric current according to (6).

The necessary number of modes in a specific problem can be determined from a convergence study. In case of plane-wave axial incidence only the m = ± 1 modes are excited.

III. B-Splines Basis Functions in BOR Analysis

In this section the use of cubic B-splines as the basis functions in t is discussed. The domain of interest is limited to the interval $[0,T_F]$, where T_F is the total arclenght of the generating curve. In order to construct cubic (order n=4, degree n−1=3) B-splines on this bounded interval the first step is to define a partition of K+1 nodal points (knots): { t_i }$_{i=1,K}$, where $0 = t_0 < ...< t_K = T_F$. In this work a uniform spaced partition will be used. Additional points are placed at the ends of the interval (multiple knots): $t_{-3} = t_{-2} = t_{-1} = 0$ and $t_{K+1} = t_{K+2} = t_{K+3} = T_F$.

Let's define :

$$\gamma_n(s;t) = (s-t)_+^{n-1} \equiv \begin{cases} (s-t)^{n-1} & s \geq t \\ 0 & s < t \end{cases} \qquad (8)$$

Then the (normalized) B-spline of order n is given as the n-th divided difference of $\gamma_n(s;t)$ in s on t_i , ..., t_{i+n} for fixed t [12], i. e.,

$$\beta_{n,i}(t) = (t_{i+n} - t_i)\gamma_n(t_i,...,t_{i+n};t), \quad \text{for all i} \qquad (9)$$

Fig.2 shows cubic B-splines (n = 4) on a unit interval with uniform spacing of five interior knots. Explicit expressions for (9) can be found in [13].

The above cubic B-splines present a series of potential advantages when used as a basis set. First, they have a local support which permits a fast evaluation of the integrals in (7). Second, they are smooth, having a spectrum concentrated at low frequencies, as the Fourier transform of the central B- spline of order n is given by

$$\beta_n(t) \leftrightarrow \text{sinc}^n(f) \quad \text{with} \quad \text{sinc}(f) = \sin \pi f / \pi f .$$ This is an important characteristic to fast convergence modeling of currents on smooth scatterers, as discussed in section I. B-splines are thus essentially limited both in the spatial (time) and the wavenumber (frequency) domains. Indeed, it can be shown [10] that B-splines converge to Gaussian functions pointwise as the order of the spline

tends to infinite. Gaussian functions are optimal in terms of time/frequency localization. The approximation error for the cubic case is already less than 3% and the variance product is already within 2% of the limit specified by the uncertainty principle (Fig. 3).

instabilities in the ϕ current component in regions where J_t dominates both equations in (5) [11], as will be shown in the next section.
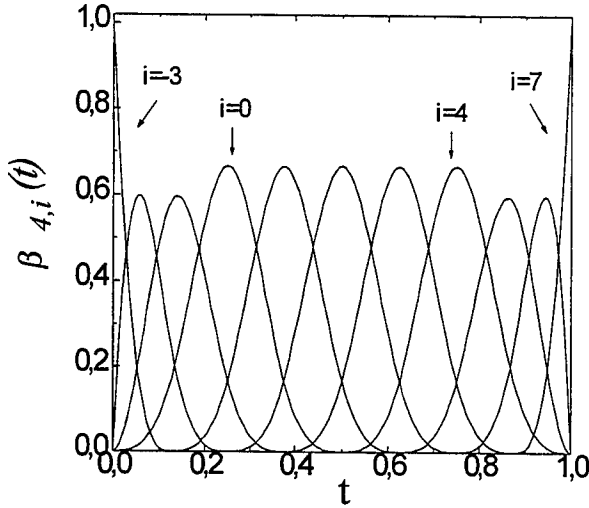
Fig. 2- B-splines basis functions in the unit interval with uniform spacing (K=8).
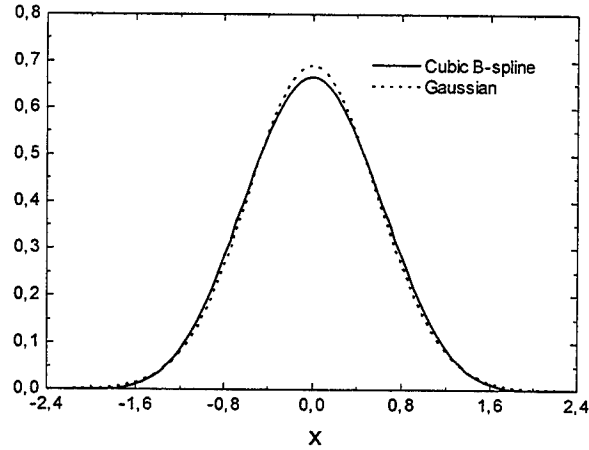
Fig. 3- Cubic B-spline with its corresponding Gabor approximation:
$\beta_4(x) \approx (1.5/\pi)^{1/2} \exp(-1.5x^2)$

A third attractive characteristic is that such bases are also local in the sense of a small degree of overlap, i. e. , at every point, except very near the ends of the interval, only three B-splines are non-zero. Moreover, through the use of multiple knots they tend to be more localized and to have a higher spectral content near the ends of the interval. This is just what is needed for an improved description of currents near the edges, where a singular behavior for the currents is expected.

Finally, the analytical simplicity of cubic B-splines is also of importance. In particular, its polynomial form permits a more accurate analytic extraction of singularities when evaluating the integrals that define the elements of the impedance matrix in (7) (see Appendix).

The expression for the basis functions in (6) in terms of the B-splines is written as:

$$f_i^t(t) = t\beta_{4,i-4}(t) \qquad i=1,...,K+n-2=N_t \qquad (10a)$$

$$f_i^\phi(t) = \beta_{4,i-4}(t) \qquad i=1,...,K+n-1=N_\phi \qquad (10b)$$

The factor t enforces a priori the condition J_t $(t=0) = 0$ in case of an edge at his point $(\rho(t=0) \neq 0)$ and cancels the factor $1/\rho(t)$ in case of $\rho(t=0) = 0$. It also avoids

Two other sets of basis functions are used in the examples of the next section. Entire-domain functions are defined by a series of sinusoids [3]:

$$f_i^t(t) = \sin(\frac{i\pi t}{T_f}) \qquad i=1,...,N_t \qquad (11a)$$

$$f_i^\phi(t) = \cos\left[\frac{(i-1)\pi t}{T_f}\right] \qquad i=1,..., N_\phi \qquad (11b)$$

Quasi-localized, bandlimited sampling-like functions, are defined as [7], [8]:

$$f_i^t(t) = t\mathrm{sinc}[\alpha(\kappa t - \tau_i)]\mathrm{sinc}(\kappa t - \tau_i)$$
$$i=1,...,N_t \qquad (12a)$$

$$f_i^\phi(t) = \mathrm{sinc}[\alpha(\kappa t - \tau_i)]\mathrm{sinc}(\kappa t - \tau_i)$$
$$i=1,..., N_\phi \qquad (12b)$$

with $\alpha = 0.3$, $\kappa = N_t /T_F$ and $\tau_i = (i - 1)$. The above functions are truncated at the first zero of the factor $\mathrm{sinc}[\alpha(\kappa t - \tau_i)]$. It gives a negligible degradation on the bandlimited characteristic of these functions, due to the fast decay $(1/d)^2$ they present from the middle-point.

In the examples studied (open bodies), the number of basis functions for t and ϕ components are

9

related through $N_\phi = N_t + 1$. As a consequence of this choice, the J_t component is forced *a priori* to satisfy the boundary condition at the edge, vanishing at $t = T_F$ (for the case of open bodies) in expansions (10)-(12).

IV. NUMERICAL RESULTS

In this section two numerical examples are presented. The first one involves the determination of the induced current on a 4 λ diameter infinitely thin circular disk. The axially incident electric field is a plane wave x-polarized (Fig. 4). In this case only the $m = \pm 1$ modes will be excited and the current will likewise be x-directed.
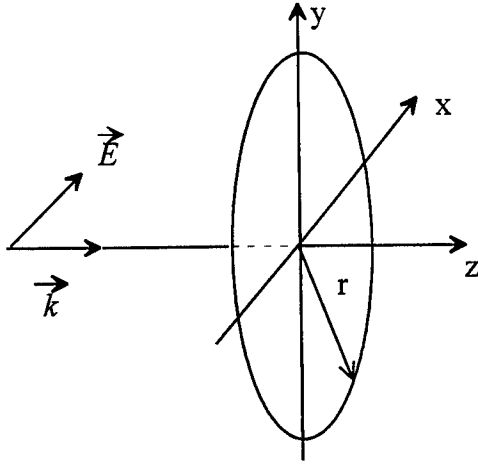
Fig. 4- PEC circular disk illuminated by an axially incident plane-wave

Figs. 5 (a) and (b) show the calculated current (normalized to $| \vec{H}^{inc} |$) when using the three basis sets with $N_t = 10, N_\phi = 11$. The current is t-directed at $\phi = 0^0$ and ϕ-directed at $\phi = 90^0$. For the t-component (Fig. 5(a)), the results obtained are virtually equivalent. The current shows an oscillation with a wavenumber $k \approx k_0$ around the value predicted by the physical optics approximation ($\vec{J}_{PO} = 2\hat{n} \times \vec{H}^{inc}$).

For the ϕ-component (Fig. 5(b)), the currents agree well except for the behavior near the edge. At this point the B-spline expansion produces a better modeling of the current singular behavior. This characteristic is present as the number of basis functions is increased. Fig. 6 illustrates the ϕ-component when employing basis functions with $N_\phi = 19$. The sinusoidal and the sampling-like sets give essentially the same results for the current. A small (apparently non-physical) oscillation in the ϕ-component for the sinusoidal and sampling-like sets can also be observed.

Regarding the CPU time involved in the calculation of the impedance matrix, the sinusoidal (entire-domain) set is clearly the most demanding. The disk is discretized by 20 segments. In each segment, a 5-point Gaussian quadrature is use to integrate over t. Having a spatial support Δ equal to T_F , a total of $100^2=(\Delta/T_F)^2$ integrand evaluations are required to calculate each term of an entire-domain impedance matrix element.
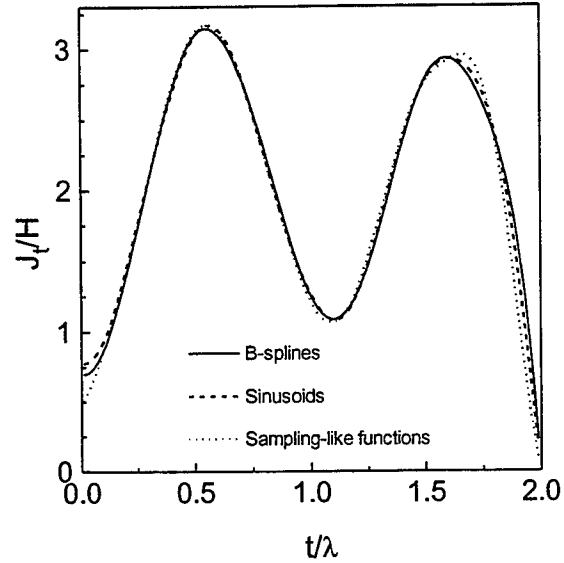
Fig. 5(a)- Induced t- component on a PEC disk. Ten functions used in t direction.
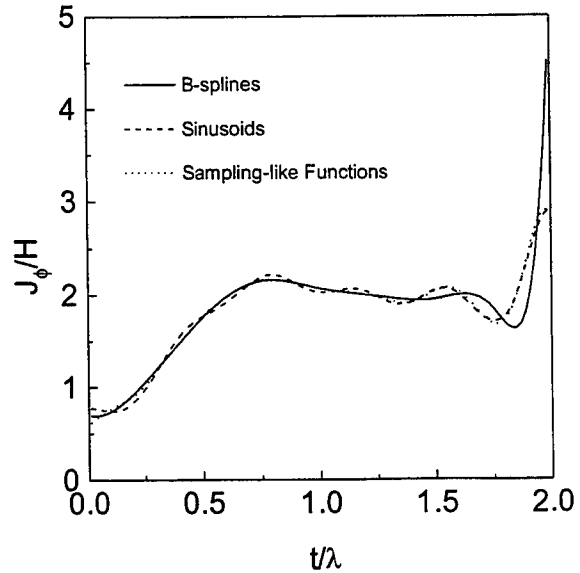
Fig. 5(b)- Induced ϕ- component on a PEC disk. Eleven basis functions used in ϕ direction.

10
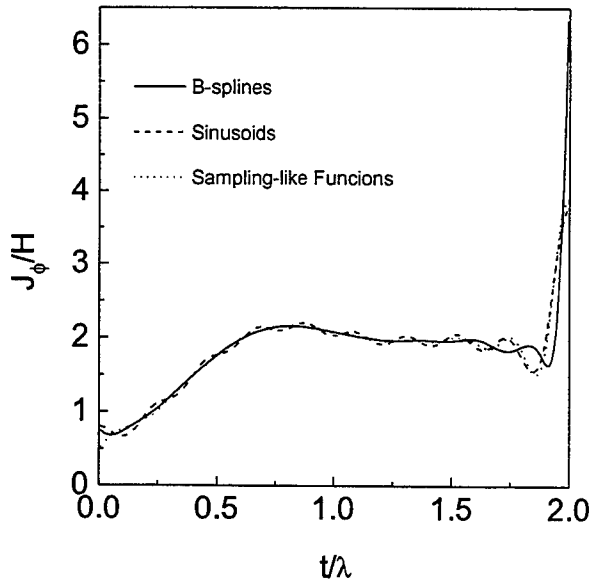
Fig. 6- Induced ϕ- component on a PEC disk. Nineteen basis functions used in ϕ direction.

observed in [11]. This is exactly what happens when B-splines are used without the factor t in the expansion (10a), as Fig. 8(a) depicts.

Fig. 7- Finite PEC hollow cylinder illuminated by an axially incident plane wave.

In the case of sampling-like functions the spatial support (except for the functions near the edge which have a smaller support) equals to $2/\alpha\kappa \approx 6.67 T_F /N_t$. When $N_t = 10$, a maximum of approximately $100^2 \times (6.67/10)^2$ integrand evaluations for each term in the impedance matrix elements are required, 44% of the entire-domain situation. When $N_t = 18$, this relative number is even smaller, $\approx 13.5\%$. For the B-spline case, the maximum spatial support equals to $T_F /2$ and $T_F /4$, respectfully. It corresponds to a number of integrand evaluations of 25% ($N_t = 10$) and 6.25% ($N_t = 18$), relative to the entire-domain situation. Table I illustrates those observations, showing the (normalized) overall CPU time required to fill the impedance matrix.

(normalized) CPU TIME		
BASIS FUNCTIONS	Nt = 10	Nt = 18
Sinusoids	0.32179	1.0000
Sampling-like	0.10246	0.10728
B-splines	0.05475	0.05560

TABLE I

The second numerical example comprises an axially incident plane-wave and a finite hollow cylinder with radius a and extending from $z = 0$ to L (Fig. 7). Twenty segments were used in the discretization of the generating curve. In this example, the strong coupling between the two component equations of EFIE (5) and the dominant behavior of the t-component may cause a spurious oscillatory behavior in the ϕ-component as

The non-enforcement a priori of the boundary condition J_t $(t = 0) = 0$ for this case also implies a spurious behavior of this component near $t = 0$ (Fig. 8(b)). In contrast, when the expansion in (11) is used, the spurious result are eliminated, as Figs. 8 (a) and (b) illustrate. Also superposed in these Figures are the currents calculated using sinusoidal functions. In all cases, $N_t = 10$. The same observations previously done with respect to the required CPU time for the matrix fill also apply for this example. Again, the description of the current near the edge with the use of B-splines with multiple knots is more accurate.
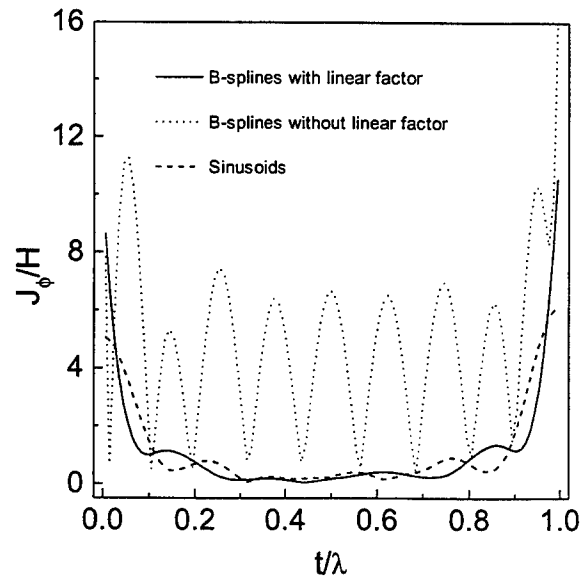
Fig. 8(a)- ϕ- component of the induced current on the hollow cylinder illuminated by an axially incident plane wave.

11
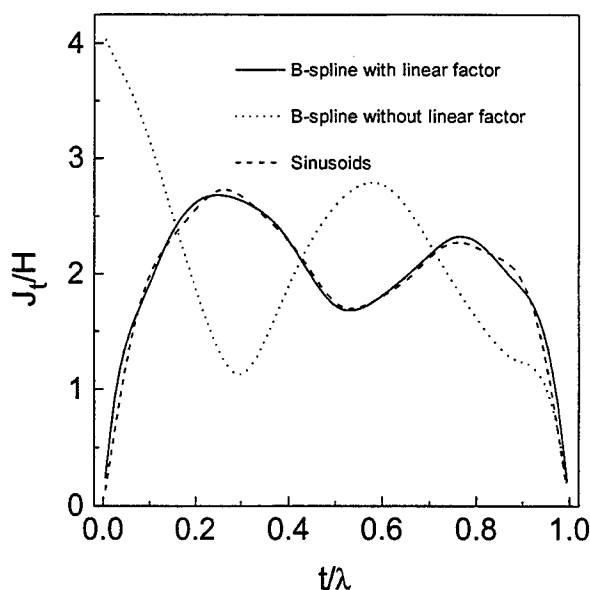
Fig. 8(b)- t- component of the induced current on the hollow cylinder illuminated by an axially incident plane wave.

V. CONCLUSIONS

An adequate choice for the basis functions is of great importance to the computational efficiency of the MoM solution. While a plethora of choices exists, two basic requirements should be satisfied by an efficient basis set: resemblance to the unknown current, thus leading to a convergent solution with few number of terms, and provision of a short computational time.

In this work, different choices for basis functions are addressed in the context of BoR scattering. Concepts like time and frequency localization, as well as the description of the current singularity near the edges, are discussed. It is shown that functions with a limited spectrum can lead to an economic representation in case of smooth BoRs, although near the edge the singular behavior can be overlooked. In this respect, the use of B-splines with multiple knots permitted a more accurate description at the edge. When impedance matrix fill time is compared, entire-domain functions present a basic limitation, as the fill time increases impressively with the number of unknowns. The possibility of eliminating the spurious behavior in the current due to the strong coupling in the EFIE components is investigated. In particular, a linear factor introduced for the t-component, is potentially capable of stabilizing the solution at the same time that it enforces, *a priori*, the boundary conditions.

Two other observations can be made with respect to the implementation of B-splines as basis functions. First, the use of an adaptive mesh grading (AMG) technique arises naturally with B-splines. It consists of concentrating the number of knots in critical regions where a faster variation in the solution is expected. This can be done by redistributing the knot points with respect to, e. g., a weighted combination of the arclength, curvature and edge proximity. Second, B-splines are also present in the context of Multiresolution Analysis (MRA). By using B-splines as a starting point (scaling functions) a sequence of "wavelet subspaces" can be generated [13], with asymptotic convergence to Gabor functions (modulated Gaussian) [10], which are optimally concentrated in both time and frequency domain.

REFERENCES

[1] R. F. Harrington, "The Method of Moments in Electromagnetics", *J. Electromag. Waves and Appl.*, vol.1, no.3, pp.181-200, 1987.

[2] L. N. Medgyesi-Mitschang and C. Eftimiu, "Scattering from Wires and Open Circular Cylinders of Finite Length Using Entire Domain Galerkin Expansions", *IEEE Trans. Antennas Propag.*, vol.30, no.4, pp.628-636, 1982.

[3] M. R. Barclay and W. V. T. Rusch, "Moment-Method Analysis of Large, Axially Symmetric Reflector Antennas Using Entire-Domain Functions" , *IEEE Trans. Antennas Propag.*, vol.39, no.4, pp.491-496, 1991.

[4] E. Alanen, "Pyramidal and Entire Domain Basis Functions in the Method of Moments", *J. Electromag. Waves and Appl.*, vol.5, no.3, pp.315-329, 1991.

[5] J. R. Mautz and R. F. Harrington, "Radiation and Scattering from Bodies of Revolution" , *Appl. Sci. Res.*, vol.20, pp.405-435, 1969.

[6] A. W. Glisson and D. R. Wilton, "Simple and Efficient Numerical Methods for Problems of Electromagnetic Radiation and Scattering from Surfaces", *IEEE Trans. Antennas Propag.*, vol.28, no.5, pp.593-603, 1980.

[7] G. F. Hermann, "Note on Interpolational Basis Functions in the Method of Moments", *IEEE Trans. Antennas Propag.*, vol.38, no.1, pp.134-137, 1990.

[8] F. L. Teixeira, J. R. Bergmann, "Global vs. Bandlimited Basis Functions in the Analysis of Axisymmetric Reflector Antennas", *IEEE Antennas Propag. Int. Symp. 1995 Digest*, vol.2, pp.1166-1169, 1995.

[9] D. R. Wilton and S. Govind, "Incorporation of Edge Conditions in Moment Method Solutions", *IEEE Trans. Antennas Propag.*, vol.25, no.6, pp.845-850, 1977.

[10] M. Unser, A. Aldroubi and M. Eden, "On the Asymptotic Convergence of B-Spline Wavelets to Gabor Functions" , *IEEE Trans. Information Theory*, vol.38, no.2, pp.864-872, 1992.

12

[11] W. A.Davis and R. Mittra, "A New Approach to the Thin Scatterer Problem Using the Hybrid Equations", *IEEE Trans. Antennas Propag.*, vol.25, no.3, pp.402-406, 1977

[12] C. de Boor, "On Calculating with B-Splines", *J. Approx. Theory*, vol. 6, pp.50-62, 1972.

[13] C. Goswami, A. K. Chan and C. K. Chui, "On Solving First-Kind Integral Equations Using Wavelets on a Bounded Interval", *IEEE Trans. Antennas Propag.*, vol.43, no.6, pp.614-622, 1995

APPENDIX

The objective of this appendix is twofold. First, it reviews the pseudo-analytic procedure used to remove singularities in the integrals that form the impedance matrix elements. Second, it shows how this singularity extraction can be done in a more exact manner by using B-splines.

The singular integrals that arise in the calculation of impedance matrix elements (7) have the following generic form [5] :

$$I = \int_0^{T_F} dt \int_0^{T_F} dt' \alpha_1(t)\alpha_2(t') \int_0^{\pi} d\phi \cos\phi \cos n\phi \frac{e^{-jkR}}{R}$$

where

$$R = \left[(\rho - \rho')^2 + (z - z')^2 + 4\rho\rho' \sin^2 \phi/2\right]^{1/2}$$

and $\alpha_1(t), \alpha_2(t)$ are functions that depend on the choice of basis functions. The above integral has a singularity at $\rho = \rho', z = z', \phi = 0$ which does not permit numerical integration. It is rewritten as:

$$I = \int_0^{T_F} dt \int_0^{T_F} dt' \alpha_1(t)\alpha_2(t')\left[\int_0^{\pi} d\phi(\cos\phi \cos n\phi \frac{e^{-jkR}}{R} - \frac{1}{R}) \right.$$

$$\left. + \int_0^{\pi} \frac{d\phi}{R} \right] = I_1 + I_2$$

I_1 is a proper integral and the singularity is isolated in I_2. Define: $R_1 = \left[(\rho - \rho')^2 + (z - z')^2\right]^{1/2}$,

$\beta_1 = \frac{2\sqrt{\rho\rho'}}{R_1}$ and $\xi = \phi/2$; Then:

$$I_2 = 2 \int_0^{T_F} dt \int_0^{T_F} dt' \alpha_1(t)\alpha_2(t') \int_0^{\pi/2} \frac{d\xi}{R_1\sqrt{(1 + \beta_1^2 \sin^2 \xi)}}$$

$$= 2 \int_0^{T_F} dt \int_0^{T_F} dt' \alpha_1(t)\alpha_2(t') \frac{K(\beta_2)}{R_2}$$

with $R_2 = \left[(\rho + \rho')^2 + (z - z')^2\right]^{1/2}$; $\beta_2 = \frac{2\sqrt{\rho\rho'}}{R_2}$

where $K(\beta_2)$ is the complete elliptical integral of the first kind. The integral in ϕ was solved, but the above integral is still singular when $\rho = \rho'$ and $z = z'$ (equivalently, $t = t'$). The behavior of $K(\beta_2)$ as $t \to t'$ is given by:

$$\lim_{t \to t'} \frac{K(\beta_2)}{R_2} = \frac{1}{2\rho}\left[\ell n4 + \ell nR_2 - \ell nR_1\right]$$

Only the last term is singular. It is added and subtracted so that I_2 is written as:

$$I_2 = I_{21} - I_{22} = 2\int_0^{T_F} dt \int_0^{T_F} dt' \alpha_1(t)\alpha_2(t')\left[\frac{K(\beta_2)}{R_2} + \frac{\ell nR_1}{2\rho}\right]$$

$$- \int_0^{T_F} dt \int_0^{T_F} dt' \alpha_1(t)\alpha_2(t') \frac{\ell nR_1}{\rho}$$

I_{21} is a proper integral and can be numerically calculated. I_{22} is written as:

$$I_{22} = \frac{1}{2}\int_0^{T_F} dt \frac{\alpha_1(t)}{\rho} \sum_{i=1}^N \int_{\varepsilon_i} dt' \alpha_2(t')\ell nR_{1,i}^2$$

where the interval $[0, T_F]$ was divided in N subintervals. Each subinterval defines a segment of the generating curve C where the dependency of ρ' and z' with t' is linearized: $\rho' = \rho_i' + a_i(t' - t_i')$; $z' = z_i' + b_i(t' - t_i')$ and $R_{1,i}^2 = (t' - t_{0i})^2 + t_{1i}^2$ with $t_{0i} = t_{0i}(t_i', z_i', \rho_i', a_i, b_i)$ and $t_{1i} = t_{1i}(z_i', \rho_i', a_i, b_i)$. In each segment ε_i the function $\alpha_2(t')$ is proportional to the basis function $f_i^p(t')$. The integrals over each ε_i can be evaluate through a local approximation: $\alpha_2(t') \approx a_0 + a_1t' + a_2t'^2 + a_3t'^3$ since integrals of the form

$$I_{22i} = \int t^n \ell n\left[(t - t_0)^2 + t_1^2\right] dt \quad n=0,1,2,3.$$

are tabulated. With the use of B-splines, the coefficients of the local polynomial approximation equal the B-spline coefficients and thus no further numerical error is introduced.

Electromagnetic Properties of a Chiral-Plasma Medium

Hector Torres-Silva[(1)], Norma Reggiani, and Paulo H. Sakanaka

Instituto de Física 'Gleb Wataghin',
Universidade Estadual de Campinas, UNICAMP,
13083-970, Campinas, São Paulo, Brazil.
[(1)]Leave-of-absence from Universidad de Tarapaca,
Faculdad de Ingenieria, Dep. de Eletronica
Casilla 6-D, Av. 18 de Septiembre 2222, Arica - Chile

Abstract- The theoretical properties of a composite chiral-plasma medium are developed. Using the reaction theorem, we obtain the proof of nonreciprocity based upon the constitutive relationships between the electromagnetic vectors $\vec{E}$, $\vec{B}$, $\vec{H}$, $\vec{D}$. Using the Maxwell's equations and the proposed constitutive relations for a chiral-plasma medium, we derive the $\vec{E}$ and $\vec{H}$ vector equations and from these equations, dispersion relations and $\vec{E}$-field polarizations are found.

Keywords: wave polarization, Faraday rotation, chiral-plasma medium

INTRODUCTION.

Chiral medium [1,2] and ferrite medium [3] have been studied over the last decade for many applications. Chiral-medium have been examined as coating for reducing radar cross section, for antennas and arrays, for antenna radomes in waveguides and for microstrip substrate. Here, we examine a chiral-plasma medium, where the plasma part of the composite medium is non-reciprocal due to the external magnetic field. To find the general dispersion relation giving ω against $\vec{k}$ behavior, the vector phasor Helmholtz based equations are derived. We determine the modal eigenvalue properties in the chiral-plasma medium, which is doubly anisotropic. For the case of waves which propagate parallel to the magnetic field it is a cold magnetized chiro-plasma. We compare our results with the typical results obtained for a cold plasma [4]. Also we obtain the chiral-Faraday rotation which can be compared with the typical Faraday rotation for a pair of right- and left-handed circularly polarized waves.

THEORETICAL FOUNDATIONS.

We propose the following constitutive relations for chiral-plasma medium

$$\vec{D} = \overleftrightarrow{\epsilon} \cdot \vec{E} + t_1\vec{H} \qquad (1)$$

$$\vec{B} = \mu\vec{H} + t_2\vec{E} \qquad (2)$$

Plasma medium constitutive relations are [4]

$$\vec{D}_p = \overleftrightarrow{\epsilon}_p \cdot \vec{E}_p \qquad (3)$$

$$\vec{B}_p = \mu_0\vec{H}_p \qquad (4)$$

where

$$\overleftrightarrow{\epsilon}_p = \begin{vmatrix} \epsilon_1 & i\epsilon_2 & 0 \\ -i\epsilon_2 & \epsilon_1 & 0 \\ 0 & 0 & \epsilon_3 \end{vmatrix} \qquad (5)$$

where $\overleftrightarrow{\epsilon}$ and $t_{1,2}$ represent the permittivity tensor and chirality parameters of the composite medium, respectively. The lossless character of the magnetized cold plasma medium is implied by the Hermitian nature of the tensor $(\overleftrightarrow{\epsilon}_p^*)^T = \overleftrightarrow{\epsilon}_p$. The superscripts $*$ and T denote complex conjugate and transpose, respectively.

In the search for new medium, which displays non-reciprocal properties, it is essential to establish the nature of the chirality parameters t_1 and t_2. The anisotropic reaction theorem [5] is

$$\int \vec{E}_b \cdot \vec{J}_a dv = \int \vec{E}_a \cdot \vec{J}_b dv \qquad (6)$$

Here, we see that source currents $\vec{J}_a$ and $\vec{J}_b$ produce fields $\vec{E}_a$, and $\vec{E}_b$, respectively, and the *tilde* over the fields indicates a new medium altered from the original medium, thus, we obtain 6×6 constitutive tensors

$$\tilde{A} = \begin{vmatrix} \hat{\epsilon}^T & -\hat{t}'^T \\ -\hat{t}^T & \hat{\mu}^T \end{vmatrix} \qquad (7)$$

and

$$\hat{A} = \begin{vmatrix} \hat{\epsilon} & -\hat{t} \\ -\hat{t}' & \hat{\mu} \end{vmatrix} \qquad (8)$$

with $\hat{t}$ and $\hat{t}'$ being the optical activity 3×3 tensors.

Reciprocity occurs only if

$$\int \vec{E}_b \cdot \vec{J}_a \, dv = \int \vec{E}_a \cdot \vec{J}_b \, dv$$

that is, by (6) it requires that

$$\tilde{A} = \hat{A} \qquad (9)$$

For chiral medium we must obtain

$$\hat{\epsilon} = 0, \quad \hat{t} = t_1 I, \quad \hat{t}' - t_2 I, \quad \hat{\mu} = 0 \qquad (10)$$

To obtain reciprocity, (9) imposes

$$-t_2 I^T = t_1 I, \quad -t_1 I^T = t_2 I \qquad (11)$$

that is,

$$t_1 = -t_2 \qquad (12)$$

For plasma medium (3) and (4) hold leading to

$$\hat{\epsilon} = \overleftrightarrow{\epsilon}, \quad \hat{t} = \hat{t}' = 0, \quad \hat{\mu} = \mu_0 = 1. \qquad (13)$$

Then for the proposed constitutive relations ((1) and (2)) we have

$$\vec{D} = \overleftrightarrow{\epsilon} \cdot \vec{E} + t_1 \vec{H} \qquad (14)$$
$$\vec{B} = \mu_0 \vec{H} + t_2 \vec{E} \qquad (15)$$

Vector Helmholtz Equations

The E-field vector Helmholtz equation is derived by inserting the constitutive relation (14) and (15) into Maxwell's equations

$$\nabla \times \vec{E} = -i\omega \vec{B} \qquad (16)$$
$$\nabla \times \vec{H} = i\omega \vec{D} + \vec{J} \qquad (17)$$

so

$$\nabla \times \vec{E} = -i\omega \mu_0 \vec{H} - i\omega t_2 \vec{E} \qquad (18)$$
$$\nabla \times \vec{H} = i\omega \overleftrightarrow{\epsilon} \cdot \vec{E} + i\omega t_1 \vec{H} \qquad (19)$$

Solving for $\vec{H}$, (18) gives

$$\vec{H} = \frac{1}{\mu_0} \left(\frac{i}{\omega} \nabla \times \vec{E} - t_2 \vec{E} \right) \qquad (20)$$

and putting this into (19) we obtain

$$\nabla \times \vec{H} = \frac{1}{\mu_0} \frac{i}{\omega} (\nabla \times \nabla \times \vec{E}) - \frac{t_2}{\mu_0} \nabla \times \vec{E} \qquad (21)$$

Then the $\vec{E}$-field vector equation is given by

$$\nabla \times \nabla \times \vec{E} + i\omega(t_2 - t_1)\nabla \times \vec{E}$$
$$-\omega^2 \mu_0 \epsilon_0 \left(\frac{\overleftrightarrow{\epsilon}}{\epsilon_0} - \frac{t_1 t_2}{\mu_0 \epsilon_0} \right) \cdot \vec{E} = 0 \qquad (22)$$

Here, the plasma current is included in the permittivity tensor $\overleftrightarrow{\epsilon}$.

Similarly the $\vec{H}$-field equation is given by

$$\nabla \times \overleftrightarrow{\epsilon}^{-1} \nabla \times \vec{H} + i\omega(t_2 \overleftrightarrow{\epsilon}^{-1} \nabla \times \vec{H} - t_1$$
$$\nabla \times \overleftrightarrow{\epsilon}^{-1} \times \vec{H}) - \omega^2 \mu_0 \left(I - \frac{t_1 t_2}{\mu_0} \overleftrightarrow{\epsilon}^{-1} \right) \vec{H} = 0 \quad (23)$$

The inverse permittivity tensor is given by

$$\overleftrightarrow{\epsilon}^{-1} = \begin{vmatrix} \epsilon_1 & -i\epsilon_2 & 0 \\ i\epsilon_2 & \epsilon_1 & 0 \\ 0 & 0 & \frac{\epsilon_1^2 - \epsilon_2^2}{\epsilon_3} \end{vmatrix} \qquad (24)$$

Dispersion Relation.

Dispersion relation for the propagation vector $\vec{k}$ against ω can be obtained from $\vec{E}$- or $\vec{H}$-vector equation. We start with the $\vec{E}$-field relation which is simpler than the $\vec{H}$-equation.

Defining $\vec{E}$ as

$$\vec{E} = \vec{E}_0 e^{-i\vec{k} \cdot \vec{r}} \qquad (25)$$

We obtain

$$-\vec{k} \times \vec{k} \times \vec{E}_0 + \omega(t_2 - t_1)\vec{k} \times \vec{E}_0$$
$$-\omega^2 \mu_0 \epsilon_0 \left(\frac{\overleftrightarrow{\epsilon}}{\epsilon_0} - \frac{t_1 t_2}{\mu_0 \epsilon_0} \right) \vec{E}_0 = 0 \qquad (26)$$

Putting $\vec{E}_0$ into rectangular coordinates

$$\vec{E}_0 = E_x \hat{x} + E_y \hat{y} + E_z \hat{z} \qquad (27)$$

we obtain a three component system of equations which determine the eigenvector, and the determinant of the coefficient component matrix M_k will determine the eigenvalues, thereby yielding the ω against $\vec{k}$ dispersion diagram in phase-space. Writing $Det(M_k) = 0$, with $k_x = 0$ and with symmetry about the z-axis we obtain

$$\begin{vmatrix} 1 - \dfrac{\epsilon_1}{n^2\epsilon_0}\left(1 - \dfrac{t_1 t_2}{\mu_0\epsilon_1}\right) & -\dfrac{i\epsilon_2}{n^2\epsilon_0} - \dfrac{\cos\theta(t_2 - t_1)}{n\sqrt{\mu_0\epsilon_0}} & \dfrac{\sin\theta(t_2 - t_1)}{n\sqrt{\mu_0\epsilon_0}} \\[2mm] \dfrac{i\epsilon_2}{n^2\epsilon_0} + \dfrac{\cos\theta(t_2 - t_1)}{n\sqrt{\mu_0\epsilon_0}} & \cos^2\theta - \dfrac{\epsilon_1}{n^2\epsilon_0}\left(1 - \dfrac{t_1 t_2}{\mu_0\epsilon_1}\right) & -\sin\theta\cos\theta \\[2mm] -\dfrac{\sin\theta(t_2 - t_1)}{n\sqrt{\mu_0\epsilon_0}} & -\sin\theta\cos\theta & sin^2\theta - \dfrac{\epsilon_3}{n^2\epsilon_0}\left(1 - \dfrac{t_1 t_2}{\epsilon_3\mu_0}\right) \end{vmatrix} = 0 \quad (28)$$

Here, the refractive index n is defined as

$$n = \frac{ck}{\omega}, \quad \text{where} \quad c = \frac{1}{\sqrt{\mu_0\epsilon_0}}.$$

If $\mu_0 = 1$, $\epsilon_0 = 1$, $t_1 = t_2 = 0$ we obtain the same results given by Krall and Trivelpiece for a magneto-plasma [4].

For a lossless chiroplasma, i.e., $t_1 = it\sqrt{\mu_0\epsilon_0}$ and $t_2 = -it\sqrt{\mu_0\epsilon_0}$, the non-trivial solution of this system comes from setting the determinant of the coefficients equal to zero, giving

$$f(0) = F(n^2, \omega, \epsilon_1, \epsilon_2, t, \epsilon_3, k) \quad (29)$$

Equation (29) is then the general dispersion relation for waves propagating in a cold collisionless homogeneous chiroplasma in a uniform magnetic field. For given plasma frequency ω_p, cyclotron frequency ω_c, wave frequency ω and direction of propagation θ, (29) can be solved for the index of refraction n, having as parameter the chirality t.

In terms of k, the dispersion relation is given by

$$a_1 k^4 + a_2 k^3 + a_3 k^2 + a_4 k + a_5 = 0 \quad (30)$$

where

$$a_1 = -\left[\omega^2\epsilon_1\mu_0\left(1 - \frac{t^2\epsilon_0}{\epsilon_1}\right) sin^2\theta \quad (31)\right.$$
$$\left. -\omega^2\epsilon_3\mu_0\left(1 - \frac{t^2\epsilon_0}{\epsilon_3}\right) cos^2\theta \right]$$

$$a_2 = 0 \quad (32)$$

$$a_3 = w^4\mu_0^2\left[\epsilon_1\epsilon_3\left(1 - \frac{t^2\epsilon_0}{\epsilon_1}\right)\left(1 - \frac{t^2\epsilon_0}{\epsilon_3}\right)\right] \quad (33)$$
$$w^4\mu_0^2\left[\epsilon_1\epsilon_3\left(1 + \frac{3t^2\epsilon_0}{\epsilon_1}\right)\left(1 - \frac{t^2\epsilon_0}{\epsilon_3}\right)\right]cos^2\theta$$
$$w^4\mu_0^2\left[\left(\epsilon_1\left(1 + \frac{t^2\epsilon_0}{\epsilon_1}\right)\right)^2 - \epsilon_2^2 - 4\epsilon_0^2 t^4\right]sin^2\theta$$

$$a_4 = -4\mu_0^2\sqrt{\mu_0\epsilon_0}\,w^5 t\epsilon_2\epsilon_3\left(1 - \frac{t^2\epsilon_0}{\epsilon_3}\right)cos\theta \quad (34)$$

$$a_5 = \mu_0^3 w^6\left[\epsilon_3\left(\epsilon_2^2 - \epsilon_1^2\right)\left(1 - \frac{t^2\epsilon_0}{\epsilon_3}\right)\right. \quad (35)$$
$$\left. +2\epsilon_0 t^2\epsilon_1\left(\epsilon_3 - \epsilon_0 t^2\right) - \epsilon_0^2 t^4\left(\epsilon_3 - \epsilon_0 t^2\right)\right]$$

Here, there are four different eigenmodes for $\vec{k}$ as implied by (30). The components of the permittivity tensor are obtained using the constitutive equations (14) and (15), and are given by:

$$\epsilon_1 = 1 - t^2 - \frac{w_p^2}{w^2 - w_{ce}^2} \quad (36)$$

$$\epsilon_2 = \frac{w_{ce}}{w}\frac{w_p^2}{w^2 - w_{ce}^2} \quad (37)$$

$$\epsilon_3 = 1 - t^2 - \frac{w_p^2}{w^2}, \quad (38)$$

where w_p is the plasma frequency and w_{ce} is the electron gyrofrequency given by:

$$w_p^2 = \frac{4\pi n_e e^2}{m_e} \quad (39)$$

$$\omega_{ce} = \frac{eB_0}{m_e c}. \quad (40)$$

We can observe that for $t = 0$ we obtain the same expressions given by Krall and Trivelpiece [4] for a plasma medium.

HIGH-FREQUENCY WAVES WITH $\vec{k} \parallel \vec{B}_0$ AND $\vec{k} \perp \vec{B}_0$.

Setting $\theta = 0$, it is possible to find circularly polarized waves from (28) by writing the $\vec{E}$-field vector equation in the form

$$(n^2 - \epsilon_R)E_R = 0,$$
$$(n^2 - \epsilon_L)E_L = 0,$$
$$\epsilon_3\left(1 - \frac{t^2}{\epsilon_3}\right)E_z = 0 \quad (41)$$

where

$$\epsilon_{R,L} = \epsilon_1\left(1 - \frac{t^2}{\epsilon_1}\right) \pm \epsilon_2\left(1 - \frac{2tn}{\epsilon_2}\right) \quad (42)$$

16

and

$$E_{R,L} = E_x \pm iE_y. \quad (43)$$

It is useful to explore these solutions in terms of the wavenumbers k_R and k_L given by

$$k_R = \frac{t\omega}{c} \pm \frac{\omega}{c}\sqrt{\epsilon_1 - \epsilon_2} \quad (44)$$

and

$$k_L = -\frac{t\omega}{c} \pm \frac{\omega}{c}\sqrt{\epsilon_1 + \epsilon_2} \quad (45)$$

where k_R is the wave number for a circularly polarized wave which drives electrons in the direction of their cyclotron motion, i.e., right circularly polarized waves and k_L is the wave number for a circularly polarized wave which drives electrons in the direction opposite to their cyclotron motion, i.e., left circularly polarized waves. The t parameter modifies the typical plot of $\omega(k)$ shown by Kral and Trivelpiece, where the cutoff frequencies are shifted. In Figure 1 we present the modifications introduced by the parameter t in the dispersion relations of the right and left polarized waves. In this Figure the dispersion relations of the right and left circularly polarized waves are indicated by circles and stars, respectively. When $t \neq 0$, ϵ_1 and ϵ_3 depend on t and k_R and k_L have a linear term, $t\omega/c$, as can be seen in (44) and (45). In this way, rather than to modify the curves that exist for $t = 0$, the parameter t permits that the wave propagates in a region of frequencies that is forbidden in the case $t = 0$. Another effect caused by the presence of the parameter t is a conversion of modes. We can observe in Figure 1 that for $t = 0$, there is no intersection of the dispersion relations of the right and left circularly polarized waves. When $t \neq 0$ we can observe that there is an intersection of these curves, indicating that the presence of the t parameter permits that a wave changes its polarization.

In Figure 1 for $t = 0$ we can also observe that there is a region where only right circularly polarized waves propagate, a region where only left circularly polarized waves propagate and a region where both propagate. If their amplitudes are equal, the effect of the superposition of a left and right circularly polarized wave is to produce a plane wave with a particular plane of polarization. Because the two polarizations propagate at different velocities, the plane of polarization rotates as the wave propagates along the magnetic field. This effect is called Faraday rotation.

The global rotation of the plane of polarization as a function of distance in the direction of propagation is given by

$$\frac{E_x}{E_y} = \cot\left(\frac{k_L - k_R}{2}\right)z. \quad (46)$$

which means that the presence of the t parameter affects also the Faraday rotation. The chiral-Faraday rotation can be used as a plasma probe. In a laboratory experiment this would be done by launching a planewave along the magnetic field in a chiroplasma. Considering that the plane of polarization of this wave can be determined by an antenna and that we know the magnetic field, the density of the plasma and the frequency of the launched wave, the measurement of the plane of polarization away from the source can determine the value of the parameter t. For instance, considering for the plasma frequency, $w_p = 5s^{-1}$, for the electron gyrofrequency, $w_{ce} = 2s^{-1}$, and for the launched wave, $w = 6.5s^{-1}$, the value of the plane of polarization 10 mm away from the source is $E_x/E_y = 85.76$, $E_x/E_y = 118.17$ and $E_x/E_y = 186.11$ for $t = 0$, $t = 0.05$ and $t = 0.1$, respectively.

Setting $\theta = \pi/2$, we obtain the following dispersion relations:

$$k_X = \pm\frac{\sqrt{A - \sqrt{B}}}{\sqrt{2(\epsilon_1 - t^2)}} \quad (47)$$

and

$$k_O = \pm\frac{\sqrt{A + \sqrt{B}}}{\sqrt{2(\epsilon_1 - t^2)}}, \quad (48)$$

where

$$A = \frac{\omega^2}{c^2}\left[\epsilon_1^2 - \epsilon_2^2 + \epsilon_1\epsilon_3 + t^2(\epsilon_1 - \epsilon_3) - 2t^4\right] \quad (49)$$

and

$$\begin{aligned} B = & \frac{\omega^4}{c^4}\Big[\left((\epsilon_1^2 - \epsilon_2^2) - \epsilon_1\epsilon_3\right)^2 + \\ & t^2(6\epsilon_1^3 - 6\epsilon_1\epsilon_2^2 - 2\epsilon_1\epsilon_3^2 + 12\epsilon_1^2\epsilon_3 - 2\epsilon_2^2\epsilon_3) + \\ & t^4(-15\epsilon_1^2 + 8\epsilon_2^2 - 18\epsilon_1\epsilon_3 + \epsilon_3^2) + \\ & 8t^6(\epsilon_1 + \epsilon_3)\Big] \end{aligned} \quad (50)$$

It should be pointed out that the eletric field of the extraordinary wave, k_X is perpendicular to the magnetic field and the eletric field of the ordinary wave, k_O, is parallel to the magnetic field.

In Figure 2 we present the effect of the parameter t on the dispersion relations for the case $\theta = \pi/2$. In this Figure the ordinary and extraordinary waves are indicated by circles and stars, respectively. When $t = 0.05$, for $\theta = \pi/2$, the effect of the parameter is very small. We can observe that the dispersion relations are a little modified, but the parameter is not able to break up the forbidden regions that exist when $t = 0$. When $t = 0.5$, the dispersion relations show very different curves with respect to the curves for $t = 0$, and there is no more bands of forbidden frequencies.

The difference in the way the t parameter acts in the parallel and perpendicular directions is due to the kind of equations we have. In (44) and (45) the t parameter appears as a linear term and in (47) and (48) the t parameter appears just inside a square root. We observe also that for $\theta = \pi/2$ the parameter t does not lead to the conversion of modes, as it happens for $\theta = 0$.

REFERENCES

[1] D. L. Jaggard, J. C. Liu, and X. Sun, *Electron. Lett.*, **27**, 77, (1991).

[2] C. M. Krowne, *IEE Proceedings-H*, Vol. **140**, 242, (1993).

[3] N. Engheta and P. Pelet, *Optical Letters*, **14**, 593, (1989).

[4] N. A. Krall and A. K. Trivelpiece, *"Principles of Plasma Physics"*, McGraw Hill, (1973).

[5] C. M. Krowne, *IEEE Trans. Antennas Propag.*, **32**, 1273 (1984).

Figure 2: Dispersion relations for various values of the parameter t when the direction of propagation is perpendicular to the magnetic field ($\theta = \pi/2$).

Figure 1: Dispersion relations for various values of the parameter t when the direction of propagation is parallel to the magnetic field ($\theta = 0$). W is the angular frequency normalized to hte plasma frequency.

MTRT - A Modified Transverse Resonance Technique

Alfrêdo Gomes Neto †, Creso S. da Rocha ‡, Hervé Aubert #, D. Bajon #, H. Baudrand #
†CEFET-PB, Av. 1 de maio, 720, João Pessoa, PB, 58015-430, BRAZIL
‡DEE, UFPB, Cx.Postal 10053, Campina Grande, PB, 58109-970, BRAZIL
Lab. d'Electronique, ENSEEIHT, 2 rue C. Chamichel, Toulouse, FRANCE

Abstract — **In this work a modified formulation of the transverse resonance technique (TRT) is presented. The difference between the usual TRT and the formulation presented here, MTRT, is the equivalent network considered. With the MTRT proposed formulation, mode solution identification requires less arduous work. The complete equation set is described. Numerical results are presented for dispersion characteristics of microstrip lines, coupled microstrip lines and conductor-backed coplanar waveguides (CBCW). When compared to results obtained by other methods, a good agreement is observed.**

I. INTRODUCTION

The recent developments made in microwave and millimeter-wave circuits (MIC), especially in the monolithic form (MMIC) where it is very difficult to tune the circuits once they are fabricated, have required extremely accurate computer aided design (CAD) programs [1]. Along with this, the considerable advances in computers have allowed a rapid evolution of the usual numerical techniques. In this sense, a modified formulation of the transverse resonance technique (MTRT) is presented in this work. One of the advantages of the MTRT, when compared to the usual TRT, is the possibility of analyzing open side structures exactly, without the use of auxiliary geometry, which permits considerable reduction in the work for mode solutions identification. Numerical results are presented for dispersion characteristics of microstrip lines, coupled microstrip lines and conductor-backed coplanar waveguides (CBCW). When compared to results obtained by other methods, a good agreement is observed.

II. THEORY

In the conventional formulation of the TRT, a suitable equivalent network is established, representing discontinuity planes and boundary conditions, to compute the cutoff frequencies and possibly some additional characteristics of the structures [2]. The difference between the conventional and the modified TRT is the equivalent network adopted. In the TRT, the discontinuity planes are parallel to the conductor

strips (Fig. 1), whereas in the MTRT they are perpendicular (Fig. 2). Figures 1 and 2 present equivalent networks and respective matrix admittances for a microstrip. Mode coupling, that occurs at each discontinuity, is represented by generic voltage sources. The different transmission line sections represent the different waveguide sections (in

$$[Y] = [[Ya] + [Yb]]$$
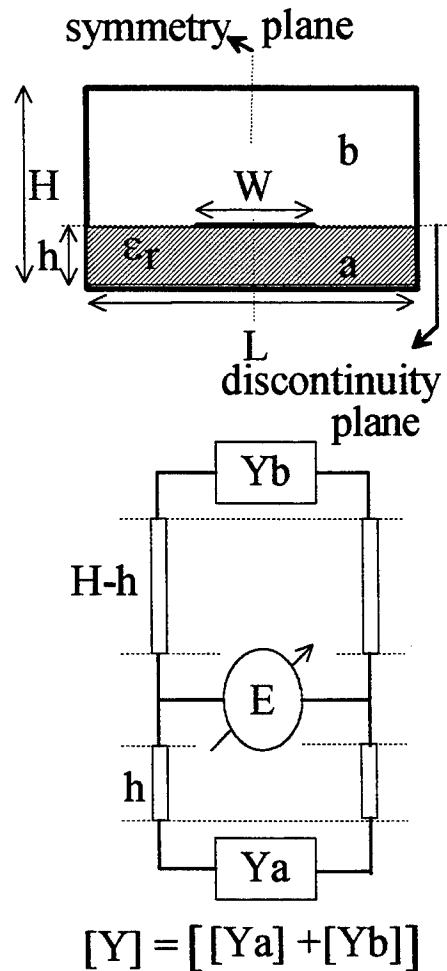
Figure 1: TRT

the MTRT case, two homogeneous waveguides (**a** and **b**) and one inhomogeneous (**cd**)). The admit-

tances $(Y_{a,b,cd})$ represent the boundary conditions.

symmetry plane

discontinuity plane

$$[Y] = \begin{bmatrix} [Ya] + [Y^a_{cd}] & [Y^{ab}_{cd}] \\ [Y^{ba}_{cd}] & [Yb] + [Y^b_{cd}] \end{bmatrix}$$

Figure 2: MTRT

The matrix admittance $[Y]$ is obtained by the use of Kirchhoff's laws and it is deduced in the following way:

$$[J_a] - [J'] = [Y_a][E_a] \qquad (1)$$

$$[J_b] - [J'] = [Y_b][E_b] \qquad (2)$$

$$[J'] = [Y_{cd}]([E_a] + [E_b]) \qquad (3)$$

Substituing (3) into (1) and (2) yields

$$[J_a] - ([Y_{cd}]([E_a] + [E_b])) = [Y_a][E_a] \qquad (4)$$

$$[J_b] - ([Y_{cd}]([E_a] + [E_b])) = [Y_b][E_b] \qquad (5)$$

The equations (4) and (5) can be rewritten as

$$[J_a] = ([Y_a] + [Y_{cd}])[E_a] + [Y_{cd}][E_b] \qquad (6)$$

$$[J_b] = [Y_{cd}][E_a] + ([Y_b] + [Y_{cd}])[E_b] \qquad (7)$$

or in the matrix form

$$\begin{bmatrix} [J_a] \\ [J_b] \end{bmatrix} = \begin{bmatrix} ([Y_a] + [Y_{cd}]) & [Y_{cd}] \\ [Y_{cd}] & ([Y_b] + [Y_{cd}]) \end{bmatrix} \begin{bmatrix} [E_a] \\ [E_b] \end{bmatrix} \qquad (8)$$

If it is assumed that suitable inner products $(\langle \,|\, \rangle)$ can be determined, equation (8) may be written as

$$\begin{bmatrix} [J_a] \\ [J_b] \end{bmatrix} =$$

$$\begin{bmatrix} \langle \,|\, \rangle ([Y_a] + [Y_{cd}]) \langle \,|\, \rangle & \langle \,|\, \rangle [Y_{cd}] \langle \,|\, \rangle \\ \langle \,|\, \rangle [Y_{cd}] \langle \,|\, \rangle & \langle \,|\, \rangle ([Y_b] + [Y_{cd}]) \langle \,|\, \rangle \end{bmatrix}$$

$$\begin{bmatrix} [e_a] \\ [e_b] \end{bmatrix}$$

$$(9)$$

Note that when $\langle \,|\, \rangle [Y]_{cd} \langle \,|\, \rangle$ involves only testing function in the region $a(b)$ the notation $\langle \,|\, \rangle [Y_{cd}^{a(b)}] \langle \,|\, \rangle$ is adopted. The notation $\langle \,|\, \rangle [Y_{cd}^{ab}] \langle \,|\, \rangle$, or $\langle \,|\, \rangle [Y_{cd}^{ba}] \langle \,|\, \rangle$, is adopted to indicate that testing functions in regions a and b are used in the inner products. In Fig. 2, the inner product symbol, $\langle \,|\, \rangle$, is omitted. Matrix terms are detailed in the following equations.

$$[Y_{\nu_1}] = \sum_{n=0}^{n\nu_1} \begin{bmatrix} [Y_{\nu_1,n(yy)}] & [Y_{\nu_1,n(yz)}] \\ [Y_{\nu_1,n(zy)}] & [Y_{\nu_1,n(zz)}] \end{bmatrix} \qquad (10)$$

$$[Y_{\nu_1,n(yy)}] = \langle \phi_y^{\nu_1} | f_{y,n}^{\nu_1} \rangle Y_{\nu_1,n} \langle f_{y,n}^{\nu_1} | \phi_y^{\nu_1} \rangle \qquad (11)$$

$$[Y_{\nu_1,n(yz)}] = \langle \phi_y^{\nu_1} | f_{y,n}^{\nu_1} \rangle Y_{\nu_1,n} \langle f_{z,n}^{\nu_1} | \phi_z^{\nu_1} \rangle \quad (12)$$

$$[Y_{\nu_1,n(zy)}] = \langle \phi_z^{\nu_1} | f_{z,n}^{\nu_1} \rangle Y_{\nu_1,n} \langle f_{y,n}^{\nu_1} | \phi_y^{\nu_1} \rangle \quad (13)$$

$$[Y_{\nu_1,n(zz)}] = \langle \phi_z^{\nu_1} | f_{z,n}^{\nu_1} \rangle Y_{\nu_1,n} \langle f_{z,n}^{\nu_1} | \phi_z^{\nu_1} \rangle \quad (14)$$

with $\nu_1 = a, b$

$$[Y_{cd}^a] = \sum_{n=0}^{na} \begin{bmatrix} \left[Y_{cd,n(yy)}^a \right] & \left[Y_{cd,n(yz)}^a \right] \\ \left[Y_{cd,n(zy)}^a \right] & \left[Y_{cd,n(zz)}^a \right] \end{bmatrix} \quad (15)$$

$$\left[Y_{cd,n(yy)}^a \right] = \langle \phi_y^a | f_{y,n}^c \rangle Y_{cd,n} \langle f_{y,n}^c | \phi_y^a \rangle \quad (16)$$

$$\left[Y_{cd,n(yz)}^a \right] = \langle \phi_y^a | f_{y,n}^c \rangle Y_{cd,n} \langle f_{z,n}^c | \phi_z^a \rangle \quad (17)$$

$$\left[Y_{cd,n(zy)}^a \right] = \langle \phi_z^a | f_{z,n}^c \rangle Y_{cd,n} \langle f_{y,n}^c | \phi_y^a \rangle \quad (18)$$

$$\left[Y_{cd,n(zz)}^a \right] = \langle \phi_z^a | f_{z,n}^c \rangle Y_{cd,n} \langle f_{z,n}^c | \phi_z^a \rangle \quad (19)$$

$$[Y_{cd}^b] = \sum_{n=0}^{nb} \begin{bmatrix} \left[Y_{cd,n(yy)}^b \right] & \left[Y_{cd,n(yz)}^b \right] \\ \left[Y_{cd,n(zy)}^b \right] & \left[Y_{cd,n(zz)}^b \right] \end{bmatrix} \quad (20)$$

$$\left[Y_{cd,n(yy)}^b \right] = \langle \phi_y^b | f_{y,n}^d \rangle Y_{cd,n} \langle f_{y,n}^d | \phi_y^b \rangle \quad (21)$$

$$\left[Y_{cd,n(yz)}^b \right] = \langle \phi_y^b | f_{y,n}^d \rangle Y_{cd,n} \langle f_{z,n}^d | \phi_z^b \rangle \quad (22)$$

$$\left[Y_{cd,n(zy)}^b \right] = \langle \phi_z^b | f_{z,n}^d \rangle Y_{cd,n} \langle f_{y,n}^d | \phi_y^b \rangle \quad (23)$$

$$\left[Y_{cd,n(zz)}^b \right] = \langle \phi_z^b | f_{z,n}^d \rangle Y_{cd,n} \langle f_{z,n}^d | \phi_z^b \rangle \quad (24)$$

$$[Y_{cd}^{ab}] = \sum_{n=0}^{na} \begin{bmatrix} \left[Y_{cd,n(yy)}^{ab} \right] & \left[Y_{cd,n(yz)}^{ab} \right] \\ \left[Y_{cd,n(zy)}^{ab} \right] & \left[Y_{cd,n(zz)}^{ab} \right] \end{bmatrix} \quad (25)$$

$$\left[Y_{cd,n(yy)}^{ab} \right] = \langle \phi_y^a | f_{y,n}^c \rangle Y_{cd,n} \langle f_{y,n}^d | \phi_y^b \rangle \quad (26)$$

$$\left[Y_{cd,n(yz)}^{ab} \right] = \langle \phi_y^a | f_{y,n}^c \rangle Y_{cd,n} \langle f_{z,n}^d | \phi_z^b \rangle \quad (27)$$

$$\left[Y_{cd,n(zy)}^{ab} \right] = \langle \phi_z^a | f_{z,n}^c \rangle Y_{cd,n} \langle f_{y,n}^d | \phi_y^b \rangle \quad (28)$$

$$\left[Y_{cd,n(zz)}^{ab} \right] = \langle \phi_z^a | f_{z,n}^c \rangle Y_{cd,n} \langle f_{z,n}^d | \phi_z^b \rangle \quad (29)$$

$$[Y_{cd}^{ba}] = \sum_{n=0}^{nb} \begin{bmatrix} \left[Y_{cd,n(yy)}^{ba} \right] & \left[Y_{cd,n(yz)}^{ba} \right] \\ \left[Y_{cd,n(zy)}^{ba} \right] & \left[Y_{cd,n(zz)}^{ba} \right] \end{bmatrix} \quad (30)$$

$$\left[Y_{cd,n(yy)}^{ba} \right] = \langle \phi_y^b | f_{y,n}^d \rangle Y_{cd,n} \langle f_{y,n}^c | \phi_y^a \rangle \quad (31)$$

$$\left[Y_{cd,n(yz)}^{ba} \right] = \langle \phi_y^b | f_{y,n}^d \rangle Y_{cd,n} \langle f_{z,n}^c | \phi_z^a \rangle \quad (32)$$

$$\left[Y_{cd,n(zy)}^{ba} \right] = \langle \phi_z^b | f_{z,n}^d \rangle Y_{cd,n} \langle f_{y,n}^c | \phi_y^a \rangle \quad (33)$$

$$\left[Y_{cd,n(zz)}^{ba} \right] = \langle \phi_z^b | f_{z,n}^d \rangle Y_{cd,n} \langle f_{z,n}^c | \phi_z^a \rangle \quad (34)$$

where:

$\phi_{\nu_2}^{\nu_1}$ are testing functions that satisfy boundary conditions in the discontinuity planes, in region $\nu_1(\nu_1 = a, b)$, on the axis $\nu_2(\nu_2 = y, z)$.

$f_{\nu_2,n}^{\nu_3}$ is the nth basis function, which describe the electric and magnetic fields in the region ν_3, on the axis $\nu_2(\nu_2 = y, z)$.

Y_{ν_4} is the admittance, that represents the boundary conditions of the transmission line section, shifted to the discontinuity plane, in the region $\nu_4(\nu_4 = a, b, cd)$.

The adopted testing functions are:

$$\phi_{y,n}^{a,b} = \sqrt{\zeta_n/h'}\cos\left(n\pi y'/h'\right) \quad (35)$$

$$\phi_{z,n}^{a,b} = \sqrt{\zeta_n/h'}\sin\left(n\pi y'/h'\right) \quad (36)$$

$$h' = \begin{cases} h, & \\ & for \\ (H-h), & \end{cases} \quad \begin{array}{c} a \\ \\ b \end{array} \quad (37)$$

$$\gamma_y = n.\pi/h' \quad (38)$$

$$y' = \begin{cases} y, & \\ & for \\ (H-y) & \end{cases} \quad \begin{array}{c} a \\ \\ b \end{array} \quad (39)$$

$$\zeta_n = \begin{cases} 1, & n \ even \\ & for \\ 2, & n \ odd \end{cases} \quad (40)$$

As the regions a and b correspond to homogeneous waveguides, the basis functions are TE and TM electric field equations, on the axis y and z.

TE modes,

$$f_{y,n}^{a,b} = e_{y,n}^{a,b} = \left(\frac{-\gamma_z\sqrt{\zeta_n/h'}}{\sqrt{\kappa_1(\kappa_2+\gamma_y^2)}}\right)\cos(\gamma_y y')e^{-\gamma_z z} \quad (41)$$

$$f_{z,n}^{a,b} = e_{z,n}^{a,b} = \left(\frac{\gamma_y\sqrt{\zeta_n/h'}}{\sqrt{\kappa_1(\kappa_2+\gamma_y^2)}}\right)\sin(\gamma_y y')e^{-\gamma_z z} \quad (42)$$

TM modes,

$$f_{y,n}^{a,b} = e_{y,n}^{a,b} = \left(j\frac{\gamma_y}{\gamma_z}\frac{\sqrt{\zeta_n/h'}}{\sqrt{\kappa_1(\kappa_2+\gamma_y^2)}}\right)\cos(\gamma_y y')e^{-\gamma_z z} \quad (43)$$

$$f_{z,n}^{a,b} = e_{z,n}^{a,b} = \left(-j\frac{\sqrt{\zeta_n/h'}\sqrt{\kappa_2}}{\sqrt{\kappa_1(\kappa_2+\gamma_y^2)}}\right)\sin(\gamma_y y')e^{-\gamma_z z} \quad (44)$$

For the regions c and d that correspond to inhomogeneous waveguides, the basis functions are LSE and LSM electric current density ($\vec{J} = -\sqrt{\frac{\mu_0}{\epsilon_0}}\vec{H}\times\vec{a_x}$) field equations [2], on the axis y and z.

LSE modes,

$$f_{y,n}^c = J_{y,n}^c = \left(\frac{\cosh(\xi_{y,2}h'')}{\cosh(\xi_{y,1}h)}\right)\left(\frac{\xi_{y,2}}{jK_0}\right)\left(\frac{\gamma_z}{\gamma_x}\right)\cosh(\xi_{y,1}y)e^{\gamma_{xz}} \quad (45)$$

$$f_{z,n}^c = J_{z,n}^c = \left(\frac{\sinh(\xi_{y,2}h'')}{\sinh(\xi_{y,1}h)}\right)\left(\frac{\xi_{y,2}^2+K_0^2}{jK_0\gamma_x}\right)\sinh(\xi_{y,1}y)e^{\gamma_{xz}} \quad (46)$$

$$f_{y,n}^d = J_{y,n}^d = \left(\frac{\xi_{y,2}}{jK_0}\right)\left(\frac{\gamma_z}{\gamma_x}\right)\cosh(\xi_{y,2}(H-y))e^{\gamma_{xz}} \quad (47)$$

$$f_{z,n}^d = J_{z,n}^d = \left(\frac{\xi_{y,2}^2+K_0^2}{jK_0\gamma_x}\right)\sinh(\xi_{y,2}(H-y))e^{\gamma_{xz}} \quad (48)$$

LSM modes,

$$f_{y,n}^c = J_{y,n}^c = -\sqrt{\mu_0/\epsilon_0}\left(\frac{cosh(\xi_{y,2}h'')}{\cosh(\xi_{y,1}h)}\right)\cosh(\xi_{y,1}y)e^{\gamma_{xz}} \quad (49)$$

$$f_{z,n}^c = J_{z,n}^c = 0 \quad (50)$$

$$f_{y,n}^d = J_{y,n}^d = -\sqrt{\mu_0/\epsilon_0}\cosh(\xi_{y,2}(H-y))e^{\gamma_{xz}} \quad (51)$$

$$f_{z,n}^d = J_{z,n}^d = 0 \quad (52)$$

with,

$$h'' = (H-h) \quad (53)$$

$$e^{\gamma_{xz}} = e^{-(\gamma_x x + \gamma_z z)} \quad (54)$$

$$\kappa_1 = e^{-\gamma_z z}.(e^{-\gamma_z z})^* \quad (55)$$

$$\kappa_2 = \gamma_z.(\gamma_z)^* \quad (56)$$

$$K_0 = \omega\sqrt{\mu_0\epsilon_r} \quad (57)$$

$$\gamma_{x,a(b)}^2 = -K_0^2\epsilon_{r,a(b)} - \gamma_z^2 + \gamma_y^2 \quad (58)$$

22

and $\xi_{y,1}$ and $\xi_{y,2}$ are obtained from the solution of the following equation system:

$$\begin{cases} \xi_{y,1}\coth(\xi_{y,1}h) + \xi_{y,2}\coth(\xi_{y,2}h'') = 0 \\ \xi_{y,1}^2 + \xi_{y,2}^2 = K_0^2(1-\epsilon_r) \end{cases} \quad (59)$$

$$\begin{cases} \gamma_{x,cd}^2 = -(K_0^2\epsilon_r + \gamma_z^2 + \xi_{y,1}^2) \\ = -(K_0^2 + \gamma_z^2 + \xi_{y,2}^2) \end{cases} \quad (60)$$

The admittances are defined as functions of the boundary conditions and are given by:

Electric symmetry

$$Y_{a(b),n}(x=W/2) = Y_n^{a(b)}\coth(\gamma_{x,a(b)}W/2) \quad (61)$$

Magnetic symmetry

$$Y_{a(b),n}(x=W/2) = Y_n^{a(b)}\tanh(\gamma_{x,a(b)}W/2) \quad (62)$$

with

$$Y_n^{a(b)} = \frac{\gamma_{x,a(b)}}{jK_0\epsilon_{r,a(b)}}, \quad TE \quad modes \quad (63)$$

$$Y_n^{a(b)} = \frac{jK_0\epsilon_{r,a(b)}}{\gamma_{x,a(b)}}, \quad TM \quad modes \quad (64)$$

For electric side walls

$$Y_n^{cd} = \frac{1}{N^*}\coth\left(\gamma_{x,cd}(L-W)/2\right) \quad (65)$$

with magnetic side walls

$$Y_n^{cd} = \frac{1}{N^*}\tanh\left(\gamma_{x,cd}(L-W)/2\right) \quad (66)$$

and for open sides structures

$$Y_n^{cd} = \frac{1}{N^*} \quad (67)$$

where $1/N^* = 1/\langle \vec{e}|\vec{j}\rangle$ is defined in [3], and given by:

LSE modes

$$N = \nu_1\left(\frac{\sinh(2\xi_{y,1}h)}{4\xi_{y,1}} - \frac{h}{2}\right)\left(\frac{\xi_{y,1}^*}{\xi_{y,1}}\right) + \\ \nu_2\left(\frac{\sinh(2\xi_{y,2}h'')}{4\xi_{y,2}} - \frac{h''}{2}\right)\left(\frac{\xi_{y,2}^*}{\xi_{y,2}}\right) \quad (68)$$

LSM modes

$$N = \nu_3\left(\frac{\sinh(2\xi_{y,1}h)}{4\xi_{y,1}} + \frac{h}{2}\right) + \\ \nu_4\left(\frac{\sinh(2\xi_{y,2}h'')}{4\xi_{y,2}} + \frac{h''}{2}\right) \quad (69)$$

where

$$\nu_1 = \frac{\left(\frac{\sinh(\xi_{y,2}h'')}{\sinh(\xi_{y,1}h)}e^{\gamma_{xz}}\right)^*}{\left(\frac{\sinh(\xi_{y,2}h'')}{\sinh(\xi_{y,1}h)}\right)\left(\frac{\xi_{y,2}^2+K_0^2}{jK_0\gamma_x}\right)e^{\gamma_{xz}}} \quad (70)$$

$$\nu_2 = \left(\frac{\xi_{y,2}^2+K_0^2}{jK_0\gamma_x}\right)e^{\gamma_{xz}}(e^{\gamma_{xz}})^* \quad (71)$$

$$\nu_3 = \frac{\left(\frac{\cosh(\xi_{y,2}h'')}{\sinh(\xi_{y,1}h)}\right)\left(\frac{\xi_{y,2}^2+K_0^2}{j\omega\epsilon_0\epsilon_r\gamma_x}\right)e^{\gamma_{xz}}\right)^*}{\left(\sqrt{\mu_0/\epsilon_0}\frac{\cosh(\xi_{y,2}h'')}{\cosh(\xi_{y,1}h)}e^{\gamma_{xz}}\right)} \quad (72)$$

$$\nu_4 = \left(\frac{\xi_{y,2}^2+K_0^2}{j\omega\epsilon_0\gamma_x}e^{\gamma_{xz}}\right)^*\sqrt{\mu_0/\epsilon_0}\,e^{\gamma_{xz}} \quad (73)$$

Equations (9)-(73) are detailed in [4]. Equations for the coupled microstrip lines and CBCW are similar to these presented here and are also detailed in [4].

III. NUMERICAL RESULTS

Numerical results presented in this section were obtained by a computer program on a personal computer. In Fig. 3 the dispersive characteristics for a shielded microtrip are presented. Along with de quasi-TEM mode, higher order modes are considered. When compared to results of [5], a good agreement is observed.

In Fig. 4 the dispersive characteristics are presented for open coupled microstrip lines. For the cases considered (ϵ_r=2.35 and ϵ_r=9.7), the results obtained are in accordance with the ones obtained in [6].

In Fig. 5 results are presented for a boxed CBCW. The dispersive characteristics for the quasi-TEM mode are presented for two different strips spacing (S=0.10mm and S=0.40mm). When compared to results of [7], obtained by the usual TRT, a good agreement is observed.

IV. CONCLUSIONS

In this work, a modified formulation of the transverse resonance technique (MTRT) is presented, which is a versatile technique to compute dispersive characteristics of transmission structures. With the MTRT proposed formulation, mode solution identification requires less work, especially when higher order modes are considered. The complete equation set is described. Numerical results are presented for dispersive characteristics of microstrip lines, coupled

H=L=12.7mm, h=W=1.27mm, ϵ_r=8.875

Figure 3: ϵ_{eff} x frequency (GHz)

a) H=L=2.5mm, h=0.20mm, S=W=0.10mm,
ϵ_r=12.9

b) H=L=2.5mm, h=0.20mm, S=4W=0.40mm,
ϵ_r=12.9

Figure 5: ϵ_{eff} x frequency (GHz)

a) h=0.79mm, W=3.16mm, $\frac{S}{2}$=0.395mm, ϵ_r=2.35
b) h=0.64mm, W=0.48mm, $\frac{S}{2}$=0.32mm, ϵ_r=9.7
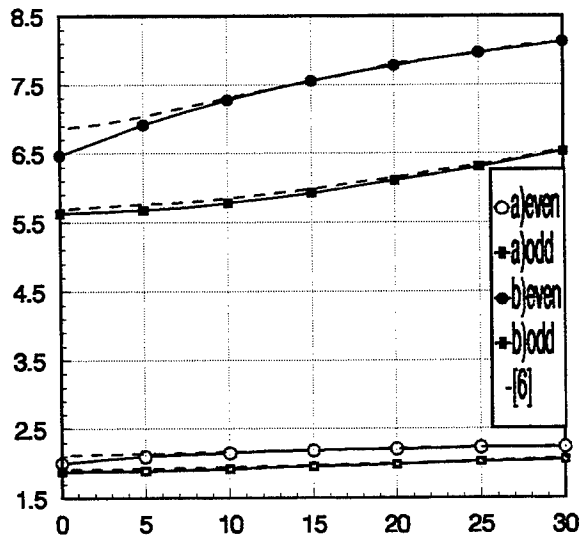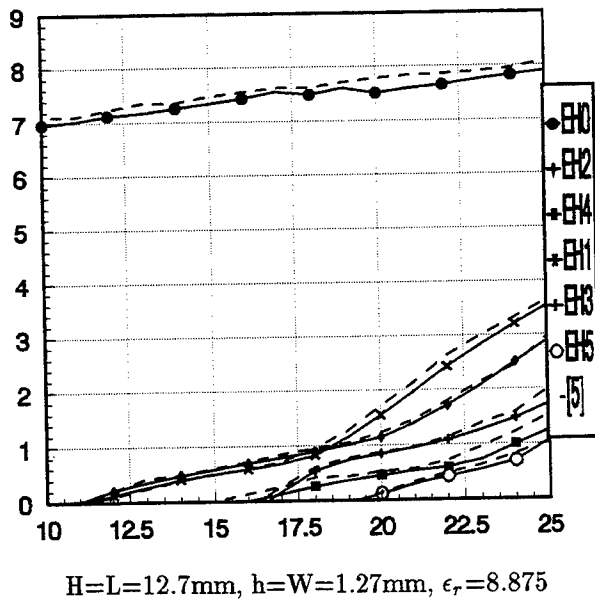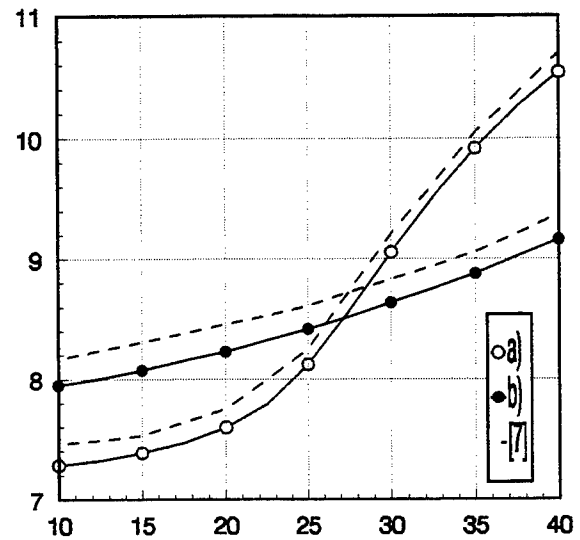
Figure 4: ϵ_{eff} x frequency (GHz)

microstrip lines and CBCW. When compared to results obtained by other methods, a good agreement is observed.

References

[1] Tatsuo Itoh, editor. *Numerical Techniques for Microwave and Millimeter-Wave Passive Structures*. John Wiley and Sons, Inc., New York, New York, 1989.

[2] R. Sorrentino. *Transverse Resonance Technique - in Numerical Techniques for Microwave and Millimeter-Wave Passive Structures*. chap. 11, T. Itoh, Ed., John Wiley and Sons, Inc., New York, New York, 1989.

[3] H. Baudrand. *Méthodes Numériques en Propagation*. E.N.S.E.E.I.H.T., Toulouse, France, 1992.

[4] Alfrêdo Gomes Neto. *An Alternative Formulation of the Transverse Resonance Technique (in Portuguese)*. Dr. Tese, UFPB, Campina Grande, Paraíba, Brazil, December 1994.

[5] Eikichi Yamashita and Kazuhiko Atsuki. "Analysis of microstrip-like transmission lines by nonuniform discretization of integral equations". *IEEE Transactions on Microwave Theory and Techniques*, 24:195–200, April 1976.

[6] M. Kirschning and R. H. Jansen. "Accurate wide-range design equations for the frequency-dependent characteristic of parallel coupled microstrip lines". *IEEE Transactions on Microwave Theory and Techniques*, 32:83–90, January 1984.

[7] H. Baudrand, F. Bouzidi, D. Bajon, and V. Fouad Hanna. "Analysis of conductor-backed coplanar waveguide". In *23rd European Microwave Conference Proceedings*, pages 627–630, Madrid, Spain, September 1993.

EFFECT OF THE MAGNETIC ANISOTROPY ON THE CHARACTERISTICS OF MICROSTRIP ANTENNAS WITH SEVERAL LAYERS

José de Ribamar Silva Oliveira
Federal Center of Technological Education of Maranhão
Av. Getúlio Vargas, 04 - Monte Castelo
65025-001 São Luís, MA, Brazil

Adaildo Gomes d'Assunção
Federal University of Rio Grande do Norte
C.P. 1655, 59072-970 Natal, RN, Brazil
e-mail: adaildo@ncc.ufrn.br

Abstract - The main objective of this work is to show how the properties of a ferrimagnetic material change the characteristics of a microstrip patch with several layers. Particularly, it is investigated how the resonant frequency and the radiation pattern are changed by varying the ferrimagnetic layer thickness or the magnitude and/or direction of the external applied magnetic field. The analysis is carried on by using Hertz potentials and Galerkin method.

I. INTRODUCTION

The development of microstrip structures using ferrites has been considered by several authors [2]-[6]. The basic idea is to take advantage of tuning possibilities, which are provided by varying the magnitude / directions of the external magnetic field.

It was observed that, a special attention has been dedicated to the study of microstrip antennas and resonators on anisotropic dielectric [1] and ferrimagnetic [2]-[4] substrates. The effect of dielectric and magnetic anisotropies on the resonant frequency, quality factor, bandwidth and radiation patterns of a single layer microstrip patch were reported.

In this work, Hertz vector potentials, in the spectral domain, and the moment method were used to analyze the behavior of the resonant frequency for a microstrip resonator on a two-layer substrate, where the grounded one is ferrite and the other one is an isotropic dielectric substrate.

Microstrip antennas / resonators are built by considering a conducting patch which lies on a substrate mounted on a ground plane. Several materials suitable for microwave applications may show some kind of anisotropy, either electric or magnetic. The microstrip antennas structures obtained by using anisotropic substrate have been studied since the 70's and some advantages have been reported, specially when this patch is compared to conventional antennas. Among these advantages are low cost, small dimensions and light weight. Of course, there are some disadvantages like the small bandwidth, high losses and low power handling capabilities.

II. THEORY

Fig. 1 shows the structure considered in this work. It is obtained by letting a conducting patch on a two-layer substrate, which is mounted on a ground plane. Furthermore, the ground layer (region 1) is ferrite and the top one (region 2) is filled with an isotropic dielectric material.
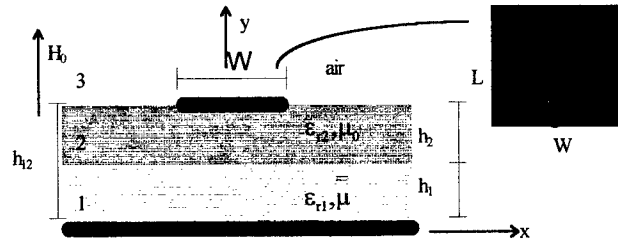
Fig. 1 : Geometry of a microstrip patch on a two-layer ferrimagnetic substrate.

The analysis is carried on by assuming that an external magnetic field, H_0, is applied along the y direction in Fig. 1. For region 1, filled with a ferrimagnetic material, the tensor permeability is then given by

$$\overline{\overline{\mu}} = \mu_0 \cdot \begin{bmatrix} \mu_r & 0 & -jk_r \\ 0 & 1 & 0 \\ jk_r & 0 & \mu_r \end{bmatrix} \qquad (1)$$

where

$$\mu_r = 1 - \frac{(\gamma H_0)(\gamma 4\pi M_s)}{f^2 - (\gamma H_0)^2} \qquad (2)$$

and

$$k_r = \frac{\gamma 4\pi M_s f}{f^2 - (\gamma H_0)^2} \qquad (3)$$

In (1) to (3), γ is the gyromagnetic ratio, $4\pi M_s$ is the magnetization saturation and f is the operation frequency.

The electric, $\overline{\Pi}_e$, and magnetic, $\overline{\Pi}_h$, Hertz vector potentials are assumed to be in the same direction as $\overline{H}_0$, giving

$$\overline{\Pi}_e = \Pi_e \hat{a}_y \qquad (4)$$

$$\overline{\Pi}_h = \Pi_h \hat{a}_y \qquad (5)$$

The expressions for the electric and magnetic fields, as functions of $\overline{\Pi}_e$ and $\overline{\Pi}_h$, are obtained from Maxwell's equations as

$$\overline{E}_1 = -j\omega\mu_0\mu_r \nabla \times \overline{\Pi}_{h1} + \omega^2\varepsilon_{r1}\varepsilon_0\mu_0\left(\frac{\mu_r^2 - k_r^2}{\mu_r^2}\right)\overline{\Pi}_{e1} +$$

$$\frac{1}{\mu_r}\nabla\nabla \cdot \overline{\Pi}_{e1} \qquad (6)$$

$$\overline{H}_1 = j\omega\varepsilon_{r1}\varepsilon_0\mu_0\left(\frac{\mu_r^2 - k_r^2}{\mu_r^2}\right)(\overline{\overline{\mu}})^{-1}\nabla \times \overline{\Pi}_{e1} +$$

$$\omega^2\varepsilon_{r1}\varepsilon_0\mu_0\mu_r\overline{\Pi}_{h1} + \nabla\nabla \cdot \overline{\Pi}_{h1} \qquad (7)$$

and should satisfy the wave equations given below

$$\nabla^2\overline{\Pi}_{e1} + \omega^2\varepsilon_{r1}\varepsilon_0\mu_0\left(\frac{\mu_r^2 - k_r^2}{\mu_r}\right)\overline{\Pi}_{e1} = 0 \qquad (8)$$

$$\nabla^2\overline{\Pi}_{h1} + \omega^2\varepsilon_{r1}\varepsilon_0\mu_0\overline{\Pi}_{h1} - \left(\frac{\mu_r - 1}{\mu_r}\right)\frac{\partial^2\overline{\Pi}_{h1}}{\partial y^2} = 0 \qquad (9)$$

In the Fourier domain [1], the wave equations are obtained as

$$\frac{\partial^2\widetilde{\Pi}_{e1}}{\partial y^2} - \gamma_e^2\widetilde{\Pi}_{e1} = 0 \qquad (10)$$

and
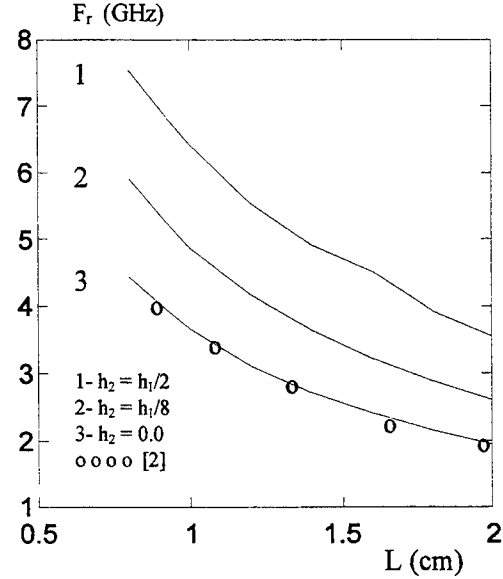
Fig. 2 : Resonant frequency versus patch length: w = 0.4 cm, h_1 = 0.127 cm, ε_{r1} = 15.2, ε_{r2} = 2.35, H_0 = 5024 Oe, $4\pi M_s$=1200 G.

$$\frac{\partial^2\widetilde{\Pi}_{h1}}{\partial y^2} - \gamma_h^2\widetilde{\Pi}_{h1} = 0 \qquad (11)$$

where

$$\gamma_e^2 = \alpha^2 + \beta^2 - \omega^2\varepsilon_{r1}\varepsilon_0\mu_0\left(\frac{\mu_r^2 - k_r^2}{\mu_r}\right) \qquad (12)$$

$$\gamma_e^2 = \mu_r(\alpha^2 + \beta^2) - \omega^2\varepsilon_{r1}\varepsilon_0\mu_0\mu_r \qquad (13)$$

For dielectric regions 2 (isotropic) and 3 (air), the electric and magnetic fields are obtained from (4) to (13) by imposing μ_r = 1 and k_r = 0 and replacing ε_{r1} by ε_{r2} (for region 2) or by ε_{r3} = 1 (for region 3).

After some algebraic manipulations, the transformed electric field components, $\widetilde{E}_x$ and $\widetilde{E}_z$, at the interface y = h_{12} (Fig. 1), are expressed as functions of the transformed surface current density components, $\widetilde{J}_x$ and $\widetilde{J}_z$, as

$$\widetilde{E}_x = \widetilde{Z}_{xx}\widetilde{J}_x + \widetilde{Z}_{xz}\widetilde{J}_z \qquad (14)$$

$$\widetilde{E}_z = \widetilde{Z}_{zx}\widetilde{J}_x + \widetilde{Z}_{zz}\widetilde{J}_z \qquad (15)$$

Then, Galerkin method is used as described in [7]. The basis functions used in this work are those given by [7]. The determinantal equation which gives the patch complex resonant frequency (F_{res} = F_r + jF_i) is obtained.

To determine the radiation pattern, the far field is expressed as function of the transformed electric field

27

components at $y = h_{12}$ (Fig. 1), by using the phase stationary method [8]. The far field expressions are [9]

$$E_\theta (\phi,\theta) \propto \sin\phi \ \widetilde{E}_z(\alpha,\beta) \qquad (16)$$

$$E_\phi (\phi,\theta) \propto \cos\theta \cos\phi \ \widetilde{E}_z(\alpha,\beta) + \sin\phi \ \widetilde{E}_x(\alpha,\beta) \qquad (17)$$

with

$$\alpha = \omega^2 \mu_0 \varepsilon_0 \sin\theta \cos\phi \qquad (18)$$

$$\beta = \omega^2 \mu_0 \varepsilon_0 \cos\theta \qquad (19)$$

III. NUMERICAL RESULTS

The results obtained for the resonant frequency and the radiation pattern are depicted in Fig. 2 to 5. In Fig. 2, the patch resonant frequency is shown against its length, for several values of h_2. Notice that the shape of the curves obtained for different values of h_2 is about the same. This is an expected result because of the high value of $H_0 = 5024$ Oe. $\gamma = 2.855$ MHz/Oe. A very good agreement was observed for microstrip patches on a single ferrimagnetic layer, when the results obtained in this work are compared to those available in [2].

The radiation patterns are shown in Figs. 4 and 5, for the E and H planes, respectively. The shapes of these curves are similar to those obtained for microstrip patches on isotropic dielectric substrates. Once again this is due to the high value of $H_0 = 5024$ Oe. $\gamma = 2.855$ MHz/Oe.

Fig. 3 depicts the behavior of the resonant frequency against the normalized external magnetic field, $H_0 / (4\pi M_s)$. Note that, when $H_0 / (4\pi M_s)$ increases, the resonant frequency increases, suggesting tuning possibilities, through the variation of the magnitude of $\overline{H}_0$.

A comparison between the results of this work, for the particular case of a suspended microstrip patch on isotropic substrate is shown in Fig. 6. The results of this analysis were obtained by setting $\mu_r = 1$ and $k_r = 0$. A very good agreement was observed with the results from [1], for suspended microstrip patch antennas.

IV. CONCLUSION

The analysis of rectangular microstrip patches on layers were studied, in order to investigate the effect produced by the magnetic anisotropy of the grounded layer. The analysis was developed in the Fourier domain, by using Hertz potentials and moment method, showing accuracy and efficiency. The theoretical analysis and the

numerical results suggest that this analysis may be used to investigate other parameters of the antenna and/or their arrays.
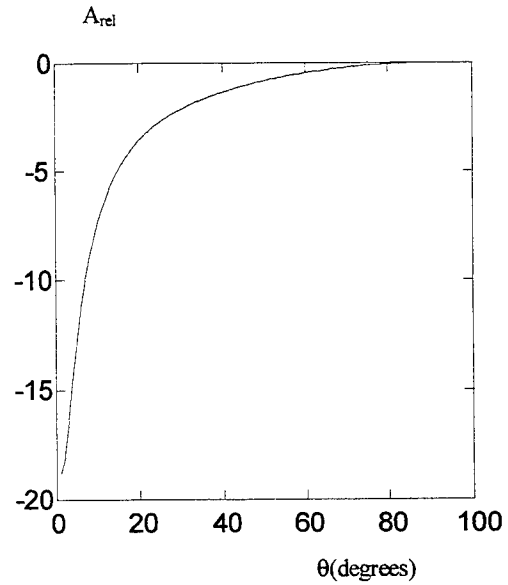
Fig. 4 : Radiation pattern $E_\theta(\phi = \pi/2, \theta)$: w = 0.4 cm; L = 1.0 cm; $h_1 = 0.127$; $h_2 = h_1/2$; $\varepsilon_{r1} = 15.2$; $\varepsilon_{r2} = 2.35$; $H_0 = 5024$ Oe; $4\pi M_s = 1200$ G; $F_r = 6.43 + j0.0064$ GHz.
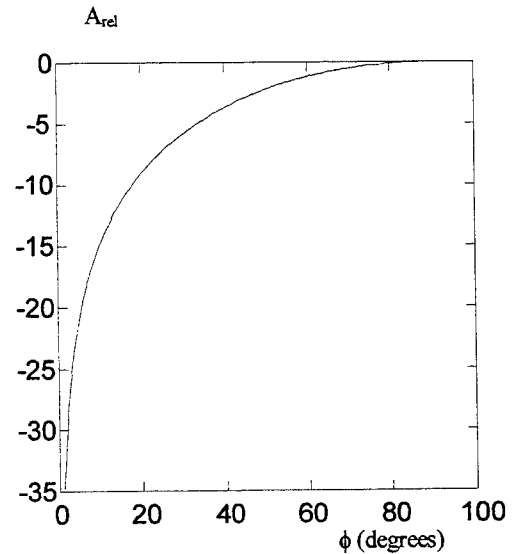
Fig. 5 : Radiation pattern, $E_\theta(\phi, \theta = \pi/2)$: w = 0.4 cm, L = 1.0 cm, $h_1 = 0.127$, $h_2 = h_1/2$, $\varepsilon_{r1} = 15.2$, $\varepsilon_{r2} = 2.35$, $H_0 = 5024$ Oe, $4\pi M_s = 1200$ G, $F_{res} = 6.43 + j0.0064$

ACKNOWLEDGMENT

F_r (GHz)
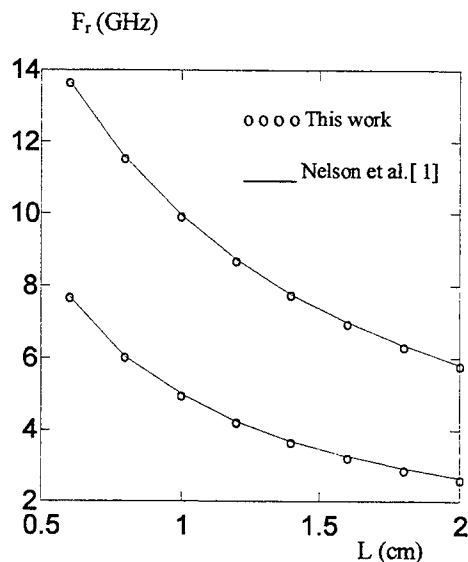
Fig.6: Resonant frequency versus patch length :
____ w = 0.1 cm, h_1 = 0.1651 cm, h_2 = 0.0254 cm,
    ε_{r1} = 1.0, ε_{r2} = 9.6
- - - - w= 0.4 cm, h_1 = 0.127 mm, h_2 = 0.0, ε_{r1} = 9.6.

REFERENCES

[1] - R.M. Nelson, D.A. Rogers and A.G. d'Assunção, "Resonant frequency of a rectangular microstrip patch on several uniaxial substrates", *IEEE Trans. Antennas Propagat.*, v. AP-38, N. 7, pp. 973-981, July 1990.

[2] - A.G. d'Assunção and E.J.A. Dantas, "On the resonant frequency of magnetized rectangular microstrip patch resonators", *IEEE AP-S Antennas Propagation Symp.*, Ann Arbor, MI, pp. 1508-1511, June 1993.

[3] - D.M.Pozar, "Radiation and scattering characteristic of microstrip antennas on normally biased ferrite substrates", *IEEE Trans.Antennas Propagat.*, AP-40, N. 9, pp. 1084-1092, September 1992.

[4] - M.R.M.L.Albuquerque, A.G.d'Assunção and A.J. Giarola, "Dynamic characteristics of microstrip lines on magnetized ferrimagnetic substrates", *20th European Microwave Conf. Dig.*, p. 1317-1321, Budapest, Hungary, 1990.

[5] - E.J.A.DANTAS, "Características do ressoador retangular de microfita sobre substratos ferrimagnéticos Magnetizados" (M.Sc. thesis). Federal University of Rio Grande do Norte, Natal, RN, Brazil, 1993, 80 p.

[6] - H.-Y. Yang, J.A. Castanheda and G. Alexoupolos, "The RCS of a microstrip patch on an arbitrarily biased ferrite substrate", *IEEE Trans. Antennas Propagat.*, AP-41, N. 12, pp. 1610-1614, December 1993.

[7] - D.M. Pozar, "Radiation and scattering from a microstrip patch on a uniaxial substrate", *IEEE Trans. Antennas Propagat.*, vol. AP-35, N. 6, pp. 613-621, June 1987.

[8] - R.E.Collin and F.J.Zucker, *Antenna theory*, McGraw-Hill Company, 1969.

[9] - T. Itoh and W. Menzel, "A full-wave analysis method for open microstrip structures", *IEEE Trans. Antennas Propagat.*, vol. AP-29, N. 1, pp. 63-67, January 1981.

Adaildo Gomes d'Assunção received the B. S. E. E. degree (with honors) from the Federal University of Rio Grande do Norte, RN, Brazil, in 1974, and the M. S. and doctoral degree in electrical engineering from the State University of Campinas, SP, Brazil, in 1977 and 1981, respectively. From 1975-1976, he worked with radar and telemetry systems at the Launching Center of Barreira do Inferno, Natal, RN, Brazil. He has been with the Federal University of Rio Grande do Norte since 1976, where he is an Associate Professor of Electrical and Electronics Engineering. From 1985-1987, he was a Postdoctoral Visiting Scientist in the Department of Electrical and Electronics Engineering at North Dakota State University, Fargo. He is currently teaching and conducting research on antennas microwave integrated circuits and millimeter waves. Dr. d'Assunção is a member of the Brazilian Microwave and Optoelectronics Society (SBMO) and of the Brazilian Telecommunication Society (SBT).

José de Ribamar Silva Oliveira received the B. S. E. E. degree from the Federal University of Maranhão, in 1980, and the M. S. E. E. degree from the Federal University of Rio Grande do Norte, in 1990. He has been with the Federal Center of Technological Education of Maranhão since 1983 where he is a professor of Electronics and Electricity. He is currently working toward a Ph. D. degree at the Federal University of Paraiba, in Campina Grande, Brazil, working in the areas of microstrip antennas and transmission lines. He is a member of the Brazilian Telecommunications Society (SBT) and of the Brazilian Microwave and Optoelectronics Society (SBMO). He is also a member of the IEEE Microwaves Theory and Technique and Antennas and Propagation Societies.

DISPERSIVE ANALYSIS OF CIRCULAR CYLINDRICAL MICROSTRIPS AND BACKED SLOTLINES

Laércio Martins de Mendonça and Adaildo Gomes d'Assunção

Federal University of Rio Grande do Norte
Caixa Postal 1655, 59072-970 Natal, RN, Brazil
e-mail: adaildo@ncc.ufrn.br

Abstract - In this work, the full-wave analysis of circular cylindrical microstrips and backed slotlines is performed, by using a combination of Hertz vector potentials and Galerkin method. The analysis is developed in the spectral domain.

I. INTRODUCTION

The dispersive analysis using Hertz vector potentials in the Fourier domain was first used to analyze planar structures, such as microstrip transmission lines [1] and patch antennas and resonators [1]-[4]. This work describes an extension of this technique to study non-planar structures, such as those considered in [5]-[11], in order to determine accurately their characteristics and to investigate its application in (monolithic) microwave integrated circuits (M)MIC. The analysis of circular cylindrical microwave integrated structures is usually quite complex, requiring a large amount of computer time. To overcome this problem, accurate and efficient algorithms were developed [8]. A very good agreement was observed between the results of this work and those available in the literature, in particular [2]-[4], [12].

II. THEORY

A. Circular Cylindrical Microstrip Lines (CCML)

The microstrip structure considered in this work is shown in Fig. 1, where $w = 2\alpha \, r_2$ and α is half of the strip angle. In this analysis, the following approximations are assumed: a) the dielectric substrate is isotropic, linear and homogeneous, b) the ground and conducting strip losses are neglected, c) harmonic dependence for the electric and magnetic fields is assumed, and d) the conducting strip thickness is neglected.

In this analysis, the electric and magnetic field components are expressed in terms of the electric and magnetic Hertz vector potentials, $\bar{\pi}_{ei}$ and $\bar{\pi}_{hi}$, respectively, which are defined for each dielectric region i (i=1,2 in Fig. 1) as [8],[13]

$$\bar{\pi}_{ei} = \pi_{ei} \, \hat{a}_r \qquad (1)$$

$$\bar{\pi}_{hi} = \pi_{hi} \, \hat{a}_r \qquad (2)$$

where $\hat{a}_r$ is the radial unit vector.

In the analytical procedure of the Hertz vector potentials technique, Maxwell's equations are used, giving

$$\bar{B}_i = j\omega\mu_0\varepsilon_i \, \nabla \times \bar{\pi}_{ei} \qquad (3)$$

$$\bar{E}_i = -j\omega\mu_0 \nabla \times \bar{\pi}_{hi} \qquad (4)$$

where μ_0 is the free space permeability, ε_i is the electric permittivity for dielectric region i (i = 1,2 in Fig. 1) and ω is the angular operating frequency. After some algebraic manipulation, the electric and magnetic field components are obtained. They are refered to the propagation TE and TM waves (with respect to r-direction, in Fig. 1). Then, the total electric and magnetic field expressions are obtained by superposition and given by

$$\bar{E} = -j\omega\mu_0\nabla\times\bar{\pi}_{hi} + \omega^2\mu_0\varepsilon_i\bar{\pi}_{ei} + \nabla\nabla.\bar{\pi}_{ei} \qquad (5)$$

$$\bar{H} = j\omega\varepsilon_i \, \nabla\times\bar{\pi}_{ei} + \omega^2\mu_0\varepsilon_i\bar{\pi}_{hi} + \nabla\nabla.\bar{\pi}_{hi} \qquad (6)$$

respectively.

Furthermore, the electric and magnetic Hertz potentials should satisfy the wave equations

$$\nabla^2 \bar{\pi}_{ei} + \omega^2 \mu_0 \varepsilon_i \bar{\pi}_{ei} = 0 \qquad (7)$$

$$\nabla^2 \bar{\pi}_{hi} + \omega^2 \mu_0 \varepsilon_i \bar{\pi}_{hi} = 0 \qquad (8)$$

respectively.

The transformation to the spectral domain is obtained using the following definition [8]

$$\tilde{\Omega}(r,m) = \int_{-\infty}^{\infty}\Omega(r,\phi) \, \exp(-j\omega\phi) \, d\phi \qquad (9)$$

30

$$\Omega(r,\phi) = \sum_{m=-\infty}^{m=\infty} \widetilde{\Omega}(r,m) \exp(jm\phi) \qquad (10)$$

where "$\sim$" means the transformed function and m is the spectral variable.

The wave equations for $\widetilde{\pi}_{ei}$ and $\widetilde{\pi}_{hi}$ are determined from, and are given by (7) to (10)

$$\frac{d^2}{dr^2}\widetilde{\pi}_{ei,hi}(r,m) + \frac{1}{r}\frac{d}{dr}\widetilde{\pi}_{ei,hi}(r,m) - \zeta_i^2\widetilde{\pi}_{ei,hi}(r,m) = 0 \qquad (11)$$

with

$$\zeta_i^2 = \gamma_i^2 - (m/r)^2 \qquad (12)$$

$$\gamma_i^2 = k_i^2 - \beta^2 \qquad (13)$$

where γ_i is the propagation constant and k_i is the wave number.

$$\phi = 0$$
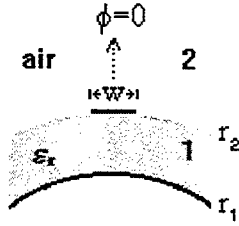
Figure 1: Cross sectional view of a circular cylindrical microstrip line.

The solutions of (11) have the general form shown below [8]

$$\widetilde{\pi}_{e1}(r,m) = A(m)\, J_m(\gamma_1 r) + B(m)\, N_m(\gamma_1 r) \qquad (14)$$

$$\widetilde{\pi}_{h1}(r,m) = C(m)\, J_m(\gamma_1 r) + D(m)\, N_m(\gamma_1 r) \qquad (15)$$

for dielectric region 1 ($r_1 < r < r_2$, in Fig. 1), and

$$\widetilde{\pi}_{e2}(r,m) = E(m)\, H_m^{(2)}(r,m) \qquad (16)$$

$$\widetilde{\pi}_{h2}(r,m) = F(m)\, H_m^{(2)}(r,m) \qquad (17)$$

for dielectric region 2 ($r > r_2$, in Fig. 1), which is air-filled.

In (14) to (17), the expressions for the unknown coefficients A(m), B(m),..., F(m) are determined from the boundary conditions; $J_m(.)$ and $N_m(.)$ are Bessel's functions of 1st and 2nd kind, respectively; and $H_m^{(2)}(.)$ is the Hankel function of 2nd kind.

In this work, the transformed field components are expressed as functions of $\widetilde{\pi}_{hi}(r,m)$, for the TE modes,

and $\widetilde{\pi}_{ei}(r,m)$, for the TM modes. By using superposition and imposing the boundary conditions, the expressions for the total electric and magnetic field components are obtained.

At the interface dielectric-air ($r = r_2$, in Fig. 1), the transformed tangential electric field components, $\widetilde{E}_\phi$ and $\widetilde{E}_z$, are expressed in terms of the transformed current density components, $\widetilde{J}_\phi$ and $\widetilde{J}_z$, as

$$\widetilde{E}_\phi(m,\beta) = \widetilde{Z}_{\phi\phi}(m,\beta)\widetilde{J}_\phi(m) + \widetilde{Z}_{\phi z}(m,\beta)\widetilde{J}_z(m) \qquad (18)$$

$$\widetilde{E}_z(m,\beta) = \widetilde{Z}_{z\phi}(m,\beta)\widetilde{J}_\phi(m) + \widetilde{Z}_{zz}(m,\beta)\widetilde{J}_z(m) \qquad (19)$$

where, $\widetilde{Z}_{\phi\phi}, \widetilde{Z}_{\phi z}, \widetilde{Z}_{z\phi}$ and $\widetilde{Z}_{zz}$ are the transformed impedance matrix components in the spectral domain.

Once the impedance matrix $[\widetilde{Z}]$ was determined, the Galerkin method [14] is used and a linear system of equations is obtained, according to

$$[K][c] = 0 \qquad (20)$$

where the matrix $[K]$ components are given by

$$K_{ip}^{\phi\phi} = \sum_{m=-\infty}^{m=\infty} \widetilde{f}_{\phi i}(m)\widetilde{Z}_{\phi\phi}(m,\beta)\widetilde{f}_{\phi p}(m) \qquad (21)$$

$$K_{ip}^{\phi z} = \sum_{m=-\infty}^{m=\infty} \widetilde{f}_{\phi i}(m)\widetilde{Z}_{\phi z}(m,\beta)\widetilde{f}_{\phi p}(m) \qquad (22)$$

$$K_{jp}^{z\phi} = \sum_{m=-\infty}^{m=\infty} \widetilde{f}_{z j}(m)\widetilde{Z}_{z\phi}(m,\beta)\widetilde{f}_{\phi p}(m) \qquad (23)$$

$$K_{iq}^{zz} = \sum_{m=-\infty}^{m=\infty} \widetilde{f}_{z j}(m)\widetilde{Z}_{zz}(m,\beta)\widetilde{f}_{z q}(m) \qquad (24)$$

In (21) to (24), $\widetilde{f}_{\phi i}, \widetilde{f}_{\phi p}, \widetilde{f}_{z j}$ and $\widetilde{f}_{z j}$ are basis functions, which should be properly chosen in order to reduce the computational effort. The characteristic equation for the propagation constants in the structure considered is obtained by imposing det $[K] = 0$. Therefore, the effective permittivity is readily determined.

B. *Circular Cylindrical Backed Slotline (CCBS).*

The geometry of the CCBS is shown in Fig. 2, where $w = 2\alpha\, r_2$ and α is half of the slot angle. This analysis is performed by taking advantage of that presented for CCML structures. In the case of CCBS structures, an

31

admittance matrix has to be derived. Nevertheless, this algebraic manipulation is avoided by setting [8]

$$[\widetilde{Y}] = [\widetilde{Z}]^{-1} \qquad (25)$$

where the matrix $[\widetilde{Z}]$ components are those shown in (18) and (19).
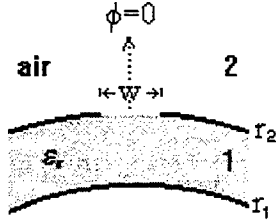
Figure 2: Cross sectional view of a circular cylindrical backed slotline (CCBS).

By using Galerkin method, the characteristic equation for the propagation constants is obtained, as well as the effective permittivity.

III. RESULTS

A new parameter was defined to show the numerical results, which is $R = r_1 / r_2$ (see Figs. 1 and 2). For small values of r_1 and r_2, R is always lower then 1, while for large values of them, R is close to 1. The dielectric thickness of region 1, H $(=r_2 - r_1)$, is kept constant.

Fig. 3 shows the dispersive behavior of the normalized wavelength, λ_s / λ_0, for a circular cylindrical microstrip line (CCML) with W/H=1.0; R=0.98; ε_{r1} = 9.6 and ε_{r2}=1.0.

Results obtained for the normalized wavelength, λ_s / λ_0, and the effective permittivity, ε_{eff}, against frequency for circular cylindrical backed slotlines (CCBS) are shown in Figs. 4 and 5, respectively.

The results shown in Fig. 4, for λ_s / λ_0, were obtained for a quasi-planar CCBS, with $R = r_1 / r_2 = 0.98$; ε_{r1} = 20.0 and ε_{r2} = 1.0. Results for a planar (not backed) slotline with same values for W, H, ε_{r1} and ε_{r2} obtained from [12] are presented. As expected the results for these different structures approach each other because large values for W/H (=5.568) and ε_r were considered.

Fig. 5 shows the numerical results for ε_{eff} that were obtained for a quasi-planar backed slotline, or a CCBS with a large value for R $(=r_1 / r_2)$, where w=40 μm, H =600 μm, ε_{r1}= 12.9, ε_{r2}= 1 and R = 0.98. The numerical
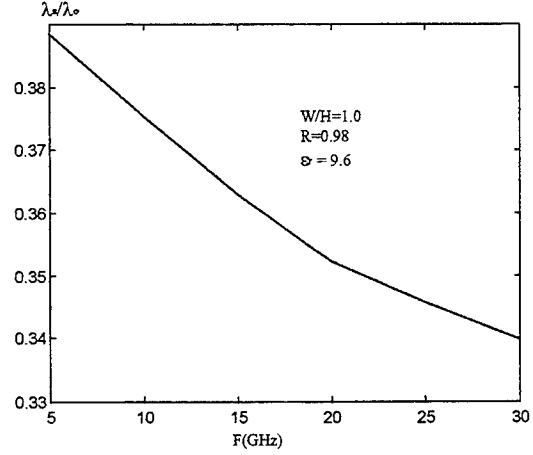
Figure 3: Dispersive behavior of the normalized wavelength, λ_s / λ_0, for a circular cylindrical microstrip line (CCML), with W/H=1.0; R=0.98; ε_{r1}= 9.6 and ε_{r2}=1.0.

results from [6], for a (planar) backed slotline with same values for w, H, ε_{r1} and ε_{r2} are presented. A close agreement is observed, as expected.

IV. CONCLUSION

The analyses of circular cylindrical microstrip lines (CCML) and circular cylindrical backed slotlines (CCBS) were performed by using a combination of Hertz vector potentials and Galerkin method, in the spectral domain. These structures are used in (M)MIC, applications, such as antennas, resonators and phase-shifters.

Numerical results were presented for the normalized wavelength and the effective permittivity versus frequency for different structural parameters.

A comparison between the results of this work and those available in the literature for the CCML showed a very good agreement. For CCBS, the results of this work were plotted with those obtained for similar structures, mainly planar structures, studied by other authors, showing agreement, as expected.

Finally, the technique used in this work is accurate efficient and can be used to analyze other non-planar structures, such as those of single and coupled transmission lines on anisotropic substrates.

REFERENCES

[1] M. G. R. Maia, A. G. d'Assunção and A. J. Giarola, "Dynamic analysis of microstrip lines and finlines on uniaxial anisotropic substrates", IEEE

Trans. Microwave Theory Tech., vol. MTT-35, pp. 881-886, 1987.

[2] M.R.M.L. Albuquerque, A.G. d'Assunção and A. J.Giarola, "Spectral domain analysis of coupled microstrip lines on magnetized ferrite substrates", Int. Journal of Infrared and Millimeter Waves, vol. 14, pp.1531-1544, 1993.

[3] A.G. d'Assunção and E.J.A. Dantas, "On the resonant frequency of magnetized rectangular microstrip patch resonators", IEEE Int. Symp. Antennas Propagat., Ann Arbor, MI, pp. 1508-1511, 1993.

[4] J. R .S. Oliveira, A. G. d'Assunção and C. S. Rocha, "Characteristics of a suspended rectangular microstrip patch antenna on a uniaxial substrate", 9th Int. Conf. Antennas and Propagation (ICAP'95), Eindhoven, The Netherlands, vol. I, pp. 37-40, April 1995.

[5] P. P. Delogne and A. A. Laloux, "Theory of the slotted coaxial cable", IEEE Trans. Microwave Theory Tech., vol. MTT-28, No. 10, pp. 1102-1107, Oct. 1980.

[6] J. Bornemann, "A scattering-type transverse resonance technique for the calculation of (M)MIC transmission line characteristics", IEEE Trans. Microwave Theory Tech., vol. MTT-39, No. 12, 1991.

[7] N. G. Alexópoulos and A. Nakatani, "Cylindrical substrate microstrip line characteristics", IEEE Trans. Microwave Theory Tech., vol. MTT-35, No. 9, pp. 843-849, 1987.

[8] L.M. Mendonça, "Novos Procedimentos para a Análise de Linhas de Transmissão Não-Planares (in Portuguese)", PhD thesis, Federal University of Paraíba, C. Grande, PB, Brazil, Dec. 1994.

[9] F. Medina and M. Horno, "Spectral and variational analysis of generalized cylindrical and elliptical strip and microstrip lines", IEEE Trans. Microwave Theory Tech., vol. MTT-38, No. 9, Sept. 1990.

[10] C.M. Krowne, "Cylindrical-rectangular microstrip antenna", IEEE Trans. Antennas Propagat., vol. AP-31, pp. 194-199, Jan. 1983.

[11] K.-L. Wong, Y.-T. Cheng and J.-S. Row, "Resonance in a superstrate-loaded cylindrical-rectangular microstrip structure", IEEE Trans. Microwave Theory Tech., vol. MTT-41, No. 5, pp. 814-819, May 1993.

[12] K.C. Gupta, R. Garg and I. J. Bahl, *Microstrip Lines and Slotlines*, Artech House, 1979.

[13] R. E. Collin, *Field Theory of Guided Waves*, McGraw-Hill, New York, 1960.

[14] R.F. Harrington, *Field Computation by Moment Methods*, MacMillan, New York, 1968.
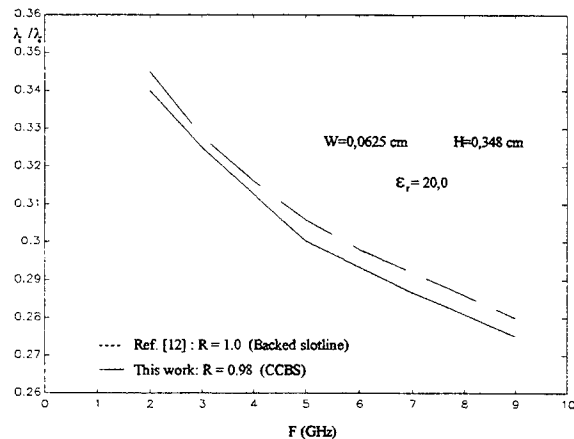
Figure 4: λ_s / λ_0 versus frequency for a CCBS and a slotline (not backed).
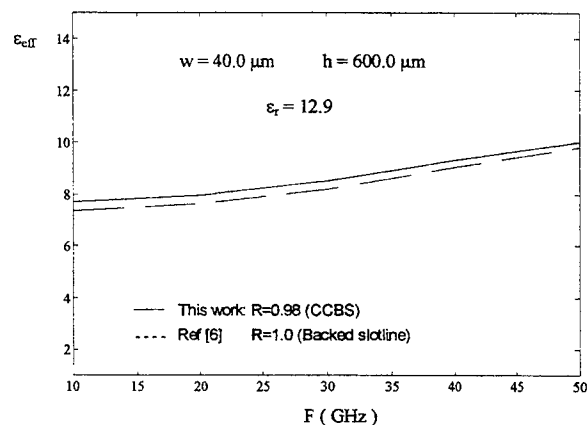
Figure 5: Effective permittivity versus frequency for a circular cylindrical backed slotline (CCBS) and a backed (planar) slotline.

Adaildo Gomes d'Assunção received the B. S. E. E. degree (with honors) from the Federal University of Rio Grande do Norte, RN, Brazil, in 1974, and the M. S. and doctoral degree in electrical engineering from the State University of Campinas, SP, Brazil, in 1977 and 1981, respectively.

From 1975-1976, he worked with radar and telemetry systems at the Launching Center of Barreira do Inferno, Natal, RN, Brazil. He has been with the Federal University of Rio Grande do Norte since 1976, where he is an Associate Professor of Electrical and Electronics Engineering. From 1985-1987, he was a Postdoctoral Visiting Scientist in the Department of Electrical and Electronics Engineering at North Dakota State University, Fargo. He is currently teaching and conducting research on antennas microwave integrated circuits and millimeter waves.

Dr. d'Assunção is a member of the Brazilian Microwave and Optoelectronics Society (SBMO) and of the Brazilian Telecommunication Society (SBT).

Laércio Martins de Mendonça received the BSEE and the MSEE degrees from the Federal University of Rio Grande do Norte in 1977 and 1987, respectively. In December 1994 he obtained the doctoral degree from the Federal University of Paraíba. He joined the Federal University of Rio Grande do Norte in 1983, where he is currently an associate professor. Dr. Mendonça's research activities are in microwave integrated circuits, millimeter waves, non-planar transmission lines and antennas.

He is a member of the Brazilian Microwave and Optoelectronics Society (SBMO) and of the Brazilian Telecommunications Society (SBT).

33

FINITE ELEMENT ANALYSIS AND EVALUATION OF ELECTROMAGNETIC FIELDS GENERATED BY ATMOSPHERIC DISCHARGES

E.H.R. Coppoli*, R.R. Saldanha*, A. Konrad**
* Universidade Federal de Minas Gerais-DEE-CPDEE-Brasil
**University of Toronto-Toronto, Ontario, Canada M5S 1A4

Abstract - A lightning return stroke channel is modeled by a high loss transmission line. The differential equations that represent its dynamic behavior are solved by the application of the one-dimensional finite element method (FEM). By the combination of FEM results with the use of Maxwell equations applied to the dipole method, electric and magnetic (EM) fields are evaluated at various positions in space.

I. INTRODUCTION

The great increase in the number of components in new electronic equipment constitutes an everpresent concern for engineers dealing with problems of electromagnetic compatibility. As a consequence of the phenomenon, inaccurate readings may occur and system regulatory and control functions may be improperly activated. In a worst case scenario, this may lead to the destruction of the equipment. In general, the components operate at low voltage levels and thus remain quite susceptible to electromagnetic disturbances. The disturbances may originate from various sources, but the ones caused by lightning are among those principally responsible for the most serious occurrences [1].

During the last decade, much progress has been made in solving electromagnetic transient problems on digital computers. Ultimately, the usefulness of computer simulations must be proved by comparing the results with measurements obtained from field tests [2]. This will check not only the correctness of the algorithms but also the adequacy of the models. A careful error analysis of the measurements is often essential if differences have to be explained.

To evaluate the electromagnetic field generated by lightning return strokes more accurately, it is of fundamental importance to choose a model which can adequately represent the evolution of surge along the channel. An adequate, representative model can be defined by using a physical or mathematical construction which behaves as, or approximates closely, the natural phenomenon in question. The Bruce-Golde (BG) model, the Transmission Line (TL) model, the Traveling Current Source (TCS) model, and others [1]-[5] are among some of the commonly employed models.

The work presented here is based on the determination of EM fields generated by lightning return strokes, using a high loss transmission line model of the channel. The equations that govern the dynamics of this problem are solved through finite analysis, with results then applied to calculate EM fields at diverse points in space [2],[6]-[8].

II. THE TRANSMISSION LINE MODEL FOR STROKE

Consider a lossy transmission line where L', C', G' and R' are the inductance, capacitance, conductance and resistance per unit length, respectively [3]. At a point x along the line, voltage and currentare related by

$$
\begin{cases}
-\dfrac{\partial v(x,t)}{\partial x} = R'i + L'\dfrac{\partial i(x,t)}{\partial t} \\
-\dfrac{\partial i(x,t)}{\partial x} = G'v + C'\dfrac{\partial v(x,t)}{\partial t}
\end{cases}
\tag{1}
$$

The general solution of (1) was obtained by Heaviside and Poincaré. Using the Heaviside operator

$$
\begin{cases}
-\dfrac{\partial v(x,t)}{\partial x} = \left(R' + L'p\right) i(x,t) \\
-\dfrac{\partial i(x,t)}{\partial x} = \left(G' + C'p\right) v(x,t)
\end{cases}
\tag{2}
$$

$$
\begin{cases}
v(x,t) = e^{\gamma x}f_1(t) + e^{-\gamma x}f_2(t) \\
i(x,t) = -\sqrt{\dfrac{G'+C'p}{R'+L'p}}\left(e^{\gamma x}f_1(t) - e^{-\gamma x}f_2(t)\right)
\end{cases}
\tag{3}
$$

With appropriate algebra the solution of (3) for an infinite line excited by a unit step function can be written as

$$
\begin{cases}
v(x,t) = e^{\frac{-\alpha x}{v}} + \beta\dfrac{x}{v}\int_{\frac{x}{v}}^{t}\dfrac{e^{-\alpha t}I_1(\beta k)}{k}dt \\
i(x,t) = \sqrt{\dfrac{C'}{L'}}\left[e^{-\alpha t}I_0(\beta k) + (\alpha - \beta)\int_{\frac{x}{v}}^{t}e^{-\alpha t}I_0(\beta k)dt\right]
\end{cases}
\tag{4}
$$

for $t > x/v$, where $k = \sqrt{t^2 - x^2/v^2}$, I_0 and I_1 are are

zeroeth-order and first-order Bessel functions of imaginary arguments, respectively [5], and

$$v = \frac{1}{\sqrt{L'C'}} \quad \text{speed of propagation, (5)}$$

$$\alpha = \frac{1}{2}\left(\frac{R'}{L'} + \frac{G'}{C'}\right) \quad \text{attenuation constant, (6)}$$

$$\beta = \frac{1}{2}\left(\frac{R'}{L'} - \frac{G'}{C'}\right) \quad \text{propagation constant., (7)}$$

The determination of the waveform at any point x on the line from (4) involves a numerical integration that is prohibitively time-consuming for an infinite line. A simplified solution can be obtained from the lossless transmission line equations [4], where the losses are represented by resistances at the ends and center of the transmission line; This is a good approximation for R<< Z.

III. POINT-MATCHED FINITE ELEMENT METHOD

This method [4,8-12] requires the line to be subdivided into a one-dimensional finite number of subregions called elements. Each element has several points called interpolation nodes. This allows "v" and "i" to be written in the form:

$$\begin{cases} v(x,t) = \sum_{i=1}^{M} \phi_i(x)\, V_i(t) \\ i(x,t) = \sum_{j=1}^{N} \psi_j(x)\, I_j(t) \end{cases} \quad (8)$$

where "M" and "N" represent the number of nodes of the "V" and "I" finite element segments, respectively, and ϕ_i and ψ_j are basis functions that interpolate the voltage and current within each element using the values at the nodes as interpolation coefficients.

This approach is referred to as the point-matched time domain finite element method (TDFE) because $\phi_i(x)$ and $\psi_j(x)$ are defined to be

$$\begin{cases} \phi_i(x) = \begin{cases} 1 \text{ at } x = x_i \\ 0 \text{ at other nodes} \end{cases} \\ \psi_j(x) = \begin{cases} 1 \text{ at } x = x_j \\ 0 \text{ at other nodes} \end{cases} \end{cases} \quad (9)$$

In the leap-frog scheme, the time derivatives are represented by the forward Euler difference given by

$$\begin{cases} \dfrac{\partial V_i^{n+\frac{1}{2}}}{\partial t} \approx \dfrac{V_i^{n+1} - V_i^{n}}{\Delta t} \\ \dfrac{\partial I_j^{n}}{\partial t} \approx \dfrac{I_j^{n+\frac{1}{2}} - I_j^{n-\frac{1}{2}}}{\Delta t} \end{cases} \quad (10)$$

where I_j^n is the current at x_j at time $n\Delta t$ and $V_i^{n+\frac{i}{2}}$ is the voltage at x_i at time $(n+1/2)\Delta t$.

Using appropriate interpolation functions, the following final equations are obtained

$$\begin{cases} V_i^{n+1} = \dfrac{2C'-G'\Delta t}{2C'+G'\Delta t} V_i^{n} - \dfrac{2\Delta t}{(2C'+G'\Delta t)\,\Delta x}\left(I_{j+1}^{n+\frac{1}{2}} - I_j^{n+\frac{1}{2}}\right) \\ I_j^{n+\frac{1}{2}} = \dfrac{2L'-R'\Delta t}{2L'+R'\Delta t} I_j^{n-\frac{1}{2}} - \dfrac{2\Delta t}{(2L'+R'\Delta t)\,\Delta x}\left(V_{i+1}^{n} - V_i^{n}\right) \end{cases} \quad (11)$$

Note that the solution to the Finite Element Method represented by (11) is stable [8] if

$$v \le \frac{\Delta x}{\Delta t} \quad (12)$$

where "v" is the wave propagation speed. This implies that the wave must not propagate more than one subdivision in space during one time step. To obtain the solution [8] set

$$\Delta x = v\Delta t. \quad (13)$$

IV. ANALYTICAL FORMULATION FOR DISTANT FIELDS

The lightning return stroke channel is modeled by a transmission line which is approximately represented as a thin wire vertical antenna attached to ground. Then, evaluations of the far EM fields generated by the channel are made.

The particular case of a vertical antenna of negligible thickness and height "H" above a perfectly conducting ground plane, and carrying a conduction current i(z,t) is illustrated in Fig.1; The boundary conditions at the ground plane are satisfied by constructing a mirror image of the antenna as shown in Fig.1 [7].

Starting with Maxwell's equations, one can determine the electromagnetic fields in terms of retarded potentials:

$$\begin{cases} \vec{E} = -\vec{\nabla}\phi - \dfrac{\partial \vec{A}}{\partial t} \\[2mm] \vec{B} = \vec{\nabla} \times \vec{A} \end{cases} \qquad (14)$$

subject to the Lorentz gauge given by

$$\vec{\nabla} \cdot \vec{A} + \frac{1}{c^2}\frac{\partial \phi}{\partial t} = 0 \qquad (15).$$

By manipulating (14) and (15) in the case of a rising current pulse in the z-direction of the channel, one obtains the following set of differential equations for the EM fields:

$$d\vec{E}_{real} = \frac{\mu_0 c^2}{4\pi}(pz-z)px\left[\frac{3i}{ra^4 c} + \frac{3}{ra^5}\int_0^t i\,d\tau + \frac{1}{ra^3 c^2}\frac{\partial i}{\partial t}\right]\hat{a}_x dz$$

$$+\frac{\mu_0 c^2}{4\pi}(pz-z)py\left[\frac{3i}{ra^4 c} + \frac{3}{ra^5}\int_0^t i\,d\tau + \frac{1}{ra^3 c^2}\frac{\partial i}{\partial t}\right]\hat{a}_y dz$$

$$+\frac{\mu_0 c^2}{4\pi}\left[\left(-px^2 - py^2 + 2(pz-z)^2\right)\left(\frac{i}{ra^4 c} + \frac{1}{ra^5}\int_0^t i\,d\tau\right)\right.$$

$$\left. -(px^2 + py^2)\frac{1}{ra^3 c^2}\frac{\partial i}{\partial t}\right]\hat{a}_z dz \qquad (16)$$

$$d\vec{B}_{real} = \frac{\mu_0}{4\pi}py\left[\frac{i}{ra^3} + \frac{1}{ra^2 c}\frac{\partial i}{\partial t}\right]\hat{a}_x dz +$$

$$+\frac{\mu_0}{4\pi}px\left[\frac{i}{ra^3} + \frac{1}{ra^2 c}\frac{\partial i}{\partial t}\right]\hat{a}_y dz \qquad (17)$$

where $i=i(z,t')=i(z,t-ra/c)$, and t' is the retardation time.
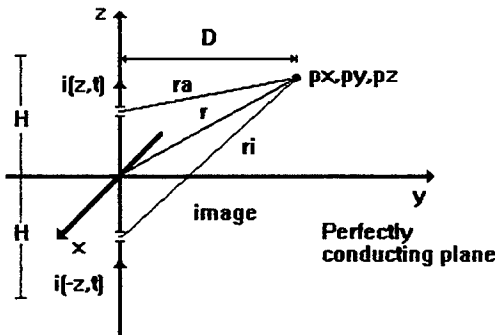
Fig.1:Vertical antenna of height "H" above a perfectly conducting ground plane

With regard to the contributions of the image antenna, it should be noted that they are calculated in a manner analogous to a real antenna by substituting "ra" for "ri" in Fig.1. In this way, the resultant EM fields can be obtained by integration along these two antennas in the z-direction, with the values of i(z,t) and i(-z,t) obtained from the solution of the transmission line equations (1) through the use of the finite element method.

V. RESULTS

For the lightning return stroke simulations that follow, typical channel parameters encountered in the relevant literature were used [1,4,7]. Channel height was assumed to be 4 km, and the following additional parameters were used: C'=3.5 pF/m, $v = 1/\sqrt{L'C'} = 80$ m/μs, G'=0 S/m. The losses (R') vary from 0 to 1 Ω/m. A triangular current function (1.125 x 25 μs) with a 10 kA peak value placed at ground level was used as the source of the channel model. Simulations were also carried out by using the formulation proposed by Uman [7] for a lossless line; The results are presented and compared with the solutions obtained from the formulation given in this paper, viz. equations (11). Finally, by the introduction of a finite value of resistance in the channel, EM fields are estimated for specific points in space.
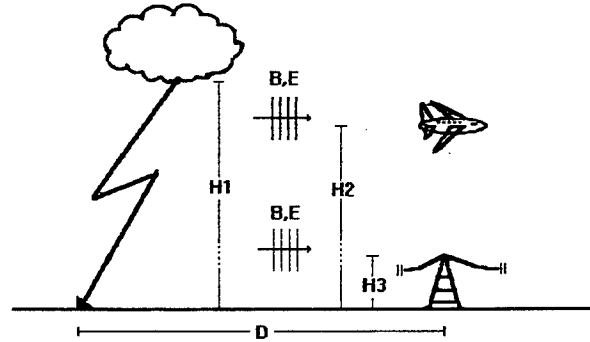
Fig.2: Cloud to ground lightning discharge and the resulting electromagnetic interference.

The results obtained with the finite element method show considerable accuracy in comparison with similar results obtained with Uman formulation [7] (see Figures 3 through 6). The oscillations observed in Figures 4, 6, 8 and 9 are due to problems caused by the influence of the retardation time and by the definition of the time step used to calculate the current and EM fields.

Introduction of resistance in the channel yields interesting results which can be observed in the EM waveforms (Figures 7 through 9). Some attenuation and distortion in B was expected and occured once the introduction of resistance attenuated and distorted the current waveform in the channel.

36
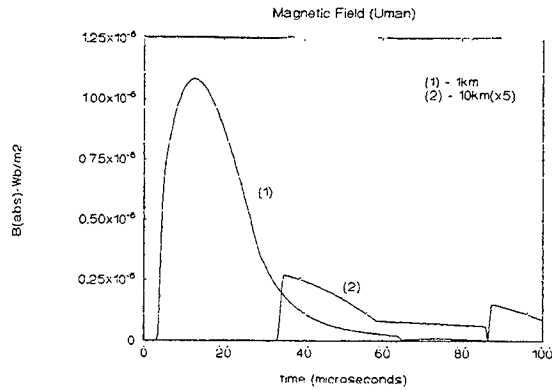
Fig.3: Magnetic field at distances of 1.0 and 10.0 km from the lightning return stroke, in the xy-plane (Uman) [7].
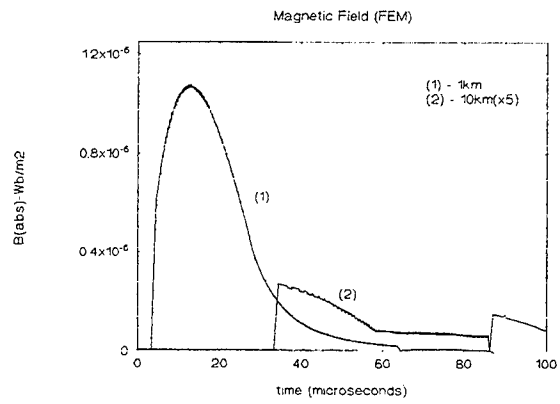
Fig.4: Magnetic field at distances of 1.0 and 10.0 km from the lightning return stroke, in the xy-plane, with R'=0 Ω/m (FEM).
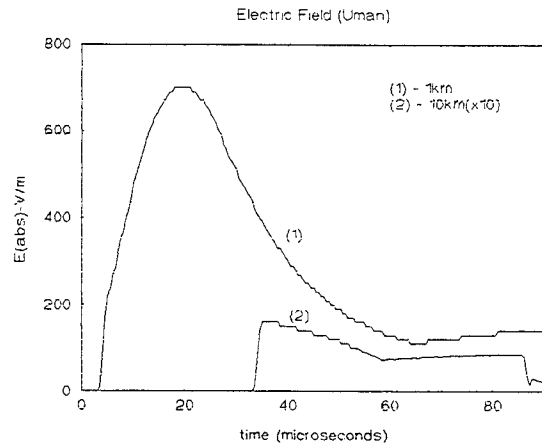
Fig.5: Electric field at distances of 1.0 and 10.0 km from the lightning return stroke, in the xy-plane (Uman) [7].
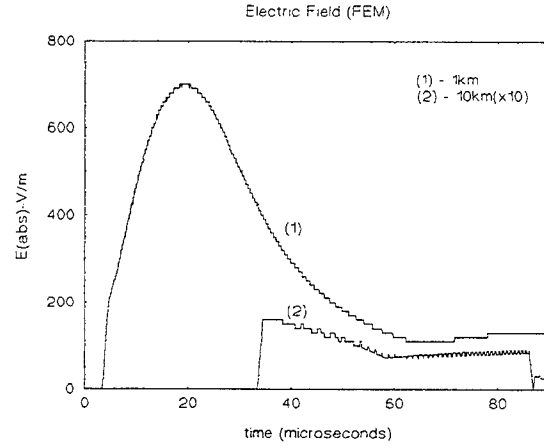
Fig.6: Electric field at distances of 1.0 and 10.0 km from the lightning return stroke, in the xy-plane, with R'=0 Ω/m (FEM).
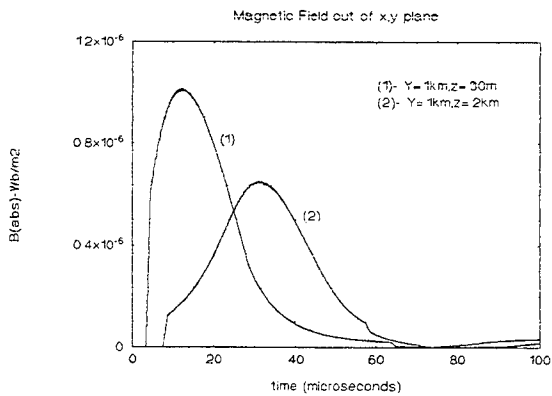
Fig.7: Magnetic field at z=30 m, y=1 km and z=2 km, y=1 km with R=1 Ω/m (FEM).
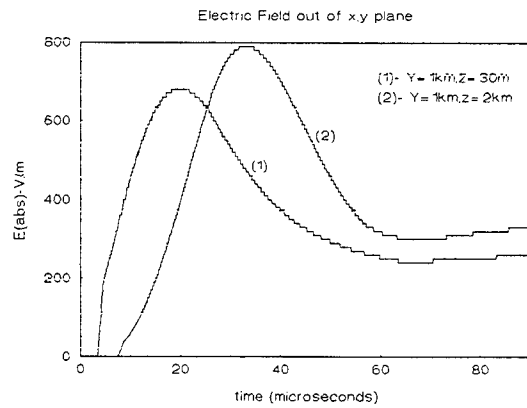
Fig.8: Electric field at z=30 m, y=1 km and z=2 km, y=1 km with R = 1 Ω/m (FEM).

37

Electric and Magnetic Fields
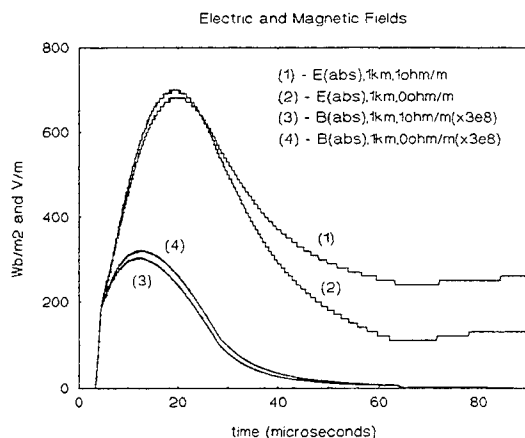
Fig.9: EM fields at a distance of 1 km from the lightning return stroke, in the xy-plane, with R=0 Ω/m and R=1 Ω/m (FEM).

Regarding the electric field E, the following observation can be made: its curve increased and decreased more slowly, suggesting a channel charge and discharge time alteration caused by the introduction of finite values of resistance R' in the channel (equation (11)).

Finally, in Figures 7 and 8, EM field waveforms were obtained at points with $pz \neq 0$, suggesting situations such as those shown in Fig.2.

It is important to note that the following simplifications were made in the construction of the model: (a) the channel was considered uniform and vertical, (b) a perfectly conducting ground plane was used, and (c) the absence of subsequent discharges was assumed.

VI. CONCLUSIONS

A consistent mathematical model of a lightning return stroke channel was presented, with the objective to evaluate the EM fields generated by the natural phenomenon of lightning at specific points in space. Different simulations were carried out, and the results compared favorably with those in the referenced literature.

The elevated losses introduced in the lightning return stroke channel, as suggested in the referenced literature [10,12], cause numerical problems in most mathematical models of representation. On this point, a great contribution in flexibility by the use of the finite element method was observed, which properly treats the phenomenon of propagation in transmission lines with elevated losses. It is worth emphasizing that the utilization of the finite element method in the various problems goes far beyond others. Its flexibility can be properly applied to other lightning return stroke

characteristics, such as corona effect, nonuniform parameters in lightning channels, and so on.

REFERENCES

[1] P. R. P. Hoole, "Modeling the lightning earth flash return stroke for studying its effects on engineering systems", IEEE Trans. Magn., Vol.29, No.2, pp.1839-1844, Mar. 1993.

[2] Y.T. Lin, M.A. Uman, and R.B. Standler, "Lightning return stroke models," J. Geophysical Research, Vol.85, No.C3, pp.1571-1583, Mar. 20, 1980.

[3] G. Diendorfer, "Induced voltage on an overhead line due to nearby lightning," IEEE Trans. Electromagnetic Compatibility, Vol.32, No.4, pp.292-299, Nov. 1990.

[4] E.H.R. Coppoli, V.M.Silva, G.C.Miranda, R.R. Saldanha, J.P. Filho, and A. Konrad, "The time domain finite element method applied to a lightning return stroke model, "EMC'94 Roma, Int. Symp. Electromagnetic Compatibility, pp.729-733, Sep. 13-16, 1994.

[5] L.B. Bewley, Traveling Waves on Transmission Systems, New York: Wiley, 1951.

[6] V. Amoruso, and F. Lattarulo, "The electromagnetic field of an improved lightning return stroke representation", IEEE Trans. Electromagnetic Compatibility, Vol.35, No.3, pp.317-326, Aug. 1993.

[7] M.A. Uman, D.K. Mclain, and E. P. Krider, "The electromagnetic radiation from a finite antenna," American Journal of Physics (AJP), Vol.43, pp.33-38, Jan. 1975.

[8] S. Y. Lee, A. Konrad, and R. R. Saldanha, "Lossy transmission line transient analysis by the finite element method," IEEE Trans. Magn., Vol.29, No.2, pp.1730-1732, Mar. 1993.

[9] G.C. Miranda, R.R. Saldanha, and J.P. Filho, "Comparacão de métodos de simulação de transitórios eletromagnéticos em linhas de transmissão sem perdas," pp.305-310, Proc. X Congresso Brasileiro de Automática, 1994 (in Portuguese).

[10] G.C. Miranda, E.H.R. Coppoli, R.R. Saldanha, A. Konrad, and J.P. Filho, "Point-matched time domain finite element method for transmission line transient simulation - Part II: Application to non-linear problems," Proc. IASTED Int. Conf. Appl. Modeling and Simulation, pp.12- 14, Vancouver, Canada, Jul. 21-23, 1993

[11] W.H. Press, W.T. Vetterling, S.A. Teukolsky, B.P. Flannery, Numerical Recipes, Second Edition, New York: Cambridge University Press, 1992.

[12] E.H.R. Coppoli, R.R. Saldanha, and A. Konrad, "Análise finita na avaliação de campos eletromagnéticos gerados por descargas atmosféricas", Proc. CBmag95 - Congresso Brasileiro de Eletromagnetismo, pp.287-290, Florianópolis, Brazil, May 14-17, 1995.

Point-Matched Time Domain Finite Element Method Applied to Multi-Conductor Electromagnetic Transients Analysis

Glássio Costa de Miranda

Universidade Ferderal de Minas Gerais - **High Voltage Laboratory**
Cx. Postal 209 - CEP 30161-970 - Belo Horizonte, Minas Gerais (BRAZIL)
e-mail: glassio@cpdee.ufmg.br

Abstract – A point-matched time domain finite element method (TDFE) applied to the analysis of electromagnetic transients in multi-conductor transmission line network is presented. The TDFE method solves the partial differential transmission line equations based on a semi-discrete approximation using the finite element method and leap-frog scheme. Some oscillations can occur due to the stability condition of the technique. Using the modal analysis these oscillations can be eliminated. A surge propagation in a simple multi-conductor network is presented and the results are compared with the Electromagnetic Transients Program (EMTP) simulations.

1. INTRODUCTION

A transient is the situation that occurs when the initial stability of the system is disturbed and the system is forced to settle in other stability condition. They are usually of short duration and decreasing amplitude with respect to time, space or both. In engineering practice, studies of these conditions are of increasingly importance.

The transient response of transmission line networks can be found by accounting for all interactions between forward and backward traveling waves as a result of discontinuities or disturbances. The evolution of the waveforms on the lines can be computed by solving a system of linear nodal equations in discrete time steps.

Some transmission line problems cannot be adequately modeled by the equivalent circuit approach. For transient scattering applications the point-matched time domain finite element (TDFE) method has been used [1-10] with great advantages. One of the great difficult with this approach is the errors due to the stability condition necessary to obtain the numerical solution (the others are the boundary conditions) which can introduce high frequency oscillations in the simulations.

This paper presents the modal analysis applied to the point-matched time domain finite element method for multi-conductor transmission line transient problems. In this approach, the propagation of disturbance on multi-conductor transmission line is simulated numerically in the modal domain by solving a n-dimensional boundary value problem at each time step. Results are presented for a simple network and compared with the Electromagnetic Transients Program (EMTP).

2. TRANSMISSION LINE EQUATIONS

The time domain formulation of multi-conductor transmission line problems (in the TEM approximation) can be described by a system of partial differential equations in (x,t) [11,12]

$$-\frac{\partial v(x,t)}{\partial x} = Ri(x,t) + L\frac{\partial i(x,t)}{\partial t},$$

$$-\frac{\partial i(x,t)}{\partial x} = Gv(x,t) + C\frac{\partial v(x,t)}{\partial t}, \quad (1)$$

where $v(x,t)$ and $i(x,t)$ are column vectors of the phase voltages and currents and R, G, L and C are the resistance, conductance, inductance and capacitance matrices per unit length respectively. There are n voltage and current equations describing the system and they are correspondingly increased in their number of terms to accommodate the couplings between the conductors. The simultaneous solution of these equations reveals n modes of propagation with, in the general case, each having its own velocity. Analytical solutions can be obtained for simple cases (e.g., lossless and distortionless lines) [11].

3. FINITE ELEMENT METHOD

Using the finite element method in the solution of time-dependent problems, the spatial approximation is considered first and the time approximation next. Such a procedure is commonly known as *semidiscrete approximation* (in space) [13]. The finite element method requires the line to be subdivided into a finite number of regions called elements. Each element has

39

points called interpolation nodes. This allows the voltage v and the current i to be written in the form

$$v(x,t) = \sum_{i=1}^{M} \phi_i(x)V_i(t),$$

$$i(x,t) = \sum_{j=1}^{N} \psi_j(x)I_j(t),$$

(2)

where M and N are the number of nodes of the finite element segments, and $\phi_i(x)$ and $\psi_j(x)$ are basis functions which interpolate the voltage and current within each element, defined as

$$\phi_i(x) = \begin{cases} 1 & x = x_i \\ 0 & \text{at other nodes,} \end{cases}$$

$$\psi_j(x) = \begin{cases} 1 & x = x_j \\ 0 & \text{at other nodes.} \end{cases}$$

(3)

The two nodes of a first-order finite element are located such that each voltage element contains an interpolation node for the current and each current element contains an interpolation node for the voltage. Only the interpolation functions associated with the adjacent nodes contribute to the summation in (2). Hence, substitution of (2) into (1), using (3) yields

$$RL^{-1}I_j + \frac{dI_j}{dt} = -L^{-1}\sum_{a=1}^{2}\frac{d\phi_a}{dx}V_a(t)$$

$$j = 1,2,\dots,N,$$

(4)

$$GC^{-1}V_i + \frac{dV_i}{dt} = -C^{-1}\sum_{a=1}^{2}\frac{d\psi_a}{dx}I_a(t)$$

$$i = 1,2,\dots,M.$$

In this equation, $\phi_a = \phi_a(x)$, $\psi_a = \psi_a(x)$, V_a represents the value of the two voltage nodes adjacent to the current I_j, and I_a represents the value of the two current nodes adjacent to the voltage node V_i.

This completes the semidiscrete finite-element formulation of (1), resulting in a set of ordinary differential equations in time. The second step is the time approximation, using the leap-frog scheme [3,4,14]. In the leap-frog scheme, the time derivatives in (4) are approximated by the Euler method, where the current time derivative is computed one-half time step

before the voltage time derivative. Substituting the independent current and voltage terms in equation (4) by the interpolated values at $t=n+\frac{1}{2}$ and $t=n-\frac{1}{2}$, the following equations are obtained

$$I_j^{n+1/2} = Z_1(2L - R\Delta t)I_j^{n-1/2} - \frac{2\Delta t}{\Delta x}Z_1\sum_{a=1}^{2}\frac{d\phi_a}{dx}V_a^n$$

$$j = 1,2,\dots,N,$$

(5)

$$V_i^{n+1} = Z_2(2C - G\Delta t)V_i^n - \frac{2\Delta t}{\Delta x}Z_2\sum_{a=1}^{2}\frac{d\psi_a}{dx}I_a^{n+1/2}$$

$$i = 1,2,\dots,M,$$

where $Z_1 = (2L + R\Delta t)^{-1}$ and $Z_2 = (2C + G\Delta t)^{-1}$. The approximation functions $\phi_i(x)$ and $\psi_j(x)$ depend on the type of element (number of nodes). Using $\phi_i(x)$ and $\psi_j(x)$ as first-order interpolation polynomials, (5) reduces to the following final equations [3,4]

$$I_j^{n+1/2} = (2L - R\Delta t)Z_1 I_j^{n-1/2} - \frac{2\Delta t}{\Delta x}Z_1(V_{j+1}^n - V_j^n)$$

$$j = 1,2,\dots,N,$$

(6)

$$V_i^{n+1} = (2C - G\Delta t)Z_2 - \frac{2\Delta t}{\Delta x}Z_2(I_i^{n+1/2} - I_{i-1}^{n+1/2})$$

$$i = 2,\dots,N+1.$$

4. STABILITY CRITERION

The solution to the leap-frog scheme approximation represented by (6) is stable [1,14] if

$$u\frac{\Delta t}{\Delta x} \leq 1,$$

(7)

where u is the wave propagation speed. This implies that the wave must not propagate more than one subdivision in space during one time step. Condition (7) can be analyzed using the step response of a single-conductor system shown in Figure 1 [5].

Using a fixed time step (Δt), for space discretization (Δx) greater than Δt, the solution for the transmission line differential equations is incorrect. For the matrix system presented in (6) the errors obtained with the TDFE method applied to the solution of the partial differential equations are due to a unique value of space

40

discretization used for different wave propagation speed.
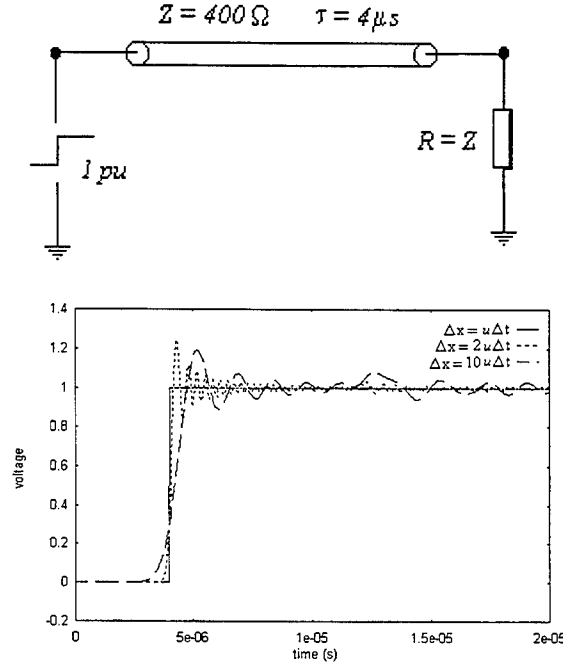
Figure 1 - Stability criterion

5. MODAL ANALYSIS

Wedephol [15] and Bickford [12] show that it is possible to normalize (1) and thereby replace them by a similar set of equations free of mutual terms. The problem then reduces to the solution of n single-phase equations of the same general form [16]. Just as the solution of the single-circuit wave equation leads to the mode of propagation and relationship between current and voltage (wave speed propagation and surge impedance) for the voltage and current waves on the single circuit, so the solution of these equations yields the n modes of propagation for the multiple conductor system.

Rewriting (1) in the frequency domain, one can obtain

$$\frac{\partial^2 v(x,w)}{\partial^2 x} = (ZY)v(x,w)$$

$$\frac{\partial^2 i(x,w)}{\partial^2 x} = (YZ)i(x,w)$$

(8)

where $Z = R + jwL$, $Y = G + jwC$. The approach used to decouple each one of those equations is similar to diagonalize either ZY or YZ [17]. In the diagonalization

process, two transformation matrices are needed: matrix Q for the currents ($I_{phase} = QI_{mode}$) and matrix P for the voltages ($V_{phase} = PV_{mode}$). P and Q are the solutions of the eigenproblems

$$P^{-1}(ZY)P = \gamma^2$$

(9)

$$Q^{-1}(YZ)Q = \gamma^2$$

where γ_i is the i-th eigenvalue and the columns of P and Q are the eigenvectors of ZY and YZ respectively. The transformation matrices are theoretically complex and frequency-dependent. With a frequency-dependent transformation matrix, modes are only defined at the frequency at which the transformation matrix is calculated. Then the concept of converting a multi-conductor line into decoupled single-conductor lines (in the modal domain) cannot be used over the entire frequency range. It is possible to find an approximate transformation matrix which is real and constant. The errors of this approximation vary with frequency. They are small in one particular region and large in other regions, depending on how the approximation is chosen. However, the problem of how to choose this constant transformation matrix remains.

There is a class of conductor configuration in which the process of diagonalization is greatly simplified. It is called balanced system. A balanced transmission line is defined as a line where all diagonal elements of Z and Y are equal among themselves, and all off-diagonal elements are equal among themselves. Balanced lines have a useful property, that is, the transformations to decouple their differential equations are independent of the particular system. There are several well-known transformations for balanced lines: symmetrical components, Clark's transformation, Karrenbauer's transformation, among others. For Karrenbauer's transformation

$$P = Q = \begin{pmatrix} 1 & 1 & 1 & . & . & 1 \\ 1 & 1-n & 1 & . & . & 1 \\ 1 & 1 & 1-n & . & . & 1 \\ . & . & . & . & & . \\ . & . & . & & . & . \\ 1 & 1 & 1 & . & . & 1-n \end{pmatrix}$$

(10)

where N is the number of conductors. For lossless high frequency approximation one can show that (10) is a

41

good approximation and can be used to solve some problems.

6. NUMERICAL EXAMPLE

A performance test is considered using the circuit shown in Figure 2. This simple geometry was chosen for two reasons. First, its boundary conditions are stable (open ended lines and simultaneous switch closing) and easy to compute. Secondly, a balanced lossless three-phase transmission line is used for simplification of the modal analysis application.
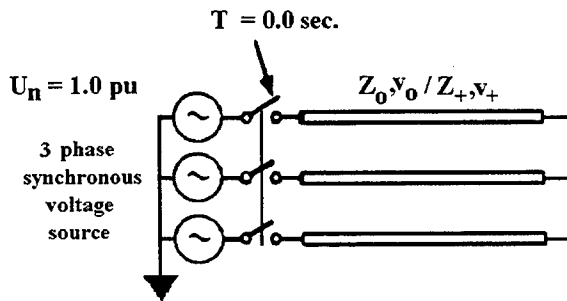
Figure 2 - Example circuit

Table I shows the switching surge modal parameters for the system of Figure 2. A switching surge is computed considering that the switches close at time $t=0$, for maximum voltage at phase 1. Figure 3 shows the voltage at the end of the line (phase 2) where high-frequency oscillations can be seen due to the different wave propagation speed.

Table I - Modal parameters

mode	Impedance (Ω)	Velocity (m/s)
zero	966.98	2.58E8
positive	362.59	2.30E8
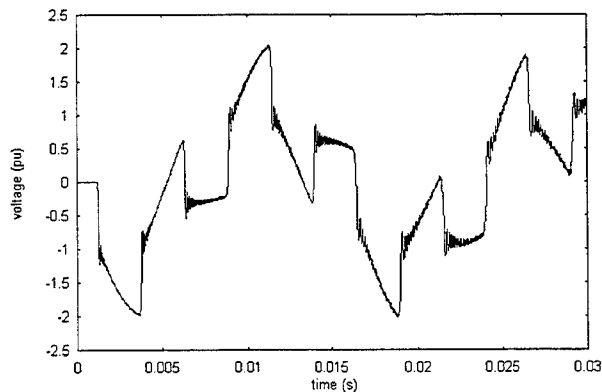
Figure 3 - TDFE method

Figure 4 shows the results for the numerical simulation using the modal analysis. Using three equivalent decopled single-conductor lines the oscillations due to the stability criterion are eliminated. For comparison, Figure 5 shows the same results obtained from the EMTP simulation (Microtran version [18]).
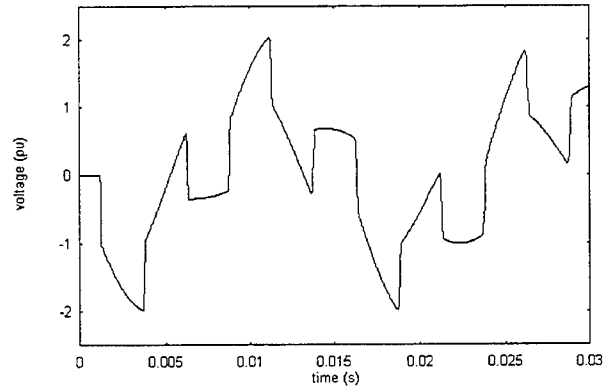
Figure 4 - TDFE method with modal analysis
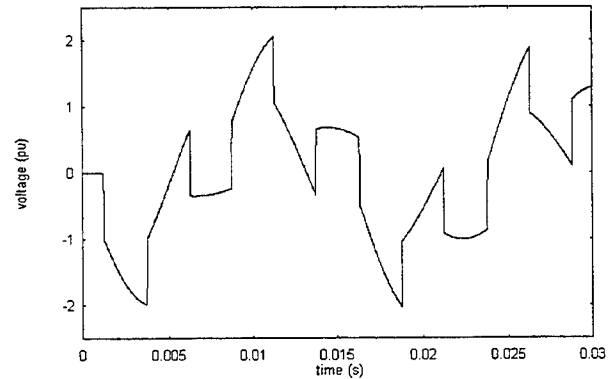
Figure 5 - EMTP simulation

7. CONCLUSIONS

The point-matched time domain finite element method applied to the numerical solution of the multi-conductor transmission line partial differential equations is stable but some high frequency oscillations can occur due to the different line speed wave propagation.

Applying the modal analysis to the numerical solution, the simulation errors are corrected. Some simplifications were made to obtain the transformation matrices. Work is in progress to obtain better results by modifying the constant-frequency approximate transformation matrices.

42

ACKNOWLEDGMENTS

REFERENCES

[1] Cangellaris, C.H. Lin, K.K. Mei, "Point-matched time domain finite element methods for electromagnetic radiation and scattering", *IEEE Trans. Antennas and Propagation*, Vol. AP-35, No. 10, October 1987, pp. 1160-1173.

[2] J. Joseph, T.J. Sober, K.J. Gohn, A. Konrad, "Time domain analysis by the point-matched finite element method", *IEEE Trans. Magnetics*, Vol. 27, No. 5, September 1991, pp.3852-3855.

[3] A. Konrad, R. Saldanha, S. Y. Lee, J. C. Sabonnadiere, "Application of the point-matched time domain finite element method to the analysis of transmission line transients", *Journal de Physique*, Vol. 2, No. 11, November 1992, pp. 2139-2154.

[4] S.Y. Lee, A. Konrad, "Lossy transmission line transient analysis by the finite element method", *IEEE Trans. Magnetics*, Vol. 29, No. 2, March 1993, pp. 1730-1732.

[5] G.C. Miranda, R.R. Saldanha, A. Konrad, J. Pissolato Filho, "Point-mached time domain finite element method for transmission line transient simulation part I: comparison with bergeron's method". *Proc. of IASTED International Conference on Applied Modelling and Simulation*, Vancouver (CAN), Vol. 1, August 1993, pp. 9-11.

[6] G.C. Miranda, E.H.R. Coppoli, R.R. Saldanha, A. Konrad, J. Pissolato Filho, "Point-mached time domain finite element method for transmission line transient simulation part II: application to non-linear problems". *Proc. of IASTED International Conference on Applied Modelling and Simulation*, Vancouver (CAN), Vol. 1, August 1993, pp. 12-14.

[7] E.H.R. Coppoli, V.M. Silva, G.C. Miranda, R.R. Saldanha, "Time domain finite element method applied to a lightning return stroke model", *Proc. of International Symposium on Electromagnetic Compatibility*, Rome (Italy), Vol II, 1994, pp. 729-733.

[8] G.C. Miranda, "Point-matched time domain finite element method applied to a non-uniform transmission line lightning return stroke model", *Proc. of IEEE International Conference on EMC,* Kuala Lanpur (Malaysia), Vol. 1, June 1995, pp. 67-72.

[9] G.C. Miranda, R.R. Saldanha, J. Pissolato Filho, "Point-matched time domain finite element method for corona effects on transmission lines", *Proc. of 9th International Symposium on High Voltage Engineering*, Graz (Austria), Vol. 8, September 1995, pp. 8321-1/8321-4.

[10] G.C. Miranda, A.E.A. Araújo, R.R. Saldanha, J. Pissolato Filho, "Finite Element Method for Transmission Line Corona Effect Simulation using the EMTP", submitted to IEEE PES winter meeting 1996.

[11] S. Bewley, *Travelling Waves on Transmission Systems*, John Willey & Sons, 1951.

[12] J.P. Bickford, N. Mullineux, J.R. Reed, *Computation of Power System Transients*, Peter Peregrinus LTD., Stevenage (UK), 1980.

[13] I.N. Reed, *An Introduction to the Finite Element Method*. McGraw-Hill, Singapore, 1984.

[14] W.H. Press, B.P. Flannery, S.A. Teukolsky, W.T. Vetterling, *Numerical Recipes*, Cambridge University Press, Second Edition, 1986.

[15] I. M. Wedephol, "Application of Matrix Methods to the Solution of Travelling-Wave Phenomena in Polyphase Systems", *Proceedings of IEE*, Vol. 110, No. 12, December 1963, pp. 2200-2212.

[16] A. Greenwood, *Electrical Transients in Power Systems*, John Willey & Sons, 1991.

[17] A.E.A. Araújo, *Transformation Matrices and Time Domain Transients Simulation - Overhead Lines*, notes, Vancouver (CAN), January 1991.

[18] *Microtran - Transients Analysis Program for Personal Computer*, Microtran Power Systems Analysis Corporation, Vancouver (CAN), 1992.

Glássio Costa de Miranda was born in Brazil in 1964. He received the B.Sc. and M.Sc. degrees in Electrical Engineering from Universidade Federal de Minas Gerais, Brazil, in 1987 and 1990, respectively and the D.Sc. degree from the Universidade Estadual de Campinas, Brazil, in 1994. Since 1992 he has been with the Department of Electrical Engineering of Universidade Federal de Minas Gerais, Brazil. His main research interest is in high voltage engineering, electromagnetic transients and electromagnetic compatibility.

Error Estimators in Self-Adaptive Finite Element Field Calculation

L.Lebensztajn, J.R.Cardoso
Escola Politécnica da Universidade de São Paulo
Departamento de Engenharia de Energia e Automação Elétricas
Av.Prof.Luciano Gualberto, Travessa 3, n° 158
05508-900 São Paulo SP Brazil
tel: +55 11 8185309 fax +55 11 8185719
e-mail: leb@pea.usp.br, cardoso@pea.usp.br

Abstract: The aim of this paper is to present different error estimates to improve accuracy in linear and nonlinear self- adaptive finite element field calculation. The first estimator is based on the polynomial theory, the second one makes an estimation of the flux density divergence, the third one is linked to a magnetomotive force associated to elements sides, and the fourth one is based on the use of the bilinear element. All methods were implemented in our software named LMAG2D developed at "Escola Politécnica da Universidade de São Paulo", Brazil.

I. INTRODUCTION

The design of an electromagnetic device has always been a hard task for both electrical and electronic engineers. The development of the Finite Element Method (FEM) and Computer Aided Design (CAD) techniques have changed several topics associated to the design of electromagnetic devices.

The Finite Element Method is reliable when the domain is wisely divided and self-adaptive schemes can greatly improve the quality of the mesh.

Self adaptive schemes [1] provide an adequate mesh to analyze the electromagnetic phenomena. The solution of the problem is more accurate, therefore more reliable. Consequently some relevant electromagnetic quantities such as flux, force and torque become more reliable.

A self-adaptive scheme is always based on an error evaluation. Several methods have been proposed to estimate the error on finite element analysis. Usually, the error estimators are based either on complementary methods, or on approximated estimation using field derivatives [2][3].

In this work, four estimators are proposed. The first one based on the polynomial theory is a modification of the estimator proposed by Fernandes et al [3]. This error evaluation was modified so as to allow for non-homogeneous domains. The second method is associated to a local error estimator and makes an evaluation of the flux density divergence for every element within the mesh. The third one is based on the inter-element discontinuity of the magnetic field intensity, when the magnetic potential vector is used. In the fourth method, the error estimation is based on the difference of two unlike fields: one is calculated with first order finite element triangular calculation and the other with a bilinear quadrilateral element.

II THE ERROR ESTIMATORS

All estimators here proposed are associated to a bidimensional magnetostatic problem linked to a finite element model, where the magnetic vector potential is applied.

The first error estimator is based on polynomial interpolation theory. According to Dhatt and Touzot[4], for first order triangular element, the error can be written as:

$$e = C_0 l^2 \text{Max}(\frac{\partial^2 A}{\partial x^2} ; \frac{\partial^2 A}{\partial x \partial y} ; \frac{\partial^2 A}{\partial y^2}) \qquad (1)$$

where C_0 is a constant
  A is the magnetic vector potential
  l is the element biggest side

The procedure for calculating the second derivative of the potential is similar to the one proposed by Fernandes [3], i.e.,

Step 1: The flux density in each vertex is the average of the flux density vectors in triangles that contain this vertex.

In this calculation the triangles must have the same magnetic property; thus, in non-homogeneous problems, the adopted procedure to evaluate the error is based on a multi-valued flux density at the interfaces.

This change makes Fernandes's error estimation more reliable.

Step 2: The flux density calculated in Step 1 leads the calculation of the second potential derivative by the use of the following hypothesis: the flux density is a linear interpolation of the nodal flux density. This hypothesis is assumed only for error calculation.

The second proposed error estimator is based on the divergence of the flux density. Firstly, the flux density vector is calculated in each node as the average of the flux density vectors in triangles that contain the vertex. The same procedure has already been adopted in the first error estimator (Step 1). To calculate the flux density vector within the triangles, the same shape functions applied to the magnetic vector potential were used. The determination of this vector divergence can be, in the whole domain, assumed as an evaluation for the solution error.

$$e = div\vec{B} = div(N_i\vec{B}_i) = \sum_{i=1}^{3}[(gradN_i)\bullet\vec{B}_i] \qquad (2)$$

Both estimators use the same flux density nodal evaluation, whereas the error evaluation reached by each method is different.

The third proposed method calculates the tangential magnetic field vector discontinuity on the sides of the triangles. Such discontinuity is associated to the solution error when the magnetic potential vector is used.

The discontinuity is only due to the numerical solution and it is linked to a magnetomotive force on the element side, because around this side Ampere's law is not satisfied by the numerical solution.Thus, in each triangle side, there is a magnetomotive force (J_{12}), which can be understood as a "side error" evaluation:

$$J_{12} = |H_{t1} = H_{t2}|l_{12} \qquad (3)$$

On each side of the mesh, Equation (3) shows that side error (J_{12}) is associated to the jump of the tangential component of the magnetic intensity, multiplied by the side length.

In this work, the error is associated to the nodes because this procedure does not require significant changes in the main code, or in the data structure. The nodal error can be written as:

$$e_i = \left(\sum_{j=1}^{NV}(J_{ij}/2)\right)/n_i \qquad (4)$$

Where: NV is the total number of vertex and n_i is the total number of the sides that contain the node i.

So the nodal error e_i is the arithmetic mean of all side errors associated to the node.

The fourth method to evaluate the error is based on the use of a bilinear element. In a first order triangular

mesh, a set of quadrilateral elements can be build (Fig.1). Each element has three neighbor triangles, from which it is possible to have three different quadrilateral elements built. If, however, two neighbor triangles have different magnetic proprieties, the quadrilateral can not be created, for the quadrilateral element must have only one magnetic propriety.
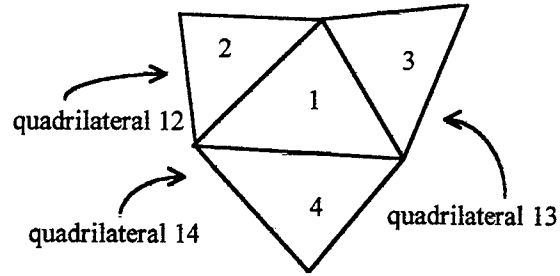
Figure 1 Three neighbor triangles

The local error can be written as:

$$e = \int_{\Omega}|\vec{B} - \vec{B}_q|d\Omega \qquad (5)$$

where $\vec{B}$ is the flux density, calculated by the finite element method, using a first order triangular element; $\vec{B}_q$ is the flux density, calculated using quadrilateral elements and Ω is one of the quadrilateral elements.

Thus, in the general case, a set of three error values can be computed for each triangular element. The local error in each element is assumed as being the highest value in the set.

For all proposed estimators, the applied adaptive refinement is a combination of a bisection, a Delaunay triangulation and an optimization of the nodal coordinates.

III TEST CASES

The efficacy of an electromagnetic field solution with a self-adaptive procedure can be measured either in cases where the analytic solution is known, or in problems where the numeric solution has been exhaustively tested by an electromagnetic field solution software, or in cases where experimental results are available.

Three test cases were then analyzed. The first one has an analytical solution through conformal transformations. It consists on the L-shaped region as can be seen in Figure 2.
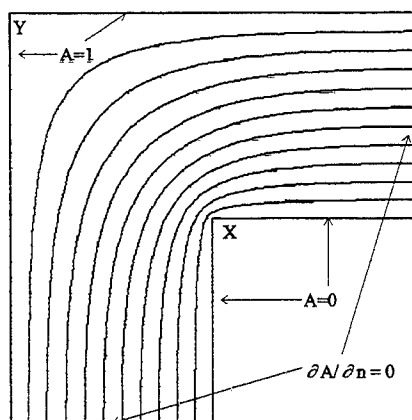
Figure 2- Geometry and Field Distribution for the First Problem

Simkin[5] has proposed a problem, where the main objective is the force computation in an iron part. The geometry of the problem is shown in Figure 3. Lowther [6] suggests solutions to this problems.
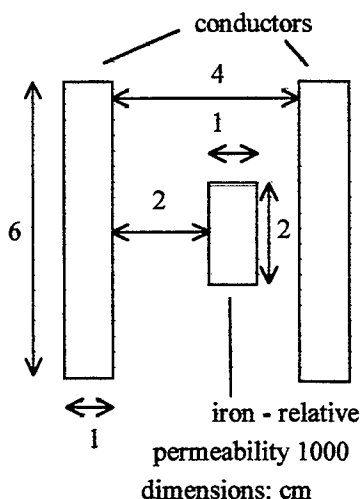
Figure 3 Geometry for the second case

The third case is a 75 kW permanent-magnet electric motor, which has a nonlinear behavior. This case was divided into three different subcases: an open-circuit test, a test to evaluate the inductance per phase, and one on-load condition test.

IV RESULTS

The indicators showed a satisfactory performance, concerning precision and convergence ratio related to local and global quantities for the analyzed cases.

Figure 4 shows the energy convergence of the first case for the first three adaptive proposed procedures.

They are also compared to a regular mesh in figure 4 and all estimators have a high convergence ratio and provide a minimum of energy with fewer nodes than the regular method.
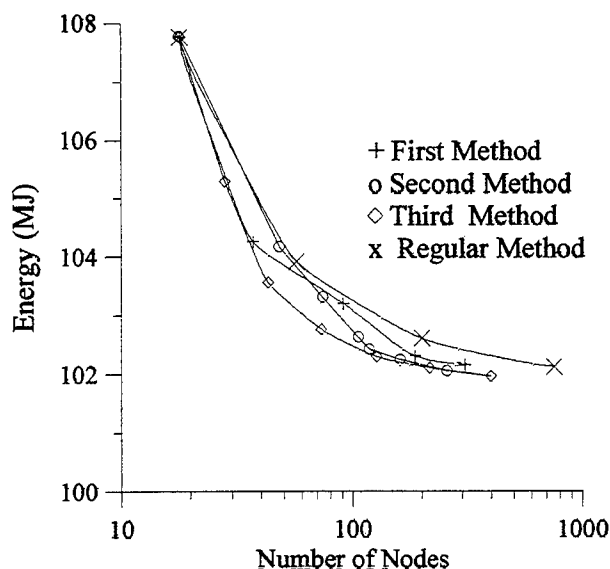
Figure 4 Energy Convergence

To calculate the precision on the magnetic vector potential along XY segment (Figure 2), analytical and numerical solutions are compared, and the deviation between them both was computed. Figure 5 shows the deviation on the magnetic vector potential along this segment, when the estimator based on the divergence is applied. High errors were reached only on the vicinity of the singular point (X) [7].
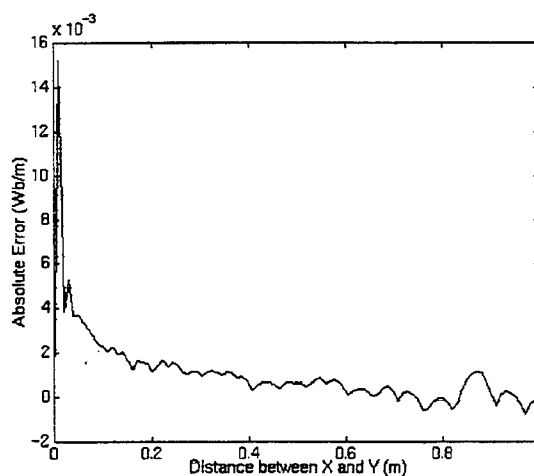
Figure 5 Error on the Potential – Case 1

46

In the second case, more complex than the first one, satisfactory results were obtained for the calculated force, applying the virtual work principle. Figure 6 shows the field distribution, and Figure 7 shows the obtained mesh when the third method was used.
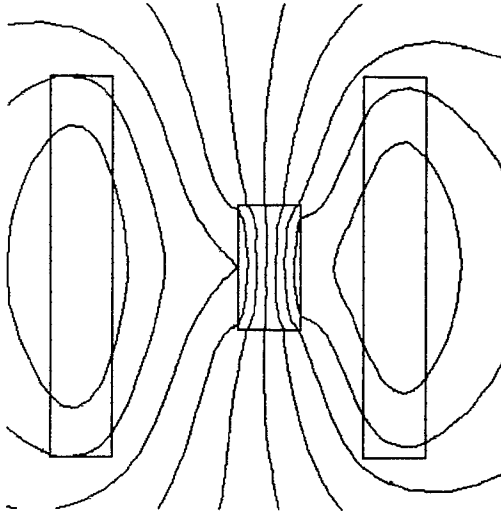
Figure 6 Field Distribution for the Second Case
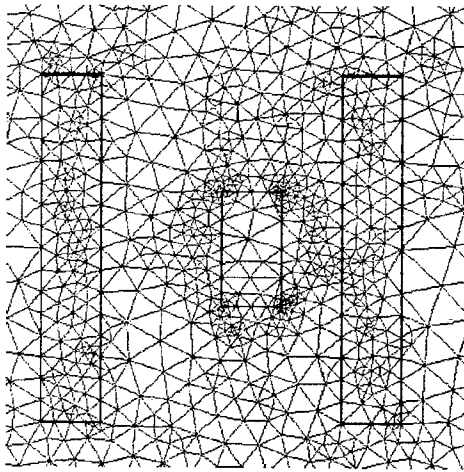
Figure 7 Mesh for the second problem

Table 1 shows some important results linked to the second case.

Method	Force (N)	Nodes	Lowther's Result (N)	Iterations
1	6170	3010		8
2	6280	2892	6146	6
3	6130	1445		7
4	6158	2215		6

High accuracy was obtained by methods 1, 3 and 4 because these error estimators identify more elements for refinement on the corners of the iron part and on the conductors.

According to Simkin [5], a refinement on the corners of the ferromagnetic part is the key to achieve a high precision force calculation.

The deviation of method 2 is the highest because the iron-air interface is well divided in triangles, but the conductors and the surrounding air around the part do not have a proper discretization.

The third case presents a nonlinear behavior of the ferromagnetic material. The self-adaptive scheme provides a good mesh and good results, compared to the prototype, for the four error estimators proposed.

Figure 8 shows the field distribution for the PM motor at no-load, using method 1. The self-adaptive scheme provides a minimization of the errors and symmetry can be observed in the figure.
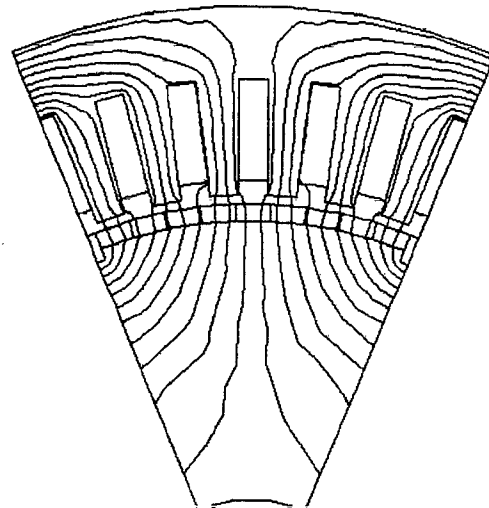
Figure 8 Field Distribution for the PM Motor at no-load

An electromotive force at no-load in an auxiliary winding was calculated and compared to the experimental data and a good agreement was reached. Table 2 shows, for the four estimators, the main data for the self-adaptive processes.

47

TABLE 2 COMPARATIVE RESULTS: THIRD CASE – E.M.F.

Method	Number of Nodes	Iterations	Calculated e.m.f. (V)	Measured e.m.f. (V)
1	1276	4	3.42	
2	1779	3	3.40	3.61
3	769	6	3.41	
4	1651	4	3.37	

The calculation of the inductance per phase was also performed, and the end-winding inductance was considered using analytical methods. Figure 9 shows the mesh obtained and Figure 10 shows the field distribution, using method 2. There is a high density mesh around the energized conductor and also in the air-gap, because both regions have high density energy.
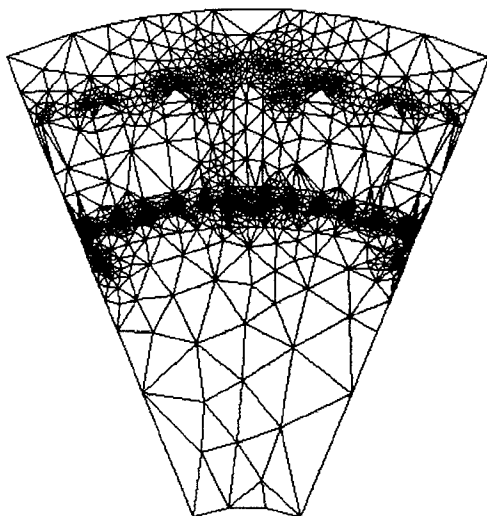
Figure 9 Mesh for the third problem: inductance calculation
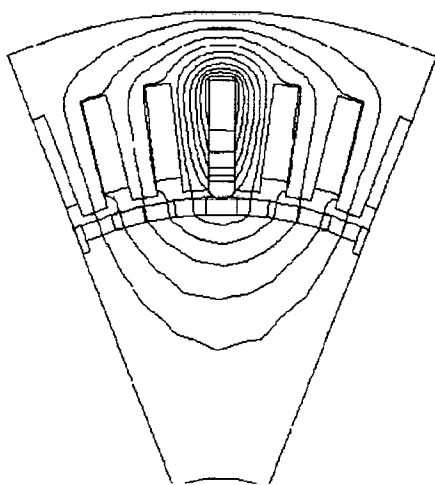
Figure 10 Field Distribution: inductance calculation

Table 3 shows some relevant data related to the self-adaptive processes, using the four proposed estimators. A good agreement between experimental and calculated data was achieved.

TABLE 3 COMPARATIVE RESULTS – INDUCTANCE CALCULATION

Method	Number of Nodes	Iterations	Calculated Inductance (mH)	Measured Inductance (mH)
1	1589	5	7.12	
2	2015	3	7.17	7.09
3	2369	3	7.21	
4	1043	4	7.13	

A calculation of an on-load condition of the PM-motor was performed. Figure 11 shows the obtained mesh, and Figure 12 shows the field distribution when the fourth method was used.
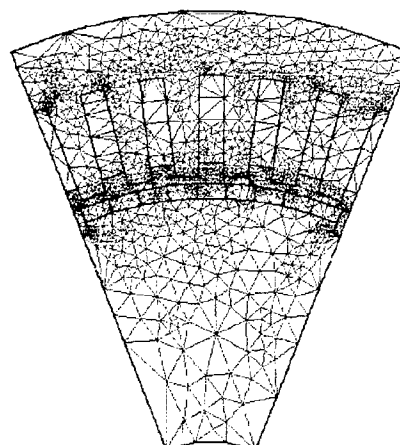
Figure 11 Mesh for the third problem: PM-motor on-load
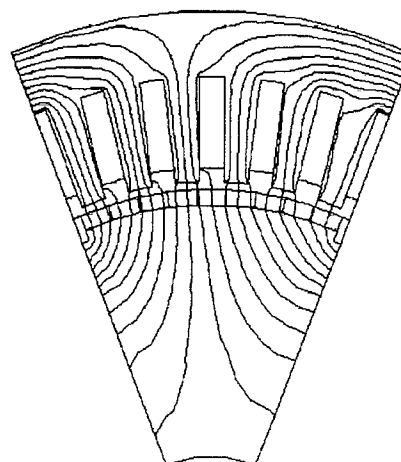
Figure 12 Field distribution for the third problem: PM motor on load

Table 4 shows a comparison between the experimental and computed torque for the four proposed estimators. A good agreement was reached for all methods because the air gap was wisely subdivided in elements. The Finite Element Method can model accurately the armature reaction and the developed torque, only if the air-gap is wisely subdivided.

TABLE 4 COMPARATIVE RESULTS – TORQUE CALCULATION

Method	Nodes	Computed Result (N.m)	Experimental Result (N.m)	Iterations
1	1075	320		4
2	1809	329	328	3
3	1961	332		3
4	1823	327		4

V CONCLUSIONS

This paper analyzes four error estimators. The first and the fourth error estimators provide adequate element mesh to analyze electromagnetic field phenomena.

Relevant to say that the first error estimator implies in shorter CPU times than the fourth one due, to its simplicity. The use of a multi-value density flux at interfaces made it more effective in calculation with heterogeneous media. However, the fourth error estimator is also reliable.

The second and the third error estimator produce a reability that is lower if compared to the other two estimators. Even though, the obtained results show better accuracy for most analyzed cases. The CPU time for this estimators is usually shorter.

Results show that a self-adaptive scheme is a powerful tool to improve accuracy in a finite element field calculation, even with nonlinear cases.

REFERENCES

[1] Lebensztajn, L. Processos Auto-Adaptativos de Solução de Campos Eletromagnéticos pelo Método dos Elementos Finitos, Tese - Doutorado, Escola Politécnica da Universidade de São Paulo, 1995

[2] Li, C. ,Ren, Z. ,Razek, A. Application of Complementary Formulations and Adaptive Mesh Refinement to Non-Linear Magnetostatic Problems IEEE Transactions on Magnetics Vol31 N°3 Mar.1995 pp1376-9.

[3] Fernandes, P. et alli Local Error Estimates for Adaptive Mesh Refinement IEEE Transactions on Magnetics Vol24(1) Jan 1988 pp209 -302.

[4] Dhatt,G. ,Touzot,G. Une Présentation de la Méthode des Élements Finis Maloine Editeur Paris Deuxième Édition.

[5] Simkin, J. Recent Developments in Field and Force Computation Journal de Physique, Colloque C1, Vol45, January 1984 pp851-860.

[6] Lowther, D.A., Rong, R.,Forghani,B. Field Smoothing and Adaptive Mesh Generation IEEE Trans. on Magnetics Vol29 (2) March 1993 pp 1890-1893.

[7] Lebensztajn,L., Hermann, M.R.,Cardoso, J.R. Estimadores de Erro para Processos Auto-Adaptativos para Cálculo de Campos Eletromagnéticos Proceedings: Congresso Brasileiro de Calculo de Campos Eletromagnéticos CBMag'95 May 95 pp136-139.

Transient Voltage and Electric Field Distributions
in Air Core Reactors

S. L. Varricchio
CEPEL - Electrical Energy Research Center
Caixa Postal 68007, Rio de Janeiro, RJ
21.944-970 - Brazil

N. H. C. Santiago
UFRJ - Federal University of Rio de Janeiro
Caixa Postal 68504, Rio de Janeiro, RJ
21.945-970 - Brazil

Abstract - This work presents a computational model for the evaluation of transient voltage and longitudinal electric field distributions in single layer air core reactors. The influence of a grounded shielding concentric to the reactor is considered. The validity of the model is verified by comparing computed and measured voltage responses at three taps of a test reactor. Analyses showing the influence of the grounded shielding, front time and front wave shape of the applied voltage on the maximum longitudinal electric stresses along the reactor winding are presented.

1. INTRODUCTION

The evaluation of transient voltage and longitudinal electric field distributions in equipment windings are important for their optimum electric insulation design.

The aim of this work is to develop an accurate model representing a simple single layer air core reactor. The knowledge acquired with the development and use of this model is an important basis for the development of accurate models of more complex equipment, such as three phases power transformers. In order to demonstrate that, a grounded shielding concentric to the reactor was modeled.

The accuracy of the model supports the authors' belief that this work is a relevant contribution to the general effort in modeling winding equipment.

2. EQUIVALENT ELECTRIC CIRCUIT

The lumped parameter model for the calculation of the voltage and electric field distributions is obtained by dividing the reactor into a number N of sections which are electrically and magnetically coupled [1,2,3]. This procedure leads to the equivalent circuit shown in Fig. 1.
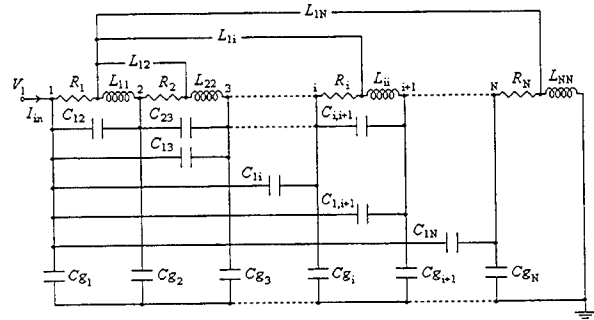
Fig. 1: Equivalent electric circuit

L_{ii} : Self inductance of section i
L_{ij} : Mutual inductance between sections i and j
Cg_i : Capacitance to ground of section i
C_{ij} : Mutual capacitance between sections i and j
R_i : Resistance of section i
V_1 : Applied voltage
I_{in} : Input current

The influence of a grounded shielding cylinder, concentric to the reactor, is taken into account using the same procedure as for the reactor, i.e., dividing the shielding into a number M of sections that are electrically and magnetically coupled among themselves and the reactor sections.

3. COMPUTATION OF THE ELEMENTS OF THE EQUIVALENT CIRCUIT

3.1 Capacitance Matrix

The calculation of the capacitance matrix is done by using the Galerkin's method as describe in [3] or by an integral-equation technique described in [4].

The reactor and the grounded shielding are modeled by equipotential cylindrical surfaces divided into N and M cells (sections), respectively, which are not necessarily equal in length. The potential ϕ_i at a cell i is given by:

$$\phi_i = \sum_{j=1}^{N+M} p_{ij}\, Q_j \ , \quad i = 1,\, N+M \qquad (1)$$

where Q_j is the total surface charge on cell j and p_{ij} is the potential coefficient between cells i and j.

Equation (1) forms a system of symmetric linear equations which can be written in a matrix form as:

$$[\phi] = [p][Q] \qquad (2)$$

Solving this system for the charges $[Q]$ yields:

$$[Q] = [c][\phi] \qquad (3)$$

where $[c] = [p]^{-1}$ is the partial capacitance coefficient matrix [4,5], since its elements represent the capacitance coefficient among parts (cells) of the equipotential cylindrical surfaces.

The capacitance matrix $[C]$ as well as the capacitances to ground of several cells are found from matrix $[c]$ [6].

The potential coefficient between two coaxial cylindrical cells [3], as shown in Fig. 2, is given by:

$$p_{ij} = \frac{1}{2\pi^2 \varepsilon_0\, l_i\, l_j} \int\limits_{h_j-l_j}^{h_j+l_j} \int\limits_{h_i-l_i}^{h_i+l_i} \left[\frac{F(k_1)}{A_1} - \frac{F(k_2)}{A_2} \right] dZ_i\, dZ_j \qquad (4)$$

where ε_0 is the air permittivity, $F(k_1)$ and $F(k_2)$ are complete elliptic integrals of the first kind with

$$A_1 = \left[\left(Z_i - Z_j\right)^2 + \left(R_i + R_j\right)^2 \right]^{1/2}, \quad k_1 = \frac{2\left(R_i R_j\right)^{1/2}}{A_1}$$

$$A_2 = \left[\left(Z_i + Z_j\right)^2 + \left(R_i + R_j\right)^2 \right]^{1/2}, \quad k_2 = \frac{2\left(R_i R_j\right)^{1/2}}{A_2}$$

In the expression (4) the ground plane is accounted for by the introduction of the image charges.
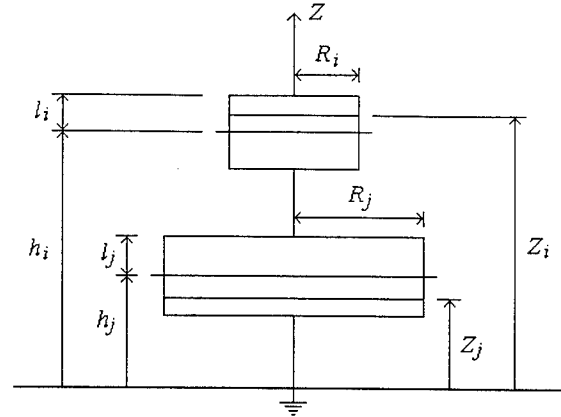
Fig. 2: Two coaxial cylindrical cells

3.2 Inductance Matrix

Consider the cells shown in Fig. 2 as two infinitesimally thin circular coaxial coils. From the application of Neumann's formula [6,7] to the turns localized at Z_i and Z_j, the mutual inductance between the coils is given by:

$$L_{ij} = \mu_0 n_i n_j \int\limits_{h_j-l_j}^{h_j+l_j} \int\limits_{h_i-l_i}^{h_i+l_i} \int\limits_{0}^{\pi} \frac{R_i R_j \cos\varphi\, d\varphi\, dZ_i\, dZ_j}{\sqrt{R_i^2 + R_j^2 + \left(Z_i - Z_j\right)^2 - 2R_i R_j \cos\varphi}} \qquad (5)$$

where n_i and n_j are the number of turns per unit length and φ is the azimuthal angle. All of the other variables have the same meaning illustrated in Fig. 2.

The computation of the numerical value of L_{ij} is carried out by using a technique based on Bartky's transformation which is described in detail in [7].

3.3 Resistance Matrix

Since the model presents low sensitivity to the resistance frequency dependence [1,3], the d.c. values of R_i are used.

4. SOLUTION OF THE EQUIVALENT CIRCUIT

The numerical technique used in solving the electric equivalent circuit shown in Fig. 1 is based on two variable sets. The first set is formed by the total input current and by the voltages at the numbered nodes from 2 to N. The second set is formed by the currents through the inductive branches of the circuit.

Thus, two matricial equations involving these variable sets are necessary. The first equation is obtained by establishing the relationship between the two variable sets by means of the resistive and inductive elements and the second equation by means of the capacitive elements.

The discretization of the circuit equations is achieved by applying the trapezoidal integration rule.

For the consideration of a grounded shielding concentric to the reactor, it is necessary to include another variable set. This new set is formed by the circulating induced currents at the M sections of the grounded shielding, according to the discretization shown in Fig. 3. These currents are induced by the magnetic coupling between the reactor winding and the grounded shielding.

Further details of the mathematical development are given in [2,3].
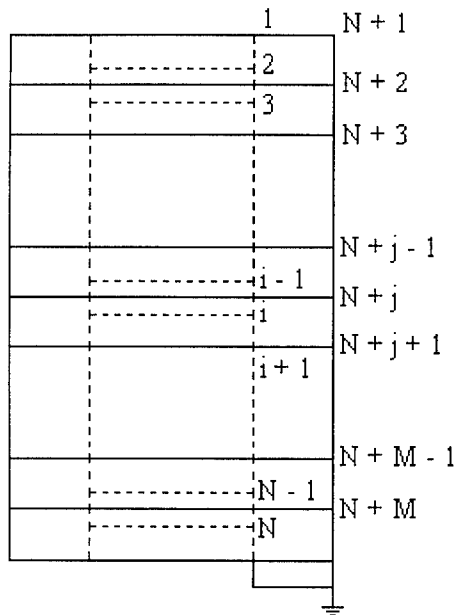
Fig. 3: Discretization of the system formed by the reactor and the grounded shielding

5. EXPERIMENTAL VERIFICATION OF THE THEORETICAL MODEL

In the following a brief description of the experimental setup is given. In order to show the validity of the model, a small sample of the comparative cases between the experimental and computed results is presented. Additional details are given in [1,2,3].

5.1 Experimental Setup

A test reactor and two shieldings were built. The dimensions of the reactor are shown in Table I.

Table I: Reactor dimensions

Length (m)		1.0
Diameter (m)		0.110
Wire Diameter (mm)		0.813
Number of turns		1130
Height above ground (m)		0.150
Measuring tap positions from reactor top (m)	Tap 1	0.2
	Tap 2	0.5
	Tap 3	0.8

The shieldings consisted of thin aluminum cylinders with equal lengths of 1.0 m and diameters of 0.26 m and 0.22 m.

Three reactor configurations were used, as follows:

Conf. 1 - Reactor without grounded shielding.
Conf. 2 - Reactor with a grounded shielding of 0.26 m diam.
Conf. 3 - Reactor with a grounded shielding of 0.22 m diam.

The applied voltage wave shapes were produced by two low voltage sources (impulse and step wave shape generators).

Measurements were performed using a digital oscilloscope with two probes. One probe was used to measure the applied voltage wave shape (V_1) and the other one was used to measure the voltage response in one of the measuring taps as shown in Fig. 4.
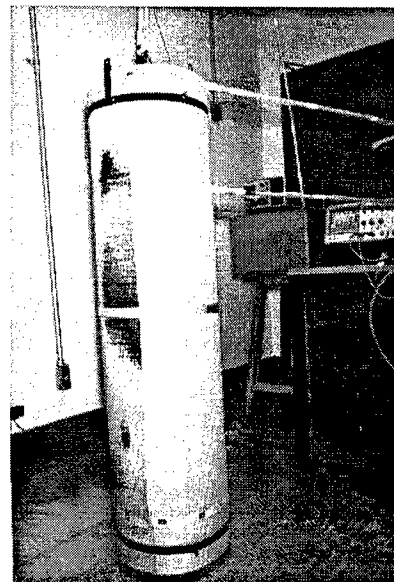
(a)
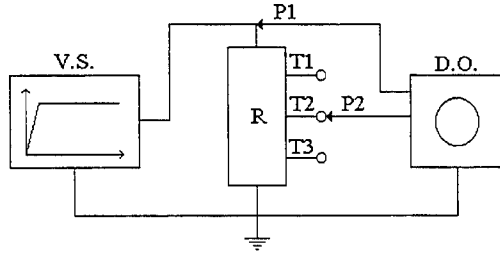
V.S.   : Voltage source
D.O.   : Digital oscilloscope
R   : Reactor with/without grounded shielding
P1, P2   : Probes
T1, T2, T3 : Measuring taps

(b)

Fig. 4: Experimental setup: (a) photo, (b) schematic diagram

5.2 Comparison between Measured and Computed Voltage Responses

Fig. 5 shows the measured and computed voltage responses at taps 1 and 3 for an impulse voltage applied to the test reactor as in Conf. 2. The front time and time to half value [8] for the impulse voltage were $0.750\ \mu s$ and $44\ \mu s$, respectively.
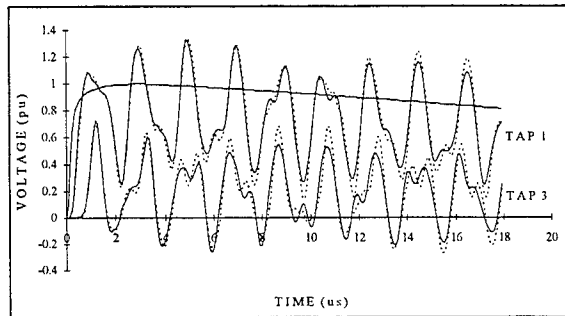
Fig. 5: Measured (full line) and computed (dotted line) voltages responses

6. EVALUATION OF THE LONGITUDINAL ELECTRIC FIELD ON THE REACTOR WINDING

The relationship among the electric and magnetic potentials and the electric field is given by:

$$\bar{E} = -\nabla V - \frac{\partial \bar{A}}{\partial t} \qquad (6)$$

Where $\bar{E}$ is the electric field, V is the electric scalar potential, $\bar{A}$ is the magnetic vector potential and t is the time.

For cylindrical windings which present current distributions characterized by $J_z = 0$, similarly to the winding of the test reactor, the following applies:

$$A_z = 0 \qquad (7)$$

where J_z is the longitudinal component of the superficial current density, $\bar{J}$, and A_z is the longitudinal component of $\bar{A}$.

Regarding Fig. 6 and equations (6) and (7), one has the following expression for the longitudinal component of the electric field E_z on the reactor winding:

$$E_z(r_0, z, t) = -\frac{\partial V(r_0, z, t)}{\partial z} \qquad (8)$$

Considering a specific time instant, the above equation can be approximated by:

$$E_z(z_i) = \frac{V(i+1) - V(i-1)}{2\Delta z} \qquad (9)$$

where:

z_i $\rightarrow$ Position on the reactor winding corresponding to node i of the equivalent electric circuit.

$E_z(z_i)$ $\rightarrow$ Longitudinal component of the electric field at position z_i on the reactor winding.

$V(i)$ $\rightarrow$ Voltage at node i of the equivalent electric circuit corresponding to position z_i on the reactor winding.

Δz $\rightarrow$ Distance between positions corresponding to two consecutive nodes of the equivalent electric circuit.
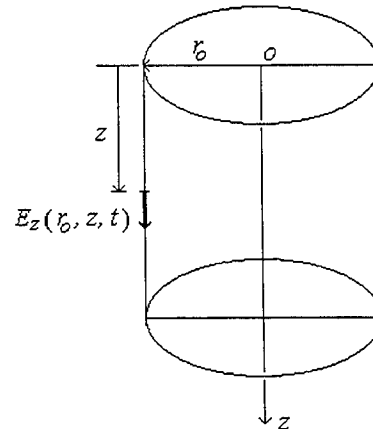
Fig. 6: Electric field on the reactor winding

Figs. 7(a) and (b) show spatial distributions of voltage and electric field, respectively, along the winding for a 0.750/44 μs impulse voltage applied to the test reactor as in Conf. 2. These distributions were computed at time instants which represent, approximately, 30%, 60% and 90% of the front time of the applied voltage.

In Fig. 7(b), E_{unif} represents the electric field due to a uniform voltage distribution, given by:

$$E_{unif} = \frac{V_{max}}{l} \qquad (10)$$

Where V_{max} is the peak value of the applied voltage and l is the total test reactor length.
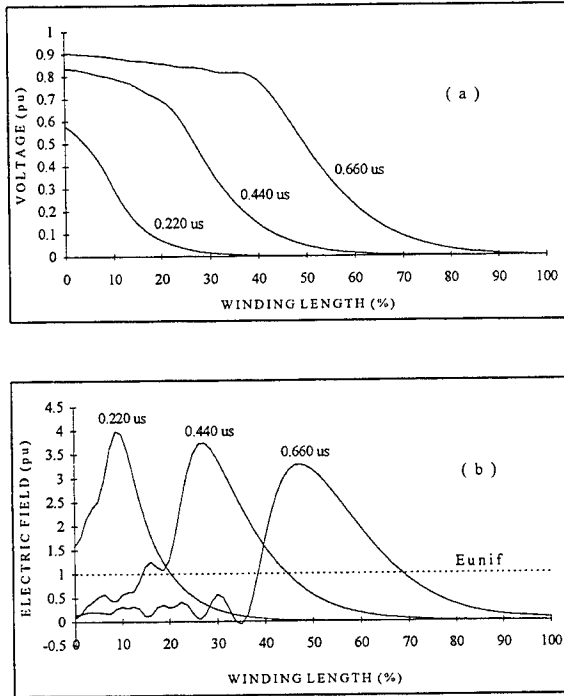
Fig. 7: Spatial distributions of (a) voltage and (b) electric field

7. INFLUENCE OF SOME FACTORS ON THE MAXIMUM LONGITUDINAL ELECTRIC STRESSES ALONG THE WINDING

7.1 Grounded Shielding

Fig. 8 shows the envelopes of the longitudinal electric field along the winding for an impulse voltage applied to the test reactor for all configurations. These envelopes represent the maximum values of the

longitudinal electric field which occurred along the winding during the application of the applied voltage.
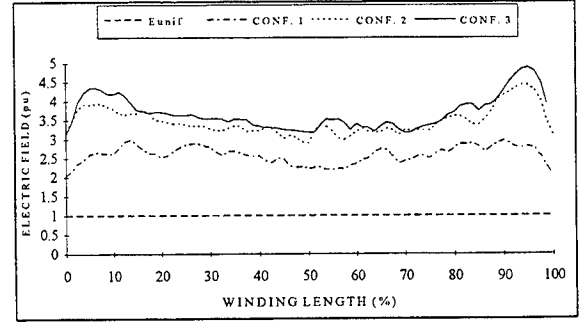
Fig. 8: Influence of the grounded shielding on the maximum longitudinal electric stresses

7.2 Front Time

Fig. 9 shows the envelopes of the longitudinal electric field along the winding of the test reactor as in Conf. 2. These envelopes were due to 0.750/44 μs, 0.950/44 μs and 1.150/44 μs applied voltages. The same behavior was found for the remaining configurations.
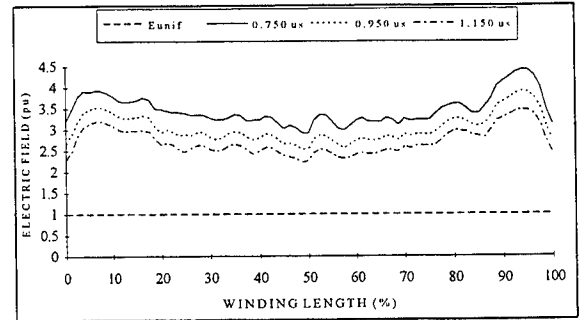
Fig. 9: Influence of the front time on the maximum longitudinal electric stresses

7.3 Front Wave Shape

Fig. 10 shows two applied voltage wave shapes which have the same front time and time to half value, i.e., 0.750/44 μs.

Fig. 11 shows the envelopes of the longitudinal electric field along the winding for the test reactor as in Conf. 2. These envelopes were due to the applied voltage wave shapes shown in Fig. 10.

54
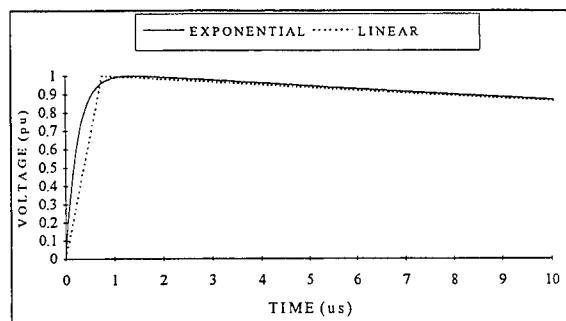
Fig. 10: 0.750/44 μs impulse voltages with different front wave shapes
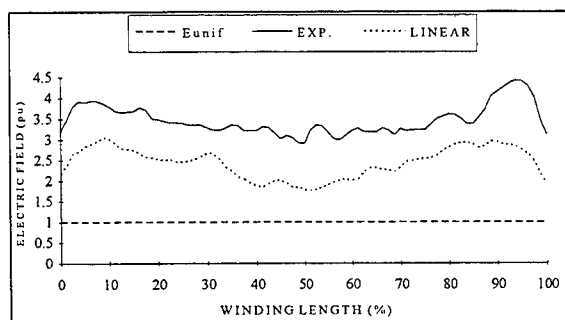
Fig. 11: Influence of the front wave shape on the maximum longitudinal electric stresses

8. CONCLUSIONS

An efficient discrete model to compute transient voltage and longitudinal electric field distributions in single air core reactor has been developed.

The validity and accuracy of the model were verified by comparing experimental and computational results.

A grounded shielding concentric to the reactor increases the maximum longitudinal electric stresses along the winding (Fig. 8). It must be pointed out that the stresses are higher for Configuration 3, showing that the higher the values of the winding capacitances to ground, the higher the maximum longitudinal electric stresses along the winding.

Regarding Figs. 9 and 11, one can conclude that the maximum longitudinal electric stresses along the winding are strongly dependent on the front time and the front wave shape of the applied voltage.

9. REFERENCES

[1] S. L. Varricchio, N. H. C. Santiago, "Transient Voltage Distribution in Air Core Reactors", Eighth International Symposium on High Voltage Engineering, No. 68.06, pp. 221-224, Yokohama, Japan, August 23-27, 1993.

[2] S. L. Varricchio, N. H. C. Santiago, "Electrical Strength in Air Core Reactors", Proceedings of the 4th International Conference on Properties and Applications of Dielectric Materials, No. 7236, pp. 876-879, Brisbane, Australia, July 3-8, 1994.

[3] S. L. Varricchio, "Transient Voltage Distribution in Air Core Reactors", M.Sc. Thesis - Federal University of Rio de Janeiro, Rio de Janeiro, Brazil, April, 1994 (in Portuguese).

[4] Albert E. Ruehli and Pierce A. Brennan, "Efficient Capacitance Calculation for Three-Dimensional Multiconductor Systems", IEEE Trans. Microwave Theory Tech., Vol. MTT-21, No. 2, pp. 76-82, 1973.

[5] A. E. Ruehli, "Electrical Analysis of Interconnections in a Solid-State Circuit Environment", IEEE Int. Solid-State Circuit Conf. Dig., pp. 64-65, 1972.

[6] S. Ramo, J. R. Whinnery and T. V. Duzer, Fields and Waves in Communication Electronics. New York: Wiley, 1965.

[7] Tharwat H. Fawzi and P. E. Burke, "The Accurate Computation of Self and Mutual Inductances of Circular Coils", IEEE Trans., Vol. PAS-97, No. 2, pp. 464-468, 1978.

[8] IEC 60-1, "High-voltage test techniques - Part 1: General definitions and test requirements", 1989.

Calculation of Electric Field Created by Transmission Lines, by 3D-FE Method Using Complex Electric Scalar Potential

Ricardo Marçal Matias & Adroaldo Raizer (ACES Member)
Departamento de Engenharia Elétrica - Universidade Federal de Santa Catarina
Cx. Postal 476 - CEP 88040 900 - Florianópolis - SC - Brazil
ricardo@grucad.ufsc.br / raizer@grucad.ufsc.br

Abstract - This paper presents a methodology for tridimensional analysis of the electric field produced by transmission lines. It utilizes the complex electric scalar potential, which makes it possible to consider variation of module and phase in the voltages of supply lines. The Finite Element Method (FEM) is applied to solve the differential equation that describes the phenomenon in the domain of this study. Finally, a comparison is established between the results obtained applying the proposed methodology and the values reached through the classical method of charge simulation.

I. INTRODUCTION

With a voltage level increase for transmission of large quantities of electrical energy, the effect of electrostatic field becomes an important factor in transmission lines (TL's) design.

This problem has been receiving increasing attention in recent years, from electrical power companies throughout the world. The origin of this concern is due, not only to the constant increase in the voltage levels in transmission systems, but also to the steady growth of urban concentrations, resulting in an increasing number of residential areas with TL's.

It is a well-known fact that the electric field produced by TL's at ground level, acting on a person, can cause nasty sensations, such as sparkling in the skin, attraction of the hair, organic and physiological alterations, when exposed for a prolonged period to a field of high intensity.

There exists the further risk of people touching objects with a high degree of isolation in relation to the ground (such as vehicles, fences, antennas and others) and being in contact with electric currents that can reach alarming levels, as a result of the electrostatic energy stored up by these objects when exposed to electric fields.

Although the gravity of some effects may still be debatable, the influence of the electrostatic field on men and the environment may become critical with the advent of high voltage and extra-high voltage TL's.

There is also the problem of the interference that these systems (TL's) can cause in other nearby installations, such as pipelines for the transport of fluids (oil ducts, gas ducts, aquaducts, etc.), railways and communication systems, etc. For this reason, a study of the electromagnetic compatibility (EMC) between these installations and the environment in which they are inserted, has become a matter of fundamental importance. One way of evaluating the EMC of these installations (in terms of disturbances of electrical origin) is through a knowledge of the values and distribution in the electrical field produced by them. For this purpose, the availability of precise and versatile calculation tools becomes necessary in order to guarantee the quality of the results.

The great majority of softwares for calculating the electric field of TL's are based on the axial symmetry that characterizes the fields in this installations, thus permitting a bidimensional analysis [1,6]. However, there are several different situations in which such a consideration could not apply, without giving incorrect results, or due to the very complexity of the geometry (for example, crossing among TL's).

The proposed methodology allows for a tridimensional analysis, making possible the study of a series of practical and interesting situations, such as considering various TL's, with some laid out assymetrically in relation to others [2]. Another important aspect concerns the utilization of the complex electric scalar potential, that permits to calculate the field for a sinusoidal applied voltage, still making possible a temporal analysis of the phenomenon throughout a cicle alternation voltage.

II. MATHEMATICAL FORMULATION

The Maxwell's equations used are:

$$\text{curl}\,\bar{H} = \bar{J} + \frac{\partial \bar{D}}{\partial t} \tag{1}$$

$$\text{curl}\,\bar{E} + \frac{\partial \bar{B}}{\partial t} = 0 \tag{2}$$

$$\text{div}\,\bar{B} = 0 \tag{3}$$

where $\bar{H}$ is the magnetic field (A/m), $\bar{E}$ the electric field (V/m), $\bar{B}$ the magnetic flux density (Tesla), $\bar{D}$ the

electric flux density (C/m^2), $\bar{J}$ the current density (A/m^2) and t the time (s).

The constitutive relations, concerning isotropic and linear materials are:

$$\bar{D} = \varepsilon \bar{E} \tag{4}$$

$$\bar{J} = \sigma \bar{E} \tag{5}$$

where ε is the electric permissivity (F/m) and σ the electric conductivity $(\Omega m)^{-1}$.

Utilizing equations (2) and (3) and knowing that (curl grad) is always zero [2], yields:

$$\bar{E} = -\text{grad} V - \frac{\partial \bar{A}}{\partial t} \tag{6}$$

But considering that in the case of the TL's, the electric field originated mainly due to the potential to which the conductors are submitted and, assuming that the variation of the values are sufficiently slow that the effect of the potential vector $\bar{A}$ can be ignored $(\frac{\partial \bar{A}}{\partial t} \cong 0)$, we can define the electric field as:

$$\bar{E} = -\text{grad} V \tag{7}$$

However, the electric scalar potential V is not sufficient to represent the total characteristics of the electric field produced by TL's, for the voltages in the line supply are sinusoidal, showing variations in module and angle of phase [2].

Therefore is necessary to utilize the complex electric scalar potential, defined how:

$$\dot{V} = V_0 \, e^{j(\omega t + \alpha)} \tag{8}$$

where V_0 is the voltage to which the line conductors are submitted (V), α is the phase angle (rad), ω is the angular frequency (rad/s) and t the instant of time considered (s).

Applying the divergent operator in the equation (1) and using equations (4) and (5), we get the equation that describes the phenomenon in the domain of this study:

$$\text{div} [(\sigma + j\omega\varepsilon)\text{grad}\dot{V}] = 0 \tag{9}$$

In this problem the following boundary conditions are considered:

• Dirichlet boundary condition, where the value of complex electric scalar potential is specified.

$$\dot{V} = \dot{V}_0 \tag{10}$$

• Neumann boundary condition, where the normal derivative of complex electric scalar potential is specified.

$$\frac{\partial \dot{V}}{\partial n} = 0 \tag{11}$$

Since an analytic solution to equation (9) is difficult, numerical techniques are utilized to solve it. Applying the FEM to solve this equation, subject to contour conditions (10) and (11), for each element in the mesh, a matrix, called the matrix of elementary contributions, is obtained. In our case, the elementary contribution matrix is complex and symmetrical. Its generic term is given by:

$$\dot{g}_{ij} = \int_{\Omega_e} \left[(\sigma + j\omega\varepsilon)\text{grad} N_i^t \, \text{grad} N_j \right] d\Omega_e \tag{12}$$

where i and j are lines and columns positions in the matrix, N_i and N_j are functions of nodal interpolation and Ω_e represents the domain of the finite element being considered.

The sum of all the elementary matrixes will form a global matrix system, where all the elements of the mesh are considered. This could be represented by:

$$\sum_{i=1}^{nno} \dot{g}_{ij}\dot{V}_j = 0 \qquad i = 1, nno \tag{13}$$

where $\dot{V}_j$ is the value of complex electric scalar potential at node j and nno is the total number nodes in the mesh.

The resolution of this matrix system gives the value of complex electric scalar potential at the nodes of the mesh.

For its resolution the method of conjugated orthogonally conjugated gradients (COCG) is utilized [5]. Once the system is solved, the electric field can be obtained by (7).

III. RESULTS

In the following section, results obtained for three situations will be shown, in order to demonstrate the validity of the methodology utilized.

A. Analysis of the 1050 kV three-phase transmission line

Here, a curve on the lateral profile of the electric field is shown. It was obtained by FEM, for a three-phase

transmission line of 1050 kV (Fig. 3.1.2) and will be compared with the result given by the classical method of charge simulation and also with the values measured.

The picture below (Fig. 3.1.1), shows the view in the plan of the domain of study.
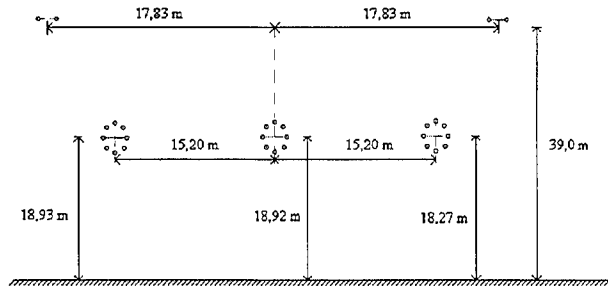
Fig. 3.1.1 Domain of study.

In this case, the domain of the study was separated into 10586 elements. 79 iterations were needed to obtain convergence and a 4 minute and 28 second calculation time in a station Sun SparkStation 2.

Table I, below, shows the main characteristics of the TL being studied [1].

Table I - Main features of 1050 kV transmission line.

Voltage (kV)	1050
Conductors per phase	8
Diameter of conductors (m)	0,03307
Diameter of lighting conductors (m)	0,01016
Distance between phases (m)	15,20
Height of phases (m)	18,93; 18,92; 18,27
Distance between lightning conductors (m)	35,66
Height of lightning conductors (m)	39,0

It was adopted for ABC phase sequence calculations from left to right and $t = 0$.
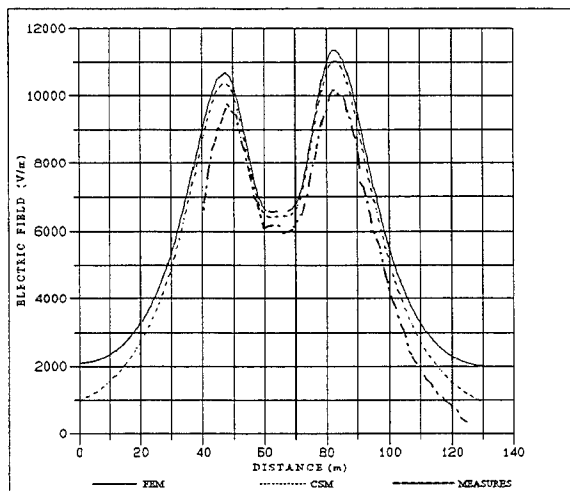
Fig. 3.1.2 Electric field calculated by FEM, CSM and measured values.

It is observed in Fig 3.1.2 that the results supplied by FEM are satisfactory. In Fig 3.1.3 equipotential lines are shown with the application of FEM. They provide a notion of potential distribution within the domain of this study and also point to regions where the electric field is or is not uniform.
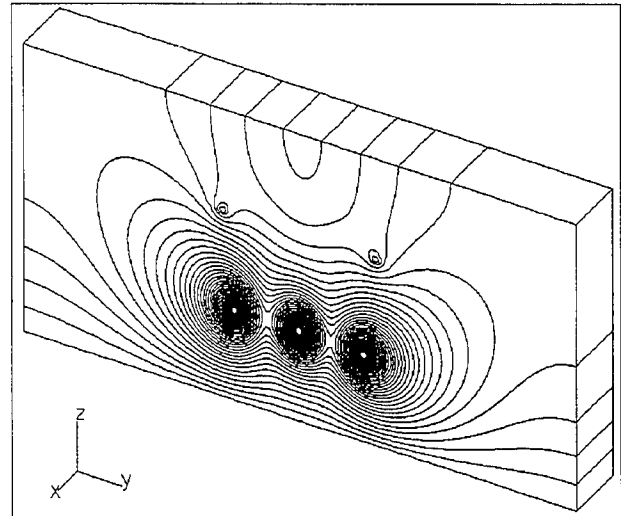
Fig. 3.1.3 Equipotential lines.

B. 1050 kV Line in the presence of material conductors

In this case, we consider the existence of two metallic sheds, under phases of 1050 kV transmission line. The figure that follows shows the domain of this study.

P1 and P2 are lightning conductors and A, B and C are phase conductors.
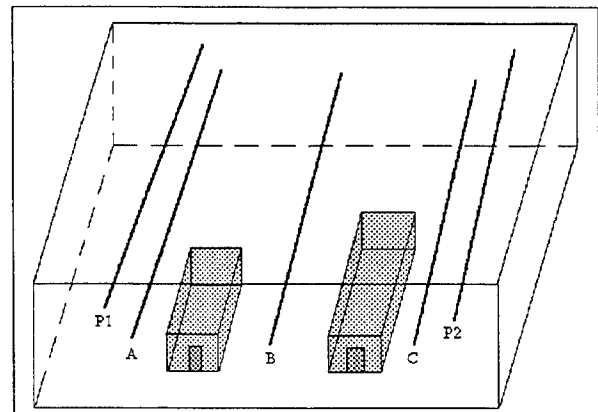
Fig. 3.2.1 Domain of study.

Fig. 3.2.2, presents a view of the equipotential lines, obtained for this study.

58
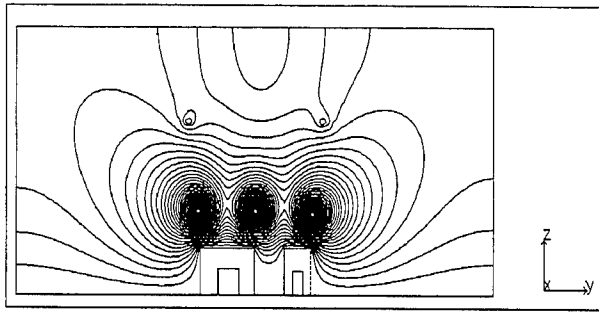
Fig. 3.2.2 Equipotential lines.

The influence of the metal sheds on the potential distribution is observed, and consequently the distribution of values in the electric field.

Due to the continuity of the tangential component of the electric field, the appearance of electric current density is observed in the inner superficial part of the conductor materials.

C. Hypothetical case of crossing between two TL's

Here we imagine the crossing (at 90°) between two TL's, one of 138 kV and the other of 500 kV. In the literature, no similar case is registered, which justifies the difficulty and even the impossibility of making such an analysis, with methods that were then available. For this case two curves on the lateral profile of the electric field were obtained, one on the y axis, that is, on the central phase of the 138 kV line (Fig. 3.3.2) and the other on the x axis, on the central phase of the 500 kV line (Fig. 3.3.3). The equipotential lines is shown in Fig. 3.3.4.

In the picture below (Fig. 3.3.1) is observed the approach of the domain of the considered study.

In this case, the domain of study was separated into 39,600 elements. 35 iterations were needed in order to obtain convergence, as well as a calculation time of 5 minutes and 23 seconds in a station Sun SparkStation 2.
Tables II and III shown below, present the characteristics of each one of the lines considered.

Table II - Principal features of 138 kV transmission line.

Voltage (kV)	138
Conductors per phase	1
Diameter of conductors (m)	0,03195
Distance between phases (m)	7,0
Height of phases (m)	10,0

Table III - Principal features of 500 kV transmission line.

Voltage (kV)	500
Conductors per phase	2
Diameter of conductors (m)	0,03195
Spacing between subconductors (m)	0,40
Distance between phases (m)	15,0
Height of phases (m)	18,0
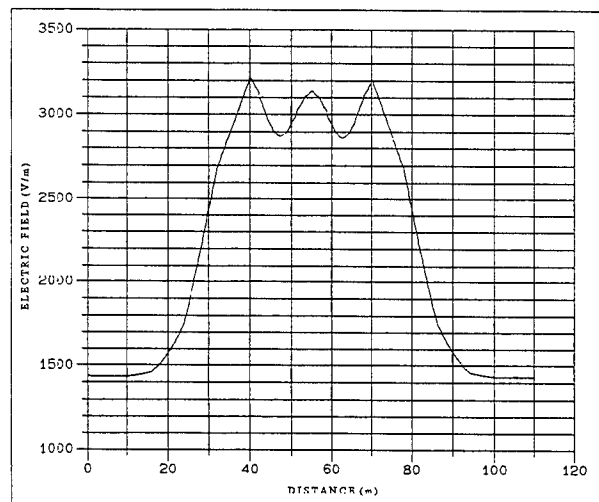
Fig. 3.3.2 Curve on the lateral profile of electric field on the y axis.

Fig. 3.3.1 Approach of the domain of study.

59
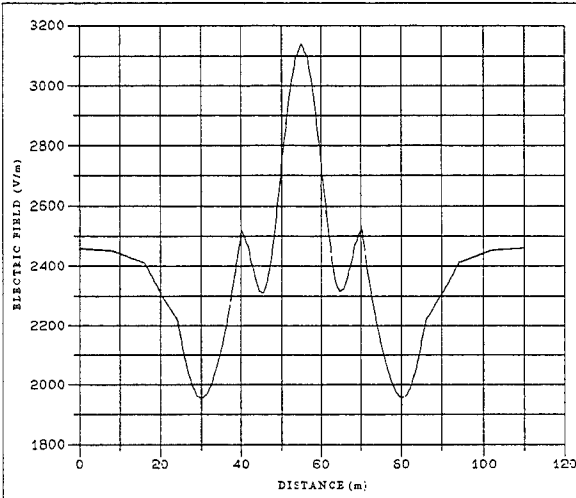
Fig. 3.3.3 Curve on the lateral profile of the electric field on the x axis.

In this case, values were not measured for comparative purposes. Nevertheless, analyzing the two lines separately, it can be observed that the results obtained are coherent.
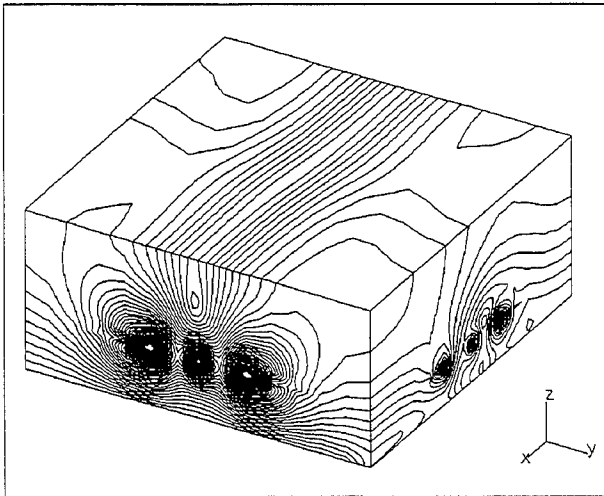
Fig. 3.3.4 Equipotential lines in crossing between two transmission lines.

IV. CONCLUSIONS

In this study, a mathematical model was presented to analyze a tridimensional electric field generated by TL's.

Values of the electric field are presented for two situations: one tri-phase transmission line of 1050 kV and the other a hypothetical case of crossing between two TL's.

Potential distribution on 1050 kV line was also shown, considering the presence of metallic objects along the line.

FEM has proved to be highly flexible, inasmuch as it easily permits the analysis of a large number of interesting practical situations, such as, the evaluation of values and of electric field distribution when there is a crossing of two or more TL's, the possibility of considering in calculations both the presence of conductor and/or multidielectrics materials, as well as irregularities of the land.

Therefore it can be demonstrated that the methodology utilized makes possible the analysis of more realistic situations, and consequently leads to obtaining more correct results.

REFERENCES

[1] Deno, D.W., "Transmission line fields", IEEE Trans. on Power Apparatus and Systems, Vol. PAS-95, No.5, pp.1600-1611, September/October, 1976.

[2] Pinho, A., Raizer, A., "Calculation of Tri and Hexa-phase Transmission Line Electric Field by Finite Element Method and Charge Simulation Method", the 1994 International Symposium on Electromagnetic Compatibility, Session III - Power System EMC, December, 1994.

[3] R. N. Allan; S. K. Salman, "Electrostatic Fields Underneath Power Lines Operated at Very High Voltages", Proc. IEE, Vol. 121, November, 1974.

[4] L. Ortiz N.; L. Perez B., "Application of Charge Simulation Method for Calculating Substation and Transmission Line Electric Field", 9Th COMPUMAG, Miami - Florida, 1993.

[5] Van der Vorst, H. A.; Mellissen, J. B. M., "A Petrov-Galerkin type Method for Solving Ax=b, Where A is Symmetric Complex", IEEE Trans. on Magn., MAG-26, 1990, pp. 706-708.

[6] M. Abdel-Salam, M. Th. El-Mohandes, H. El-Kishky," Electric Field Around Parallel dc and Multi-phase ac Transmission Lines", IEEE Transactions on Electrical Insulation, Vol.25, No.6, December 1990, pp. 1145-1152.

[7] H. Steinbigler, D. Haller., "Comparative Analysis of Methods for Computing 2-D and 3-D Electric Fields", IEEE Transactions on Electrical Insulation, Vol.26, No. 3, June 1991, pp. 529-536.

[8] O. W. Andersen., "Finite element solution of complex potential electric fields", IEEE Trans. Power App. Syst., v.96, July 1977, pp. 1156-1160.

[9] A. Konrad," Three-dimensional finite element solution of anisotropic complex potential problems", J. App. Phys., v..53, Nov.1982, pp. 8408-8410.

[10] J. R. Brauer, H. Kalfaian and H. Moreines, "Dynamic electric fields computed by finite elements", IEEE Trans. Industry Applications, v.25, Nov.1989, pp. 1088-1092.

60

Adaptive Finite Element Mesh Refinement and *'a posteriori'* Error Estimation Procedures for Electromagnetic Field Computation

K.C. Chellamuthu, Nathan Ida and Q.k. Zhang

Department of Electrical Engineering
The University of Akron
Akron, OH 44325-3904

Abstract - Adaptive Finite Element (FE) mesh refinement combined with a robust and functionally reliable error estimate provides nearly optimal solution accuracy. The efficiency of adaptivity depends on the effectiveness of the mesh refinement algorithm and also on the availability of a reliable and computationally inexpensive error estimation strategy. An adaptive mesh refinement algorithm utilizing a hierarchical minimal tree based data structure for 2D and 3D problems is discussed in this paper. Two different *'a posteriori'* error estimation schemes, one based on the local element by element method and the other using the gradient of field approach are also presented. The usefulness of the mesh refinement algorithm and the error estimation strategies are demonstrated by adaptively solving a set of 2D and 3D linear boundary value problems. The performance of the error estimates is also verified for adaptive modeling of a nonlinear problem involving the design of a permanent magnet synchronous machine.

I. INTRODUCTION

Due to the presence of discretization errors in any numerical modeling, the accuracy of the solution is limited. An accuracy in the range of 5% - 10% is often acceptable for most engineering applications. However certain scientific applications require solutions with a higher accuracy, in the range of 2%-3%. When the solution is plagued by the presence of domain singularities such as boundary layers, re-entrant corners, sharp bends, and multiple material discontinuities, it is necessary to selectively add more degrees of freedom where the solution varies abruptly. Under these situations, adaptivity helps to optimally improve the accuracy by selective spatial decomposition of a problem domain.

Many triangular and tetrahedral elements based adaptive mesh refinement techniques were proposed in the past [1,2]. However only a limited number of adaptive strategies are available for generating quadrilateral and hexahedral meshes [3]. The main reason is that the triangular elements match irregular boundaries better than quadrilateral and hexahedral elements. On the other hand, for the same number of unknowns, quadrilateral and hexahedral meshes require only about half that many elements as are needed in triangular or tetrahedral element meshes. Although triangular elements provide a good approximation to curved boundaries and complex geometries, they often produce elements with obtuse angles which need to be corrected using a Delaunay triangulation. Moreover visualizing higher order elements and refined meshes is easier in the case of quadrilateral/ hexahedral element meshes compared to triangular/ tetrahedral elements which produce unstructured meshes.

In an adaptive process, the critical areas of the problem domain are identified and refined based on a reliable error estimate. The equi-distribution of error in the problem signals the optimality of the adaptive mesh. An adaptive spatial decomposition technique employing first order quadrilateral elements in 2D and hexahedral elements in 3D utilizing a minimal hierarchical tree based algorithm is presented in the first part of this paper. Two different *'a posteriori'* error estimation strategies for activating the adaptive mesh refinement are discussed in the second part of the paper. In the third part of the paper, many numerical examples with experimental results are presented to demonstrate the application potential of the proposed mesh refinement algorithm and the error estimation strategies. The effectiveness of 'a posteriori' error estimates in adaptively solving a nonlinear problem for the computation of design parameters of a high field permanent magnet synchronous machine is presented in the last part of the paper.

II. ADAPTIVE MESH REFINEMENT TECHNIQUES

Starting with a coarse mesh, an efficient adaptive mesh refinement algorithm with the help of an error indicator and error estimator generates a nearly optimal mesh, in which the discretization error is equally distributed. It is imperative to generate a graded mesh in an adaptive process in order to produce a smooth solution. An adaptive mesh refinement algorithm should be capable of managing the computational complexity and data functions with a minimum of overhead on resources. In addition to providing an asymptotic rate of convergence, it should be able to handle different material properties and boundary conditions, while maintaining compatibility during the adaptive process. It must be flexible and robust and incorporate an efficient error estimation strategy to activate the adaptive process. Generally three different types of mesh refinement policies are available. A solution can be improved by reducing the size of an element ($h_{max}{\to}0$) or increasing the order of approximating polynomial ($p{\to}\infty$) or combining both or by moving the mesh and relocating the nodes. Accordingly the mesh refinement procedures are classified as $h, p, h\text{-}p$ and r-methods. In terms of number of degrees of freedom, the p-method is found to be nearly twice as efficient in convergence as the h-method [4]. Many different algorithms and the associated data structures were proposed in the past for automatic adaptive mesh refinement [1-3,5]. The proposed adaptive mesh refinement algorithm utilizes a h-version based mesh refinement policy.

A. *Quadrilateral & Hexahedral Mesh Refinement Strategies*

In the proposed adaptive scheme, the use of a hierarchical minimal tree data structure reduces the amount of tree travel necessary during the mesh refinement. Although most of the mesh refinement methods available in the literature employ tree based data structures they are computationally expensive. In the present approach a *one-level* rule is applied in order to generate a graded mesh with smooth mesh transition. The imposition of a *one-level* rule generates a constrained node on the boundary between two elements (common edge or face) in the quadrilateral and hexahedral meshes. Due to this, the meshes produced by this method are called 1-irregular meshes. The constraint nodes are processed in such a way that the sequence of admissible adaptive meshes produced

during the course of refinement will satisfy the compatibility and continuity conditions. Utilizing the local property of quadrilateral/hexahedral elements an element is subdivided to produce a congruent element The use of the *one-level* rule imposes the following conditions on the quadrilateral/ hexahedral mesh:

- There cannot be more than one constrained node between elements sharing an edge in 2D.
- There cannot be more than one edge or face constrained node between elements sharing a common edge or face in 3D.
- The difference in the refinement level between adjacent neighbors cannot be more than one.

Before proceeding to refine an element. a check is made on the large neighbors; if a large neighbor exists, it is refined first and the actual element is refined next. Fig. la and fig. 1b illustrate the 2D and 3D adaptive meshes with constrained and regular nodes.

● – Regular Nodes
□ – Constrained Nodes

a.

● – Represents Centroid of Parent Element
★ – Represents the Face Constrained Nodes (fcn).
□ – Represents the Edge Constrained Nodes (ecn).
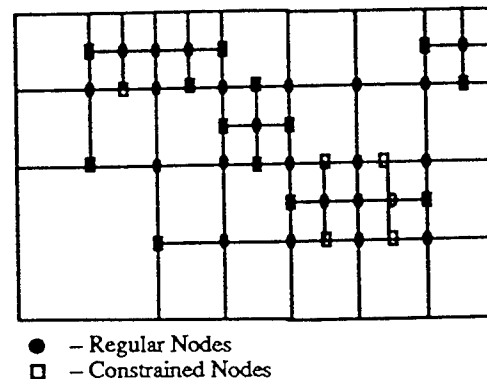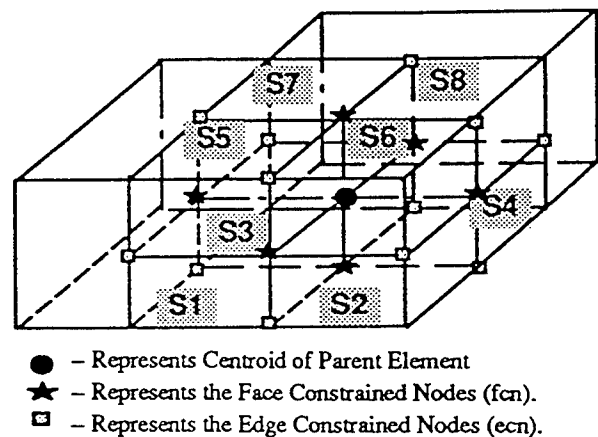
b.

Fig. 1. Regular and constrained nodes. a. In quadrilateral mesh. b. In Hexahedral mesh.

The quadrilateral and hexahedral adaptive mesh refinement algorithm is based on the assumptions that the initial meshes are structured: the subdomains and the elements generated are of the same shape and type as that of the parents; if the initial meshes are admissible then the set of meshes generated during subsequent phases of refinement are also admissible. The basic set of initial data includes the element order list, node numbers, nodal coordinates and neighbor array and node types. The refinement proceeds by connecting the mid-points of the sides of a quadrilateral and the mid-points of faces of a hexahedral to the centroid of the element. After the refinement, an element order list is generated to maintain the natural sequence in order to identify the location of elements in the domain. The dynamic data structure maintains only two levels of the tree at any point in time during the refinement. New constrained nodes are created during refinement and the existing constrained nodes may become regular nodes. The nodes after refinement are identified as regular(m), boundary(bn), edge constrained(ecn) and face constrained(fcn) nodes. In addition to the *one-level* rule the minimal tree maintains a relatively simple data structure facilitating minimum tree travel during mesh refinement and thus reducing the computational overhead.

III. 'A POSTERIORI' ERROR ESTIMATION

Minimization of the discretization error can be achieved by incorporating an efficient error estimation procedure which computes the error indicator to mark elements with more errors and error estimator which decides on the level of mesh refinement necessary. Error estimates are computed *'a posteriori'* due to the uncertain nature of the discretization error at the beginning of the adaptation. Some of the heuristic error estimation methods are based on mathematical analysis with extensive numerical results and others are based on benchmark computations satisfying specific computational goals. This is due to the fact that the error estimates are sensitive to the complexity and structure of the problem domain, the mesh quality and the nature of singularities. Most error estimation procedures use the solution, its gradient, system energy, post-processed solution, continuity conditions of field components or the residual of the solution as the primary field components to compute the error [7,8]. The error estimates not only decide an the optimal mesh but also assess the quality of the computed solution. An error estimate with a high degree of reliability

will ensure proper adaptation in all classes of problems irrespective of the nature of problems and the type of material interfaces. In order to provide an adaptive computation of electromagnetic fields, the *'a posteriori'* error estimate should be computationally inexpensive and must be able to compute errors in complex domains and singular regions. Two different types of local *'a posterior'* error estimates are briefly discussed in this paper.

A. *Error Measures*

It is important to choose a suitable error measure not only for computing error indicators and error estimators, but also to assess the quality of the computed solution. Let Φ_{ex} and Φ be the exact and approximate solutions respectively, then by using an L_2 energy norm, error measures for the local error estimate can be derived as follows,

$$\|e\|_{L_2} = \left[\int_\Omega e^T e \, d\Omega\right]^{1/2}, \quad e = |\Phi_{ex} - \Phi| \quad (1)$$

The relative energy norm error in percentage is,

$$\eta = \left[\|e\| / \left(\|\Phi\|^2 + \|\Phi\|^2\right)^{1/2}\right] * 100\% \quad (2)$$

The admissible error is derived using the global relative error and the number of elements as

$$\|e\|_a = \frac{\eta}{100}\left[\frac{\|\Phi\|^2 + \|\Phi\|^2}{N}\right]^{1/2} \quad (3)$$

A reliable error criterion for refinement can be derived as, $\zeta_i = \|e\|_i / \|e\|_a$ and an element gets refined whenever $\zeta_i > 1$, $\forall \|e\|_i > \|e\|_a$

B. *Local Error Estimates*

Local error estimates are advantageous compared to other methods since they are simple and computationally less expensive. It takes only a fraction of computational power necessary to solve a problem, since a local error estimate solves a local problem consisting of a subdomain with only a few elements. Another advantage of a local error estimate is that it accurately predicts elements to be refined in the critical regions of a problem. Of the two different types of local error estimates

presented, one makes use of an improved solution to compute the error and the other utilizes the gradient of the solution to estimate the error for adaptive mesh refinement.

C. *Element by Element Local Error Estimate*

The element by element local error method allows a solution of a small problem at the subdomain level to be solved for computing the error. Starting with a coarse mesh, a local error problem with a subdomain consisting of a patch of elements connected to a regular node is constructed. Since the local problem has only a few nodes, it is computationally less expensive. Based on the location of the regular node, Neumann and Dirichlet boundary conditions are imposed. The local problem $L\Phi = f$ thus created on each subdomain corresponding to the active node is solved using a quadratic approximation polynomial on an h-version mesh. By repeating this procedure at all the active nodes and comparing the improved solution with the original, global solution, the error on each element is computed locally. Using the error measure derived above, selected sets of elements are marked for refinement.

D. *Gradient of Field Method of Error Estimate*

In singular regions of a problem, the gradient of the field or flux will be highest, since the rate of variation of the solution is larger compared to other regions. Here the local problem is formed by creating a subdomain consisting of a patch of elements connected to an active node. With appropriate boundary conditions, the local problem is solved and an improved gradient of field is computed. The error in the gradient is computed as the difference between the gradient from the local problem and the gradient of the original solution. The derivative of the solution becomes constant in the case of a linear first-order approximation. Due to this reason the gradient g will be discontinuous across neighboring elements. In order to improve the approximation of the true gradient value, the gradient at each nodal point $\bar{g}$ is computed using the local problem formulation. Based on the fact that the nodal values are heavily influenced by the changes in the field quantities of neighboring elements, the gradient is improved by means of an averaging technique. Let g_{ex} and g be the gradient in the exact solution Φ_{ex} and in the approximate solution

Φ respectively. Also let e_g be the error in the gradient. then $e_g = |g - g_{ex}|$. Since $g_{ex} = \nabla \Phi_{ex}$ and $g_{ex} = \nabla \Phi$, the true error in the gradient is $e_g = |\nabla \Phi_{ex} - \nabla \Phi|$.

IV. TEST RESULTS AND DISCUSSION

A. *Linear Problems*

To evaluate the performance of the proposed adaptive mesh refinement algorithm and the '*a posteriori*' error estimation procedures, different sets of linear and nonlinear problems in 2D and 3D are modeled using adaptive computation. The first 2D case is the classical electrostatic problem with an L-shaped domain with a corner singularity in the form $r^{2/3}sin(2\theta/3)$, where r and θ are the polar coordinates. The second is a Poisson problem on a unit square region with a charge density $\rho = 1$ *Coulomb/m²* at the center with a permittivity of ε_0. A uniform Dirichlet boundary condition was imposed to solve the problem. For both problems, using the coarse mesh and the initial solution the proposed local error estimates are applied to initiate adaptive mesh refinement. An intermediate mesh and the final refined mesh for the L-section problem are shown in fig. 2. The corresponding equi-potential plots are shown in fig. 3. The sequence of adaptively refined meshes for the Poisson problem are shown in fig. 4. The asymetry in the meshes is due to termination of the refining process. If the process were continued, they would eventually become symmetric. The corresponding solution plots are shown in fig. 5. In the L-section problem, the singularity is present near the re-entrant corner of the problem domain. Hence the error estimate identified more elements for refinement and so the mesh is denser near the re-entrant corner. From the solution plot corresponding to the refined mesh, it can be discerned that the accuracy of solution is considerably improved.

In the Poisson problem a unit charge density exists in a small square region (0.2m x 0.2m) at the center of the domain. Due to the presence of charge density at the center, the field is stronger at the center compared to other regions and hence the refinement concentrates at the center. The sequence of solution plots verify that the accuracy of the solution is improved during each level of refinement.
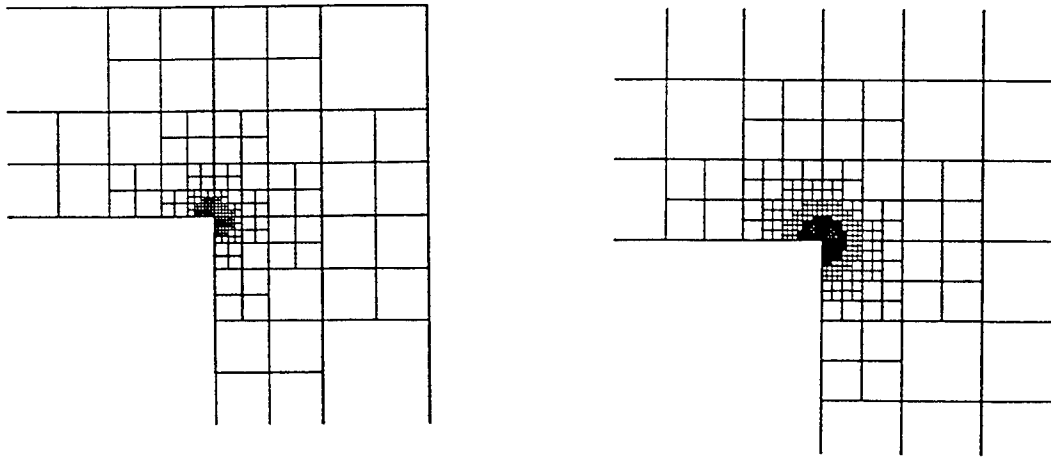
Fig. 2. Intermediate and final adaptive meshes for the L-section problem.
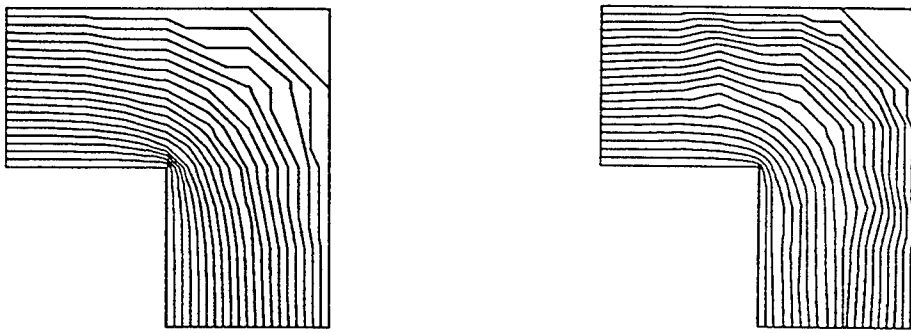
Fig. 3. Contour plots for the adaptive meshes in Fig. 2.

A magnetostatic problem in 3D is solved to compute the magnetic field and the stored magnetic energy for a given current density in a unit cube having a uniform permeability μ_0 A homogeneous boundary condition **B.n**=0 is imposed to compute the vector potential. A uniform current density $J_x=0$, $J_y=0$, $J_z=10^7 A/m^2$ is applied along the side of the cube. The magnetic vector potential is used as the primary field variable in this problem. The initial mesh and the refined meshes are shown in fig. 6. The experimental values of stored magnetic energy and the corresponding errors are shown in table-1. The error convergence plot in fig. 7 shows a notable improvement of adaptive mesh refinement in minimizing the discretization error. From the sequence of adaptive meshes and the solution plots, the performance of adaptive the mesh refinement algorithm and the error estimation strategies are verified.

V. NONLINEAR MODEL

A carefully designed adaptive mesh refinement algorithm and error estimation method are capable of performing uniformly on linear and nonlinear problems. In order to test the performance of the proposed error estimate, a nonlinear problem involving the computation of design parameters for the design of a nonlinear high-field permanent magnet synchronous motor is modeled for adaptive FE analysis. The modeling and analysis of electrical machine design parameters is a complex task particularly due to the narrow airgap and the rotating flux due to the rotor and stator coils. To achieve optimal design and improved machine performance, accurate calculations of airgap flux density distribution and core losses are necessary.

Mesh number	Number of elements	Stored magnetic energy [MJ]	Percentage of error %
1	8	1.1044	49.98
2	64	1.8983	14.03
3	288	1.9231	12.91
4	1212	2.1482	2.71

Table-1 Numerical Test Results

A. *Accuracy Improvement of Machine Design Parameters*

Permanent magnets are vital components in the design of machines. In synchronous machines, they eliminate the steady state conductor losses associated with the rotor. Since there is no need far an armature magnetizing current the stator copper losses are also reduced [9]. However most permanent magnets made of rare earth materials are very expensive. By employing different combinations of inexpensive magnets with rare earth magnets, an optimal design with improved efficiency can be obtained while maintaining the airgap field distribution. To determine the optimal design parameters, efficient modeling and computation of various design parameters is of paramount importance. The nonlinear problem modeled for adaptive accuracy improvement in this experiment involves a high-field permanent magnet synchronous machine utilizing two different types of permanent magnets for the design of the rotor. A rectangular magnet made of rare earth permanent magnets and an arc magnet made of inexpensive common materials like iron oxide are employed in the design.
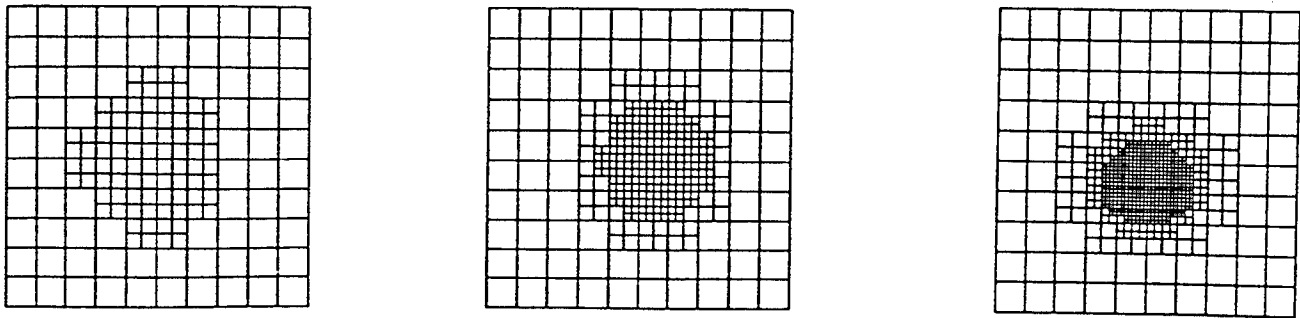
Fig. 4. Sequence of adaptive meshes for the Poisson problem.
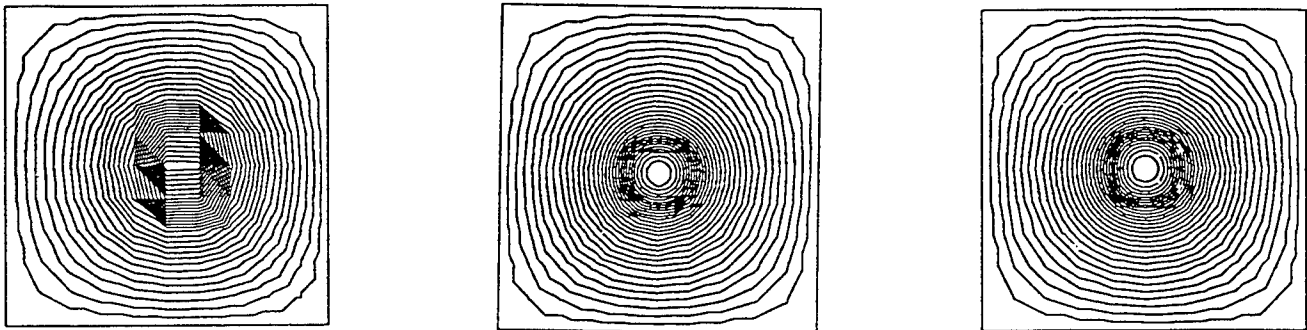
Fig. 5. Contour plots for the corresponding adaptive meshes.
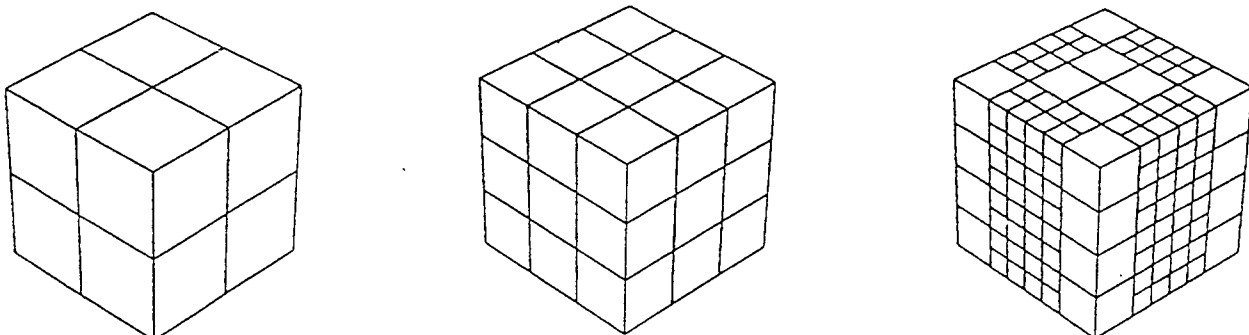
Fig. 6. Sequence of 3D adaptive meshes for the magnetostatic problem.

66
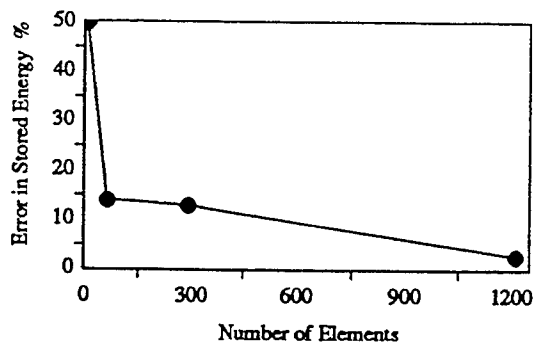
Fig. 7. Error convergence plot.

B. *Numerical Results*

Utilizing the symmetry of the domain, one fourth of the problem geometry is modeled. The modeling takes into account the steady state performance of the machine and also the sinusoidal variation of the rotor current. It is assumed that the rotor rotates at a constant synchronous speed A triangular element based *h*-version adaptive mesh refinement is employed in this model. The adaptive mesh refinement technique was initialized on a coarse mesh with 1040 triangular elements and 574 unknowns. After computing the mesh refinement parameters, the mesh refinement was allowed to progress up to 4 levels and the adaptation was terminated with 1560 elements and 838 unknowns. A sequence of adaptive meshes for the nonlinear problem and the corresponding contour plots (flux distribution) are shown in fig. 8 and fig. 9 respectively. For the sake of clarity, only an enlarged view of a section of the refined mesh is presented. From the smoothness of the flux distribution the accuracy improvement in the solution can be verified. From the numerical results the stator core loss and the airgap flux distribution can be calculated and compared with the available experimental values. The numerical test results along with the sequence of adaptive meshes and the corresponding solution plots establish the usefulness of the proposed error estimation strategy in solving a nonlinear problem for the improvement of design parameters of a permanent magnet synchronous machine.
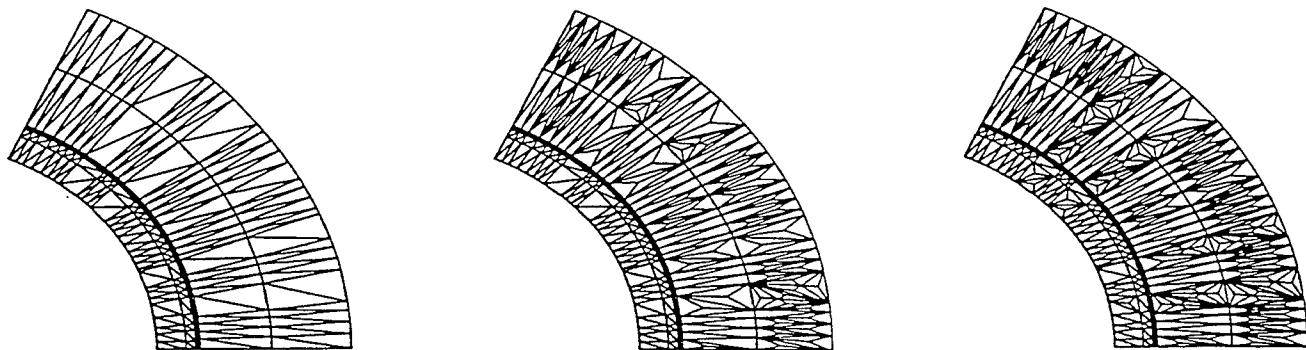
Fig. 8. Sequence of adaptive meshes for permanent magnet synchronous machine design.
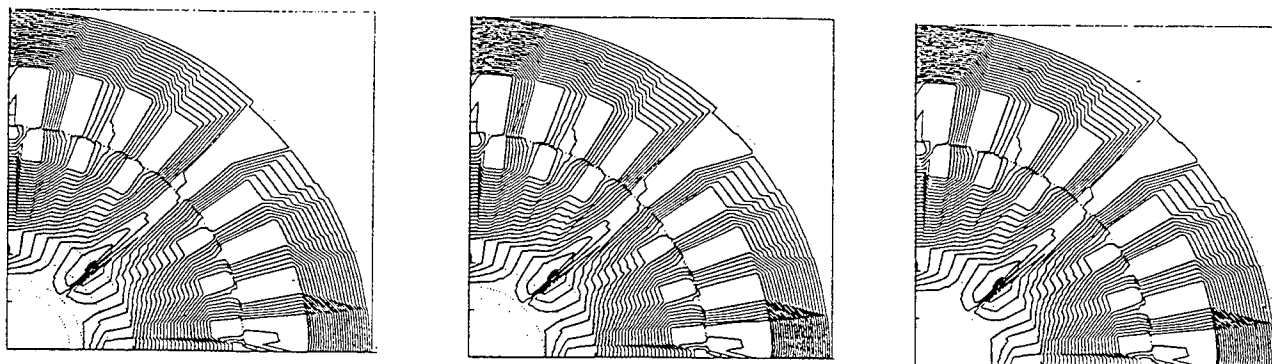
Fig. 9. Flux distribution plot for permanent magnet synchronous machine design.

VI. CONCLUSIONS

A hierarchical minimal tree based mesh refinement algorithm employing a one-level rule along with two different local *'a posteriori'* error estimation strategies are presented in this paper. The application of a minimal tree based algorithm stores only two levels of tree data structure at any step during the mesh refinement process thus reducing the tree traversal considerably, and therefore, providing a computational advantage over other tree structure based adaptive methods. The mesh refinement algorithm and the local error estimates are applied to solve linear and nonlinear elliptic boundary value problems adaptively. The numerical test results and the sequence of adaptive meshes demonstrate the application potential of the presented mesh refinement algorithm and the error estimation strategies.

REFERENCES

[1] H Seok, S.P. Hong, K. Choi, H.K Jung and S.Y. Hahn, "A three dimensional adaptive finite element for magnetostatic problems," IEEE Trans. on Magnetics, Vol. 27, No. 5, pp. 4081-4084 (1991).

[2] Z.J. Cendes dc D.N. Shenton, "Adaptive mesh refinement in the finite element computation of magnetic fields," IEEE Trans. on Magnetics, Vol. MAG-21, No. 5, pp. 1811-1815 (1985).

[3] G.F. Carey, M. Sharma and K.C. Wang, "A class of data structures for 2-D and 3-D adaptive mesh refinement ," Int. J. Num.. Meth.. Eng., Vol. 26, pp. 2607-2622 (1988).

[4] L Babuska & M. Suri, "The optimal convergence rate of the *p*-version of the finite element method", *SIAM J. Num. Analysis*, Vol. 24, No.4, pp. 750-776 (1987).

[5] M. C Rivara, "Design and data structure of fully adaptive, multigrid, finite element software," ACM Transactions on Math. software, Vol. 10, No. 3, pp. 242-264 (1984).

[6] K.C Chellamthu & N. Ida, "Algorithms and data structures for 2D and 3D adaptive finite element mesh refinement," Finite Elements in Analysis and Design, 17, pp. 205-229, (1994).

[7] J.C. Adamiak, "Local error indicator in finite element analysis of Laplacian fields on the Green integration formula," Int. J. Numer. Methods. Eng., Vol. 33, pp. 1625-1642 (1992).

[8] P. Fernandes, P. Girdinio, P. Molfino and M. Repetto, "A comparison of adaptive strategies for mesh refinement based an *'a posteriori'* local error estimation procedures," IEEE Trans. on Magnetics, Vol. 26, pp. 795-798 (1990).

[9] K.J. Binns and T.M. Wong, 'Analysis and performance of a high-field permanent magnet synchronous machine," IEE Proceedings, Vol. 131, B, 6, pp. 252-258 (1984)

DESIGN OF ELECTRICAL MACHINES AIDED BY FIELD CALCULATION AND FACTORIAL EXPERIMENTS METHOD

C.Pertusa, S.Astier, Y.Lefevre, M.Lajoie-Mazenc
Laboratoire d'Electrotechnique et d'Electronique Industrielle (L.E.E.I)
U.R.A C.N.R.S n°847, 2 rue Camichel 31071 Toulouse cedex France
tel : 61588359 fax : 61638875, e-mail : lefevre@leei.enseeiht.fr

ABSTRACT

An approach for electrical machines design by using magnetic field computation coupled to factorial experiments is presented in this paper. Principles of factorial experiments are briefly reviewed and their application to design optimisation is explained. In this application experiments are replaced by magnetic field calculations. The procedure, which performs automatically all the numerical field calculations required, is described. The whole procedure is applied to a typical problem concerning permanent magnets synchronous motor with polar pieces.

INTRODUCTION

Nowadays, magnetic field computation has became a compulsary tool in electrical machines studies. Magnetic field softwares are able to compute, in taking into account the saturation, several characteristics of a machine such as the flux or the torque waveforms, values of inductances or any other electromagnetical characteristics. Consequently, used in a particular environment, magnetic field computation provides a possible guide for electrical machine design in an attempt to optimize its dimensions with respect to the specifications.

To this aim, the introduction of magnetic field computation into a process of parameters variations and statistics processing, as factorials experiments, is proposed. Usually employed by industrials, the method of factorial experiments allows to know the behavior of a physical system with respect to a set of given factors. This knowledge is obtained by performing experiments [1]. In section one, we introduce the fundamental principles of factorial experiments adapted to the computation of the dimensions of an electrical machine by magnetic field software analysis.

In this application, simulations carried out by means of a magnetic field software analysis serve as experiments. Since there are many design factors a large amount of field calculations are required. For that, an automatic procedure for parameters variations driving the magnetic field computations

is necessary. Section two presents the method used to make an automatic link between the main design procedure and the magnetic field computation. This method frees the user from complicated task such as drawing or meshing.

Finally, as an example of the use of the whole procedure, we consider the problem of the evaluation of the influence of the following three parameters:

- air gap length;
- magnet width;
- slot openning.

on the rated torque and the torque ripples of a permanent magnet synchronous motor with polar pieces.

FACTORIAL EXPERIMENTS

In a course of a design procedure, magnetic field computation code is very helpful to analyse the behavior and the performances of a projected machine. When a machine design must be optimised, a large amount of field calculations may be required. Factorial experiments are used here in order to planned these field calculations and to reduce their number. Optimisation of a machine design by factorials experiments associated with field computation is divided into three steps.

The starting point of the procedure is a preliminary design, obtained by analytical design equations and rules deduced from the theories of electrical machines and the designers own experience. At this stage the designer may estimate that some specifications are not matched by this preliminary design and desire to modify some factors in order to improve it.

At the first step of the procedure the designer must choose the main electromagnetical characteristics to be improved and the main influent design factors. In the terminology of factorial experiments method, the first type of variables are the output data and the second ones the input data. Let the output data be $Y_1 \dots Y_k$ and the input data $X_1 \dots X_n$.

The second step consists of experimenting in order to know how the ouput data vary in function of the input data. Here experiments are replaced by magnetic field computations. From the set of magnetic field computation results the variations of

the electromagnetic characteristics (Y_k) in function of the design factors (X_j) can be modelled by polynomials. These polynomials can either be linear:

$$Y_k = \sum_{j=0}^{n} a_j^k X_j \qquad (1)$$

or quadratic:

$$Y_k = a_0 + \sum_{j=1}^{n} a_j^k X_j + \sum_{i,j=1}^{n} a_{i,j}^k X_i X_j \quad (2)$$

The coefficients a_i^k or a_{ij}^k are obtained by applying the method of multilinear regression, based on the principle of least squares, on magnetic field computations results. The choice of the set of experiments or magnetic field computations corresponding with machine design factors must be very precise. With a study of k design factors on an electromagnetical characteristic, each of this factor having p levels of variations, p^k magnetics field computations must be carried out. Each of this computation is then characterized by a particular combination of values of the k factors. A matrix X is built with p^k lines and k columns: one line per magnetic field computation and one column per each coefficient ai or aij. To reduce the size of the matrix X in keeping fiability and precision, several methods such as the fractionnal planes method or Taguchi method can be employed [2].

The matrix X is called the matrix experiments. Each line of X is composed of the value of the coefficient of a_j in relations (1) or (2) at each experiment. For instance if the modelling function is linear, the line i of X has the form:

$$1 \ X_1^i \ X_2^i ... \ X_j^i ... \ X_k^i \qquad (3)$$

where X_j^i is the value of the factor j during experiment number i, k is the number of coefficients a_j which is equal for the linear case to the number of influent factors, n is the number of experiments done. In the same manner an ouput matrix Y is built. The generic component of this matrix Y_j^i is the measure of output data number j during experiment i.

The coefficient a_i^k can be put in a matrix A. The generic coefficient of this matrix a_j^i is the coefficient relating the ouput Y_i to the input X_j. The matrix A is given by the relation:

$$[a] = \left[X^t . X\right]^{-1} . \left[X^t . Y\right] \qquad (4)$$

where X^t is the transpose matrix of X.
The last step consists of optimising the machine design. For that purpose, the polynomials of

equations (1) and (2) are used with a method of optimisation such as the simplex algorithm or steepest-descent method.

PROCEDURE FOR PARAMETERS VARIATION

To carry out the p^k electromagnetical computations, an automatic procedure for parameters variation is necessary [6].

To this aim, the notion of library of structures has been defined. A reference file including the data needed by the field calculation and an automatic data transfert module are associated to each structure of the library. A reference file is created only once for each structure of the library, from the preprocessor of the field computation software used. After choosing the reference structure, the data transfert module defines automatically the file for the field calculation. Reading the reference file, the procedure builts on the same structure the file of the studied machine by computing only some geometrical points. The geometry , areas, materials, winding and boundaries adapted to the new dimensions of the machine are included in this new file. This automatic procedure for parameters variation is simple and has been integrated in the method of factorial experiments. A little module which gives automatically the new dimensions data with respect to the chosen factors and their levels of variation of the studied machine has been developped. An overview of the whole procedure is shown on the figure 1.
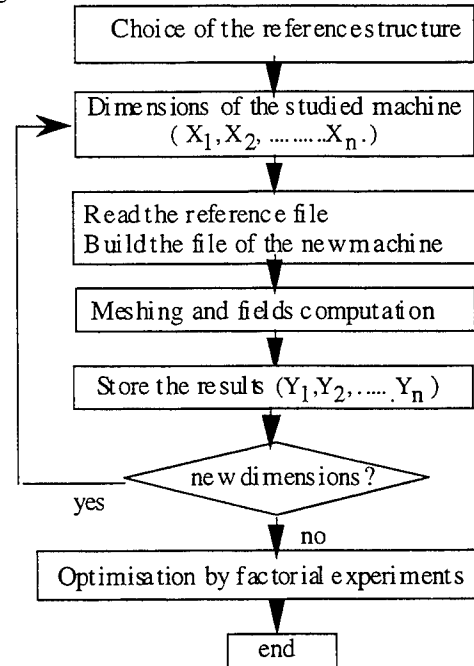
Fig. 1: Automatic procedure for parameters variations combined to factorial experiment method

APPLICATIONS

This procedure is applied on a permanent magnet motor with polar pieces (Fig. 2). The aim of this study consists in the evaluation of the influence of the three following parameters:

- the width of magnet (X_1),
- the slot openning (X_2),
- the length of air gap (X_3);

on the values of rated torque and torque ripples.
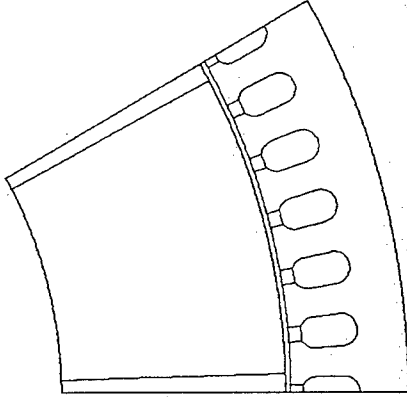
Fig. 2: One pole of the studied permanent magnet motor with polar pieces.

The motor to be optimised during this project is described by the following data :

torque : 121.3Nm	inner diameter of the stator:188 mm
number of poles:12	current density :8 A./mm^2
number of slots:72	torque ripples:16 %

The experiments planning is based on the three factors X_1 , X_2 and X_3 , each of those factors having three levels of variation (Table I) and permits to obtain a model of the characteristics from a second degree quadratic polynomial as follows:

$$Y = a_0 + a_1 X_1 + a_2 X_2 + a_3 X_3 +$$
$$a_{11} X_1^2 + a_{22} X_2^2 + a_{33} X_3^2 + \quad (5)$$
$$a_{12} X_1 X_2 + a_{13} X_1 X_3 + a_{23} X_2 X_3$$

Polynomials are calculated by using the reduced values of these three factors: -1, 0, 1.

For the at load torque computation, a magnetic field software EFCAD based on finite elements method is used [3]. This software computes whole of the electromagnetical characteristics such as the torque, the inductances [4]. This software takes into account the movement of the rotor and the saturation of magnetic material [5]. Any system of supply currents is available. In this study a supply by three phases AC currents has been considered. After magnetic field computations, the temporal evolution of the torque is analysed to obtain the average rated torque and the amplitudes of the torque ripples which are the ouput data.

Table II gives the values of output Y_1 and Y_2 obtained after the 27 magnetic field computations.

variable	X_1	X_2	X_3
type	width of magnet	slot openning	ratio air gap diameter / air gap
minimum -1	5,2510mm	45 %	225
center 0	5,5274mm	50 %	250
maximum +1	5,8037mm	55 %	275

Table I : types and values of factors

	Y_1	Y_2		Y_1	Y_2		Y_1	Y_2
1	119,8	14,9	10	121,6	13,9	19	123,6	14,4
2	120,6	15,7	11	122,0	14,8	20	123,9	15,7
3	121,1	16,4	12	122,2	15,8	21	123,9	17,0
4	119,0	16,9	13	121,0	16,0	22	123,5	16,5
5	119,6	17,5	14	121,3	16,4	23	123,6	16,7
6	119,9	17,9	15	121,3	16,5	24	123,6	17,2
7	118,2	19,2	16	120,0	18,2	25	123,4	18,8
8	118,5	20,0	17	120,5	18,8	26	123,3	18,8
9	118,6	20,5	18	120,4	19,1	27	123,3	19,1

Y_1 : rated torque (Nm)
Y_2 : torque ripples (%)

Table II magnetic fileds computation results

After defining the experiments matrix, the coefficients of the quadratic polynomials which describe the answers Y_1 and Y_2 are calculated by relation (4).

For the rated torque Y_1 , we obtain :

$$Y_1 = 121,32 + 2,0549 X_1 - 0,6671 X_2 + 0,2140 X_3$$
$$+0,3417 X_1^2 - 0,0211 X_2^2 - 0,1294 X_3^2 \quad (6)$$
$$+0,3951 X_1 X_2 - 0,1945 X_1 X_3 - 0,1543 X_2 X_3$$

And for the torque ripples, we obtain :

$$Y_2 = 16,35 - 0,279 X_1 + 1,878 X_2 + 0,587 X_3$$
$$+0,767 X_1^2 + 0,432 X_2^2 - 0,025 X_3^2 \quad (7)$$
$$-0,267 X_1 X_2 - 0,016 X_1 X_3 - 0,299 X_2 X_3$$

71

Figures 3 and 4 give an idea of the evolution of Y_1 and Y_2 in function of X_1, X_2 and X_3. Figure 3 shows the variation of the rated torque (Y_1) versus the slot opening (X_2) and the air gap (X_3) when the magnet width (X_1) is fixed. Figure 4 shows the variation of the torque ripples versus slot opening (X_2) and magnet width (X_1) when the air gap (X_3) is fixed.

To verify the validity of the models, some results obtained by them are compared to those obtained from magnetic field analyses. These comparisons are reported on figure 5. For a better comparison, the values of the three factors X_1, X_2, X_3 are not the same than those used for the building of experiment matrix X.
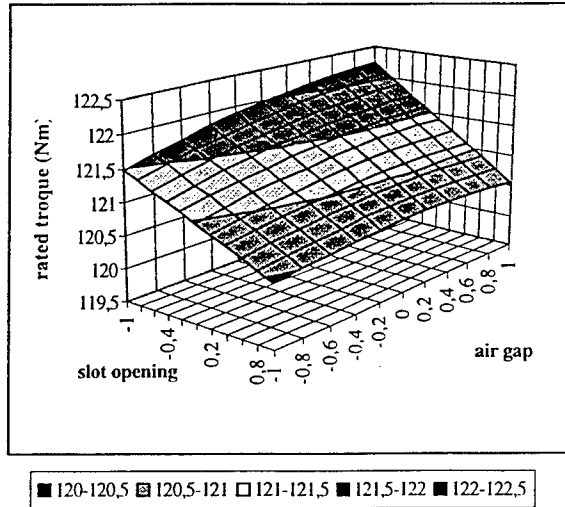
Fig 3: Isovalues of the rated torque when the magnetwidth is fixed

■ 120-120,5 ▣ 120,5-121 □ 121-121,5 ■ 121,5-122 ■ 122-122,5
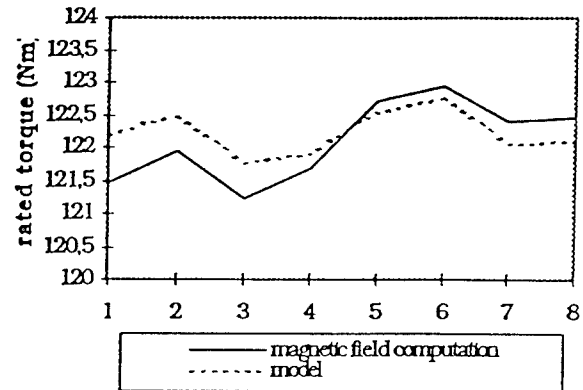
Fig 5 Comparison between the rated torque calculated by quadratic polynomial and the magnetic field computation

It can be noticed that the results obtained from the polynomial are in good agrements with those obtained from magnetic field computations. Good agreements between the results obtained from the two calculations are also obtained for the ouput Y_2. These comparisons show that the models are valid to predict the rated torque and the torque ripples for values of factors X_1, X_2, X_3 corresponding to their variation intervals.

Once the validity of models is verified, several methods of optimisation can be applied to reach an optimum value of the choosen characteristics. In this paper the interesting point is fixed by a maximum rated torque or minimum torque ripples. The two polynomials which represent the evolution of the rated torque and the torque ripples are used to obtain the three values of X_1, X_2, X_3, according with the desired optimisation. The quasi-Newton algorithm has been applied to determine the results reported in the Table III hereafter.

■ 14-15 □ 15-16 □ 16-17 □ 17-18 ▩ 18-19 ■ 19-20

Fig 4: Isovalues of the torque ripple when the air gap is fixed

72

	magnet width (mm)	slot openning%	ratio air gap diameter / air gap	optimum Nm
Y_1	5,5267	45	225	124,03
Y_2	5,8037	45	266,8	13,99%

Table III : Optimisation results

It can be noticed that the rated torque is slightly improved:
the preliminary design has a rated torque equal to 121.3 N.m and the optimised machine has a rated torque equal to 124.03 N.m. Same conclusions can be made for the torque ripples : the preliminary design gives torque ripples of about 16.4 % and the optimised machine 14 %.

CONCLUSION

An approach to the problem of optimisation of electrical machine design by using a magnetic field computation code and the factorial experiments method has been developed and presented in this paper.
The treatment of magnetic field results by factorial experiments allows us to etablish polynomials which link the design parameters to the electromagnetical characteristics. By means of those polynomials, it is possible to adjust the machine dimensions to match precise specifications.
Furthermore, once these polynomials have been calculated, it is no more necessary to use numerical code to compute electromagnetical characteristics in function of the design parameters. It's better to use these polynomials for that.

REFERENCES

[1] Gilles Sado et Marie-Christine Sado, *Les plans d'expérience, de l'expérimentation à l'assurance qualité.* Afnor technique 1992
[2] Michel G Vigier, *Pratique des plans d'expériences, méthodologie Taguchi.* Les editions d'Organisation 1991
[3] Nathan Ida, Joao P. A. Bastos, *Electromagnetics and Calculation of Fields .* Springer-Verlag 1992
[4] S. Clenet, Y. Lefèvre, N. Sadowski, S. Astier and M. Lajoie-Mazenc, *Compensation of permanent magnet motors torque ripple by means of current supply waveshapes control determined by finite element method.* IEEE Transactions on Magnetics, Vol. 29, N°2, March 1993
[5] N. Sadowski, Y. Lefèvre, M. Lajoie-Mazenc and J. Cros,, *Finite element torque calculation in electrical machines while considering the movement,* IEEE Transactions on Magnetics, Vol. 29, N°2, March 1993
[6] C. Pertusa, S. Astier, Y. Lefèvre and M. Lajoie-Mazenc, *Firt step towards a full integrated cad system for electrical machines.* ISEF'95, September 25-27 1995, Thessaloniki, Greece.

LIMITATIONS OF THE CONVENTIONAL METHODS OF FORCE AND TORQUE PREDICTION

Antônio Flavio Licarião Nogueira

Department of Electrical Engineering
University of the State of Santa Catarina - UDESC
CEP 89223-100 - Joinville - Santa Catarina - Brazil

Abstract: The calculation of forces and torques developed in electromechanical devices, and their variation with changes in position or excitation, is often what the designer is, ultimately, interested in. This paper addresses some of the problems associated with the force and torque calculations based on numerical field solutions for 2-D magnetostatic problems. The problem of calculating the cogging torque characteristic of a neodymium-iron-boron permanent-magnet motor is considered and the technique of torque measurement is described briefly.

1. INTRODUCTION

Forces developed in the air-gap of an electric machine can be resolved into two components: normal and tangential. The resultant of the tangential components provides the useful electromagnetic torque, and the resultant of the normal components has to be accommodated in the bearings. One of the sources of difficulty is that the size of the useful tangential force component is usually small compared with the radial force. Errors are more likely to occur when the force of interest is calculated in the presence of a much larger force field [1-2].

Forces can be obtained from numerical field solutions by evaluating the Maxwell stress tensor along a given integration path, by the virtual work concept, or by integration of $I(d\vec{l} \times \vec{B})$. The latter is only applicable in systems containing current carrying conductors. In general, all these methods tend to give rise to errors in the forces that are greater than the errors in the field solution.

When the problem solution is obtained in terms of the magnetic vector potential, flux densities are obtained from the curl operation

$$\vec{B} = \nabla \times \vec{A} \qquad (1.1)$$

This involves numerical differentiation and, therefore, any errors in the potential solution lead to larger errors in flux density values. This affect all subsequent post-processing operations.

The Virtual Work Method

The force acting on a movable part of a device may be evaluated by determining the variation of the magnetic stored energy of the entire device when a small displacement takes place. For the simple case where only one-dimensional movements are considered, the force is given by

$$F = \frac{\left(W_1 - W_2\right)}{d_{12}} \qquad (1.2)$$

where W_1 and W_2 represent the stored energies at the two distinct positions; d_{12} is the positional displacement and F is the estimate to the force at the intermediate position $\{(d_1 + d_2)/2\}$.

The Method of Maxwell Stress Tensor

The basis of the method is the calculation of the force and torque directly from the field distribution. The force and torque are evaluated by integrating the force density over a contour surrounding the part of interest. For a known two-dimensional flux density distribution (**B**) and a contour C enclosing a body (or the movable part of a device), the total force and torque acting on the body are given by:

$$\vec{F} = \int_C \left[\frac{1}{\mu_o} \vec{B}(\vec{B}.\vec{n}) - \frac{1}{2\mu_o} B^2 \vec{n} \right] dC \qquad (1.3)$$

and

$$\vec{T} = \vec{r} \times \vec{F} \qquad (1.4)$$

where $\vec{r}$ is a vector function with its origin taken at the action point for the torque and $\vec{n}$ is the unit vector normal to the contour.

2. ACCURACY OF FORCE CALCULATIONS

The finite element method produces a solution to the problem in terms of scalar or vector potentials. The potential distribution is only a numerical approximation to the true potential distribution, i.e. there is an inherent error in the potentials, commonly referred to as error in the approximation or shape function [3-4].

In conventional formulations, the forces and torques are directly related to magnetic flux densities, not to the vector or scalar potentials. Flux densities and magnetic field strengths are obtained from potential solutions by means of numerical differentiation. All the familiar sources of errors are present in numerical differentiation but errors in the approximation function are the most critical, even when small. This is because they are magnified by differentiation algorithms [5]. Therefore, errors in field distributions are, generally, greater than those of the corresponding potential distributions. This helps to explain why some formulations for predicting force and torque are more prone to inaccuracy problems.

In the following, an attempt is made to enumerate and analyse the factors that affect the accuracy of force and torque calculations. To simplify the analysis, it is assumed that the discretization is appropriate to the problem (i.e. the finite elements are properly shaped to model the non-uniformity of the field). The factors that affect the accuracy of force and torque calculations may be summarized as follows:

(i) For some algorithms, the quality of the force and torque prediction is dictated by the accuracy that can be achieved in determining the flux distribution. This sensitivity is evident in the Maxwell stress equations (1.3) and (1.4), but not so obviously from the virtual work equation (1.2). Here, it is worth remembering that the differences in stored energies are due to the different field configurations associated with the system displacement;

(ii) Regions where a considerable amount of field energy is stored, like geometries with pole tips, are the most critical for the force and torque calculations. In the method of Maxwell stress they contribute the main component of the line integral in equation (1.3). Similarly, in some formulations of the virtual work method these regions also contribute the main component of the area integral used to calculate the magnetic stored energy. In other words, the main contribution to the net force and torque is due to stresses (or stored energy) in regions where pronounced concentration and non-uniformity of the field occur; these areas being where an accurate field solution is most difficult to obtain;

(iii) Problems involving the computation of tangential force are often more difficult. This is because the tangential component of the force can be of a much smaller magnitude than the component in the normal direction [6]. This can be illustrated by considering a hypothetical system where the tangential force is small but non-zero. The diagram in figure 1(a) represents the "true" field distribution **B** at some point, while the approximate field distribution **B'** is shown in figure 1(b). Although the error in the magnitude of **B'** is small, the incorrect field direction will result in wrong prediction of the tangential force. Therefore, slightly incorrect flux direction is a point of concern because this causes errors in force and torque values calculated by whatever method;
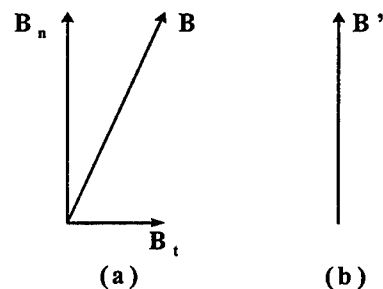
Fig. 1: two flux distributions of similar magnitude.

(iv) incorrect flux directions result from the fact the finite-element methods use some form of energy minimization to drive convergence. The homogeneous Neumann boundary conditions, for example, are not exactly satisfied and this affects, even locally, the flux direction [3]. Different flux directions imply different values of stored energies. Special algorithms are used to perform the numerical differentiation of the shape function and this feature is code-dependent. For example, some packages use the first of the two methods discussed by Binns *et all* [7] in which the continuity of the normal flux density is not imposed at the air-iron interface.

3. PROBLEMS OF IMPLEMENTATION

The above discussion identifies the factors which may affect the accuracy of force and torque obtained by whatever method. The following discussion is concerned with the aspects of each method that could result in difficulties in implementation and substantial numerical errors.

The Virtual Work Method

In contrast to the easy realization of its formulation, the implementation of the method requires a judicious choice of the positional displacement. This choice is problem-dependent

and has to take into consideration errors of conflicting nature. If, in an attempt to improve the accuracy of the approximate derivative expressed in equation (1.2), a small displacement is used, the energy values will be of similar magnitude and the subtraction (W_1-W_2) will be more sensitive to round-off error. On the other hand, a larger displacement may not be adequate to model the true non-linear characteristic that represents the variation of the system's energy with respect to position [8].

The method requires careful planning of the model and this must be followed by a critical examination of the results. In order to reduce discretization errors, one single finite element mesh must be used in all the solutions representing the sequence of the disturbed movable part [9]. In some cases the results might show that the variation of energy with respect to position is not consistent with the physical realization of the actual device, and a model re-definition may have to be done. From the observations made above it is evident that the method is computationally expensive.

The Method of Maxwell Stress tensor

Once the field distribution **B** in equation (1.3) is an approximation to the true one, i.e. there is an inherent error in the numerical field distribution, the independence of the results relative to the choice of the integration contour disappears; the definition of integration contours thus assumes a great importance. This aspect has to be considered very early, during the planning of the finite-element model, and adds complexity in the construction of the mesh.

The energy minimization used by the finite-element method produces a numerical solution to the problem that is optimal for a given discretization. This scheme has no concern for variations in local energy accuracy. Consequently, the resulting fields are globally optimal, even though may possess considerable local error [10]. The forces and torques in equations (1.3) and (1.4) are related only to flux densities of the elements crossed by a given contour (C). This makes evident why the method is so sensitive to mesh artifact and to the location of the integration contour [1].

4. FINITE ELEMENT MODEL AND TORQUE MEASUREMENT

In order to investigate the numerical problems associated to the conventional methods, the problem of calculating cogging torque in a small permanent-magnet motor has been chosen. Cogging torque values in small permanent-magnet motors are typically in the range of millinewton-

metres and, therefore, they are very difficult to compute and measure accurately.

Cogging torque is defined as the non-uniform torque that arises when only the excitation field is present (i.e. the armature current is absent). Cogging torque is a saliency effect that arises from the interaction between a salient pole on one member of the machine (rotor or stator) and the teeth on the other member. The interaction implies a magnetic field distribution which depends on the rotor position. In dc permanent-magnet motors, the interaction between the edges of the magnets and the teeth, situated on the opposite side of the air-gap, causes alternate cycles of restoring and anti-restoring torques as the rotor moves.

The test machine uses radially oriented neodymium-iron-boron magnets to provide a four-pole rotor excitation. A cross-sectional drawing of the motor is shown in figure 2. The magnet arc spans 90 mechanical degrees and the stator has 24 evenly spaced slots. The cogging torque characteristic is therefore periodic, with a period of 15 mechanical degrees.
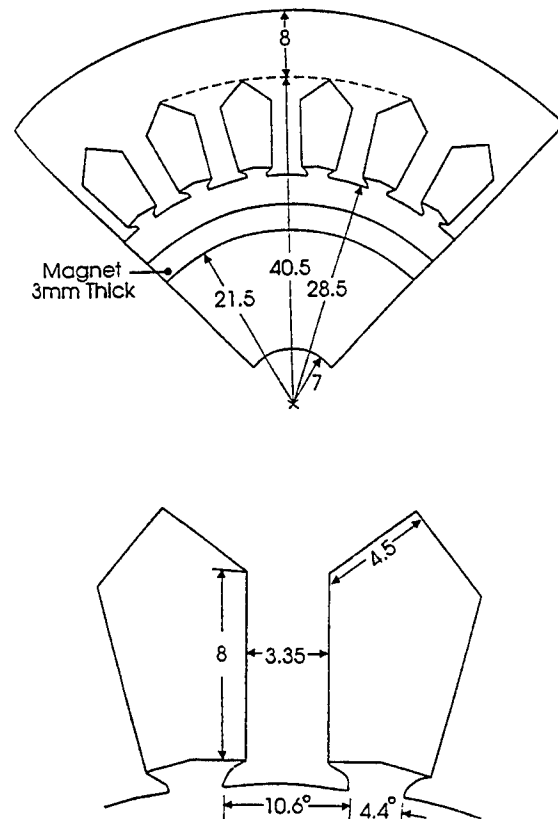
Fig. 2: Top: view of one-quarter of the test motor; Bottom: enlarged drawing of one tooth. Dimensions in millimetre.

The cogging torque is zero at any rest position where the edges of the magnets (interpolar regions) are radially aligned with the centerline of stator teeth. Such positions are stable equilibrium points for the rotor. Alignment of the interpolar regions with the centerline of the stator slots also implies symmetry, hence zero torque; but these positions are unstable equilibrium points for the rotor. The cogging torque is expected to be a smooth function of displacement in the absence of magnetic saturation.

The cogging torque characteristics of the motor were determined experimentally by displacing the rotor shaft and measuring the torque induced. The rotor shaft was rotated, via a flexible coupling and a torque sensor, by a rotary table mounted so that its axis was collinear with the rotor shaft. The rotary table was driven by a stepping motor via a worm-wheel gearbox. The resolution of the stepping motor was 200 steps per revolution and the gearbox had a speed ratio of 90:1 giving an angular resolution for rotor displacement of 0.02 degree. The estimated backlash in the gearbox was less than 0.1 degree. The torque was measured using a Lord six-component sensor. A data acquisition system capable of recording and processing up to 1000 measurements per second was used. The resolution of this system was 1.4 millinewton-metre. The effect of friction was eliminated from the measured torque-position curves by moving the shaft in one direction a total of 30 degrees (two slot pitches) and than reversing direction. Torque readings were taken in both directions and the results were averaged.

In order to investigate the accuracy obtainable by the conventional methods, a single pole pitch of the motor was modeled, subject to periodicity conditions. A commercially available two-dimensional magnetic field analysis package (MagNet Release 4) was used to solve the field problems. Initial investigations showed that magnetic saturation was not present anywhere in the machine. Therefore, in subsequent runs, all materials in the motor were considered to be magnetically linear, and a linear solver was utilized.

Values of cogging torque were computed by both the virtual work and the Maxwell stress tensor method. Each torque characteristic is associated with a series of problems representing eleven rotor positions separated by 1.5 mechanical degree (10% of the period). In order to guard against mesh artifact in the results, a single finite-element mesh is used in all eleven runs belonging to one curve. Rotor movement is simulated by redefining material properties.

To gain some idea how sensitive the methods are to mesh artifact and fineness of

discretization, solutions are obtained utilizing two different meshes. Results were firstly obtained on a reasonably fine mesh containing 952 nodes with 1834 first-order elements. A second, coarser mesh was created by deletion of nodes in the clusters of elements close to the corners of stator teeth in figure 2. The number of elements was thereby reduced to 1546, the number of nodes to 808. The two meshes only differ in the air-gap region, because this is a critical region regarding energy transfer and it is where most significant field variations occur.

5. NUMERICAL RESULTS

Figure 3 shows zoomed views of the air-gap zone illustrating different node densities and corresponding flux plots.
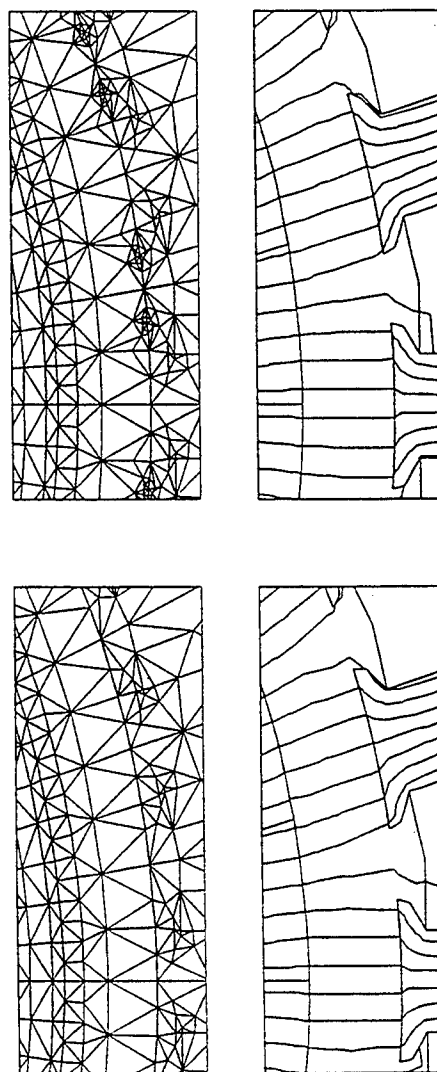
Fig. 3: Mesh detail in air-gap zone
Top: finer mesh;
Bottom: coarse mesh.

The second mesh is a great deal coarser near the tooth tips, and flux density values in the air

gap and near tooth tips are expected to loose accuracy accordingly. While most of the flux lines trace roughly similar courses on the two meshes, tooth-tip flux density distributions differ. In the regions situated slightly to the right of the corners, flux lines do not impinge the laminations at right angles, despite the contrast between the permeability values, taken as 1:10000. This helps to explain why errors in the finite-element approximations are more accentuated in these regions. The low order polynomials used in the finite-element solutions are not adequate in approximating the sharp variations in potential values that occur in these regions.

The virtual work method was used in its classical form, evaluating the stored total energy for successive rotor positions, then subtracting to give energy differences. The computed cogging torque characteristics are presented in figure 4, along with measurements.

however, are very high, exceeding 90%. Visibly, the small differences in stored energies affect the accuracy of the computed torque sufficiently to render the straightforward virtual work approach questionable for this class of problem. The sensitivity of the method in its classical form to numerical error is seen here to be very high.

Torque computations based on the Maxwell stress method were performed using different integration contours, consisting of single arcs spanning one pole pitch. Stress integration over an arc of radius 27.0 mm resulted in more accurate values. In both meshes, this contour crosses the centre of the second layer of air-gap elements. Values for the cogging torques using this contour are presented in figure 5, along with the curve that represents measured values. Table II summarizes the errors for the two sets of data related to the Maxwell stress method.

Fig. 4: Cogging torque characteristics, virtual work method.
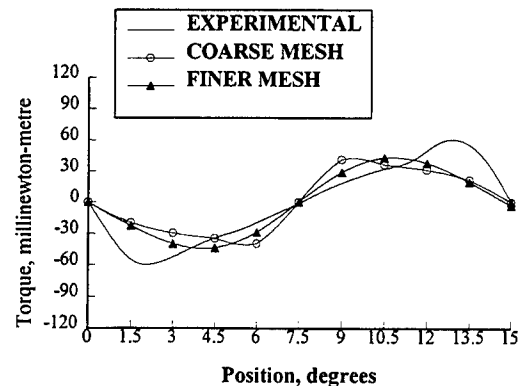
Fig. 5: Cogging torque characteristics, Maxwell stress method.

The error in torque prediction is quantified in terms of the torque magnitude error and peak torque position error. Table I summarizes the errors for the two sets of data related to the virtual work method.

Mesh	Magnitude error, %	Position error, %
Coarse	99	5
Finer	92	5

Table I: Errors, virtual work method.

The energy difference δW between successive rotor positions are in the range 0.5-2.9 mJ in a total stored energy W of about 5.4 Joules. Inspection of the results has shown that data associated with this method have produced curves with the right shape, correctly exhibiting zero average torque over the 15° period. Also, the positions associated with peak torque are close to those obtained in the measurements with errors of the order of 5%. Errors in peak-to-peak torque,

Mesh	Magnitude error, %	Position error, %
Coarse	33	23
Finer	27	13

Table II: Errors, Maxwell stress method.

None of the two curves related to the Maxwell stress method follow the curve of experimental results very closely. The errors in torque magnitude are significantly smaller than those obtained by the classical virtual work approach. Prediction of peak torque position, however, is even worse for the computations based on the Maxwell stress method. These results are not ideal, but this is to be expected when dealing with a geometry that contains sharp corners. The geometry contains 12 corners per pole pitch and this affects the level of accuracy of computed torques.

Further refinements of the mesh containing 952 nodes with 1834 elements (finer mesh) have not led to any significant improvement in results. Torque computations based on the virtual work method remain excessively high. The Maxwell stress method continues to predict peak torque at the wrong positions.

6. CONCLUSIONS

Calculation of forces and torques from numerical field solutions is a very difficult task. Usually, the solution is obtained in terms of potential distributions and, therefore, force is not the primary quantity in the computational analysis.

Among the various methods for the evaluation of force and torque, the methods of virtual work and Maxwell stress tensor have been chosen for a detailed numerical investigation. These methods have been used to solve a notoriously difficult problem: prediction of cogging torque in a small permanent-magnet motor.

Torque computations based on both methods have been compared to measured values. Numerical results have shown that, for both methods, the refinement of the finite-element mesh at an earlier stage has led to improvements in the results. For this particular problem, computations not reported in the paper and based on very coarse meshes with less than 700 nodes have produced oscillatory torque characteristics not consistent with the physical understanding of the problem. Mesh refinement at this level of discretization has, in fact, produced improvements in the results. Disappointingly, at the level of discretization of the finer mesh (952 nodes with 1834 elements), the accuracy of computed torques has not increased significantly as a result of an increase of mesh fineness.

The virtual work method in its classical form fails to predict cogging torque accurately. This is mainly due to the energy values corresponding to the two adjacent positions being of very similar magnitude.

The main problems of Maxwell stress method are related to its sensitivity to mesh artifact and to the location of the integration contour.

The key to accurate torque computation is to avoid numerical differentiation entirely. In many problems involving numerical differentiation and integration, the order of differentiation and integration can be so rearranged that all integrations are done numerically, all differentiations analytically. Torque computations based on the technique of mean and difference potentials use the magnetic vector potential directly and can produce results which agree with measured values to within a few percent, within the limits of measurement accuracy and the approximations inherent in two-dimensional analysis.

7. REFERENCES

[1] Simkim, J., *Recent developments in field and force computation*, Journal de Physique, Colloquium C1, Vol. 45(C-1), pp. 851-860, France, 1984.

[2] Hamdi, E.S. and Licarião-Nogueira, A.F., *Force calculations by numerical field solutions*, Advances in Electrical Engineering Software [P.P. Silvester, ed.], pp. 331-339. Southampton and Heildelberg: Computational Mechanics and Springer-Verlag, 1990.

[3] Silvester, P.P. and Ferrari, R.L., *Finite elements for electrical engineers*, 2nd. ed., Cambridge University Press, 1990.

[4] Tarnhuvud, T. and Reichert, K., *Accuracy problems of force and torque calculation in FE-systems*, IEEE Transactions on Magnetics, Vol. 24, No. 1, pp. 443-446, 1988.

[5] Scheid, F., *Theory and problems of numerical analysis*, McGraw-Hill Book Company, USA, 1986.

[6] Penman, J., *Efficient calculation of force in electromagnetic devices*, IEE Proceedings, Vol. 133, Pt. B, N. 4, 1986.

[7] Binns, K.J., Riley, C.P. and Wong, M., *The efficient evaluation of torque and field gradient in permanent-magnet machines with small air-gap*, IEEE Transactions on Magnetics, Vol. MAG-21, No. 6, pp. 2435-2438, 1985.

[8] Licarião-Nogueira, A.F., *Computation of cogging torques in permanent-magnet machines using the finite element method*, Ph.D. Thesis, University of Wales College of Cardiff, UK, 1993.

[9] Lowther, D.A. and Silvester, P.P., *Computer-aided design in magnetics*, Springer-Verlag, New York, 1986.

[10] McFee, S. and Lowther, D.A., *Towards accurate and consistent force calculation in finite element based computational magnetostatics*, IEEE Transactions on Magnetics, Vol. MAG-23, N. 5, pp. 3771-3773, 1987.

Comparison of Convergence Rates of Edge and Nodal Finite Elements for Magnetostatic Problems

M. L. y Gonzalez[1] , R. C. Mesquita[1] , J. P. A. Bastos[2]
[1]Universidade Federal de Minas Gerais - Belo Horizonte - MG - Brazil.
[2]Universidade Federal de Santa Catarina - Florianópolis - SC - Brazil.
E-mail : manuel@novell.cpdee.ufmg.br

Abstract — Mathematical theory is used to obtain convergence estimations for magnetostatic formulations using nodal and edge elements. Numerical results of two closed boundary problems that confirm the theory are presented.

I. INTRODUCTION

Much research has been done recently with nodal and edge elements in electromagnetic problems. However, it has not been discussed how an approximate solution, obtained by the finite element method, converges to the exact solution of the problem, when the mesh is successively refined. Recent papers [1, 2] show the characteristics of those elements and their convergence rates, when the field variable interpolated is the magnetic field **H**. In [3] and [4], convergence rates for regular meshes of nodal finite elements are presented, when the field variable interpolated is the magnetic vector potential **A**. In approximately closed boundary magnetostatic problems, the obtained results confirm the theoretical convergence rates [3,4].

Nevertheless, the authors do not know any convergence study that compares the edge and nodal elements when the magnetic vector potential **A** is being used as the field variable.

In this paper, convergence rates for nodal and edge elements with one degree of freedom per edge (also named Nédélec elements or Mixed elements), applying regular meshes, are established. Convergence rates of closed boundary problems are also presented, applying nodal and Nédélec elements.

II. DESCRIPTION OF THE ELEMENTS

Nodal elements represent vector functions with continuous components and show good results in homogeneous domains. Edge elements guarantee the continuity of the tangential components of these functions across the element's interfaces, allowing the discontinuity of the normal component. They can be applied in homogeneous or inhomogeneous domains, and they are better than the nodal elements in the treatment of the singularity of re-entrant corners [1,5].

The nodal elements in 3-D have 3 degrees of freedom per node, while the Nédélec elements have 1 degree of freedom per edge. Some results seem to indicate that the Nédélec elements are more efficient computationally than the nodal elements [1]. If the following assumptions are made: (i) there exists a large mesh with hexahedral finite elements; (ii) the reduction of the number of unknowns due to the boundary conditions can be ignored; (iii) no gauge is applied in the problem; then it is found that the number of nonzero elements in the global matrix is equal to 236 Ne for nodal elements, and 99 Ne for edge elements, where Ne is the number of elements in the mesh [6]. So, it seems that, in terms of memory occupation, edge elements are better than nodal elements.

III. MATHEMATICAL FORMULATION

In the computation of magnetostatic fields using the magnetic vector potential, the following equation is used:

$$\nabla \, x \, (\, \upsilon \, \nabla \, x \, \mathbf{A} \,) \; = \; \mathbf{J} \, , \qquad (1)$$

where υ is the magnetic reluctivity and **J** the current density in the problem domain Ω. This equation is a partial differential equation of second order that has the weak form

$$\mathbf{D}(\mathbf{A}, w) = \mathbf{f}(\mathbf{J}, w) \qquad \forall w \in \mathcal{V}, \qquad (2)$$

where **D** and **f** are symmetric bilinear forms that consist of integrals over Ω, and $\mathcal{V}$ is the space of admissible functions. This weak form has only derivatives of first order.

IV. ERROR ESTIMATES AND CONVERGENCE RATES

A. Nodal Elements

Let A_h be an approximate solution found by the finite element method to the magnetic vector potential, and A the exact solution of the problem. Let $e = A - A_h$ be the error between A and A_h, then we define the following Sobolev norms:

$$\|e\|_{H^m(\Omega)} = \left[\int_\Omega \sum_{\alpha=0}^m \left(e^\alpha\right)^2 dx \right]^{1/2} \tag{3}$$

and

$$\|A\|_{H^{k+1}(\Omega)} = \left[\int_\Omega \sum_{\alpha=0}^{k+1} \left(A^\alpha\right)^2 dx \right]^{1/2}, \tag{4}$$

where k is the order of the polynomials used in the local basic functions, m the order of derivatives that appear in (2), e^α and A^α all the derivatives of order α of e and A, with $\alpha = (\alpha_1, \alpha_2, \ldots, \alpha_n) \in Z_+^n$ (Set of all ordered n-tuples of non-negative integers), and $|\alpha| = \alpha_1 + \alpha_2 + \ldots + \alpha_n$. Considering that the finite element mesh is regular, and using the Aubin-Nitsche theorem [8, 9], the following estimate for the error norm is obtained:

$$\|e\|_{H^s(\Omega)} \le C_0 h^\mu \|A\|_{H^{k+1}(\Omega)}, \tag{5}$$

for $0 \le s \le m$ and $\mu = \min [k+1-s, 2(k+1-m)]$. h is the parameter of the mesh, defined by the diameter of the smallest circle that contains the largest element of the mesh, and C_0 is a constant independent of A and h.

If our interest is in $\|e\|_{H^0(\Omega)}$, and we know that $\|A\|_{H^{k+1}(\Omega)}$ is constant, we can set $C_1 = C_0 \|A\|_{H^{k+1}(\Omega)}$, obtaining

$$\|e\|_{H^0(\Omega)} \le C_1 h^\mu. \tag{6}$$

But, $m = 1$, then $\mu = k + 1$ since $2k \ge (k+1)$. In this way, the convergence rate is of order $O(h^{k+1})$ for the magnetic vector potential A. As B, the magnetic flux density, is computed from A by building the curl, and

the convergence rate decreases with the derivatives [8], the convergence rate for B is of order $O(h^k)$.

B. Edge Elements

Let Γ be the boundary of the problem, η the unit normal vector in Γ, then we can define the following Hilbert spaces:

$$H(\text{curl}, \Omega) = \left\{ A \in \left(L_2(\Omega)\right)^3 : \nabla x A \in \left(L_2(\Omega)\right)^3 \right\} \tag{7}$$

and

$$H_0(\text{curl}, \Omega) = \left\{ A \in H(\text{curl}, \Omega) : A x \eta = 0 \text{ in } \Gamma \right\} \tag{8}$$

Let P_k be the polynomial space of degree $\le k$ and $\tilde{P}_k$ the homogeneous polynomial space of degree k. Then we can also define the space

$$S_k = \left\{ p(x) \in \left(\tilde{P}(x)\right)^3 : p(x).x = 0 \right\}, \tag{9}$$

where $p(x).x$ is the inner product between $p(x)$ and x, that is, $p(x)$ and x are orthogonal. Let U_h be the space of approximate function, $A_h \in U_h$, and the projection operator $\pi_h A \in U_h$, so that the following inner products are zero:

$$\left(\nabla x (A - \pi_h A), \nabla x V\right) = 0, \qquad \forall V \in U_h \tag{10}$$

and

$$\left(A - \pi_h A, \nabla p(x)\right) = 0, \qquad \forall p(x) \in S_k. \tag{11}$$

Then, we have the following theorem [7]:

Consider a regular mesh and assume that $A \in H_0(\text{curl}, \Omega)$ and $\pi_h A$ is defined as above. Then

(i) if $A \in \left(H^{k+1}(\Omega)\right)^3$, then

$$\|A - \pi_h A\|_{H^0(\Omega)} \le C h^k \|A\|_{H^{k+1}(\Omega)}. \tag{12}$$

(ii) if $\nabla x A \in \left(H^k(\Omega)\right)^3$, and $\pi_h A$ is well defined as above, then

$$\|\nabla x (A - \pi_h A)\|_{H^0(\Omega)} \le C h^k \|\nabla x A\|_{H^k(\Omega)}. \tag{13}$$

81

Let $\mathbf{A}_h = \pi_h \mathbf{A}$ and $\mathbf{B}_h = \nabla x \mathbf{A}_h$. Then we notice that the convergence rates for $\mathbf{A}$ and $\mathbf{B}$ are of order $\mathbf{O}(h^k)$.

V. RESULTS

Using 3-D electromagnetic field computation programs developed by our research groups, the error estimates for the following problems have been determined:

(i) Infinite square coaxial nonmagnetic cable in air.
(ii) Infinite rectangular magnetic busbar in air.

The problem (i) was chosen because it behaves as a closed boundary problem (null magnetic field in the proximity of the cable), when the current that flows in the outward conductor is chosen to cancel the magnetic field in the proximity of the cable, created by the current that flows in the inner conductor. In this way, it is possible to represent the boundary conditions of the problem in exact manner, and one avoids that the boundary condition errors could introduce errors in the computation of the convergence rates.

The problem (ii) was chosen because it has two permeabilities and behaves as a closed boundary problem when the permeability of the busbar is much greater than the air permeability.

In the following section all those problems are presented with their convergence rates. The analytic solutions are found in [10].

Infinite Square Coaxial Nonmagnetic Cable in Air

A cable with an inner conductor of 10 cm x 10 cm, and an outward conductor of 50 cm x 50 cm with a thickness of 10 cm was considered, as shown in Fig. 1. A current of 10,000 A was assumed in both conductors. The current flows axially in opposite senses in the inner and in the outer conductors. The boundary condition $\mathbf{A} = 0$ was considered to be 10 cm outside of outward conductor.

Let us substitute $\mathbf{B}$ in (5) and (6). Then, L_2 error for $\mathbf{B}$ is

$$L2Berr = \left[\int_\Omega (\mathbf{B} - \mathbf{B}_h)^2 \ dx \right]^{1/2}. \qquad (14)$$

The results obtained for this error norm in the nodal and Nédélec Elements, when the finite element mesh is refined (-log h is increased), are shown in Fig. 2 and 3 respectively.

Using linear regression, we have found a convergence rate of $\mu = 0,961$ for the nodal elements [4] and $\mu = 0,959$ for the edge elements. As these computations were executed with interpolating polynomials of 1st degree ($k = 1$), the rates are near 1, and confirm the theory.

Infinite Rectangular Magnetic Busbar

it was considered a busbar of 10 cm x 20 cm with magnetic permeability $\mu_r = 1000$. The current of 400 A flows axially in the busbar, and the boundary condition $\mathbf{A} = 0$ was assumed at a distance of 15 cm from busbar center, as shown in Fig. 4.

The computation of the values of L2Berr is shown in Figs. 5 and 6. Using also linear regressions, we obtained a convergence rate of $\mu = 0.991$ [3] for the nodal elements and $\mu = 0,987$ for the edge elements.

10 cm

50 cm

(a) Total View

Outward Conductor

Boundary Condition
A = 0

(b) Plant View
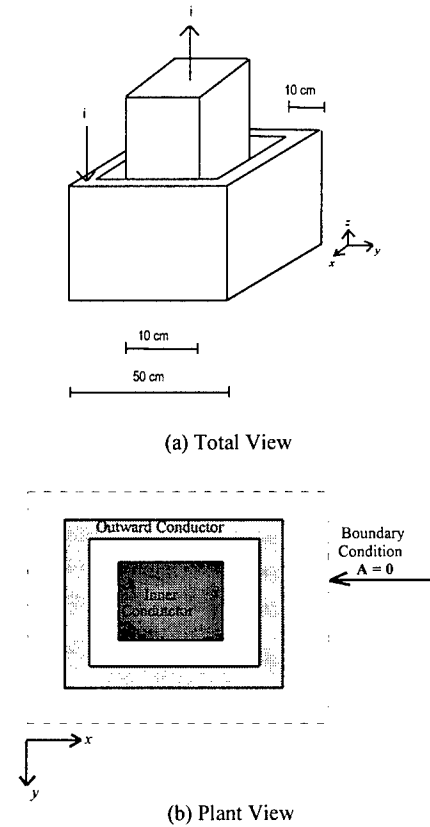
Fig. 1 - View of Coaxial Cable
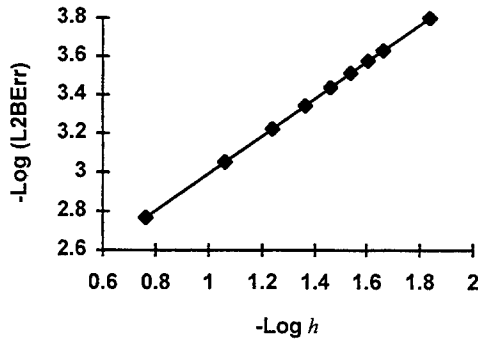
Fig. 2 - Results of Coaxial Cable with Nodal elements
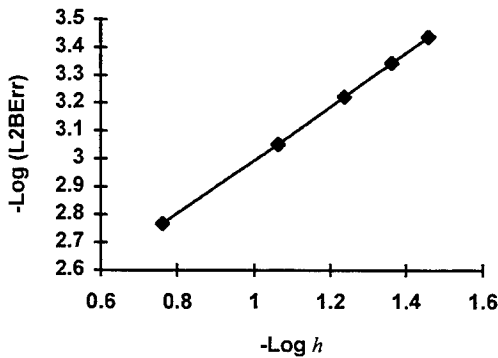
Fig. 3 - Results of Coaxial Cable with Edge Elements
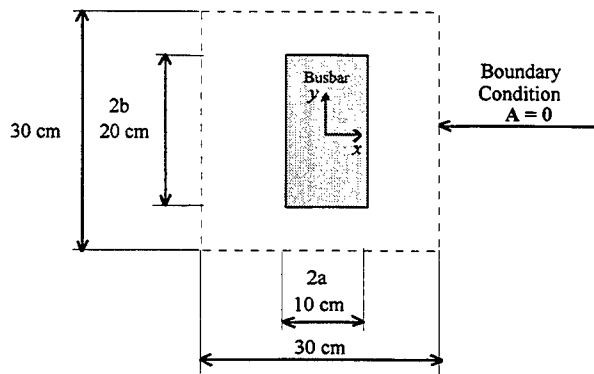
Fig. 4 - View of Magnetic Busbar
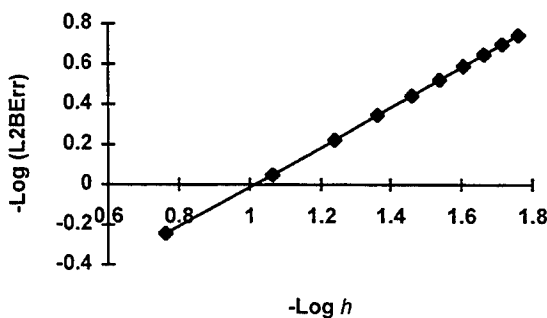
Fig. 5 - Results for Magnetic Busbar with Nodal Elements
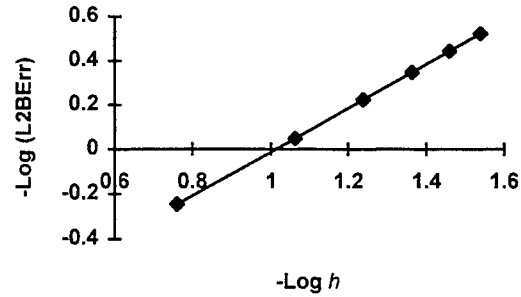
Fig. 6 - Results for Magnetic Busbar with Edge Elements

VI. CONCLUSIONS

The convergence rates for magnetic vector potential formulations using nodal and edge finite elements with one degree of freedom per edge (Nédélec Elements) and regular meshes were presented.

Theoretically, when nodal elements are used, the convergence rates are of order $O(h^{k+1})$ for the magnetic vector potential A and $O(h^k)$ for the magnetic flux density B. When edge elements are used, the convergence rate is of order $O(h^k)$ for A and B.

Finally, some computational examples that confirm the theoretical results are presented.

REFERENCES

[1] G. Mur, "Edge Elements, Their Advantages and their disadvantages", *IEEE Transactions on Magnetics*, Vol. 30, no. 5, pp. 3552-3557, 1994.

[2] B. Bandelier, F. Rioux-Damidau, "Edge Elements or Nodal Elements for the Computation of Magnetic Fields and Eddy-Currents? How to choose?", COMPUMAG, MIAMI, Nov/93.

[3] M. L y Gonzalez, R. C. Mesquita,"Convergence Properties of Magnetostatic Formulations", *IEEE Transactions on Magnetics*, Vol. 30, no. 5, pp. 2869-2872, 1994.

[4] M. L y Gonzalez, R. C. Mesquita,"Influence of the Boundary Conditions on the Convergence Rates of Finite Element for magnetostatic Problems" (In Portuguese), XV CILAMCE - Ibero Latino-Americano Congress on Computational Methods for Engineering, Belo Horizonte (Brazil), 30/11-02/12/94.

[5] J. P. Webb, "Edge Elements and What They Can Do For You", *IEEE Transactions on Magnetic*, Vol 29, no. 2, pp. 1460-1465.

[6] E. J. Silva, R. C. Mesquita, R. R. Saldanha, "Formulation for Computation of Magnetostatic Fields Using Edge Elements" (In Portuguese), XIV CILAMCE - Ibero Latino-Americano Congress on Computational Methods for Engineering, São Paulo, Brazil, IPT, 1993.

[7] P. Monk, "An Analysis of Nédélec Method for The Spatial Discretization of Maxwell's Equations", *Journal of Computational and Applied Mathematics* 47 (1993), pp. 101-121.

[8] J. T. Oden, J. N. Reddy, *"An Introduction to the Mathematical Theory of Finite Elements"*, New York, John Wiley & Son, 1976.

[9] J. T. Oden, G. F. Carey, *"Finite Elements - Mathematic Aspects - Volume IV "*, New Jersey, Prentice-Hall, 1983.

[10] M. L y Gonzalez, "Mathematical Properties of Finite Elements for the Magnetostatic Fields Computation Using The Magnetic Vector Potential" (In Portuguese), *Master Thesis*, CPDEE - UFMG, Belo Horizonte, MG, Brazil, 1995.

Finite Element Simulation of an Out-of-Phase Synchronization of a Synchronous Machine

Silvio Ikuyo Nabeta

Equipe de Simulação de Fenômenos Eletromagnéticos - Depto. de Engenharia de Energia e Automação Elétricas
Escola Politécnica da Universidade de São Paulo
Av. Prof. Luciano Gualberto trav. 3 n° 158 Cidade Universitária CEP 05508-900 São Paulo, Brazil

Albert Foggia, Jean-Louis Coulomb, Gilbert Reyne
Laboratoire d'Electrotechnique de Grenoble (INPG) URA CNRS 355
BP 46, 38402 Saint-Martin d'Hères Cedex, France

Abstract—This paper presents the finite element simulations of the out-of-phase synchronization of a synchronous machine with an external electric system. Two cases were analysed regarding to the phase angle: 120° and 180°. Computed results are analysed and compared to analytical values.

INTRODUCTION

A very current and important stress for a synchronous machine arises during an out-of-phase synchronization.

An out-of-phase synchronization is a faulty three phase operation that occurs when the generator is switched to the system and the equality of voltage and/or frequency and/or phase are not respected.

In this work we assume that the voltage is equal for the system and the generator, and the phase angle is different.

Fig.1 shows the representation of this assumption.

A,B,C: Generator
A',B',C': System
λ: angle between phases
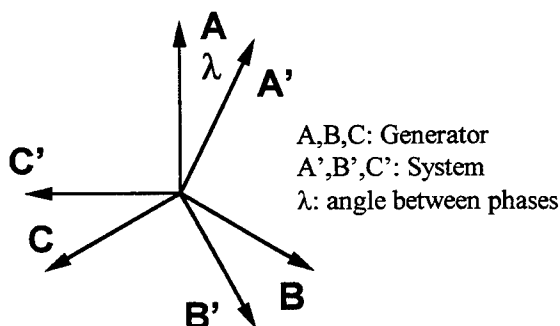
Fig.1: Angle lag between generator and system voltages

In such condition two important cases arise:

1. out-of-phase synchronization with 180° of angular lag;
2. out-of-phase synchronization with 120° of angular lag.

In the first case the armature currents reach the maximum value whereas in the second case the electromagnetic torque reaches its maximum value.

The analytical study of those cases is done by the Park theory [1].

Nevertheless, the equations development is very fastidious and some simplifying hypothesis must be taken in order to obtain useful expressions.

Nowadays, the availability of modern numerical programs allows a closer investigation of the magnetic behaviour in the synchronous machine.

Hence a more accurate solution can be reached by computing the flux distributions in detail avoiding simplifications in modelling.

This paper presents the linear, two-dimensional , time-stepping finite element simulations of the out-of-phase synchronization in the two cases previously mentioned.

These simulations considered the rotor movement by means of the air-band technique [5] and the external system by coupling electric circuit equations to the Finite Element Method (FEM) [2], [3], [4].

Computed results are compared to analytical ones.

OUT-OF-PHASE SYNCHRONIZATION - THEORETICAL OVERVIEW

Consider a unloaded synchronous generator. The armature voltages can be written as:

$$V_{a0} = e.sin(\omega t + \theta_0)$$
$$V_{b0} = e.sin\left(\omega t + \theta_0 - \frac{2\pi}{3}\right) \quad\quad (1)$$
$$V_{c0} = e.sin\left(\omega t + \theta_0 - \frac{4\pi}{3}\right)$$

As stated before only the phase equality is not respected.

Thus the system voltages are expressed as:

$$V_{a1} = e.sin(\omega t + \theta_0 - \lambda)$$

$$V_{b0} = e.sin\left(\omega t + \theta_0 - \lambda - \frac{2\pi}{3}\right) \qquad (2)$$

$$V_{c0} = e.sin\left(\omega t + \theta_0 - \lambda - \frac{4\pi}{3}\right)$$

where λ is the phase angle difference at the switching instant.

Applying the Park transformation to (1) and (2) we obtain:

$$V_{d0} = 0 \qquad V_{d1} = -e.sin\lambda$$

$$V_{q0} = e \qquad V_{q1} = e.cos\lambda$$

The voltage variation on the machine's terminal is:

$$\Delta V_{d0} = V_{d1} - V_{d0} = -e.sin\lambda = -2e.sin\frac{\lambda}{2}.cos\frac{\lambda}{2}$$

$$\Delta V_{q0} = V_{q1} - V_{q0} = e.cos\lambda - e = -2e.sin^2\frac{\lambda}{2} \qquad (3)$$

Using the operational notation we have:

$$\frac{\Delta V_{d0}}{p} = -p\Delta\phi_d - \omega.\Delta\phi_q - r_a.\Delta I_d$$

$$\qquad (4)$$

$$\frac{\Delta V_{q0}}{p} = -p\Delta\phi_q + \omega.\Delta\phi_d - r_a.\Delta I_q$$

with:

$$\Delta\phi_d = L_d(p).\Delta I_d$$

$$\qquad (5)$$

$$\Delta\phi_q = L_q(p).\Delta I_q$$

$L_d(p)$: D-axis operational inductance

$L_q(p)$: Q-axis operational inductance

Eliminating ΔI_d and ΔI_q in equations (4) we reach the following system:

$$\begin{bmatrix} \dfrac{\Delta V_{d0}}{p} \\ \dfrac{\Delta V_{q0}}{p} \end{bmatrix} = \begin{bmatrix} -\left(p + \dfrac{r_a}{L_d(p)}\right) & -\omega \\ \omega & -\left(p + \dfrac{r_a}{L_q(p)}\right) \end{bmatrix} \begin{bmatrix} \Delta\phi_d \\ \Delta\phi_q \end{bmatrix} \quad (6)$$

Solving (6) we obtain:

$$\Delta\phi_d(p) = \frac{1}{p\left(p^2 + 2\alpha p + \omega^2\right)} \times$$

$$\left[-\Delta V_{d0}.\left(p + \frac{r_a}{L_d(p)}\right) + \Delta V_{q0}.\omega \right]$$

$$\qquad (7)$$

$$\Delta\phi_q(p) = \frac{1}{p\left(p^2 + 2\alpha p + \omega^2\right)} \times$$

$$\left[-\Delta V_{d0}.\omega - \Delta V_{q0}.\left(p + \frac{r_a}{Lq(p)}\right) \right]$$

where: $\dfrac{1}{\alpha} = T_a$ is the armature time-constant

Considering that the out-of-phase operation is harmful in the first instants we can neglect all resistances.

So, introducing (7) in equation (5) we obtain the currents variations:

$$\Delta I_d(p) = \frac{\Delta V_{d0}}{L_d(p)\left(p^2 + 2\alpha p + \omega^2\right)} +$$

$$\frac{\omega.\Delta V_{q0}}{pL_d(p)\left(p^2 + 2\alpha p + \omega^2\right)}$$

$$\qquad (8)$$

$$\Delta I_q(p) = \frac{\Delta V_{d0}}{pL_q(p)\left(p^2 + 2\alpha p + \omega^2\right)} +$$

$$\frac{\omega.\Delta V_{q0}}{L_q(p)\left(p^2 + 2\alpha p + \omega^2\right)}$$

Moreover, assuming that $X_d^{"} = X_q^{"}$ we obtain in the time-domain terms [1]:

$$I_d(t) = \Delta I_d(t) = \frac{2e}{X_d^{"}}.sin\frac{\lambda}{2}\left[sin\left(\omega t + \frac{\lambda}{2}\right) - sin\frac{\lambda}{2}\right]$$

$$(9)$$

$$I_q(t) = \Delta I_q(t) = -\frac{2e}{X_d^{"}}.sin\frac{\lambda}{2}\left[cos\left(\omega t + \frac{\lambda}{2}\right) - cos\frac{\lambda}{2}\right]$$

and: $X_d^{"}$: D-axis subtransient reactance

And the phase-A current can be written, in per unit values, as:

$$I_a(t) = \frac{2e}{X_d^{"}}.sin\frac{\lambda}{2}\left[sin\left(\omega t - \theta_0 - \frac{\lambda}{2}\right) - sin\left(\theta_0 - \frac{\lambda}{2}\right)\right] \quad (10)$$

The torque equation is obtained by using the following equation:

$$C_e = \frac{e^2}{X_d^{"}}.\omega\left[\phi_d.I_q - \phi_q.I_d\right] \quad (11)$$

In our case we have in per unit values:

$$C_e = \frac{e^2}{X_d^{"}}\left[sin\lambda - 2sin\frac{\lambda}{2}.cos\left(\omega t + \frac{\lambda}{2}\right)\right] \quad (12)$$

It can be noted from (10) that the maximum current occurs when:

$$\lambda = \pi, \theta_0 = 0, \omega t = \pi$$

Thus:

$$I_{amax} = \frac{4e}{X_d^{"}} \quad (13)$$

Analogously, from (12) we have for the maximum torque:

$$\lambda = \pm\frac{2\pi}{3}$$

and:

$$C_{emax} = \frac{3\sqrt{3}.e^2}{2X_d^{"}} \quad (14)$$

FINITE ELEMENT METHOD

Although analytical solutions are known for the out-of-phase synchronization as presented in the previous section numerical methods have the advantage of providing solutions less affected by simplifications including results on local quantities.

This section presents the FEM for time-dependent problems.

In electromagnetic time-dependent problems the skin effect occurs in solid conductors.

Thus the partial differential equations that describe the electromagnetic phenomenon are:

for wound conductors:

$$rot(v.rotA) = j \quad (15)$$

for solid conductors:

$$rot(v.rotA) + \sigma.(\partial A/\partial t + gradV) = 0 \quad (16)$$

Applying the FEM to these equations the following systems, in commonly used notations, are reached [2]:

wound conductors:

$$[S].[A] = [C].[I] \quad (17)$$

solid conductors:

$$[S].[A] + [G]. \partial[A]/ \partial t.[C'].[\Delta V] \quad (18)$$

with:

$$S_{i,j} = l. \iint_\Omega v.grad\alpha_i.grad\alpha_j d\Omega$$

$$G_{i,j} = l. \iint_\Omega \sigma.\alpha_i.\alpha_j d\Omega$$

$$C_i' = l. \iint_{\Omega_k} \sigma.\alpha_i d\Omega$$

$$C_i = \left(\frac{N_s.l}{s_k}\right) \iint_{\Omega_k} \alpha_i d\Omega$$

α_i, α_j : interpolation functions
N_s : number of turns for wound conductors
s_k : wound conductors' region surface

It is noted that wound conductors are supplied by current sources whereas the most electromechanical devices are supplied by voltage sources.

Therefore, a technique, as shown in the following section, is necessary to take into account the two types of conductors and to allow the voltage supply in wound conductors.

Electric Circuits Coupling

A recently developed technique to model wound and solid conductors and the voltage supply is the Electric Circuits Coupling which is based on the association of Kirchhoff equations in the FEM formulations [2].

Furthermore, it allows to take into account the external components such as inductances and resistances in the analysis.

Fig.2. shows a simplified circuit coupled with a Finite Element analysis.
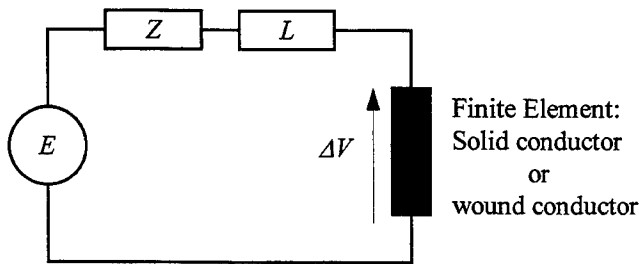
Fig.2. Electric Circuit Coupling

According to [2] the circuit coupling provides the following system:

for wound conductors:

$$[S].[A] = [C].[I] \tag{19}$$
$$[E] = [Z'].[I] + [L].\partial[I]/\partial t + [D'].[C'].\partial[A]/\partial t \tag{20}$$

for solid conductors:

$$[S].[A] + [G]. \partial[A]/\partial t - [C'].[\Delta V] = 0 \tag{21}$$
$$[E] = [Z].[I] + [L].\partial[I]/\partial t + [D].[\Delta V] \tag{22}$$
$$[\Delta V] = [R].[I] + [R].[C]^{T}. \partial[A]/\partial t \tag{23}$$

where:

[E] :vector of voltage sources

[A] :vector of magnetic potentials
[Z] :matrix of external resistances
[Z'] :matrix of external and wound conductors resistances
[L] :matrix of external inductances
[D'], [D] :matrices of currents directions
[I] :vector of currents
[R] :matrix of solid conductors resistances
[ΔV] :vector of solid conductors drop voltages

Moving-Air-Band Technique

The moving-air-band technique was implemented in order to consider the rotor movement in the FEM simulation [5].

It comprises a surface located in the air-gap with only one layer of elements.

The main advantage of this technique is the fact that the finite element meshes in the stator and rotor remain unaltered after the movement.

Remeshing is necessary only in the band region as can be seen in Fig.3.
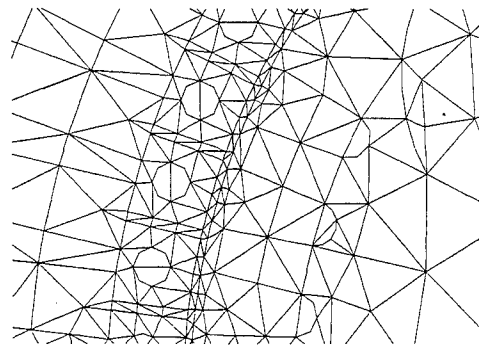
a: before
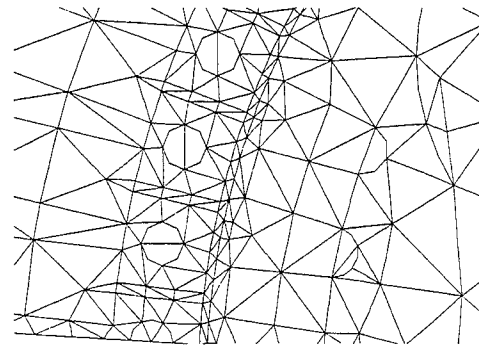
b: after

Fig.3. Moving-air-band mesh before and after a rotation of 5°

NUMERICAL SIMULATION

The numerical simulations were carried out on a 3-phase, 3 KVA, 50 Hz, 4 salient-pole generator, as shown in Fig.4.

The stator has 54 slots, 12 conductors per slot and a 2-tier, double-layer, star-connected winding.

The rotor, which is completely laminated, has 4-coil main excitation winding and a concentric wound damper winding fitted in 24 slots with 74 conductors per slot.

Figure 5 shows a magnified view of damper slots.

Due to symmetries in the study domain a half geometry was used in numerical analysis.

This allowed to reduce the matrices dimensions and the number of electric circuits.

The external system, the switches and the windings connections were taken into account in the simulations by using the electric circuit shown in Fig.6.

The software package used was FLUX2D [6].

Fig.6. Electric circuit

The first step of the simulation consisted in reaching the generator steady-state at unload condition.

It was done by a time-stepping simulation feeding the field winding with a DC voltage source and rotating the rotor at 1500 rpm.

Afterwards, switching with the appropriate angle the out-of-phase synchronization between the generator and the system was accomplished.

In this work the time-step was 0.5 ms and synchronizing angles were chosen as $\lambda = 180°$ and $\lambda = 120°$.

RESULTS

Fig.7. shows the phase-A current and the torque waveforms for the out-of-phase synchronizations at 120° and 180°.

Fig.4. Machine geometry with moving-air-band technique

a: Current

Fig.5. Magnified view of damper slots
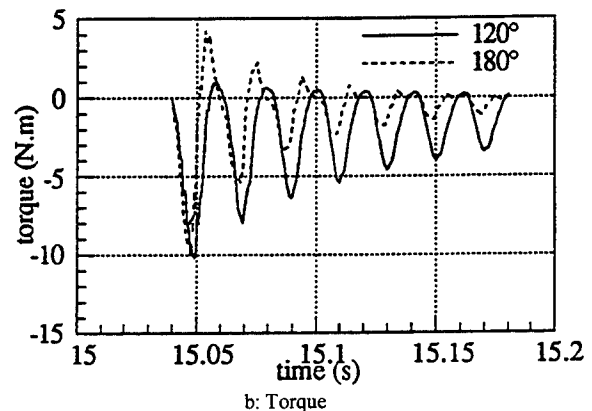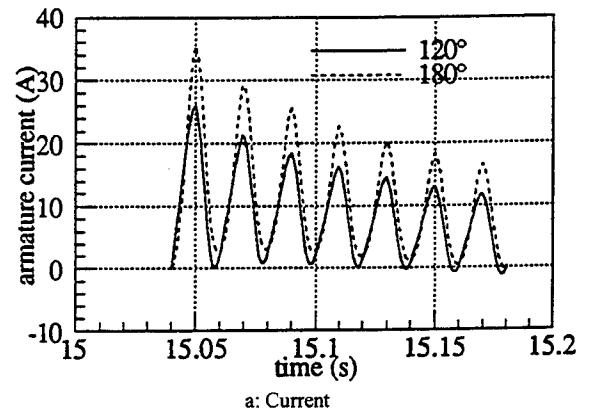
b: Torque

Fig.7. Phase-A current and torque for $\lambda=120°$ and $\lambda=180°$

Table I presents the comparison between computed and analytical results of maxima values of current and torque.

Table I: Maxima values of current and torque

Parameter Method	I_{max} (A) $\lambda=180°$	C_{max} (N.m) $\lambda=120°$
Analytical	40,3	-8,07
Simulation	35,5	-10,20

We note from Table I that for $\lambda=180°$ the analytical value for the current is greater than the simulated result.

This difference can be explained by the fact that all resistances in the analytical expressions were neglected.

Indeed, neglecting the resistances the decrements in the current waveform are not taken into account.

Furthermore, the absence of the resistances causes the non-consideration of the homopolar torque which can justify the difference between analytical and numerical results for the torque at $\lambda=120°$.

The total cpu time was 84.10^4 s and the number of unknowns was 5383.

CONCLUSIONS

Out-of-phase synchronizations between a synchronous generator and an external system were accomplished by finite element simulations.

Numerical results agree with theory and have shown that maximum current and maximum torque occur at $\lambda=180°$ and $\lambda=120°$, respectively.

Moreover, unlike analytical method, numerical simulations allow the out-of-phase synchronization study without neglecting the resistances.

Hence, complex phenomena such as the homopolar torque are taken into account and more complete results are reached.

REFERENCES

[1] P. Barret, *Régimes Transitoires des Machines Tournantes Electriques*, Editions Eyrolles, Paris, (1982).
[2] P. Lombard, G. Meunier, A general purpose method for electric and magnetic combined problems for 2D, axisymmetric and transients systems, *CEFC 92*, 3-5 aug, Claremont, USA. *IEEE Transactions on Magnetics*, vol.29, n.2, pp.1737-1740, March 1993.
[3] A. Arkkio, Finite Element Analysis of Cage Induction Motors fed by Static Frequency Converters, *IEEE Transactions on Magnetics*, vol.26, n.2, pp.551-554, 1990.
[4] N. Sadowski, B. Carly, Y. Lefèvre, M. Lajoie-Mazenc, Finite Element Simulation of Electrical Motors fed by Current Inverters, *IEEE Transactions on Magnetics*, vol.29, n.2, pp.1683-1688, March 1993.
[5] E. Vassent, G. Meunier, A. Foggia, G. Reyne, Simulation of induction machine operation using a step by step finite-element method coupled with circuit and mechanical equations, *Fifth joint MMM-Intermag Conf.* Pittsburgh, USA, 18-21 june, 1991. *IEEE Transactions on Magnetics*, vol.27, n.6, pp. 5232-5234, Nov. 1991.
[6] FLUX2D v.7.11 - Finite Element Software for Electromagnetics Applications, CEDRAT (CEE), MAGSOFT (USA).

A 3D Finite-Element Computation of Stator End-winding Leakage Inductance and Forces at Steady State Operating Conditions in Large Hydrogenerators

Viviane Cristine Silva
Escola Politécnica da Universidade de São Paulo
PEA - Depto. de Engenharia de Energia e Automação Elétricas
Av. Prof. Luciano Gualberto, n⁰ 158 - Trav. 3
Cidade Universitária - 05508-900 São Paulo SP - Brasil

Albert Foggia
LEG - Laboratoire d'Electrotechnique de Grenoble
B.P. 46 - Domaine Universitaire
38402 - Saint Martin d'Hères Cedex - France

Abstract - **The forces acting on the stator end windings of a hydrogenerator at steady state operating conditions, as well as the end-winding leakage inductance, are calculated using a 3D finite-element package. A more realistic representation for the geometry of the windings and boundaries is considered. The effects of different representations for the stator core end surface are outlined. The computed values of the inductance from time-harmonic and static simulations are presented and compared with classical analytical methods.**

I. INTRODUCTION

The electromagnetic field theory has become increasingly important in many engineering problems. An accurate knowledge of the magnetic field distribution in electric machines is of great importance in the design step. For instance, the estimation of the end-winding inductance, end-induced stray losses, and forces requires the knowledge of the leakage field of the stator end winding. Therefore, many efforts have been made to satisfactory predict the end leakage of a.c. machines. This has been possible in spite of the difficulties encountered, such as the 3D field distribution, the complicated shape of windings and boundaries, the different permeabilities, and the reaction of eddy currents induced in the boundary surfaces.

The limitations of analytical methods have led to the development of improved field calculations using numerical methods. Unfortunately, the available numerical methods [1]-[2] have the disadvantage that the field calculation is only quasi-three-dimensional, using axisymmetrical geometries. Therefore, all structural inhomogeneities in the peripheral direction are considered only approximately, as is the case in the assumption of a sinusoidal circumferential distribution for the currents as sources of magnetic field and its limitation to just the fundamental wave [2]. Of course, the neglected field harmonics decay quickly, but their greatest effect occurs in the vicinity of the conductor, just where the force is produced. Thus, a solution for this problem can only be achieved

through a 3D finite-element computation.

In this work, a method is presented so as to determine steady state forces on the stator end windings of a hydrogenerator based on a fully three-dimensional field solution. The calculations have been carried out using a three-dimensional finite-element package, in which the shape and finite cross section of the windings are both treated. In addition, the model allows for eddy current effects. These eddy currents appear mainly in the stator core flange and stator end laminations.

The end winding region of a 300-MVA 16.5-kV alternator with fifty-two rotor saliencies is used [3]. The stator winding consists of two-layer short-pitched diamond-shaped coils. A three-dimensional view of the end region of the machine is shown in Fig. 1, where only one pole pitch is represented because of symmetry.
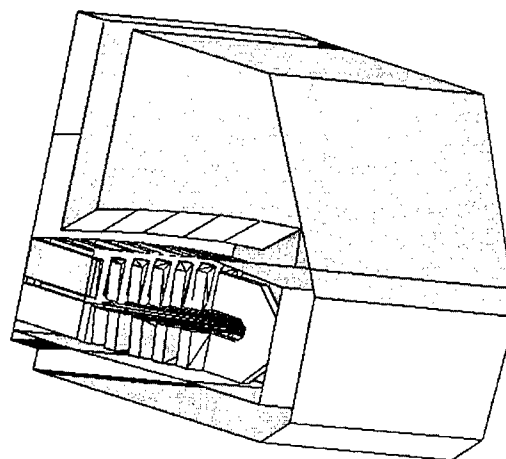
Fig. 1. Domain of study: one pole of the machine with relevant boundaries.

II. BASIC ASSUMPTIONS

A. Computation of Inductance

Three simulations were carried out for determining the

flux distribution. In the first two, the problem is treated as a magnetodynamic one with sinusoidal-time variation for the variables. Two different approaches are used to represent the stator end laminations. In the third simulation the problem is treated as a magnetostatic one, where no eddy-current effect is considered.

The assumptions made are as follows: a) the windings have a 3-phase current feeding; b) the calculation of inductance is performed for the instant at which phase A is carrying the maximum current; c) only one pole pitch is represented in the analysis, due to the periodicity of the domain; d) all materials are assumed to be linear, isotropic and homogeneous; e) the source current-density field is continuous and uniformly distributed over the area of the cross section of a coil; f) the rotor has not been represented in the model, which is an acceptable approach in large salient-pole generators at steady-state operating condition, thanks to the large air-gap characteristic of this kind of machine.

B. Computation of Forces

Several simulations were carried out to determine the flux distribution in different operating conditions. The problem is treated as a magnetodynamic one with sinusoidal time variation for the variables. Two different approaches are used for representing the stator end laminations.

The assumptions made are the same as for the computation of inductance, except for the rotor representation. It has to be taken into account in this case, and that is achieved through a suitable boundary condition prescribed on its surface.

III. 3D FORMULATIONS AND BOUNDARY CONDITIONS

In contrast to the 2D finite-element analysis of electromagnetic fields, which uses only the magnetic vector potential (MVP) as state variable, various formulations are available in 3D [4].

Usually, the use of the magnetic scalar potential (MSP), both total and reduced, as state variable is encouraged as much as possible, since it produces only one unknown per node in the finite-element mesh. The presence of source currents can be dealt with by using the reduced MSP, when the contribution of the source currents is computed by the Biot-Savart law. Nevertheless, when current-carrying conductors have complicated shapes, the application of the Biot-Savart law can be very troublesome and time-consuming. Furthermore, in the vicinity of the conductors, which is the region of interest, the precision can be very poor. These problems have been tackled by using the MVP in regions with source currents.

Hence, the field solution has been first performed in the complex domain, i.e., the quantities vary sinusoidally in time, and the formulations used are as follows [3]: a) MVP in current-carrying regions and holes of multiple-connected regions, and b) total MSP in current-free regions. Thus, in the stator end-winding region, which is limited by an enclosing box, the MVP is used. In the surrounding empty space the total MSP is employed. The relevant boundaries are shown in Fig. 1.

The boundary conditions used are as follows: a) antiperiodic boundary conditions on the two radial planes of symmetry of the pole pitch; b) surface impedance boundary condition on the surface of the stator core flange; c) tangential field on the outer boundary surfaces; d) the stator end lamination is firstly represented as a surface impedance boundary, which enables eddy-current effects to be allowed for, and then as a boundary where the field is assumed tangential; e) when the scalar and vector potentials are used in different parts of the domain, a condition of $\mathbf{A}.\mathbf{n} = 0$ (zero normal component of the vector potential) is enforced on the interface of the two formulations to ensure the uniqueness of the vector potential solution [4].

The rotor is represented as a Dirichlet boundary condition, imposed on its surface, on the total MSP. This boundary condition represents the rotor magnetomotive force (m.m.f.) and depends on the operating condition. Thus, on the rotor surface a suitable value for the magnetic scalar potential, ϕ, is set. This value is given by:

$$\phi = \phi_0 e^{j(\omega t - p\theta - \psi)},\qquad(1)$$

which represents a travelling field (with the fundamental harmonic component only). ϕ_0 is the peak value of the fundamental m.m.f., p is the number of pole pairs, θ is the circumferential displacement and ψ is a phase angle which depends on the load condition and power factor (p.f.). These quantities can be calculated either through a 2D finite-element field solution or by the classical phasor diagram. The latter method was used in this work.

IV. WINDING CURRENT DISTRIBUTION

The attribution of source currents in the end windings is by no means straightforward as is the case in two-dimensional problems, since the shape of the coils is complicated and three-dimensional. An intermediate step is therefore necessary; in this work a current-density field computation has been performed to determine the current density distribution in the stator conductors [5]. The equation of the electric conduction [6],

$$div\,(\sigma\,gradV) = 0,\qquad(2)$$

where V is the electric scalar potential and σ is the conductivity, was solved in the source-current regions. The current density, J, is then calculated by:

$$J = -\sigma \, grad \, V \qquad (3)$$

Fig. 2 shows the current-density vectors in the stator end conductors calculated in this way.
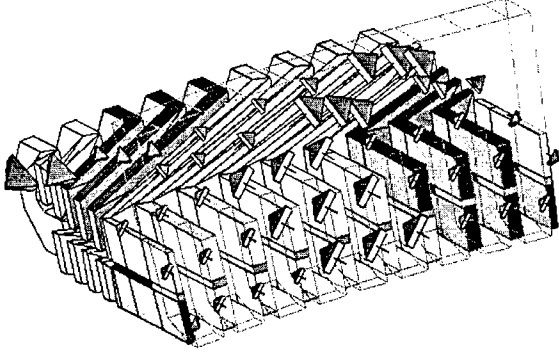
Fig. 2. Vectors of current density calculated by the current field simulation

V. FIELD SOLUTION

The domain was meshed in first-order tetrahedra. The 3D finite-element simulation provides the potential values and hence the magnetic field at every node of the finite-element mesh. Figs. 3 and 4 illustrate the field distribution in the end zone. The arrows represent flux density vectors plotted on the plane indicated.
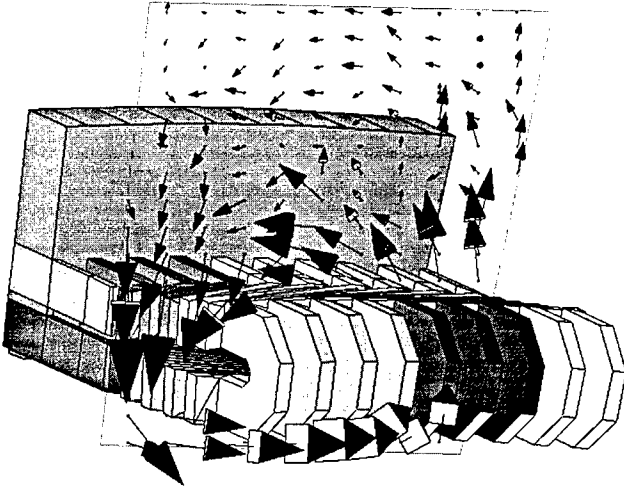
Fig. 3. Flux density vectors in the end zone with stator -winding feeding only

VI. END LEAKAGE INDUCTANCE EVALUATION

The end leakage inductance can be evaluated from the considerations of stored energy [6]:
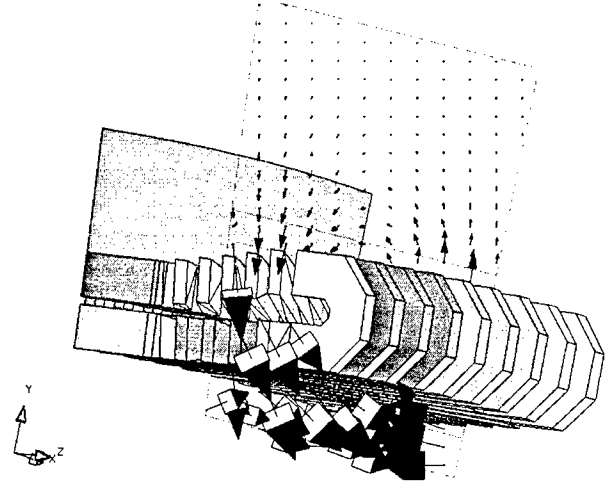
Fig. 4. Flux density vectors in the end zone; full load at 0.95 lagging power factor.

$$L = \frac{1}{I^2} \cdot \iiint_V \left[\vec{A} \cdot \vec{J} \right] dV \qquad (4)$$

From (4), it is only necessary to compute the volume integral of the scalar product of the vector potential and the current density in order to calculate the inductance. The integration must be carried out in the current-carrying regions.

VII. RESULTS FOR THE END INDUCTANCE COMPUTATION

From the discrete values of the potentials, the three-dimensional flux distribution in the end zone of a 300-MVA, 52-pole, three-phase alternator has been found through three different simulations and the leakage reactance is calculated. The results are compared with the value obtained from an empirical method [8]. These results are given in Table I.

TABLE I
NUMERICAL VS EMPIRICAL VALUES OF INDUCTANCE

3D field solution		
Simulation case	Stator boundary condition	Inductance (μH)
1 (magnetodynamic)	Surface Impedance	38.74
2 (magnetodynamic)	Tangential field	38.56
3 (magnetostatic)	Tangential field	39.55
Analytical formula [8]		30.84

It can be noticed that the numerical values correlate well with the value calculated by the established empirical formula, considering the complexity of the phenomenon and the absence of an accurate theoretical expression. Moreover, any effect due to currents induced in conducting parts, such as the core flange and end laminations, seems to be insignificant on the inductance calculation, since these parts are at relatively large distance from the current-carrying conductors in the given example.

VIII. FORCE CALCULATION

The basic formula for calculating the force acting on a current-carrying conductor in a magnetic field has a very simple form in vectorial notation. The force density F (in N/m^3) for the conductor is given by the vector product of the local current density J and the magnetic flux density B:

$$F = J \times B \qquad (5)$$

Figs. 5, 6 and 7 show the force density vectors calculated for one of the conductors at the condition of rated output and 0.95 lagging p.f.
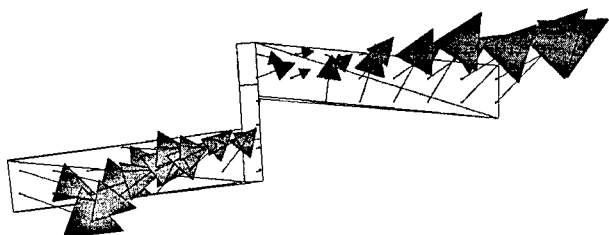
Fig. 5. Force density vectors in one conductor (projection on plane $x0y$).
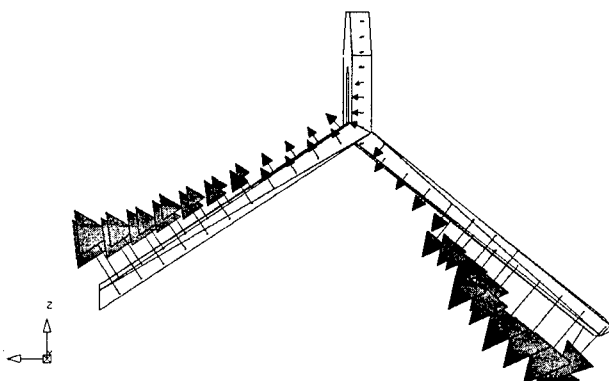
Fig. 6. Force density vectors: plane $x0z$.

IX. COMPARISON OF FORCES FOR DIFFERENT TYPES OF OPERATING CONDITIONS AND STATOR CORE REPRESENTATION

A useful way to present the forces is to calculate the total integrated value of the force over one slot pitch [1]. This is the total force from the core to the end of the end winding and for one slot pitch of circumferential distance. The integration was performed for both inner and outer layers of the end winding. The instant of time represented is that when phase A has the maximum current.
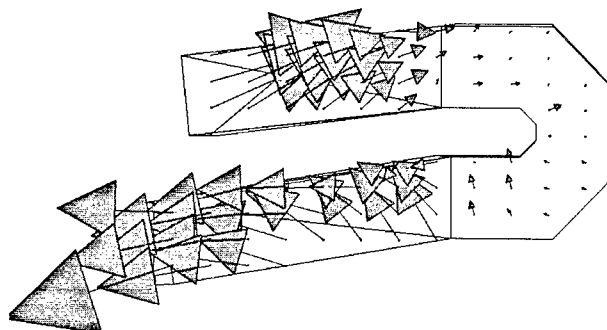
Fig. 7. Force density vectors: plane $y0z$.

Figs. 8(a), (b) and (c) show the total force (radial, peripheral and axial components, respectively) plotted over one pole of the machine, for both inner and outer layers, at rated output and 0.95 lagging p.f.

Figs. 9(a), (b) and (c) present the total force components (for the outer layer only) at three load conditions: steady-state short-circuit, rated output with 0.95 lagging p.f., and 0.95 leading p.f.

Finally, Figs. 10(a) to (c) show the resulting forces in two different situations: (i) considering induced currents in the stator core end laminations by imposing an impedance boundary condition at the stator core end surface, and (ii) neglecting their effects by considering the end surface as one where the field is tangential.

The resulting system of equations had about 80.000 unknowns and the field solution took about six hours on a HP9000 series 700 workstation.

It is not possible to validate the force calculation directly. An indirect verification could be made by measuring the flux densities, but these measurements were not available at the time of producing this work. However, a qualitative check can be made by noticing that, as previously reported [1]-[2], the radial component of the force is the highest one, and the forces at rated output and 0.95 leading p.f. are slightly higher than those at 0.95 lagging p.f. Also, a reversal in the direction of the peripheral force between phase belts can be observed, as illustrated by Fig. 11.

It can be noticed from Figs. 10(a), (b) and (c) that there is virtually no sensible difference in the resulting peripheral and axial forces and little effect in the radial force when changing the stator outer lamination representation from a tangential

93

field to a surface impedance boundary. Thus, the usual assumption of an infinitely permeable surface for the stator core end can be adopted.
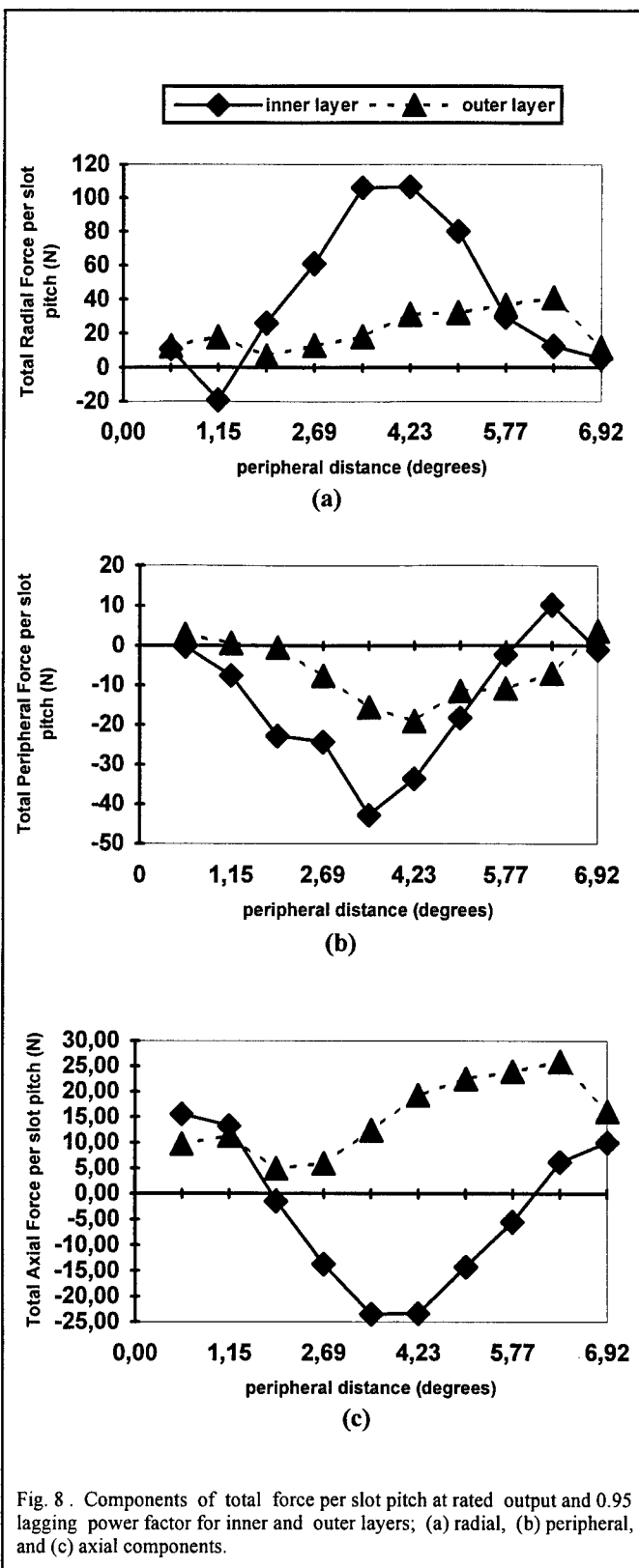
Fig. 8 . Components of total force per slot pitch at rated output and 0.95 lagging power factor for inner and outer layers; (a) radial, (b) peripheral, and (c) axial components.
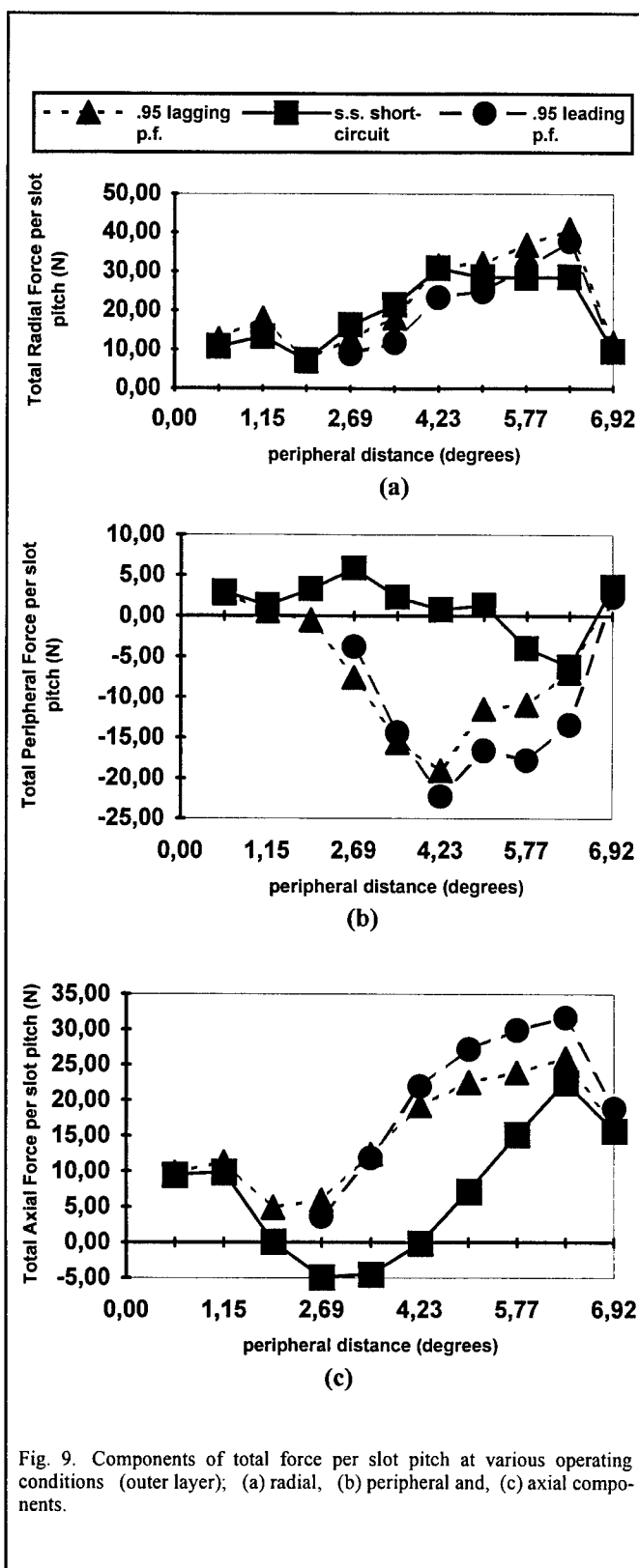
Fig. 9. Components of total force per slot pitch at various operating conditions (outer layer); (a) radial, (b) peripheral and, (c) axial components.
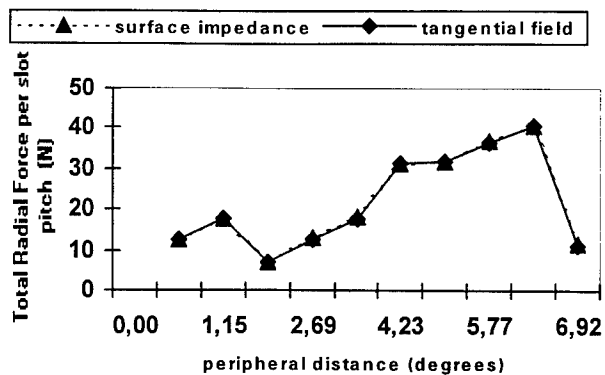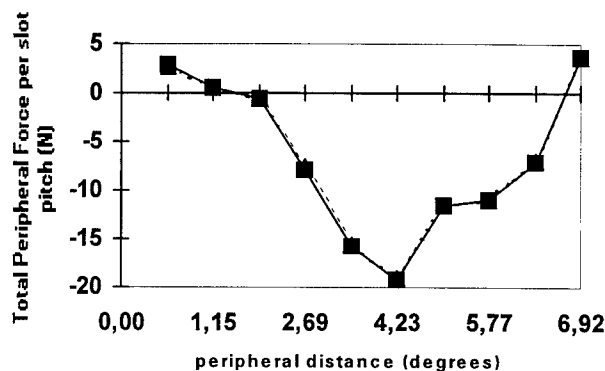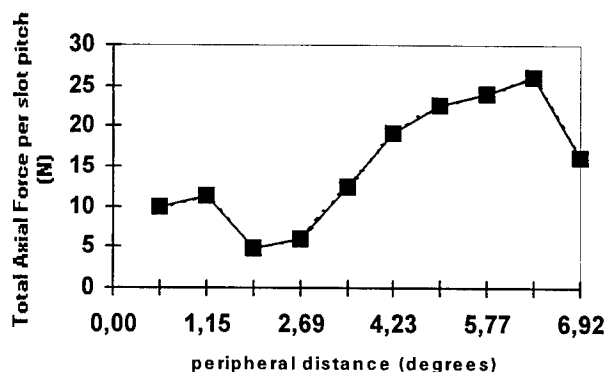
Fig. 10 . Components of total force per slot pitch for distinct stator core end representations; (a) radial, (b) peripheral, and (c) axial components.
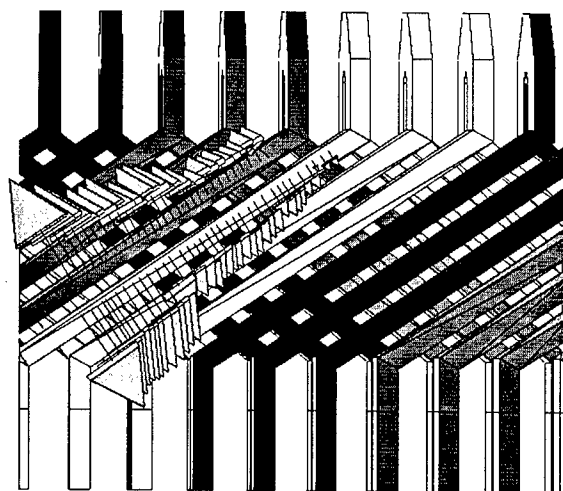
Fig. 11. Force density vectors between phase belts.

X. CONCLUSIONS

A method has been presented to determine the flux distribution in the end region of a large synchronous machine and to calculate the end-winding electromagnetic forces at steady state conditions, as well as to compute the stator end-winding leakage inductance with reasonable accuracy. It uses a fully three-dimensional field solution.

The results for the calculated inductance, when compared with an available empirical formula, present an acceptable correlation. For the forces, the results seem to be also acceptable, when compared with earlier works, albeit no measurements were available for validating this method quantitatively.

The traditional design calculations do not adequately take account of all the complex factors involved in the end region, such as the complex geometry and boundaries, while the approach presented here can handle them properly.

The results show that eddy currents induced in stator end laminations have little effect on the end-winding forces, at least in the example treated here. This may be due to the relatively large distance between these eddy-current surfaces and the source-current regions.

The magnetodynamic simulation, however, cannot be used to predict the forces in transient conditions. In this case, a time-stepped solution associated with an explicit representation of the rotor windings is required. This approach, which obviously requires larger computational resources, is currently under investigation.

95

REFERENCES

[1] D. J. Scott, S. J. Salon, and G. L. Kusic, "Electromagnetic forces on the armature end winding of large turbine generator: I - Steady state conditions", *IEEE Transactions on Power Apparatus and Systems*, vol. PAS-100, n^{Ω} 11, November 1981, pp 4597-4603.

[2] G. K. M. Khan, G. W. Buckley, N. Brooks, Calculation of forces and stresses on generator end windings: Part I - Forces", *IEEE Transactions on Energy Conversion*, vol. 4, n^{Ω} 4, December 1989, pp 661-670.

[3] V.C. Silva, "Etude Tridimensionnelle par Eléments Finis des Effets d'Extrémités dans des Parties Frontales des Machines Synchrones", *PhD Thesis*, INPG - Institut National Polytechnique de Grenoble, December 1994.

[4] O. Biro, K. Preis, "On the use of the magnetic vector potential in the finite element analysis of three-dimensional eddy currents", *IEEE Transactions on Magnetics*, vol. 25, n^{α} 4, July 1989, pp 3145-3159.

[5] A. Taieb Brahimi, A. Foggia, and G. Meunier, "End winding reactance computation using a 3D finite element program", *IEEE Transactions on Magnetics*, vol. 29, n^{Ω} 2, March 1993, pp 1411-1414.

[6] J. L. Coulomb, "Analyse Tridimensionnelle des Champs Electriques et Magnétiques par la Méthode des Eléments Finis", *Thèse de Docteur Es-Sciences Physiques*, INPG - Institut National Polytechnique de Grenoble, June 1981.

[7] T. Bratoljic, "Comparison of two methods for calculating end-winding forces", *SM100 - International Conference on the Evolution and Modern Aspects of Synchronous Machines*, Zurich, Switzerland, 27-29th August 1991, pp 642-647.

[8] V. B. Honsinger, "Theory of End-winding leakage inductance", AIEE Transactions, pp 417-426, August 1959.

96

IMPROVING THE CHARGE SIMULATION METHOD FOR THE COMPUTATION OF HIGH VOLTAGE ELECTRIC FIELDS WITH EFFICIENT LEAST SQUARES TECHNIQUES

J. N. Hoffmann
Companhia Paranaense de Energia
(COPEL) - P.O.Box 318
80.020.000 - Curitiba, PR, Brazil
fax nr. 55-41-331-3115

P. Pulino
Universidade Estadual de Campinas
(UNICAMP) - P.O.Box 6065
13.081.000 - Campinas, SP, Brazil
fax nr. 55-19-239-5808

Abstract : The well known *ChargeSimulation Method*, which is commonly used for electric field calculations, is shown to be a particular and ill-conditioned case of the *Least Squares Charge Simulation Method*. By solving a practical problem, it is shown how to efficiently handle a least squares problem, thus obtaining results of higher precision if compared to the traditional ChargeSimulation Method. For the solution of the resulting linear system, several mathematical methods are analyzed and compared, being stated that the optimum combination of higher precision, lesser error propagation, lesser CPU time and lesser computer RAM are simultaneously reached when applying the *Least Squares Charge Simulation Method*, solved with the *QR decomposition* and *Householder transformations*.

Key words : Electric fields, numerical methods, high voltage engineering, electrical engineering computing, digital simulation, least squares methods.

1. INTRODUCTION

The Carge Simulation Method (CSM) has been very commonly used for electric field computations in the last 20 years. From its introduction by [1], the method was modified with optimization techniques (OCSM) [2], least squares techniques (LSCSM or LSEM) [3], and in combination with other numerical methods (finite elements and finite differences) [4,5]. References [6,7] also present a good overview and some applications of the method.

While the mathematical formulation of the OCSM is somewhat more complicated, the CSM and the LSCSM reduce to few and relatively easy steps:

• Choose arbitrary points over the boundaries where electric potentials are known (vector Φ),

• Choose arbitrary electric charges placed inside the given electrode (vector q),

• Solve the system of linear equations $P q = \Phi$ then obtained,

• Calculate the electric potential ϕ and the electric field vector E where desired, using the solution vector q.

P is a full matrix obtained from known relations between points and charges (the *Maxwell Electric Potential Coefficients* [1]), which depend essentially on geometric data. In the CSM, the number of contour points is equal to the number of simulated charges, while in the LSCSM a lesser number of simulated charges is chosen.

As shown above, the CSM and the LSCSM are simple to apply. In some cases, however, the CSM lead to poor results (see section 2). On the other hand, if the LSCSM is used with the so called *normal equations* (see [3], Appendix 3), it may result in a system of linear equations with a *condition number* (see Appendix V) many times higher that the CSM itself. In this case the increased error propagation may also lead to poor results.

Considering these points, the present work is intended to show how to deal with these methods in a more efficient way. The result is that the LSCSM, if properly applied, presents incontestable advantages over the traditional CSM.

Section 3 is devoted to a detailed error analysis, stating the optimum relation *number of charges / number of contour points*. Section 4 deals with the problem from the condition number point of view. Section 5 presents the *QR Decomposition* and the *Singular Value Decomposition* methods for the solution of the LSCSM, allowing the resulting linear system a condition number many times smaller than the CSM or than the LSCSM with normal equations. In addition, nine different mathematical methods are analysed and compared for the solution of the problem. Appendices I and V include the mathematical background necessary for a full understanding of the problem.

Based in the results obtained with the new proposed formulation for the LSCSM, it can be concluded that, with an adequate relation number of charges / number of contour points, and with an adequate mathematical and computational treatment, the LSCSM results remarkably more efficient that the CSM. As a matter of fact, the LSCSM constitutes the generalization for the methods of simulated charges, where the traditional CSM is a particular and ill-conditioned case.

2. APPLICATION

Consider the three-dimensional axi-symmetric problem of Figure 1, to be solved with the CSM and the LSCSM. The same problem was also solved by [6], using the CSM only. Note that problem 2 is similar to problem 1, except that it includes different electrical permittivities. The simulated (ring) charges and contour points were considered as shown in Table I.

TABLE 1 – NUMBER OF CHARGES AND CONTOUR POINTS						
	Problem 1			Problem 2		
	contour points	charges		contour points	charges	
		CSM	LSCSM		CSM	LSCSM
Electrode	66	66	27	66	66	27
Enclosure	12	12	04	12	12	04
In dielectric, near air	–	–	–	16	16	06
In air, near dielectric	–	–	–		16	06
T o t a l	88	88	31	104	120	43
Order of the linear system	CSM – 88x88 LSCSM – 88x31			CSM – 120x120 LSCSM – 120x 43		

A detailed formulation of the CSM equations for problems 1 and 2 is found in [6]. For both cases, a systems of m linear equations and n = m unknown electric charges is obtained, which can be written as
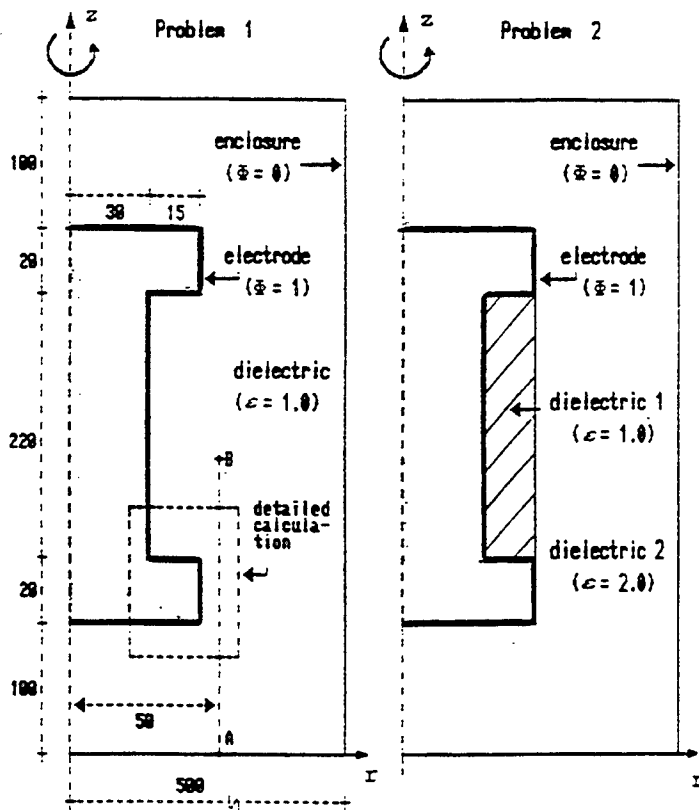
Figure 1 - Three-dimensional axi-symmetric application

Figure 2 - Equipotential lines for problem 1

$$P q = \phi, \qquad (1)$$

where

P is a full square matrix of order n x n,

q is a vector of order n, with the values of simulated
charges which represent the physical problem,

ϕ is a vector with the given electric potentials.

The same procedure is applicable to the LSCSM, except
that a smaller number of simulated charges is chosen,
resulting in a system of linear equations with m equations
and n unknown electric charges (m > n). This system can also
be written in the condensed form (1), where P is now a
rectangular matrix, of order m x n.

A comparison of various methods for the computation of q
is found in section 5. Once q is obtained, the electric
potential ϕ and the electric field E can be computed at
every desired point P, by means of

$$\phi(P) = \sum_{j=1}^{n} p_{ij} \, q_j \qquad (2)$$

$$E(P) = \sum_{j=1}^{n} (f_{ij}^{r} \, a_r + f_{ij}^{z} \, a_z) \, q_j \qquad (3)$$

where

p_{ij} and f_{ij} are Maxwell coefficients (see [1,6]),
q_j are the simulated charges obtained from q, and
a_r and a_z are unit vectors for directions r and z .

An exact solution would give the equipotential line of
ϕ = 1.0 for all P located on the electrode boundary.
However, due to the finite discretization of charges and
contour points, the CSM and the LSCSM give an equipotential
line which deviates somewhat from the electrode boundary, as
shown by Figure 2.

It is clearly shown in this figure the surprising fact
that a reduction in the number of simulated charges gives

better results, since the respective equipotential line of
ϕ = 1.0 clearly fits better to the electrode contour. The
error of each method is quantified in section 3.

In Figure 3, the electric potentials and electric field
as computed by [6] for gap A-B of Figure 1 are reproduced
and compared to the values computed with the LSCSM with data
taken from Table 1. Note that the previous unstable zone
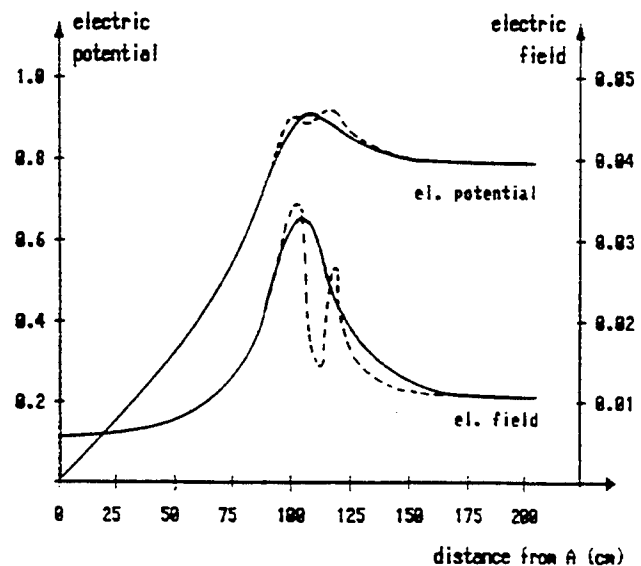
___ LSCSM with 88 contour points   ... CSM, according to [6], with
and 31 simulated ring charges   77 contour points and 77 ring,
                                     point and line charges

Figure 3 - Field calculation with CSM and LSCSM for gap AB

98

generated by the CSM (strong oscillations) is not present in the computation with the LSCSM. Furthermore, in [6] matrix P required the calculation of 77 x 77 = 5929 Maxwell coefficients, while the LSCSM used here required 88 x 31 = 2728, what means considerable reduction in CPU time, as well as in required computer RAM.

It can be concluded that the CSM is more unstable and gives poorer results if compared to the LSCSM, particularly close to the boundaries. This is due to the fact that matrix P, having logarithm terms or similar, is close to a singular (non invertible) matrix and therefore, *ill-conditioned* (see Appendix V) .

3. ERROR ANALYSIS

The conclusions of section 2 can be quantified by plotting the cumulative error of the electric potentials computed along the electrode boundary for several relations n/m, as shown in Figure 4. For instance, if we take the LSCSM with n/m = 0.90, the electric potentials computed along the electrode boundary (where the exact solution is ϕ = 1.0) have an error greater than 1 % for 50 % of the electrode contour length.
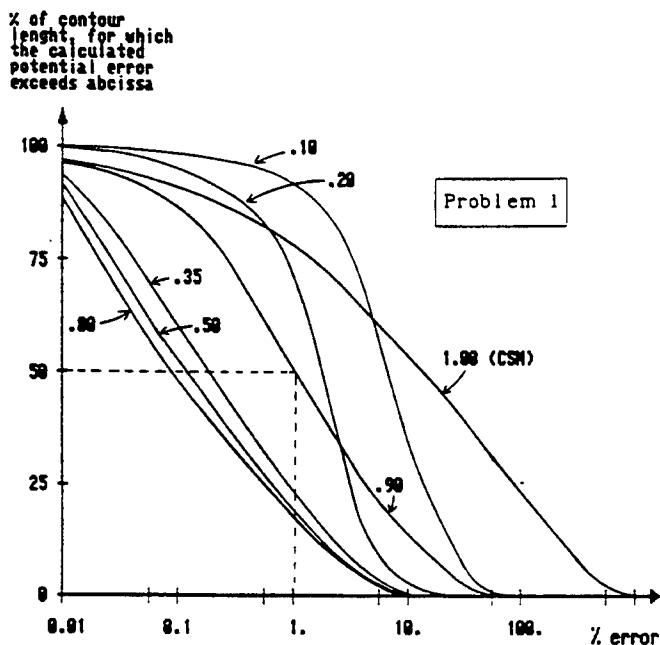
Figure 4 - Cumulative error for several relations n/m
(nr. of charges / nr. of contour points)

Figure 4 allows some important conclusions:

a) The cumulative error increases for relations n/m close to 1.0. This is due to the fact that P tends to be ill-conditioned (see section 4) and therefore, close to a singular matrix. This also affects the norm of the vector of simulated charges q, as shown by Figure 5. Note that n/m = 1.0 is the particular case that represents the CSM .

b) For the lower relations n/m, the number of simulated charges tends to be insufficient to represent the physical problem, leading to a significant residual vector r = P q - Φ , as shown by Figure 5. Therefore, the cumulative error also increases.

c) The optimum range of the relation n/m is from 0.35 to 0.80 .
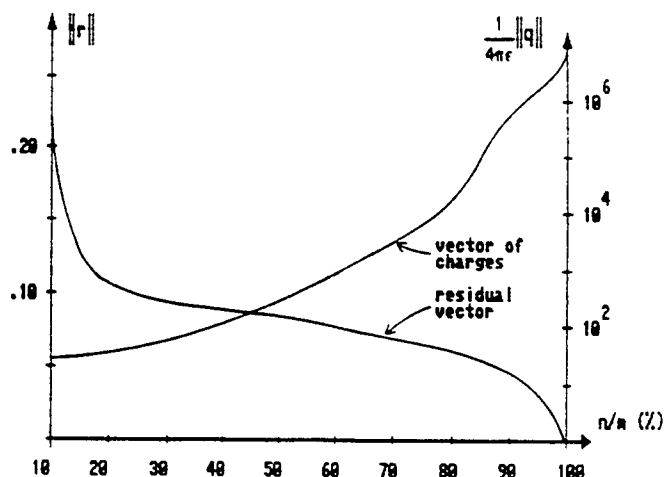
Figure 5 - $\|r\|$ and $\|q\|$ for problem 1, as funtion of n/m

4. CONDITION NUMBER ANALYSIS

The condition number of the linear system (1) depends on the relation n/m . Figure 6 shows the behavior of this parameter, which can be computed with the SVD method (see Appendix III.3) .

It is clear from Figure 6 that the method used for the solution of the LSCSM equations is of primal importance. The LSCSM equations solved by the method proposed in [3] (normal equations) may generate a matrix P with a condition number greater than the CSM itself, what may lead to severe error propagations during the computations.

On the other hand, the LSCSM equations solved by the QR decomposition (Appendix III.2) or the SVD (Appendix III.3) always result in a condition number for P which is lower than the condition number computed for the CSM and for the LSCSM with normal equations. Therefore, as far as the condition number is concerned, the QR decomposition and the SVD methods are more effective.
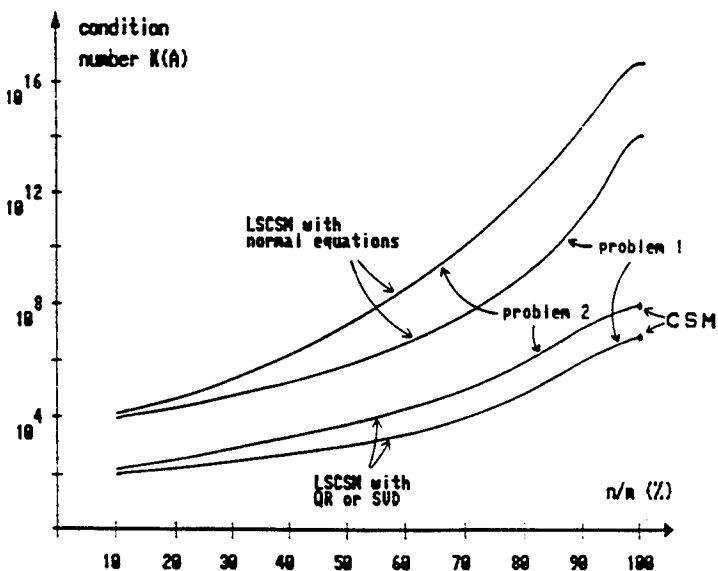
Figure 6 - Condition number as a function of n/m

5. METHODS FOR THE SOLUTION OF THE RESULTING LINEAR SYSTEM

It can be concluded from above sections that the LSCSM, with an adequate choice for the relation n/m, gives results of higher precision than the straight CSM. It was also shown that under the condition number point of view, the QR decomposition and the SVD methods are prefered to the method of normal equations used so far. .

In this section the problem is analyzed as function of the CPU time and the required computer RAM, including a good number of mathematical methods for the computation of the vector of charges q .

Note that the CPU computer time is also a good indication of the number of arithmetic operations taken by the computer. Thus, the bigger is the required CPU computer time the bigger is the possibility of a significant error propagation.

Table 2 shows the CPU time required by an IBM 3090-300S computer for the solution of problems 1 and 2, taken in percentile rates of the time required for the CSM.

TABLE 2 - COMPARISON OF VARIOUS METHODS						
Method of calculation			Condition number	Approx. RAM	CPU time(%)	
					Prob. 1	Prob. 2
CSM	LU		$K(P)$ $\cong 10^8$	$m \times m$	100	100
LSCSM (with n/m $\cong$ 0.35)	Normal Equations	CG	$K(P^t P)$ $\cong 10^6$	$m \times n$	91	66
		CGS			172	188
		CD			37	35
		LU			39	36
	QR	CLG	$K(P)$ $\cong 10^3$	$m \times n + \frac{n(n+1)}{2}$	42	38
		MOG			40	39
		GR		$m \times n$	40	37
		HD			37	33
	SVD			$m \times n + n^2$	57	66

Code	Description	Appendix
CSM	Charge Simulation method	–
LSCSM	Least Squares Charge Simulation Method	–
QR	QR decomposition	III.2
SVD	Singular Value decomposition	III.3
CG	Conjugate Gradients	IV.1.1
CGS	Conjugate Gradients Squared	IV.1.2
CD	Cholesky decomposition	IV.1.3
LU	LU (Gauss pivoting)decomposition	IV.1.4
CLG	Classical Gram-Schmidt	IV.2.1
MOG	Modified Gram-Schmidt	IV.2.2
GR	Givens rotations	IV.2.3
HD	Householder transformations	IV.2.4

From Table 2 it can be concluded that

a) The LSCSM solved with the QR decomposition and Householder transformations presented the best performance, since it requires lesser CPU computer time and lesser RAM .

b) The CGS method, which showed an excellent performance in problems with sparse matrices as reported by [5], did not show a good performance here with a full matrix .

c) All methods for the solution of the LSCSM with normal equations (i.e. CG, CGS, CD and LU) require special computational considerations in order to avoid additional RAM required for the storage of matrix $P^t P$.

6. CONCLUSIONS

The traditional Charge Simulation Method was shown to be a particular and ill-conditioned case of the Least Squares Charge Simulation Method, which is the generalization.

The best relation number of charges / number of contour points (n/m) lies in the range 0.35 < n/m < 0.80 , where the LSCSM results remarkably more precise than the straight CSM, specially close to the boundaries of the problem.

The LSCSM computed with the QR decomposition generates a system of linear equations with a condition number significantly lower than the LSCSM with normal equations as used so far, thus reducing error propagation during the computations.

The optimum combination of *higher precision, lesser error propagation, lesser CPU computer time* and *lesser computer RAM* are simultaneously reached when applying the Least Squares Carge Simulation Method, solved with the QR decomposition and Householder transformations.

APPENDIX I

Mathematical background ([8,9,10,11,12])

Let $A = [a_{ij}]$ denote a real matrix of order $m \times n$ $(m \geq n)$ with elements a_{ij}, and $x = [x_1, x_2, ..., x_n]^t$ denote a real column vector of order n with elements x_i .

The *transpose* of A is A^t, where $A^t = [a_{ji}]$. A is *symmetric* if $A^t = A$. If m=n, the *inverse* of A is denoted by A^{-1}, with $A^{-1}A = I$ (unit matrix).

The *Euclidean norm* of vector x is $\|x\| = (\sum x_i^2)^{1/2}$. Another usual vector norm is the *infinite norm* defined as $\|x\|_\infty = \max |x_i|$. A norm for matrix A can be defined as $\|A\| = \max \|Ax\|/\|x\|$, for all $x \neq 0$.

The n column vectors a_i from A, of order m, is said to be *linearly independent* if $\sum \alpha_i a_i = 0$ is satisfied only for $\alpha_i=0$. In this case, A is said to be of *rank* n. A is invertible if rank(A) = m = n .

If $x^t A x > 0$ for all vector $x \neq 0$, A is said to be *positive definite*. If rank(A) = n, $A^t A$ is symmetric and positive definite.

If $A^t A = I$, A is said to be *orthogonal* and in this case, $\|A\| = 1$. A is a *lower triangular* matrix if $a_{ij} = 0$ for all j>i, *upper triangular* if $a_{ij} = 0$ for all i>j, and *diagonal* if $a_{ij} = 0$ for all $i \neq j$.

The *inner product* of two vectors x and y is a real number denoted by $\langle x, y \rangle = \sum x_i y_i$.

APPENDIX II

Matrix decompositions

LU decomposition: If rank(A) = m = n, then only one decomposition A = LU exists, where U is upper triangular and L is lower triangular, with unit diagonal ([8,9,10]).

QR decomposition: If rank(A) = n, then only one decomposition A = QR exists, where R is upper triangular of order n×n and Q is orthogonal of order m×n ([8,9,12]).

Singular Value decomposition (SVD): A can be written as $A = U S V^t$, where U is orthogonal of order m×n, V is orthogonal of order n×n and S is diagonal of order n×n, whose diagonal elements $\sigma_1 \geq \sigma_2 \geq ... \geq \sigma_N \geq 0$ are known as the *singular values* of A ([8,9,11,12]).

Cholesky decomposition: If A is symmetric and positive definite, then only one decomposition $A = R^t R$ exists, where R is upper triangular with positive elements in the main diagonal ([8,10,12]).

APPENDIX III

Overdetermined linear systems

Let $A x = b$ be a linear system of m equations and n unknown values, so that $m > n$. This system of equations is said to be *overdetermined*, and usually have no exact solution. Let $r = b - A x$ be the *residual vector*.

It is reasonable to search for an approximate solution to this linear system, giving the lowest possible residual vector. Usually a *least squares* method is considered, which consists in determining the unique vector x which gives the lowest Euclidean norm for the residual vector (minimum $\|r\|$). A brief description of the most common methods follows.

III.1 Method of the normal equations

It is shown by [8,9,12] that vector x, solution for the least squares problem, is also the solution of the linear system

$$A^t A \ x \ = \ A^t b \qquad (4)$$

of order $n \times n$, also known as a system of *normal equations*.

Since $A^t A$ is symmetric and positive definite, some mathematical procedures are applicable (see Appendix IV.1) for the solution of (4). On the other hand, the condition number of the resulting linear system is affected since $K(A^t A) = K(A)^2$, which may compromise the solution due to increase of error propagations.

III.2 Method of the QR decomposition

It is shown by [8,9,12] that vector x, solution for the least squares problem, is also the solution of

$$R \ x \ = \ Q^t b \qquad (5)$$

where $QR = A$. This linear system of order $n \times n$ is easily solved by back-substitution since R is upper triangular. Therefore, the main computational effort is the determination of the QR decomposition of A (Appendix IV.2).

III.3 Method of the Singular Value decomposition

It is shown by [8,9,11,12] that vector x, solution for the least squares problem, is given by

$$x \ = \ V \ S^{-1} \ U^t \ b \qquad (6)$$

where $U S V^t = A$ is the Singular Value decomposition of A. Since S is a diagonal matrix, S^{-1} is easily obtained and then expression (6) reduces to simple matrix-vector produts. As in section III.2, the main computational effort is the determination the Singular Value decomposition of A (Appendix IV.3).

APPENDIX IV

Mathematical methods for least squares problems

IV.1 Methods for the solution of the normal equations (equation 4)

The *conjugate gradients* (CG), the *conjugate gradients squared* (CGS), the *Cholesky decomposition* (CD) and *Gauss pivoting* (LU decomposition) methods are analyzed in the following sections.

IV.1.1 Conjugate gradients (CG)

The CG method is only applicable to symmetric and positive definite linear systems, as (4). The algorithm is demonstrated by [8]. The matrix product $A^t A$ is avoided using the property of inner products $\langle A^t A x, y \rangle = \langle A x, A y \rangle$, which is easily demonstrated. The resulting algorithm for the solution of (4) is

$$
\begin{aligned}
&x_0 = 0 \\
&r_0 = A^t b \\
&\text{For } k = 1...n \\
&\qquad \text{if } r_{k-1} = 0 \quad\quad \text{then} \\
&\qquad\qquad \text{Set } x = x_{k-1} \text{ and quit} \\
&\qquad\qquad\qquad\qquad\qquad \text{else} \\
&\qquad\qquad \beta_k = \langle r_{k-1}, r_{k-1} \rangle / \langle r_{k-2}, r_{k-2} \rangle \quad (\beta_1 = 0) \\
&\qquad\qquad p_k = r_{k-1} + \beta_k \, p_{k-1} \quad\quad\quad (p_1 \equiv r_0) \\
&\qquad\qquad \alpha_k = \langle r_{k-1}, r_{k-1} \rangle / \langle A \, p_k, A \, p_k \rangle \\
&\qquad\qquad x_k = x_{k-1} + \alpha_k \, p_k \\
&\qquad\qquad r_k = A^t (b - A \, x_k) \\
&x = x_n
\end{aligned}
$$

IV.1.2 Conjugate gradients squared (CGS)

The CGS doesn't require A to be symmetric and positive definite, unlike the CG method. It is included here due to the good results obtained with sparse matrix as reported by [5,13]. The final algorithm [13] for the solution of (4) is

$$
\begin{aligned}
&\text{estimate } x_0 \\
&r_0 = A^t (b - A x_0) \\
&q_0 = p_{-1} = 0 \ ; \ \rho_{-1} = 1 \ ; \ n = 0 \\
&\text{while } r_n > \text{tolerance} \quad \text{do} \\
&\qquad \rho_n = \langle r_0, r_n \rangle \ ; \ \beta_n = \rho_n / \rho_{n-1} \\
&\qquad u_n = r_n + \beta_n \, q_n \\
&\qquad p_n = u_n + \beta_n \, (q_n + \beta_n \, p_{n-1}) \\
&\qquad v_n = A^t (A p_n) \\
&\qquad \sigma_n = \langle r_0, v_n \rangle \ ; \ \alpha_n = \rho_n / \sigma_n \\
&\qquad q_{n+1} = u_n - \alpha_n \, v_n \\
&\qquad x_{n+1} = x_n + \alpha_n \, (u_n + q_{n+1}) \\
&\qquad r_{n+1} = A^t (b - A \, x_{n+1}) \ ; \ n=n+1 \\
&\text{end}
\end{aligned}
$$

IV.1.3 Cholesky decomposition (CD)

Since $A^t A$ of (4) is symmetric and positive definite, it is possible to use the Cholesky decomposition $A^t A = R^t R$ (where R is upper triangular). Therefore, equation (4) becomes $R^t R \ x = A^t b$. The later is easily solved with an auxiliary vector y, according to the sequence

$R^t \ y \ = \ A^t \ b$ (y is obtained by forward substitution)
$R \ x \ = \ y$ (x is obtained by back substitution)

Note that the matrix product $A^t A$ needs to be computed before R. The elements r_{ij} of R are computed from the elements of matrix $A^t A = \mathbb{A} = [\mathbb{A}_{ij}]$, with the algorithm ([12])

$$
\begin{aligned}
&\text{For } j = 1...n \\
&\qquad \text{For } k = 1...j-1 \\
&\qquad\qquad r_{kj} = \left[\mathbb{A}_{kj} - \sum_{i=1}^{k-1} r_{ik} \, r_{ij} \right] / r_{kk} \\
&\qquad \text{end} \\
&\qquad r_{jj} = \left[\mathbb{A}_{jj} - \sum_{k=1}^{j-1} |r_{ij}|^2 \right]^{1/2} \\
&\text{end}
\end{aligned}
$$

IV.1.4 Gauss pivoting (LU decomposition)

The well known method of Gauss pivoting [8,9,10,11,12] can be used for the computation of the decomposition $A^t A = LU$ (Appendix II). Thus, equation (4) becomes $L U x = A^t b$, which is easily solved with an auxiliary vector y, according to the sequence

$L \ y = A^t \ b$ (y is obtained by forward substitution)
$U \ x = y$ (x is obtained by back substitution)

As in section IV.1.3, the matrix product $A^t A$ is computed before the LU decomposition .

101

IV.2 Methods for the QR decomposition (for equation 5)

The *Classical Gram-Schmidt, Modified Gram-Schmidt, Givens rotations* and *Householder transformations* methods are briefly described in the following.

IV.2.1 Classical Gram-Schmidt (CLG)

In this method, Matrices Q and R are sequentially computed column by column. The algorithm and detailed mathematical description are found in [8,9,12]. Once A is overwritten by Q, an additional space of dimension $n(n+1)/2$ is necessary for the storage of R.

IV.2.2 Modified Gram-Schmidt (MOG)

This is a slight modification to the CLG method, leading to a better numerical performance. Q is computed column by column, and R is computed line by line. Other comments as for CLG. See [8,9,12] for algorithm and details.

IV.2.3 Givens rotations (GR)

Algorithm and mathematical description are found in [8]. A is overwritten by R, and the product $Q^t b$ (necessary for equation 5) is computed while computing R, thus not requiring additional RAM for R as the CLG or MOG methods.

IV.2.4 Householder transformations (HT)

A matrix H of order nxn, defined as

$$H = I - 2 \, vv^t / \langle v, v \rangle$$

is said to be a *Householder transformation* (also known as *Householder matrix* or *Householder reflection*), where v is a vector of dimension n. It can be shown that H is an orthogonal matrix [8].

In this method, an adequate H_1 is chosen so that the product $H_1 A$ results in a matrix with null elements below the main diagonal of A at a given column. By a chain repetition of this product we get the matrix $R = H_n...H_2 H_1 A = Q^t A$. Algorithm and mathematical details are found in [8,12].

As in the GR method, A is overwritten by R, and the product $Q^t b$ (necessary for equation 5) is computed sequentially while computing R. Therefore, no additional RAM is necessary for R

IV.2 Methods for the Singular Value decomposition (for equation 6)

As shown in section III.3, the solution for a least squares problem by the SVD reduces to a sequence of matrix-vector products, i.e.

$$\text{make} \quad y = U^t b \, ,$$
$$\text{then} \quad z = S^{-1} y \, ,$$
$$\text{and} \quad x = V z \, .$$

Note that S is a diagonal matrix, so S^{-1} is promptly obtained.

The theoretical basis for the computation of the SVD is somewhat complicated and will not be discussed here (see [12] for instance, which uses basically Householder transformations).

Once A is overwritten by U, it is required an additional space of order nxn for the storage of matrix V. The diagonal matrix S obviously requires only a vector of dimension n for the storage of the non zero values (the *singular values* σ_i) of the main diagonal.

APPENDIX V

Condition number of a linear system

Let $Ax = b$ be a system of linear equations of order mxn so that $m \geq n$. It is important to know how much small perturbations in the elements of A or b affect the solution vector x. This can be evaluated from the *condition number of* A, written as K(A). If K(A) is large, small perturbations in A or b may cause significant perturbations in the solution vector x. In this case, A is said to be *ill-conditioned*.

The condition number is greater or equal to 1. It also indicates how much A is close to a non invertible matrix [see 9]. Therefore, it is desirable that K(A) be as low as possible.

If m=n, it is possible to show (see [8,9,11]) that $K(A) = \|A\| \cdot \|A^{-1}\|$. In general, if rank(A) = κ, we use the SVD of A (see Appendix II) to obtain $K(A) = \sigma_1/\sigma_\kappa$. The condition number defined in this way is known as the *spectral* condition number. Another important result is $K(A^t A) = K(A)^2$.

REFERENCES

[1] H. Singer, H. Steinbigler, P. Weiß, "A charge simulation method for high voltage fields," IEEE Transactions on Power Apparatus and Systems, Vol. 93 pp. 1660-1668, 1974

[2] Y. L. Chow, C. Charalambous, "Static-field computations by the method of optimized simulated charges," IEE Proceedings, Vol. 126, n• 1, pp 123-125, January 1979

[3] H. Anis, A. Zeitoun, M. El-Ragheb and M. El-Desouki, "Field calculations around non standard electrodes using regression and their spherical equivalence", IEEE transactions on Power Apparatus and Systems, Vol. 96, pp. 1721-1730, 1977

[4] H. Steinbigler, "Combined application of finite element method and charge simulation method for the computation of electric fields," 3rd International Symposium on High Voltage Engineering, section 11-11, August 1979

[5] J. N. Hoffmann and P. Pulino, "New developments on the combined application of charge simulation and numerical methods for the computation of electric fields", IEEE Summer Meeting, 1994

[6] M. D. R. Beasley et al, "Comparative study of three methods for computing electric fields", IEE Proceedings. Vol. 126, n• 1, pp 126-134, January 1979

[7] N. H. Malik, "A review of the charge simulation method and its applications", IEEE transactions on Electrical Insulation, Vol. 24, pp. 3-20, February 1989

[8] G. H. Golub and C. F. Van Loan, Matrix computations, Baltimore, The John Hopkins University Press, 1985

[9] B. Noble and J. Daniel , Applied Linear Algebra, New Jersey, Prentice Hall, 1977

[10] G. E. Forsythe and C. B. Moler, Computer Solution of Linear Algebraic Systems, New Jersey, Prentice Hall, 1967

[11] G. E. Forsythe, M. A. Malcolm and C. B. Moler, Computer Methods for Mathematical Computations, New Jersey, Prentice Hall, 1977

[12] J. J. Dongarra et al, Linpack User's Guide, Philadelphia, Society for Industrial and Applied Mathematics, 1979

[13] P. Sonneweld, "CGS, a fast Lanczos-type solver for non symmetric linear systems," Siam J. Sci. Stat. Comput., Vol. 10, n• 1, pp 36-52, January 1989

BIOGRAPHIES

João Nelson Hoffmann was born in Lapa, state of Paraná, Brazil, on April 22, 1958. He received the B.S. degree in Electrical Engineering in 1981 and the M.S. degree in Applied and Computational Mathematics in 1993. Since 1988 he is with Companhia Paranaense de Energia (COPEL), Curitiba, Paraná, Brazil, working with high voltage transmission line researches.

Petronio Pulino was born in Bebedouro, state of São Paulo, Brazil, on October 14, 1956. He received the B.S. degree in Mathematics, the M.S. degree in Applied Mathematics and the Ph.D. degree in Electrical Engineering from University of Campinas (UNICAMP). Presently he is an assistant professor at the Department of Applied Mathematics of UNICAMP.

A HYBRID FINITE DIFFERENCES & CHARGE SIMULATION METHOD
FOR THE COMPUTATION OF HIGH VOLTAGE ELECTRIC FIELDS

J. N. Hoffmann
Companhia Paranaense de Energia
(COPEL) - P.O.Box 318
80.020.000 - Curitiba, PR, Brazil
fax nr. 55-41-331-3115

P. Pulino
Universidade Estadual de Campinas
(UNICAMP) - P.O.Box 6065
13.081.000 - Campinas, SP, Brazil
fax nr. 55-19-239-5808

Abstract : A new treatment is proposed to the hybrid method of Finite Differences and Charge Simulation for the computation os electric fields, entirely applicable to the similar hybrid method of Finite Element and Charge Simulation. The resulting system of linear equations is solved by using the fixed point theory, the QR decomposition and the Conjugate Gradients Squared method with a preconditioning technique. New procedures are suggested for the discretization of the boundary conditions, which lead to results with higher precision. Case studies are included.

Key words : Electric fields, numerical methods, high voltage engineering, electrical engineering computing, digital simulation.

1. INTRODUCTION

The Finite Difference Method (FDM), the Finite Element Method (FEM) and the Charge Simulation Method (CSM) are very commonly used for field analysis of high voltage insulation systems. The CSM is suitable for unbounded problems, but becomes complicated for problems including dielectrics. On the other hand, the FDM and FEM are suitable for multi-dielectric cases, but require truncation of the domain for unbounded problems. Thus, a hybrid method may be a promising tool for unbounded problems including dielectrics, where the FDM or the FEM is applied inside a limited arbitrary region, and the CSM is applied to the unbounded exterior. Along the coupling surface continuity conditions are imposed.

Early research work [1,2,3] presented practical examples of this hybrid method, pointing out its advantages and disadvantages. Either the hybrid FDM & CSM or the FEM & CSM require the solution of a system of linear equations, whose matrix of coefficients (square in principle) is composed by full submatrices (resulting from the CSM) and sparse submatrices (resulting from the FDM or FEM). The present work deals with the formulation of adequate procedures for the solution of this linear system, which results in a significant smaller computer storage, smaller CPU computer time and results with higher precision if compared to [1,2,3]. In addition, the convergence of the proposed iterative method is not dependent on the arbitrary initial conditions as [1] does.

The application of the CSM to the unlimited exterior region as it was previously considered by [1,2,3], leads to full square submatrices and demands an excessive amount of computer memory. It is shown in section 3 that it is possible to significantly reduce the required computer memory, by choosing a number of simulated charges which is smaller than the number of contour points. This leads to a least squares problem, which is solved by means of the QR decomposition [4,5] of the resulting full rectangular submatrix, using the Modified Gram-Schmidt method. This procedure only demands from 30% to 50% of the computer memory initially required by the original problem, without loss of precision.

The application of the FDM or the FEM to the limited region leads to a sparse linear system of the $A x = b$ type. It is possible to use the Conjugate Gradients method (CG) [4], a Krylov Subspace method (KS) [6] or the Conjugate Gradients Squared method (CGS) [7] for the solution of this linear system. These methods have advantages over the traditional Gauss-Seidel, SOR and others (used by [1,2,3]), since they reach the exact solution in a number of steps at most equal to the matrix dimension. The CGS with a preconditioning technique is suggested for the solution of the problem, since it demands less CPU computer time and less computer memory than other methods (see section 4).

The hybrid method requires a discretization for the normal component of the electric flux density vector $\mathbf{D}$ (i. e. $\mathbf{n \cdot D}$) all over the arbitrary rectangular surface of discontinuity on the electrical permittivity ε (coupling boundary). This leads to a discretization of the normal derivative of the scalar electric potential function (since $\mathbf{D} = - \varepsilon \nabla \Phi$). The error of such discretization as computed by [1,2,3] for rectangular surfaces is of the order of h (i.e. O(h)), where h is the grid step (distance between two consecutive nodes). It is shown (section 5.1) by the use of the Taylor series expansion, that it is possible to obtain a simple discretization with an error of O(h^2). A discretization for curvilinear surfaces is also presented (section 5.2), being of interest when a discontinuity on ε exists. These methodologies for the discretization of $\mathbf{n \cdot \nabla \Phi}$ lead to results of higher precision if compared to those used by [1,2,3].

Finally, adequate procedures for the solution of the combined system of linear equations that results from the hybrid method are stated. A direct solution is not recommended due to the irregular structure of the coefficient matrix. Reference [1] proposes an iterative scheme which depends on a good initial estimate. In addition, it may not reach the solution for certain cases. The approach used here (section 6) is based on the fixed point theory of linear systems [4,5]. The utilization of an arbitrary but rather predictable parameter (θ) leads to convergence in a significantly greater class of problems (if not all), not depending on the initial estimates for the electric potentials. Some examples are included and the results are analysed (section 7).

Figure 1. General problem treated with the FDM & CSM

Considering the points above, it is supposed that the present work may represent a new motivation for the utilization of the hybrid FDM & CSM or FEM & CSM on the computation of two-dimensional or three-dimensional with axial symmetry electric fields, as frequently found in high voltage engineering.

2. DEFINITION OF THE COMBINED SYSTEM OF LINEAR EQUATIONS

The hybrid FDM & CSM applied to the general two-dimensional problem of Figure 1 will be considered in the following sections.

Suppose that it is needed to calculate the electric potential distribution near electrode A, sorrounded by a region (Ω_2) with electrical permittivity ε_2. An arbitrary rectangular boundary $\partial\Omega_1$ involving A and Ω_2 is defined, inside which a finite difference grid with M nodes is placed. This also will define N nodes on $\partial\Omega_1$ and W nodes on $\partial\Omega_2$. A discretization with V contour points is made on the boundary $\partial\Omega_B$ of the external electrode B, and K+L charges are simulated as indicated in Figure 1.

It was already shown by [1,2,3] that, for two-dimensional or three-dimensional problems with axial symmetry, the application of the FDM & CSM (or the FEM & CSM) to Figure 1 leads to a system of linear equations, which is represented here by the following equivalent system with submatrices :

$$\begin{bmatrix} P_1 & -I & 0 \\ P_2 & 0 & 0 \\ F & S_0 & S_1 \\ 0 & S_2 & D \end{bmatrix} \begin{bmatrix} q \\ \Phi_1 \\ \Phi_0 \end{bmatrix} = \begin{bmatrix} 0 \\ \Phi_B \\ 0 \\ c \end{bmatrix} \qquad (1)$$

where

a) The matriz equations $P_1 \, q - I \, \Phi_1 = 0$ and $P_2 \, q = \Phi_B$ result from the CSM, and

P_1 = full matrix, dimension N x (K+L)
P_2 = full matrix, dimension V x (K+L)
I = Identity matrix, dimension N x N
q = vector of simulated charges, dimension K+L
Φ_1 = vector of electric potentials on $\partial\Omega_1$, dimension N
Φ_B = vector of electric potentials on $\partial\Omega_B$, dimension V
P_1 and P_2 are the Maxwell electric potential coefficient matrices

b) The matrix equation $F \, q + S_0 \, \Phi_1 + S_1 \, \Phi_0 = 0$ results from the continuity condition $n \cdot D$ on $\partial\Omega_1$, and
F = full matrix, dimension N x (K+L)
S_0 = sparse matrix, dimension NxN
S_1 = sparse matrix, dimension NxM
Φ_0 = vector of electric potentials on Ω_1 , Ω_2 and Ω_A, dimension M
F is the Maxwell electric field coefficient matrix

c) The matrix equation $S_2 \, \Phi_1 + D \, \Phi_0 = c$ results from the FDM (discretization of the Laplacian operator [3,9]), and
S_2 = sparse matrix, dimension M x N
D = sparse matrix, dimension M x M
c = sparse vector which depends on the given electric potential vector Φ_A of the electrode A.

The form (1) is adequate for a problem with only one dielectric. A small modification is suggested for the general problem of Figure 1 (with two or more dielectrics), since it is more convenient to treat Ω_1 and Ω_2 separately, taking an

104

additional vector Φ_2 for the electric potentials on $\partial\Omega_2$.
Therefore, the problem can be formulated as follows:

On the region Ω_1 and its boundaty:

$$\Delta\Phi = 0 \qquad \text{on } \Omega_1 \tag{2}$$
$$\Phi = \Phi_1 \qquad \text{on } \partial\Omega_1$$
$$\Phi = \Phi_2 \qquad \text{on } \partial\Omega_2$$
$$\mathbf{n}\cdot\mathbf{D} = g \quad,\text{ i.e., } -\varepsilon_1\,\partial\Phi/\partial n = g \qquad \text{on } \partial\Omega_2$$

where Δ is the Laplacean operator
and g is an auxiliary function

On the region Ω_2 and its boundaty:

$$\Delta\Phi = 0 \qquad \text{on } \Omega_2 \tag{3}$$
$$\Phi = \Phi_A \qquad \text{on } \partial\Omega_A$$
$$\Phi = \Phi_2 \qquad \text{on } \partial\Omega_2$$
$$\mathbf{n}\cdot\mathbf{D} = -g \quad,\text{ i.e., } -\varepsilon_2\,\partial\Phi/\partial n = -g \quad \text{on } \partial\Omega_2$$

Joining (2) and (3) together, the following problem is obtained,

a) $\quad \Delta\Phi = 0 \qquad$ on $\Omega_1 \cup \Omega_2$ (4)
b) $\quad \Phi = \Phi_A \qquad$ on $\partial\Omega_A$
c) $\quad \Phi = \Phi_1 \qquad$ on $\partial\Omega_1$
d) $\quad \Phi = \Phi_2 \qquad$ on $\partial\Omega_2$
e) $\quad \varepsilon_1\,\partial\Phi/\partial n + \varepsilon_2\,\partial\Phi/\partial n = 0 \quad$ on $\partial\Omega_2$

The discretization of (4a) as given by [9] for two-dimensional problems (see [10] for three-dimensional problems with axial symmetry) and applied to the general node P_0 of Figure 2 is

$$h^2\Delta\Phi(P_0) \cong \frac{\Phi(P_1)}{p(p+r)} + \frac{\Phi(P_2)}{q(q+s)} +$$
$$\frac{\Phi(P_3)}{r(p+r)} + \frac{\Phi(P_4)}{s(q+s)} -$$
$$\left(\frac{1}{pr} + \frac{1}{qs}\right)\Phi(P_0) = 0$$

Figure 2. FDM discretization

where $h = $ grid step; $\quad 0 < p,q,r,s \le 1.0$.

If we have $0 < p,q,r,s \le 1.0$ when P_0 is adjacent to the boundary, and $p,q,r,s = 1.0$ in the interior region (which means a grid with square elements in the interior), then the above discretization has an error of $O(h^2)$. In any other case the error is of $O(h)$ [9].

Once the expression above is applied to every single node of the FDM region, a sparse linear system of dimension M is obtained. When P_0 is adjacent to $\partial\Omega_1$ or $\partial\Omega_2$, the corresponding equation includes some nodes from the vector Φ_1 or Φ_2 respectively. Adjacent to $\partial\Omega_A$, the equation for P_0 includes some nodes from the given electric potential vector Φ_A. Therefore, the final sparse linear system that results from (4a), (4b), (4c) and (4d) have the following matrix form (including S_3 as the additional sparse matrix associated to the new vector Φ_2)

$$S_2\Phi_1 + D\Phi_0 + S_3\Phi_2 = c \tag{5}$$

On the other hand, (4e) is applicable to the W nodes of $\partial\Omega_2$, which requires the discretization of $\partial\Phi/\partial n$ at each one of these nodes. Hence, a total of W equations can be written, including the electric potential vectors Φ_0 and Φ_2 (see section 5.2). These equations have the following matrix form:

$$S_4\Phi_0 + E\Phi_2 = 0 \tag{6}$$

Finally, (1) and the suggested forms (5) and (6) are placed together in a single system,

$$
\begin{bmatrix}
P_1 & -I & 0 & 0 \\
P_2 & 0 & 0 & 0 \\
F & S_0 & S_1 & 0 \\
0 & S_2 & D & S_3 \\
0 & 0 & S_4 & E
\end{bmatrix}
\begin{bmatrix}
q \\
\Phi_1 \\
\Phi_0 \\
\Phi_2
\end{bmatrix}
=
\begin{bmatrix}
0 \\
\Phi_B \\
0 \\
c \\
0
\end{bmatrix}
\tag{7}
$$

This system is equivalent to the more explicit form of Figure 3.

The CSM equations and the FDM are treated separately for the solution of (7), as described in the following sections.
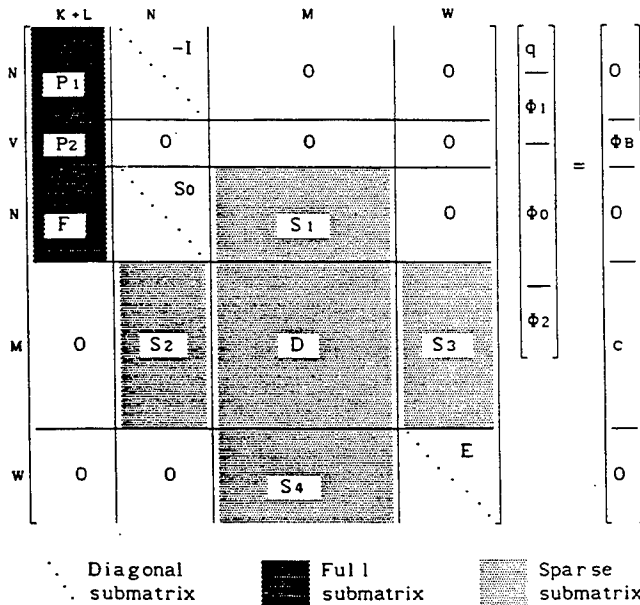
Figure 3. The complete system of linear equations

3. CSM WITH LEAST SQUARES

Suppose that the electric potentials are given on $\partial\Omega_1$ (vector Φ_1) and inside Ω_1 (vector Φ_0). Therefore, the vector of charges q can be calculated by means of the CSM, solving the following system obtained from (7)

$$
\begin{bmatrix}
P_2 \\
F
\end{bmatrix}
q =
\begin{bmatrix}
\Phi_B \\
-(S_0\Phi_1 + S_1\Phi_0)
\end{bmatrix}
\tag{8}
$$

which may be written in the condensed form $\mathbf{C}\,\mathbf{q} = \mathbf{d}$.

Since (8) has V+N equations and K+L unknown charges (and provided that V+N $\ge$ K+L), the least squares method can

be used to find the vector **q**. In this method, the calculated vector **q** minimizes the Euclidean norm of the error vector **C q - d**. One of the best ways of doing so is to utilize the method of the QR decomposition [4,5], calculating **QR = C**, where **Q** is a V+N x K+L matrix with orthonormal columns and **R** is a K+L x K+L upper triangular matrix. It is possible to show that the sparse linear system **R q = Q^{T}d** (where **Q^T** means the transpose of **Q**) provides the exact vector solution **q** for the least squares problem. This system is easily solved by back-substitution since **R** is upper triangular.

Q and **R** may be computed by the modified Gram-Schmidt method, whose mathematical description and algorithm are found in [4,5]. In a computer program, **Q** may be stored over the space of memory of matrix **C**, and the lines of **R** with only its non-zero elements can be sequentially stored as a vector.

The QR method does not require the computation of the matrix product **C^{T}C**, as the traditional least squares CSM. This advantage may significantly reduce the propagation of errors during the computations.

It will be shown (section 7) that a ratio of L/N (number of simulated charges / number of contour points) from 30% to 50% is sufficient for practical purposes.

4. FDM WITH THE CONJUGATE GRADIENTS SQUARED

Supposing that vector Φ_1 is known on $\partial\Omega_1$, vectors Φ_0 and Φ_2 can be calculated with the FDM, solving the following system obtained from (7)

$$\begin{bmatrix} D & S_3 \\ S_4 & E \end{bmatrix} \begin{bmatrix} \Phi_0 \\ \Phi_2 \end{bmatrix} = \begin{bmatrix} c - S_2\Phi_1 \\ 0 \end{bmatrix} \quad (9)$$

This system can be written in the condensed form **A Φ = b**. The matrix **A** has only about 1% of non-zero elements, and can be stored in a very simple scheme by means of the following vectors:

ILIN(k) - stores the line number of matrix **A**, associated to its k-th non-zero element

JCOL(k) - stores the column number of matrix **A**, associated to its k-th non-zero element

VAL(k) - stores the numeric value of A(ILIN(k),JCOL(k))

Having **A** stored this way, a matrix-vector product of the type y = **A** x can be easily computed with the following algorithm

```
For i = 1,NTOT
    y(ILIN(i)) = y(ILIN(i)) + VAL(i) * x(JCOL(i))
end
```

where NTOT is the total number of non-zero elements of **A** .

It is easy to see in this algorithm that no ordination is necessary to the elements of **A** when generating the vectors ILIN, JCOL and VAL. This property is specially suitable to problems of the type which we intend to study.

Therefore, any method that doesn't require operations more expensive than the product matrix-vector can be used for the solution of (9), in principle. To this class of methods belong the Conjugate Gradients and some derivations. Besides this simple way of storage, these methods have the

advantages of reaching the exact solution after a finite number of steps (theoretically at most equal to the matrix dimension), and for any initial estimate. The following was considered:

a) Conjugate Gradients (traditional) (CG) [4,5], without preconditioning and with a diagonal preconditioning,

b) Krylov Subspace method (KS) [6], without preconditioning and with a tridiagonal preconditioning,

c) Conjugate Gradients Squared (CGS) [7], without preconditioning and with a tridiagonal preconditioning.

The CG requires **A** to be a symmetric and positive definite matrix. Since this is not the general case, it only can be applied to the modified normal system **A^{T}A Φ = A^{T}b** (since **A^{T}A** is symmetric and positive definite).

The KS requires the calculation of a vector basis to the Krylov subspace (which dimension is arbitrary). This vector basis may demand a significant additional memory in the computer.

Th CGS doesn't require the product **A^{T}A** as the CG nor the additional storage as the KS and, when used with a preconditioning technique, it needs less CPU computer time (see section 7). Therefore, the CGS is suggested for the solution of (9). Appendix I includes some details as well as the algorithm used for the CGS.

5. CONTINUITY CONDITIONS ON BOUNDARIES

An adequate application of the Maxwell equations gives the necessary continuity conditions [1,2,3], i.e., Φ and **n·D** are continuous across $\partial\Omega_1$ and $\partial\Omega_2$. The condition **n·D** demands a specific equation to be applied at any contour node.

5.1 Discretization of **n·D** on $\partial\Omega_1$

Since ε is constant on both sides of $\partial\Omega_1$, the continuity of **n·D** is equivalent to the continuity of **n·∇Φ** . As already shown by [2,3], the CSM applied to **n·∇Φ** leads to the expression

$$\mathbf{n}\cdot\nabla\Phi(P_1) = -\sum_{j=1}^{K+L} f_{ij} \, q_j \, , \quad i=1...N \quad (10)$$

where f_{ij} are the Maxwell electric field coefficients.

References [2,3] use only one internal node of Ω_1 for the application of the FDM (or the FEM) to the continuity of **n·∇Φ** , which result in an expression with an error of O(h) only. A discretization with an error of O(h^2) can be obtained using the Taylor series expansion as exposed in Appendix II. then

$$\mathbf{n}\cdot\nabla\Phi(P_1) = \alpha\Phi(P_1) + \beta\Phi(P_{1-1}) + \gamma\Phi(P_{1-2}) \quad (11)$$

where P_i lies on $\partial\Omega_1$ and P_{i-1} and P_{i-2} are internal nodes of Ω_1.

The final coupling equation is a result of taking (10) = (11), or

$$\sum_{j=1}^{K+L} f_{ij} \, q_j + [\alpha\Phi(P_1) + \beta\Phi(P_{1-1}) + \gamma\Phi(P_{1-2})] = 0 \, , \quad i=1...N$$

106

which has the equivalent matrix form $F\,q + S_0\Phi_1 + S_1\Phi_0 = 0$, also included in (7). It is easy to see that F is a full matrix, S_0 is a diagonal matrix and S_1 is a sparse matrix with only two non-zero elements per line.

5.2 Discretization of $n \cdot D$ on $\partial\Omega_2$

It is seen from (4e) that this continuity condition requires the discretization of $\partial\Phi/\partial n$ in two stages

a) $\varepsilon_1 \, \partial\Phi/\partial n$, using nodes of Ω_1 ,

b) $\varepsilon_2 \, \partial\Phi/\partial n$, using nodes of Ω_2 .

The method proposed by [8] uses the node on the boundary and other three internal nodes, and is considered in some details in Appendix III. Using the proposed discretization, (4e) takes the form

$$\varepsilon_1 \sum_{j=1}^{3} a_{1j}[\Phi(P_i)-\Phi(P_{1j})] + \varepsilon_2 \sum_{j=1}^{3} a_{2j}[\Phi(P_i)-\Phi(P_{2j})] = 0 \qquad (12)$$

where P_i lies on $\partial\Omega_2$,

and P_{1j} and P_{2j} are internal nodes of Ω_1,Ω_2 respectively.

The matrix form (6) is obtained applying (12) to $i=1\ldots w$, where E is a diagonal matrix and S_4 is a sparse matrix with 6 non-zero elements per line.

6. SOLUTION OF THE COMBINED SYSTEM OF LINEAR EQUATIONS

It was already shown that the system of linear equations that represents the hybrid FDM & CSM has the matrix form (7). In order to facilitate our analysis, this system is written as

$$\begin{bmatrix} P_1 & -I & 0 \\ P_2 & 0 & 0 \\ F & S_0 & Z_1 \\ 0 & Z_2 & A \end{bmatrix} \begin{bmatrix} q \\ \Phi_1 \\ \Phi \end{bmatrix} = \begin{bmatrix} 0 \\ \Phi_B \\ 0 \\ z \end{bmatrix} \quad , \text{ where} \qquad (13)$$

$$A = \begin{bmatrix} D & S_3 \\ S_4 & E \end{bmatrix}; \ \Phi = \begin{bmatrix} \Phi_0 \\ \Phi_2 \end{bmatrix}; \ z = \begin{bmatrix} c \\ 0 \end{bmatrix}; \ Z_1 = [S_1 \ 0] \ ; \ Z_2 = \begin{bmatrix} S_2 \\ 0 \end{bmatrix}$$

Since (13) is composed by different kind of submatrices that came from distinct problems (i.e. the full rectangular submatrices from the CSM and a sparse square submatrix from the FDM), it is suggested to solve this system using an iterative method. Doing so, each part of (13) can be treated separately in an optimized way.

Notice that once the vector of charges q is known, the whole problem is solved. Therefore, an iterative method can be derived by using the general expression of the fixed point theory [4]

$$q^{n+1} = T\,q^n + u \qquad (14)$$

where T is a matrix of dimension $K+L \times K+L$,
 u is a vector of dimension $K+L$, and
 n is the iteration number.

According to the fixed point theory applied to linear systems [4], (14) converges whenever $\sigma(T) < 1$, where $\sigma(T)$ is the spectral radius (the largest absolute value in the set of eigenvalues) of T, for any initial estimate q^0 . T is also known as the "iteration matrix".

It is possible to show (Appendix IV) that an iterative method can be derived so that an expression for T results in

$$T = \theta I + (1-\theta)R^{-1}Q^T \begin{bmatrix} 0 \\ Z_1 A^{-1} Z_2 - S_0 \end{bmatrix} P_1 \qquad (15)$$

where Q and R come from the decomposition $\begin{bmatrix} P_2 \\ F \end{bmatrix} = QR$

and θ is a parameter to be chosen for every problem in order to make $\sigma(T) < 1$, and so allowing (14) to converge. It holds in general that $0 \le \theta < 1$.

Obviously $\sigma(T)$ and T do not need to be explicitly calculated. Figure 4 includes a flowchart for the iterative method which generates T precisely as expression (15).
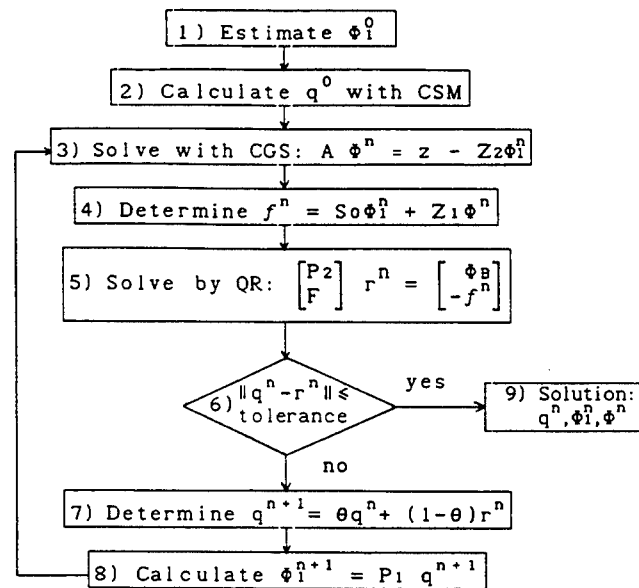
Figure 4. Iterative method for the solution of (13)

Observations:

a) The iterative method (14) is not dependent on the initial estimate q^0 . However, it is possible to obtain a good initial estimate for q by choosing Φ_1 (step 1 in Figure 4) and solving once with the QR decomposition (step 2) the following least squares problem, taken from (7)

$$\begin{bmatrix} P_1 \\ P_2 \end{bmatrix} q^0 = \bar{Q}\,\bar{R}\,q^0 = \begin{bmatrix} \Phi_1^0 \\ \Phi_B \end{bmatrix} \ \Rightarrow \ \bar{R}\,q^0 = \bar{Q}^T \begin{bmatrix} \Phi_1^0 \\ \Phi_B \end{bmatrix}$$

b) The given electrode potentials are included in vectors Φ_B and z, which do not appear in expression (15). So the convergence to the solution (which according to the fixed point theory depends on the eigenvalues of T) does not depend on the given electrode potentials.

c) In view of the complexity of (15), the parameter θ can only be estimated by experience. For most of the tested problems we had convergence with $\theta \cong 0.6$ to 0.9 .

d) The iterative method proposed by [1] corresponds somewhat to the particular case of $\theta = 0$, which doesn't mean that (14) will always converge. The possibility of a choice for $\theta \neq 0$ permits the solution of a greater class of problems.

7. APPLICATIONS

We used the hybrid FDM & CSM for the calculation of the electric potential distribution close to the surface of an infinite cylinder above earth, since this case has an exact (analytical) solution. Details are reported in [11], and indicate that for this case the electric potentials calculated with the hybrid FDM & CSM have an error of less than 1% .

In a more general case, we used the hybrid FDM & CSM for the calculation of the electric potential distribution in the two-dimensional, unbounded and multi-dielectric problem as indicated in Figure 5.

Table 1	
Error on Φ_1	
L/N	%
0.50	0.01
0.40	0.05
0.30	0.16
0.20	1.33
0.10	± 20.0

Table 2		
CPU time (s)		
Method	1	2
CG	113.5	56.9
KS	453.7	17.8
CGS	36.7	9.6
1 - without precond.		
2 - with precond.		

Table 2 shows the CPU time for the methods CG, KS and CGS (with L/N $\cong$ 33%) on an IBM 3090-300S computer. The CGS with a tridiagonal preconditioning was shown to be the fastest.

As an illustration, Figure 6 shows the computed equipotential lines inside the FDM region, considering $\varepsilon_2 = 2.0$ and $\varepsilon_3 = 5.0$.

Figure 5. Two-dimensional example
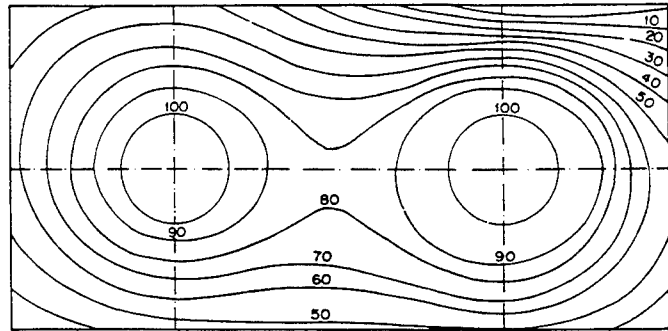
Figure 6. Equipotential lines

Submatrices P_1, P_2 and F of (7) include the Maxwell coefficients, calculated as indicated by [1,2,3]. In the FDM region, a rectangular grid with equally spaced nodes of h = 0.75 was placed, defining M = 15x31 = 465, N = 96 and W = 72. It was also chosen K = V = 4 .

Table 1 shows the maximum percentile deviation of the electric potentials calculated on $\partial\Omega_1$ (vector Φ_1), considered as a function of the relation between the number of simulated charges inside the FDM region (L) and the number of contour points on $\partial\Omega_1$ (N). The values were obtained by comparison with results computed with L/N $\cong$ 0.75 (this relation is assumed to give insignificant error for Φ_1). As a result it may be suggested that L/N $\cong$ 30% to 50% is a good choice.

Figure 7 shows the electric potential distribution along the direction 1 of Figure 5, as a function of ε_2 and ε_3 . It illustrates the effect of materials with different permittivities on the electric potential distribution.
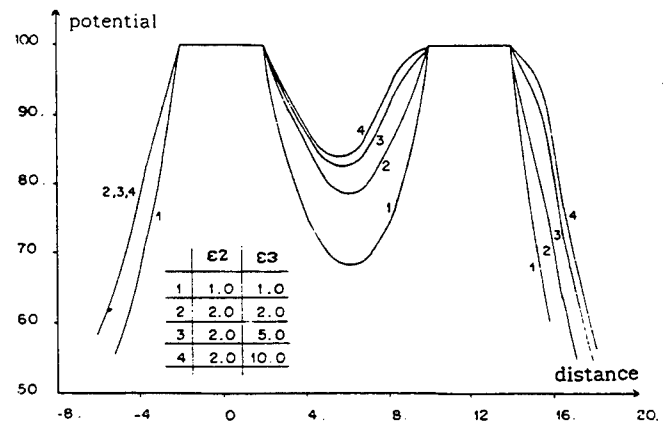
Figure 7. Electric potential as a function of ε

108

Additional comments:

a) The charges simulated inside the FDM region must be located at least approximately 1.0 to 2.0 times the grid step (h) distant from $\partial\Omega_1$. Charges located very close to $\partial\Omega_1$ lead to a severe loss of precision in the results (as also reported by [2]), due to the singularities of the expressions for the Maxwell coefficients.

b) When a simulated charge is located very close to another, the matrix Q approximates of a rank deficient matrix (see [4,5]), which may cause some difficulties in the convergence of (14). This corresponds to the case of nearly singular matrices in the traditional CSM.

c) It was considered an absolute error of 10^{-5} for the convergence of the CG, KS and CGS, and an error of 0.1% for the elements of the simulated charges vector q of (14) (22 iterations was necessary).

d) It is easy to see that all the mathematical approach exposed in this work applies to three-dimensional problems with axial symmetry as well (which in fact becomes reduced to a two-dimensional problem). This is feasible once the corresponding Maxwell coefficients for submatrices P_1, P_2 and F (see [1,2,3]) and the corresponding discretization for the Laplacean operator of equation (4) (see [10]) are considered. Thus, problems like the electric potential distribution across an insulator chain, or across an insulating column of a high-voltage equipment can be solved. Three-dimensional problems without any symmetry are also possible in principle.

8. CONCLUSION

New developments on the combined application of the Carge Simulation method with the Finite Difference or Finite Element method were shown.

The application of the Charge Simulation method as a least squares problem with the QR decomposition results in saving more than half of the original amount of computer memory, without loss of precision.

The use of the CGS method with a tridiagonal preconditioning for the solution of the discretised problem results in a significant reduction of the CPU computer time, with the consequence of costs reduction and reduced error propagation in the computer.

New procedures for the discretization of the boundary conditions were suggested, leading to results of higher precision.

An iterative method for the solution of the combined problem was presented, by making use of the fixed point theory of linear systems, which allows convergence for a greater class of electrostatic problems. Another feature of this new iterative method is the non-dependence on the initial estimate for electric potentials.

Finally, case studies show that the suggested innovations are effective in the mathematical formulation of the FDM & CSM or FEM & CSM, and they may represent a new motivation for the application of these hybrid methods on the computation of electric fields for unbounded problems.

9. REFERENCES

[1] H. Steinbigler , "Combined application of finite element method and charge simulation method for the computation of electric fields", 3rd International Symposium on HV Engineering, section 11-11, August 1979

[2] H. Okubo, M. Ikeda, M. Honda and T. Yanari, "Electric field analysis by combination method", IEEE Transactions on PAS, vol. 101, n° 10, pp. 4039-4048, October 1982

[3] M. Abdel-Salam and M. T. El-Mohandes, "Combined method based on finite differences and charge simulation for calculating electric fields", IEEE Transactions on IA, vol. 25, n° 6, pp. 1060-1066, November/December 1989

[4] G. H. Golub and C. F. Van Loan, Matrix Computations, Baltimore, The John Hopkins University Press, 1985

[5] B. Noble and J. Daniel, Applied Linear Algebra, New Jersey, Prentice Hall, 1977

[6] Y. Saad, "Krylov subspace methods on supercomputers", J. Soc. Industrial and Applied Mathematics, vol. 10, n° 6, pp. 1200-1232, November 1989

[7] P. Sonneweld, "CGS - a fast Lanczos-type solver for non-symmetric linear systems", Siam J. Sci. Stat. Comput., vol. 10, n° 1, pp 36-52, January 1989

[8] J. H. Bramble and B. E. Hubbard, "Aproximation of solutions of mixed boundary value problems for Poisson's equation by finite differences", J. of the Assoc. for Computing Machinery, vol. 12, n° 1, pp. 114-123, January 1995

[9] G. E. Forsythe and W. R. Wasow, Finite difference methods for partial differencial equations, John Willey & Sons, 1960

[10] J. T. Storey and M. J. Billings, "General digital computer program for the determination of 3-dimensional electrostatic axially symmetric fields", Proc. IEE, vol. 114, n° 10, pp. 1551-1555, October 1967

[11] J. N. Hoffmann, Numerical simulations for the electric field calculation of unbounded domains, M. S. Thesis (in Portuguese), University of Campinas (UNICAMP), IMECC Dept., Campinas/SP, Brazil, 261 pp., April 1963

APPENDIX I

CGS algorithm with preconditioning

Consider the CGS method with tridiagonal preconditioning for the solution of the system of linear equations $A x = b$. For the application of the preconditioning technique, this system is modified as

$$(LU)^{-1}(Ax) = (LU)^{-1}b$$

where L, U = matrices resulting from the LU decomposition of the tridiagonal part of A [4,5].

In this case, the algorithm for the CGS is the following [7]:

```
      estimate xo
      solve (LU) ro = (b - A xo)
      qo= p  = 0 ; p   = 1 ; n=0
          -1        -1
  10  if(rn < tolerance) end

      pn  = ro rn ; βn = pn/pn-1
      un = rn + βn qn
      pn = un + βn (qn + βn pn-1)
      solve (LU) vn =  (A pn)

      σn = ro vn ; αn = pn/σn
      qn+1 = un - αn vn
      vn = αn (un + qn+1)
      xn+1 = xn + vn
      solve (LU) rn+1 = (b - A xn+1) ; n=n+1
      go to 10
```

109

APPENDIX II

Discretization for $\mathbf{n} \cdot \nabla \Phi$

A simple discretization for $\mathbf{n} \cdot \nabla\Phi(P_i)$ is obtained using the Taylor series expansion, assuming existence of nodes arranged on a line with the same direction of $\mathbf{n}$ (Figure 8).
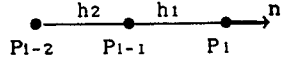
Figure 8. Discretization for $\partial\Phi/\partial n$ at P_i

Then

$$\Phi(P_{i-1}) = \Phi(P_i) - h_1\Phi'(P_i) + h_1^2\Phi''(P_i)/2 + O(h^3) \quad (16)$$

$$\Phi(P_{i-2}) = \Phi(P_i)-(h_1+h_2)\Phi'(P_i)+(h_1+h_2)^2\Phi''(P_i)/2+O(h^3) \quad (17)$$

Taking $(h_1+h_2)^2 \cdot (16) - h_1^2 \cdot (17)$,

$$\mathbf{n} \cdot \nabla\Phi(P_i) = \Phi'(P_i) = \alpha\Phi(P_i)+\beta\Phi(P_{i-1})+\gamma\Phi(P_{i-2}) + O(h^2)$$

where $\alpha = 1/h_1 + 1/(h_1+h_2)$
$\beta = -(1/h_1 + 1/h_2)$
$\gamma = 1/h_2 - 1/(h_1+h_2)$
$h = \max\{h_1,h_2\}$

So the approximation $\mathbf{n} \cdot \nabla\Phi(P_i) = \alpha\Phi(P_i)+\beta\Phi(P_{i-1})+\gamma\Phi(P_{i-2})$
has an error of $O(h^2)$.

APPENDIX III

General discretization for $\mathbf{n} \cdot \nabla \Phi$

A general discretization for $\mathbf{n} \cdot \nabla\Phi(P_i)$ on $\partial\Omega$ is obtained, not requiring the existence of nodes arranged as those of Appendix II (Figure 9).
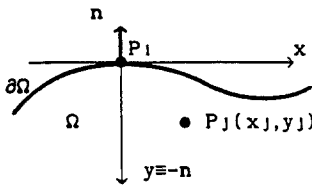
As described by [8] and according to Figure 9, a discretization for $\partial\Phi/\partial n$ at P_i may be written as

$$\frac{\partial\Phi}{\partial n} = \sum_{j=1}^{3} a_j [\Phi(P_i)-\Phi(P_j)]$$

Figure 9. Discretization for $\partial\Phi/\partial n$ at P_i
where $P_i \in \partial\Omega$
and $P_j \in \Omega$

The coefficients a_j are determined using the geodesic normal coordinates, what results in the solution of the simple system of equations (see [8] for details)

$$\begin{bmatrix} y_1 & y_2 & y_3 \\ x_1(1+y_1 \cdot K) & x_2(1+y_2 \cdot K) & x_3(1+y_3 \cdot K) \\ x_1^2 - y_1^2 & x_2^2 - y_2^2 & x_3^2 - y_3^2 \end{bmatrix} \cdot \begin{bmatrix} a_1 \\ a_2 \\ a_3 \end{bmatrix} = \begin{bmatrix} 1 \\ 0 \\ 0 \end{bmatrix}$$

where K is the curvature of $\partial\Omega$ at P_i .

APPENDIX IV

Proposed iterative method

Suppose that q^n of (14) is known. The CSM gives

$$\Phi_i^n = P_1 \, q^n. \quad (18)$$

Thus, vector Φ^n can be calculated from the application of the CGS method to the FDM problem. Theoretically, from (13),

$$\Phi^n = A^{-1}(z - Z_2\Phi_i^n) \quad (19)$$

Determine the auxiliary vector f^n, by using (19)

$$f^n = S_0\Phi_i^n + Z_1\Phi^n = (S_0 - Z_1A^{-1}Z_2)\Phi_i^n + Z_1A^{-1}z \quad (20)$$

A new vector of charges r^n can be derived from the CSM with least squares and the QR decomposition, obtained from (13)

$$\begin{bmatrix} P_2 \\ F \end{bmatrix} r^n = \begin{bmatrix} \Phi_B \\ 0 \end{bmatrix} - \begin{bmatrix} 0 \\ f^n \end{bmatrix} = \begin{bmatrix} \Phi_B \\ -f^n \end{bmatrix} \Rightarrow r^n = R^{-1}Q^T\begin{bmatrix} \Phi_B \\ -f^n \end{bmatrix}$$

Using (18) and (20) on the last expression, we obtain

$$r^n = R^{-1}Q^T\begin{bmatrix} 0 \\ Z_1A^{-1}Z_2 - S_0 \end{bmatrix} P_1 \, q^n + R^{-1}Q^T\begin{bmatrix} \Phi_B \\ -Z_1A^{-1}z \end{bmatrix} \quad (21)$$

Taking the combination $q^{n+1} = \theta \, q^n + (1-\theta) \, r^n$, where θ is an arbitrary parameter, and by using (21), the expression (15) for T is immediately obtained. This combination assures that at the end of the iterative calculations (when $r^n = q^n$), we will have $q^{n+1} = q^n = r^n$, for any chosen value of θ.

The flowchart of Figure 4 resumes the above procedure.

BIOGRAPHIES

João Nelson Hoffmann was born in Lapa, state of Paraná, Brazil, on April 22, 1958. He received the B.S. degree in Electrical Engineering in 1981 and the M.S. degree in Applied and Computational Mathematics in 1993. Since 1988 he is with Companhia Paranaense de Energia (COPEL), Curitiba, Paraná, Brazil, working with high voltage transmission line researches.

Petronio Pulino was born in Bebedouro, state of São Paulo, Brazil, on October 14, 1956. He received the B.S. degree in Mathematics, the M.S. degree in Applied Mathematics and the Ph.D. degree in Electrical Engineering from University of Campinas (UNICAMP). Presently he is an assistant professor at the Department of Applied Mathematics of UNICAMP.

Finite Element Modeling of Electrical Machines by Simultaneous Resolution of Fields and Electric Circuits Equations

N. Sadowski*, R. Carlson*, J.P.A. Bastos*, M. Lajoie-Mazenc**

* GRUCAD-EEL-CTC-UFSC	** LEEI-ENSEEIHT-U.R.A. CNRS 847
C.P. 476	2, Rue Camichel
88040-900 - Florianópolis - SC - Brazil	31071 - Toulouse Cedex - France

Abstract - In this work, we present a methodology for solving simultaneously the equations of magnetic fields and electric circuits of electrical machines. To consider the magnetic phenomena the Finite Element method is used. The machines are voltage fed and, thus, the electric circuit equations are present in the matricial system which takes into account both physical aspects. A time stepping technique is employed to simulate the steady and transient states. As result, we obtain the magnetic vector potential describing the magnetic behavior of the machine and the current established in the exciting coils.

INTRODUCTION

The modeling of electrical machines and their feeding circuits is related to two type of equations: the Poisson equation describing their magnetic behavior and the differential equations of the electrical circuits related to the exciting windings.

It is also possible to determine the equivalent electrical circuit of the machine. By this procedure, it is necessary to obtain the parameters of the machine by analytical calculations or, for better accuracy, fields calculations. The equivalent electrical circuit, obtained by this procedure is associated to the electric feeding circuits [1],[2],[3]. This methodology presents limitations mainly when the machine has massive parts (not laminated regions), where eddy currents exist. In this case, it is practically impossible to determinate the equivalent electric circuit of the machine, for both, steady and transient states.

To solve such problems, it is necessary to solve simultaneously the field and circuit equations [4],[5],[6],[7],[8],[9],[10].

In this work, we present a brief survey based in works performed by us and, after the presentation of the general equations and solving techniques, the proposed methodology is illustrated by permanent magnet and induction motors fed by different electric circuits.

INVOLVED EQUATIONS

The global equations to solve are obtained associating the equation which describes the magnetic structure of the machine with the equations representing the feeding circuits.

Equations representing the magnetic structure of the machine

The general case of an electrical machine containing magnetic materials of reluctivity v, permanent magnets with magnetization B_0 and reluctivity v_p and with conductive solid parts with electrical conductivity σ is considered bellow.

If a two dimensional representation of the machine structure is adopted and using the magnetic vector potential A, the equations describing the whole structure are:

$$\frac{\partial}{\partial x}\left[v\frac{\partial A}{\partial x}\right]+\frac{\partial}{\partial y}\left[v\frac{\partial A}{\partial y}\right]-\sigma\frac{\partial A}{\partial t}+\frac{N}{S}I =$$
$$= v_p\left[\frac{\partial B_{0y}}{\partial x}-\frac{\partial B_{0x}}{\partial y}\right] \tag{1.a}$$

$$U = RI + L\frac{dI}{dt}+\frac{N\ell}{S}\iint_S \frac{\partial A}{\partial t}\,ds \tag{1.b}$$

where:
I is the current in the machine windings,
S is the winding surface,
N is the number of turns in the winding,
ℓ is the machine depth,
U is the voltage at the machine windings,
L represents the end winding inductance, not taken into account in a two dimensional magnetic representation of the machine.

The analytical solution of equations (1) is not easy to accomplish due to the complex structure of electrical machines. Then we adopt the Finite Element method [11]. Equations (1) can then be written in the following matrix form:

$$MA+N\frac{d}{dt}A-PI = D \tag{2.a}$$

$$Q\frac{d}{dt}A+RI+L\frac{d}{dt}I = U \tag{2.b}$$

Matrices M, N, P, D, Q are dependent on the machine magnetic structure (dimensions, reluctivity,etc.).

Electrical feeding circuits equations

The differential equations representing the electric feeding circuits coupled to the machine windings can be written as:

$$\frac{d}{dt}X = H_1X + H_2E + H_3I \qquad (3.a)$$

$$U = H_4X + H_5E + H_6I \qquad (3.b)$$

where:

X is the inductance current and capacitor voltage vector of the electrical circuit connected to the machine, E is the vector of the voltage sources of the external circuit,

matrices $H_1, H_2, H_3, H_4, H_5, H_6$ are dependent on the electrical circuit topology. Equation (3.b) allows coupling between magnetic and electric equations.

Global equations

Combining equations (2) and (3), the global matrix system representing the whole electrical machine-feeding circuit is obtained and given by (4). The unknowns in this global system are [5]:

a) the magnetic potential vector in the finite element mesh A,
b) the currents in the machine windings I,
c) the capacitor voltages and inductance currents in the feeding circuit (state variables).

$$MA + N\frac{d}{dt}A - PI = D \qquad (4.a)$$

$$Q\frac{d}{dt}A + [R - H_6]I + L\frac{d}{dt}I - H_4X = H_5E \qquad (4.b)$$

$$\frac{d}{dt}X - H_1X - H_3I = H_2E \qquad (4.c)$$

RESOLUTION METHOD

Equations (4) above are solved step by step with respect to time. In this way, the time derivatives must be discretized (by means of the θ-method or Euler's scheme [12]). During the step by step solution, the following must be observed:

a) The matrix terms concerning the external circuit can be modified due to the topologic changes in the feeding circuit (commutation of the semiconductors, for example).

b) Matrix M terms are modified due to the rotor movement.

c) If magnetic non-linearity must be taken into account an interactive procedure is used. In this work the Newton-Raphson method is employed [13].

The rotor movement is considered by remeshing the airgap at each position as follows.

Movement modeling

In this work, the movement is taken into account by a method based on meshing stator and rotor and connecting these meshes by an adaptable layer of Finite Elements placed in the air gap. This method is known as the Moving Band method. Its working principle is shown in Fig.1 [4],[10].
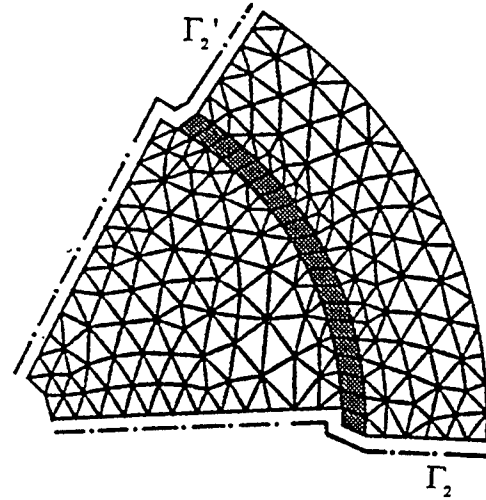
Fig. 1 : Moving Band method working principle.

According to the airgap deformation, the Moving Band technique is based in a dynamic allocation of the periodic or anti-periodic boundary conditions. With this technique, in spite of the new nodes created with the rotation of the moving part, the number of unknowns is always the same.

When using the Moving Band technique, if the rotation step is different than the discretization step, the finite elements placed in the airgap are deformed. This deformation can give rise to numerical oscillations on the voltages waveforms. To obtain better results, quadrilateral finite elements are used. These special elements are assembled in the global matrix as four triangular elements [10].

Torque calculation during the rotation

112

The choice of the method to simulate the rotor movement is related to the way employed to the torque calculation. This statement is based on studies made previously [10]. From this investigation, we concluded that the Maxwell Stress Tensor presents, with the Moving Band, very good accuracy. This method was chosen, but the following remark must be considered: if the displacement step is different of the discretization one (therefore, when there are deformations of the quadrilateral elements in the Moving Band), the torque is calculated in another layer of quadrilateral elements. This procedure is necessary to avoid numerical oscillations in the torque waveform.

APPLICATION EXAMPLES

We will present now two examples to describe the possibilities of the proposed method. These examples correspond to practical cases, which have been currently subjects of research.

Single phase line started induction motor fed by a starting circuit.

A two poles single phase induction motor used in electrical appliance applications is the first example. Its half structure as well as the calculated field distribution are shown in Fig.2 [14],[15]. In the same figure the induced current densities in the rotor bars at starting can be seen. The machine presents a different number of conductors by slot. Two windings are placed in the stator, namely the main and the auxiliary windings. A particular electric circuit shown in Fig. 3 is used to feed the machine. The resistance $R(t)$ is time dependent.
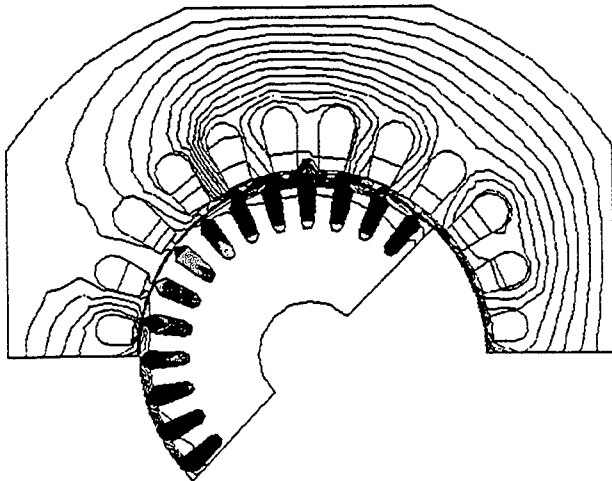
Fig. 2 : Single phase induction motor: field and induced current density distribution.
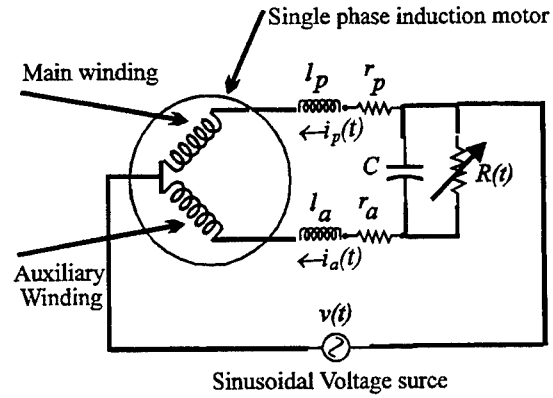
Fig. 3 : Single phase induction motor electrical feeding circuit.

Using electric circuits theory, matrices $H_1, H_2, H_3, H_4, H_5, H_6, L$ and vector E associated to the electrical circuit of Fig. 3 can be obtained. Using Euler's scheme in order to represent the time derivatives in (4), one can write:

$$H_1 = \frac{-R(t)C - \Delta t}{R(t)C\Delta t} \quad (5.a) \qquad H_2 = 0 \quad (5.b)$$

$$H_3 = \left| 0 \quad \frac{1}{C} \right| \quad (5.c) \qquad H_4 = \left| \begin{matrix} 0 \\ -1 \end{matrix} \right| \quad (5.d)$$

$$H_5 = \left| \begin{matrix} 1 \\ 1 \end{matrix} \right| \quad (5.e) \qquad H_6 = \left| \begin{matrix} 0 & 0 \\ 0 & 0 \end{matrix} \right| \quad (5.f)$$

$$R = \left| \begin{matrix} r_p & 0 \\ 0 & r_a \end{matrix} \right| \quad (5.g) \qquad L = \left| \begin{matrix} l_p & 0 \\ 0 & l_a \end{matrix} \right| \quad (5.h)$$

$$E = v(t) \quad (5.i)$$

In equations (5) $v(t)$ is the applied voltage, r_p and r_a are the main and auxiliary winding d.c. resistances. The main and auxiliary end winding inductances are represented respectively by l_p and l_a. The $R(t)$ resistance and the capacitor C, already defined, are shown in Fig. 3. The time step is Δt.

In the simulation procedure, at each time step after the solution of equations (4), the electromagnetic torque Γ_e is calculated with the Maxwell Stress Tensor. The angular speed ω_m and the rotor displacement β are determinate with the following equations:

$$\frac{d\omega_m}{dt} = \frac{1}{J}\left[\Gamma_e - \Gamma_c - B\omega_m\right] \quad (6.a)$$

113

$$\frac{d\beta}{dt} = \omega_m \qquad (6.b)$$

where B is viscous damping factor, J is the inertia and Γ_c is the load torque.

Results: the simulation of the machine starting at no-load and fed by a 60 Hz sinusoidal voltage is presented in Figure 4. The resistance $R(t)$ has a small value in the beginning of the operation and it is strongly increased after 0.3 seconds. The effects of the resistance change can be noticed in the figures.

It is possible to remark the typical behavior of a single phase induction motor; the speed and current curves present particularly the oscillations having the double of the feeding frequency. In Figure 5 the calculated and experimental results at 670 rpm are presented. One can notice the good agreement between calculation and measurements.
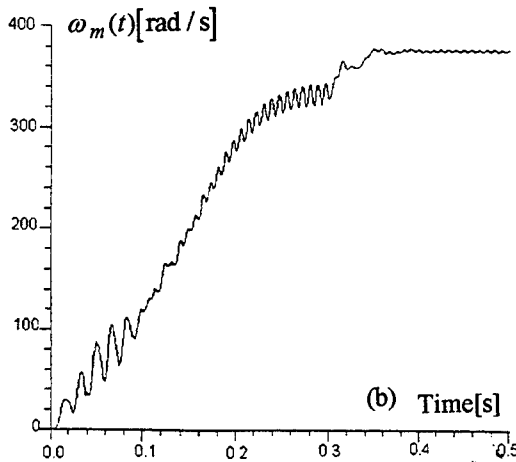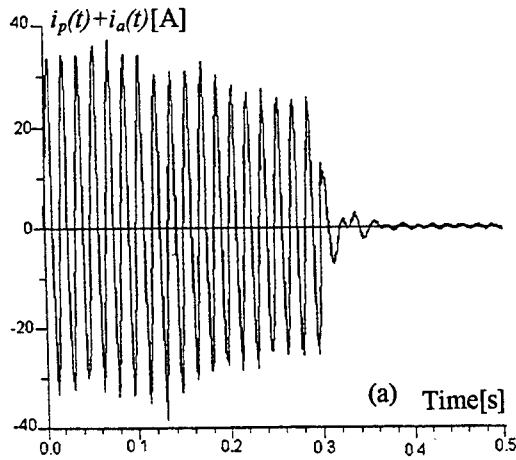
Fig. 4 : Results of the starting of the single phase induction motor.
(a) Total (source) Current $i_p(t)+i_a(t)$. (b) Speed $\omega_m(t)$.
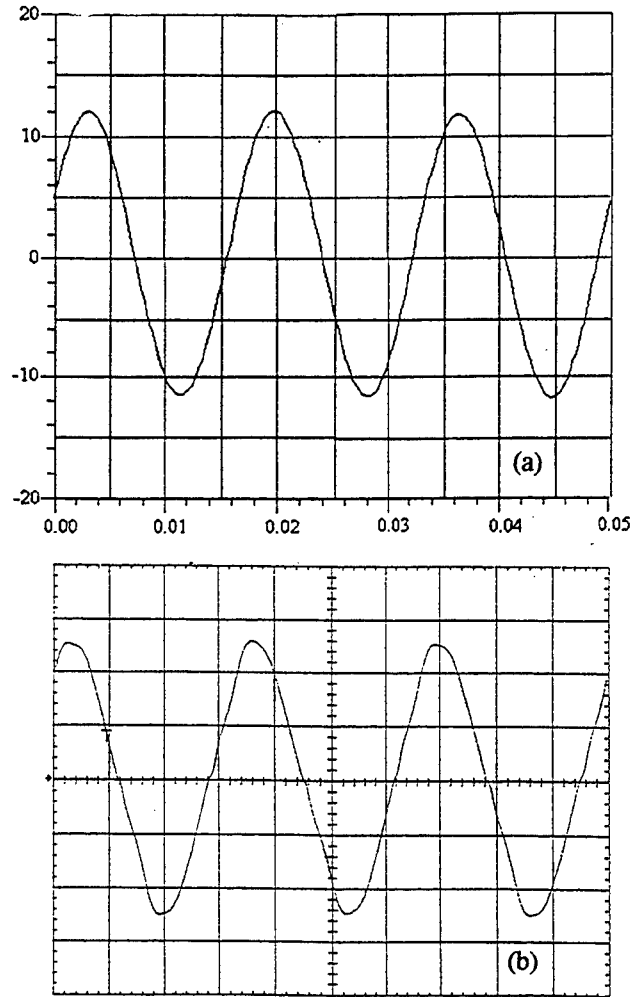
Fig. 5 :Total (source) Current $i_p(t)+i_a(t)$. (a) Calculated (5A/div.).
(b) Experimental Results (5A/div.)

Permanent magnet motor fed by current inverter

The motor under study is fed by the inverter presented in Figure 6, in which there are thyristors connected to a current source, which is obtained by a voltage source connected to an inductance having a large value. The inverter is operated by a position sensor placed on the rotor.

To simulate such a device it is necessary to consider the actual structure of the electric circuit and its configuration changes due to the conducting states of the thyristors. Furthermore, the commutation of currents in the motor and the thyristor openings are made by the voltages in the motor terminals. Thus, the inverter operation and the machine are strongly associated and a simultaneous solution is the only procedure providing accurate results. In order to simplify the simulation, we take advantage of the fact

114
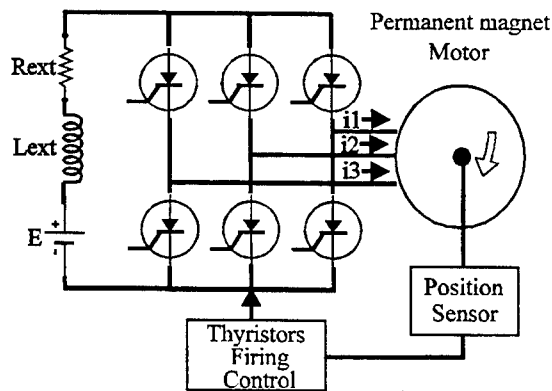
Fig. 6 : Current inverter working principle.

that the operation sequences of the inverter are known in advance and they can be described by only two sequences:

a) conduction, when two phases are fed and the third one is not connected.
b) commutation, when the three phases are connected and the voltage between two phases is zero.

These two states are successive and by circular permutation they describe the whole operation of the inverter. The electric circuits of these two sequences can be represent by the single circuit of Figure 7, where a resistance assuming values of 0 and 1 MΩ represents the respectively the commutation and the conducting sequences. This procedure allows us to keep constant the matricial system order.
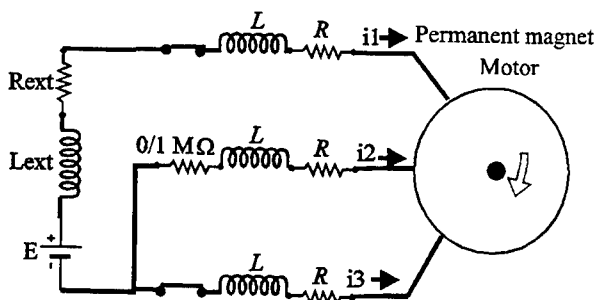
Fig. 7 : Circuit corresponding to the two working sequences.

The beginning of the commutation sequence is determinate by the position of the rotor. The end of this state occurs when the current in the commutation loop becomes zero. The motor shown in Fig. 8 was chosen for this example.

This machine presents permanent magnets in the rotor. They are mechanically sustained by an aluminum hoop and interpolar wedges, where eddy currents can be induced. Fig. 9 presents the eddy currents distribution during the motor operation.
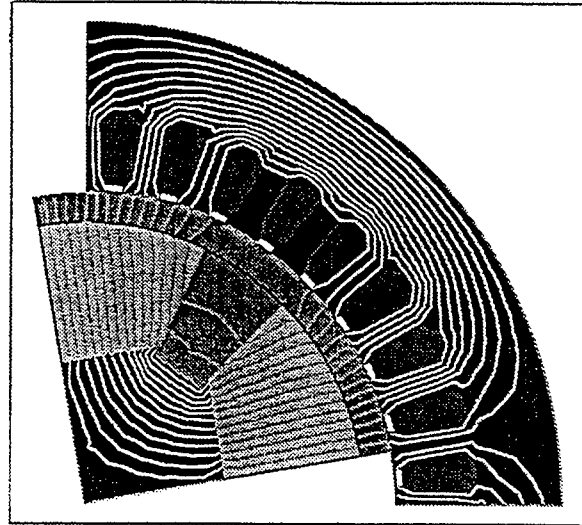
Fig. 8 : Permanent magnet structure domain.
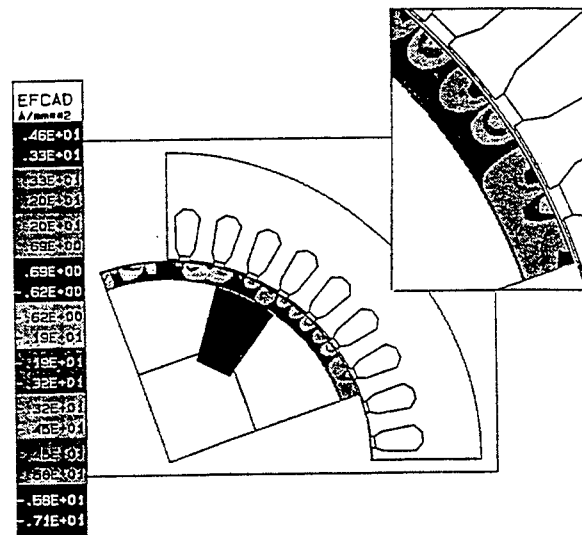
Fig. 9 : Eddy currents distribution in the conducting parts.

Figure 10 presents, using the same scales, the results obtained from the simulation and the experimental measurements. A very good agreement between these results is noticed. The eddy currents established in the aluminum hoop causes shorter commutation time, compared to the one expected for a device without induced currents.

115
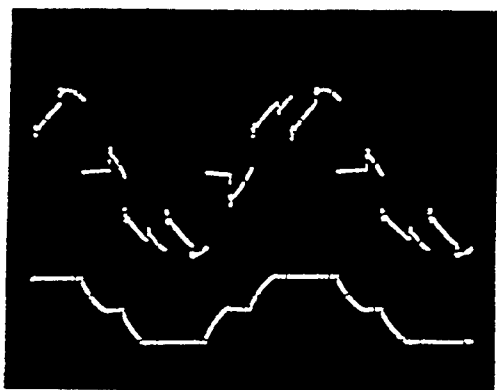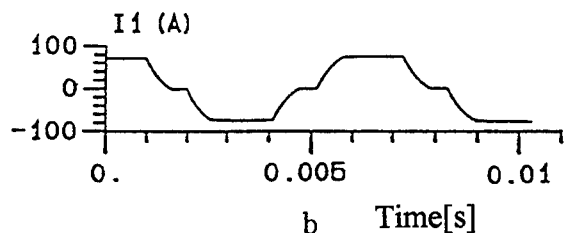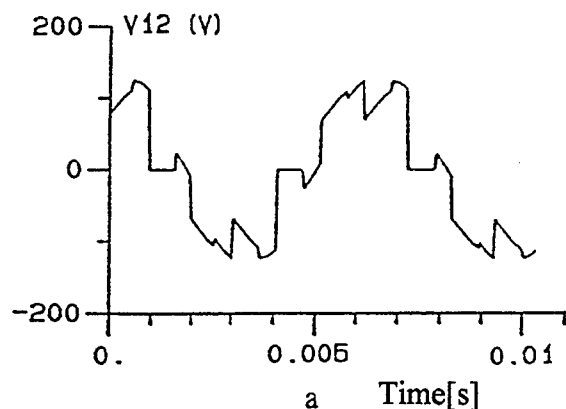
Fig. 10 : Voltage and currents of the inverter.

CONCLUSION

In this work a general modeling describing the functioning of the whole structure composed by a machine and its feeding circuit was presented. This procedure is based in the coupling between the magnetic field and the electric circuit equations.

When solving this system, the rotor movement was taken into account in the Finite Element geometric discretization of the domain. This technique is based on the concept of Moving Band using quadrilateral elements. The Maxwell Stress tensor is applied for torque calculation.

Two different simulation cases were presented: a single phase line started induction motor and a permanent magnet motor fed by a current inverter. For both cases, the calculated and the experimental results present a very good agreement.

Finally, when complex phenomena (eddy currents, non-linearity, movement and feeding by static converters) are present, the only method providing accurate results has to take into account simultaneously the different variables, as the one here proposed.

REFERENCES

[1] F.Piriou, A. Razek, "Calculation of saturated inductances for numerical simulation of synchronous machines", IEEE Trans. on Magn., Vol. MAG-19, N.6, pp.2628-2631, November 1983.

[2] F. Piriou, A. Razek, "Modélisation des machines synchrones autopilotées en considérant la saturation magnétique", Revue Générale d'Electricité, Vol. 4, pp. 293-298, 1985.

[3] B. Davat, H. Rezine, M. Lajoie-Mazenc, "Modeling of a brushless DC motor with solid parts involving eddy currents", IEEE Trans. on Industry Applications, Vol. IA-21, N. 1, pp. 202-206, January/February 1985.

[4] Ren Z., Contribution à la modélisation des machines électriques para résolution simultanée des équations du champ e des équations du circuit d'alimentation, Thèse de Docteur de l'INPT, Toulouse, 1984.

[5] Davat B., Modélisation des dispositifs électromagnétiques, Thèse de Docteur ès-Sciences Physique, INPT, Toulouse, 1984.

[6] Arkkio, A., Analysis of induction motors based on the numerical solution of the magnetic field and circuit equations, Acta Polytechnica Scandinavica, Helsinki, 1987.

[7] F. Bouillault, A. Kladas, F. Piriou, A. Razek, "Coupled electric-magnetic model for a synchronous machine associated with static converter", Proceedings of ICEM, Pisa, pp. 453-456, 1988.

[8] Preston T.W., Reece A.B.J., Sangha P.S.,"Induction motor analysis by time-stepping techniques", IEEE Trans. on Magn., Vol. 24, N.1, pp. 471-474, January 1988.

[9] Lombard P., Meunier G., "A general method for electric and magnetic coupled problems in 2D magnetodynamic domain", COMPUMAG Proceedings, Sorrento, pp. 195-198, July 1991.

[10] N. Sadowski, Modélisation des machines électriques à partir de la résolution des équations du champ en tenant compte du mouvement et du circuit d'alimentation (Logiciel EFCAD), Thèse de Docteur de l'INPT, Toulouse, 1993.

[11] N. Ida, J.P.A.Bastos, Electromagnetics and Calculation of Fields, Springer-Verlag, New York, 1992.

[12] Raviart P.A., Thomas J.M., Introduction à l'analyse numérique des équations aux dérivées partielles, Masson, Paris, 1983.

[13] Silvester P.P., Chari M.V.K., "Finite element solution for saturable magnetic fields problems", IEEE Trans. on Power Apparatus and Systems, Vol. 89, pp. 1642-1651, 1970.

[14] N. Sadowski, R. Carlson, C.A. da Silva, L. Von Dokonal, "Simulation of Single Phase Induction Motors by Simultaneous Solution of Electrical and Field Equations", Proceedings of ICEM, Paris, 1994.

[15] N. Sadowski, R. Carlson, C. A. da Silva, M. Lajoie-Mazenc, "Simulation of Single Phase Induction Motor by a General Method for Coupling Field and Circuit Equations", Proceedings of IEEE-CEFC'94, Grenoble, 1994.

[16] N. Sadowski, B. Carly, Y. Lefevre, M. Lajoie-Mazenc, S. Astier, "Finite Element Simulation of Electrical Motors Fed by Current Inverters", IEEE Trans. on Magn., Vol. 29, N. 2, March 1993, pp. 1683-1688.

[17] N. Sadowski, Y. Lefevre, M. Lajoie-Mazenc, J. Cros, "Finite Element Torque Calculation in Electrical Machines while Considering the Movement", IEEE Trans. on Magn., Vol. 28, N. 2, March 1992, pp. 1410-1413.

Shape Design Optimization of Power Frequency Electromagnetic Devices Using Numerical Methods

Jaime A. Ramirez & Ernest M. Freeman
Imperial College of Science, Technology & Medicine
Electrical & Electronic Engineering Department
Exhibition Road, London SW7 2BT, UK

C. Chat-uthai
King Mongkut's Institute of Technology Ladkrabang
Department of Electrical Engineering
Ladbrabang, Bangkok 10520, Thailand

João A. Vasconcelos
Universidade Federal de Minas Gerais
Depto. de Engenharia Elétrica
Av. do Contorno 842, 30110-060 BH, MG, Brazil

Abstract - This paper presents the mathematical formulation concerning the solution of inverse electromagnetic problems, i.e. the shape optimization of power frequency electromagnetic devices, based on a combination of numerical methods. The optimization problem is solved using deterministic methods in which the electromagnetic field problem is treated as a subproblem of the optimization process. The field problem is calculated using the finite element (FE) method. Three deterministic approaches are studied in detail, the quadratic extended penalty method (QUA), the augmented Lagrange multiplier (ALM) method and the constrained quasi-Newton method (PLBA-CR). The work highlights the advantages and drawbacks of each approach. The search direction for the optimization is found by two distinct methods, the direct differentiation of the FE matrices and the finite difference (FD) method. In total, three problems are discussed in order to show the power and applicability of the theory presented. The PLBA-CR, when combined with the direct differentiation of the FE matrices, appears to offer important advantages over the other methods.

I. INTRODUCTION

The design of electromagnetic devices, such as electromagnets, electrical machines etc., has always been a challenge for electrical engineers. This process normally involves the determination of the shapes, dimensions, position of the core, permanent magnets and windings of the device, amongst other factors, which may produce prescribed electromagnetic quantities such as flux distributions, forces and torques.

In the past, such designs were a task based very much on the engineer's experience and intuition. After the advent of the computer in the fifties and its subsequent widespread use in the eighties, the whole process of design has changed. It is now possible to

analyse electromagnetic devices using computer aided design (CAD) techniques, see for instance [1]-[3]. However, a pure field analysis package may in many situations leave the engineer in an uncomfortable situation of having to change some key parameters in the design and then rerunning the program until an acceptable result is obtained.

In recent years there has been an enormous amount of work concerning the solution of inverse electromagnetic problems by means of numerical methods, see for instance the proceedings of the last Compumags and CEFCs. In addition to the solution of particular problems there have been advancements towards the automatization of some specific tasks, the shape optimization of electromagnetic devices is one example.

Mathematically, inverse problems such as the shape optimization of power frequency electromagnetic devices may be stated as a constrained optimization problem [4]. In general one may write

Minimize

$$F = F\big(\{p\}, \varphi(\{p\})\big) \qquad (1)$$

Subject to

$$g_j\big(\{p\}, \varphi(\{p\})\big) \le 0 \quad j = 1, \ldots, l \qquad (2)$$

$$h_k\big(\{p\}, \varphi(\{p\})\big) = 0 \quad k = 1, \ldots, m \qquad (3)$$

$$p_i^L \le p_i \le p_i^U \quad i = 1, \ldots, n \qquad (4)$$

where F represents the objective function, g_j are the inequality constraints, h_k are the equality constraints, p_i stands for the design variables and φ for the field variable. It has been assumed that the field variable φ is also a function of the design variable p. It is also important to note that the lower and upper limits given in (4) define the region of search in the n-dimensional space.

Classically (1) to (4) may be solved using either stochastic or deterministic methods. What differentiates these two sets is the way their numerical methods iterate.

Stochastic methods are based on probabilistic rules, i.e. they attempt to achieve the solution by exhaustive evaluations of the objective function (1). This feature is often seen as an advantage of these methods since a global optimum may be achieved theoretically. However, in many cases that same feature is regarded as a major drawback since the computational cost may become prohibitive. Recently special attention has been paid to the method of simulated annealing and the method of genetic algorithms for solving inverse problems, see for instance [5]-[7].

Deterministic methods, on the other hand, are based on an iterative line search where the design parameters p are varied systematically until an optimum value is found. Mathematically this is expressed by

$$\{p\}^{q+1} = \{p\}^q + \alpha^q S^q \qquad (5)$$

where α stands for the step size and S for the search direction which is calculated by

$$\{S\}^q = -\nabla F^q + \beta^q \{S\}^{q-1} \qquad (6)$$

with

$$\beta^q = \left|\nabla F^q\right|^2 \Big/ \left|\nabla F^{q-1}\right|^2 \qquad (7)$$

Thus, it becomes clear that the calculation of S requires the total differentiation of F with respect to p which in turn requires the differentiation of φ with respect to p. Indeed, deterministic methods have the advantage of using the information from one iteration to move to another. In many cases this feature makes the solver converge rapidly to an acceptable solution. This can represent substantial savings in computational costs. However, due to their nature deterministic approaches suffer from the potential limitation of getting stuck in a local minimum. For some works concerning the use of deterministic methods to inverse problems in electromagnetics refer to [8]-[10].

The aim of this paper is to present the mathematical formulation for the solution of shape optimization of power frequency electromagnetic devices. This is achieved by combining deterministic methods, which are used for the optimization process, with the FE method, which is used for solving the field problem. Three deterministic approaches are investigated: the quadratic extended penalty method (QUA), the augmented Lagrange multiplier (ALM) method and the constrained quasi-Newton method (PLBA-CR).

The advantages and drawbacks of each approach are highlighted. Concerning the calculation of the search direction, the work describes in detail how (6) may be obtained by direct differentiation of the FE matrices for time-harmonic, magnetostatic and electrostatic systems. Finally three problems are solved in order to show the applicability of the theory.

II. SENSITIVITY ANALYSIS

We shall describe in this part a methodology to obtain quantitative information on how the performance of the device is affected by changes in the design variables p_i. It is this information that provides the essential guideline for the search direction S given in (5). It will be assumed that the field analysis will be made using the FE method. Calculating the total derivative of (1) with respect to p_i gives

$$\frac{dF\big(\{p\}, \varphi(\{p\})\big)}{dp_i} = \frac{\partial F}{\partial p_i} + \left\{\frac{\partial F}{\partial \varphi}\right\}^{\mathrm{T}} \left\{\frac{\partial \varphi}{\partial p_i}\right\} \quad i = 1, \ldots, n \qquad (8)$$

The first term of (8), that is $\partial F / \partial p_i$, may be found from F which is normally given. The second term of (8) involves the calculation of $\{\partial \varphi / \partial p_i\}$ which can be evaluated from the FE formulation.

Time Harmonic System

Two dimensional time harmonic problems are governed by the following equation

$$\nabla \cdot \left(\nu \nabla A^*\right) - \sigma j \omega\, A^* = -J_e \qquad (9)$$

where ν is the magnetic reluctivity (linear), σ is the conductivity, $j = \sqrt{-1}$, ω is the frequency, J_e is the source current (assumed to be flowing only in the axial direction) and A^* is the complex vector potential (entirely oriented in the axial direction). It is important to note that in this case the field variable φ is A^*. Equation (9) may be solved term by term using the finite element method together with the Galerkin's approach to yield

$$\sum_{j=1}^{n} \left[\left(K_{ij} + \sigma j \omega\, T_{ij}\right) A_j^* - R_i\right] = 0 \quad i = 1, \ldots, n \qquad (10)$$

where n is the number of nodes. The three terms K_{ij}, T_{ij} and R_i may be found in [2], [3]. Thus, the

derivative $\left\{\partial A^* / \partial p_i\right\}$ may be obtained by differentiating (10), that is

$$\sum_{j=1}^{n}\left[\left(K_{ij}+\sigma j\omega T_{ij}\right)\right]\frac{\partial A_j^*}{\partial p}=\sum_{j=1}^{n}\left\{\left\{\frac{\partial R_i}{\partial p}\right\}-\frac{\partial\left[\left(K_{ij}+\sigma j\omega T_{ij}\right)\right]}{\partial p}\left\{A_j^*\right\}\right\}$$

(11)

The right hand side of (11) may be obtained by considering the derivative of K_{ij}, T_{ij} and R_i with respect to p, that is

$$\frac{\partial}{\partial p}K_{ij}A_j^* = \sum_e \int_{\Omega_e}\nu\frac{\partial\nabla N_{ij}}{\partial p}A_j\left|G^e\right|dudv$$

$$+\sum_e \int_{\Omega_e}\nu\nabla N_{ij}A_j^*\frac{\partial\left|G^e\right|}{\partial p}dudv$$

(12)

$$\frac{\partial}{\partial p}T_{ij}A_j^* = \sum_e \int_{\Omega_e}\frac{\partial}{\partial p}\left(-\sigma j\omega N_{ij}A_j^*\right)\left|G^e\right|dudv$$

$$-\sum_e \int_{\Omega_e}-\sigma j\omega N_{ij}A_j^*\frac{\partial\left|G^e\right|}{\partial p}dudv$$

(13)

$$\frac{\partial}{\partial p}R_i = \sum_e \int_{\Omega_e}\frac{\partial}{\partial p}\left(N_iJ_e\right)\left|G^e\right|dudv$$

$$+\sum_e \int_{\Omega_e}N_iJ_e\frac{\partial\left|G^e\right|}{\partial p}dudv$$

(14)

in which $\left|G^e\right|$ is the Jacobian of the element of reference and N is the trial function. After the calculation of $\left\{\partial A^* / \partial p_i\right\}$, the expression for $\left\{\partial B^* / \partial p_i\right\}$ may be obtained using $B^* = \nabla \times A^*$.

Magnetostatic System

Two dimensional magnetostatic systems are governed by the Poisson equation

$$\nabla^2 A = -\mu J$$

(15)

in which A represents the magnetic vector potential (the state variable φ in this case), μ the magnetic permeability and J the current density (oriented in the axis direction). Similar to the previous system, equation (15) may be solved using the FE method together with the Galerkin's approach to yield

$$\sum_{j=1}^{n}K_{ij}A_j - R_i = 0 \quad i = 1,\ldots,n$$

(16)

where n is the number of nodes. The two terms K_{ij} and R_i are identical to those from the previous system. In this case the derivative $\left\{\partial A / \partial p_i\right\}$ may be obtained from (16), that is

$$\sum_{j=1}^{n}\left[K_{ij}\right]\frac{\partial A_j}{\partial p}=\sum_{j=1}^{n}\left\{\left\{\frac{\partial R_i}{\partial p}\right\}-\frac{\partial\left[K_{ij}\right]}{\partial p}\left\{A_j\right\}\right\}$$

(17)

which can be calculated using (12) and (14). Likewise, after the calculation of $\left\{\partial A / \partial p_i\right\}$, the expression for $\left\{\partial B / \partial p_i\right\}$ may be obtained using $B = \nabla \times A$.

Electrostatic System

Similar to the magnetostatic system two dimensional electrostatic problems are also described by the Poisson equation

$$\nabla^2 V = -\frac{\rho}{\varepsilon}$$

(18)

in which V represents the electric scalar potential (the state variable φ in this case), ε the electric permittivity and ρ the charge density. In this case an axisymmetric system will be considered. Equation (18) can be solved using the FE method together with Galerkin's approach to yield

$$\sum_{j=1}^{n}K_{ij}V_j - R_i = 0 \quad i = 1,\ldots,n$$

(19)

in which n is the number of nodes. In this case the two terms K_{ij} and R_i are slightly different to those from a system with Cartesian symmetry, see [3] for instance. The derivative $\left\{\partial V / \partial p_i\right\}$ may be achieved by differentiating (19), that is

$$\sum_{j=1}^{n}\left[K_{ij}\right]\frac{\partial V_j}{\partial p}=\sum_{j=1}^{n}\left\{\left\{\frac{\partial R_i}{\partial p}\right\}-\frac{\partial\left[K_{ij}\right]}{\partial p}\left\{V_j\right\}\right\}$$

(20)

The right hand side of (20) may be calculated by considering

$$\frac{\partial}{\partial p}K_{ij}V_j = \sum_e \int_{\Omega_e}\pi r_0\varepsilon\frac{\partial\nabla N_{ij}}{\partial p}V_j\left|G^e\right|dudv$$

$$+\sum_e \int_{\Omega_e}\pi r_0\varepsilon\nabla N_{ij}V_j\frac{\partial\left|G^e\right|}{\partial p}dudv$$

(21)

and

119

$$\frac{\partial}{\partial p}R_i = \sum_e \int_{\Omega_e} \pi r_0 \frac{\partial}{\partial p}(N_i \rho_e)\left|G^e\right| du\, dv$$

$$+\sum_e \int_{\Omega_e} \pi r_0 N_i \rho_e \frac{\partial\left|G^e\right|}{\partial p} du\, dv \qquad (22)$$

where r_0 represents the mean value of the distances of the vertices of a generic element to the $0z$ axis. For a linear element $r_0 = (r_1 + r_2 + r_3)/3$. The expression for $\{\partial E/\partial p_i\}$ can then be obtained using $E = -\nabla V$.

It is important to note that for the three systems described previously the global system of equations, i.e. equations (10), (16) and (19), and their derivative with respect to p_i, i.e. equations (11), (17) and (20) respectively, are characterized by the matrix $\left[K_{ij}\right]$. Therefore, the application of an appropriate method for solving (10), (16) or (19) could represent a major saving in computational time. Indeed this is achieved if the Cholesky-decomposition is used as discussed by [9]. In this case the computational effort for the calculation of a single additional gradient vector $\{\partial\varphi/dp_i\}$ is reduced to forward and backward substitutions using the already decomposed matrix $\left[K_{ij}\right]$ from the corresponding global system.

An alternative way to calculate $\{\partial\varphi/\partial p_i\}$ would be to use the finite difference method rather than using the direct differentiation of the FE matrices. In general one may write

$$\frac{\partial\varphi}{\partial p_i} = \frac{\varphi(p + h_i e_i) - \varphi(p - h_i e_i)}{2h_i} \qquad (23)$$

where h_i, $h_i > 0$, is a small perturbation that is made in the global system of equations of the respective system. Indeed, equation (23) is much simpler and easier to implement into an existing FE code. However, there are two drawbacks associated in calculation of (23). The first is concerned with the introduction of round off errors. The second is related with the high number of field calculations required. A simple comparison to illustrate the latter will be made in the analysis of the results.

III. NUMERICAL OPTIMIZATION METHODS

We shall consider in this part the mathematical formulation of three deterministic methods which are capable of solving the general optimization problem posed by (1) to (4). The advantages and limitations of each approach will be highlighted.

Deterministic methods may be divided into two sets: indirect and direct methods. Indirect approaches are also known as SUMT (sequential unconstrained

minimization techniques). The concept of these techniques is to create a pseudo function Ψ using the original objective and constraint functions and then minimize this pseudo function as an unconstrained function. In general form one may write

Minimize

$$\Psi\left(\{p\}, r_p\right) = F\left(\{p\}, \varphi(\{p\})\right) + r_p P\left(\{p\}, \varphi(\{p\})\right) \qquad (24)$$

where r_p is a penalty multiplier and P is an imposed penalty function whose form depends on the SUMT being employed. Normally, the penalty multiplier is updated according to $r_p^q = r_p^{q-1}\gamma$. In this paper two SUMT are investigated, the quadratic extended penalty function method (QUA) and the augmented Lagrange multiplier method (ALM). In both cases the unconstrained function is minimized using the BFGS method [4].

Direct methods are those approaches that tackle the original objective and constraint functions directly rather than creating a pseudo function. In this work only the constrained quasi-Newton method PLBA-CR will be investigated.

Quadratic Extended Penalty Function Method (QUA)

The quadratic extended penalty function method (QUA) was proposed in 1976 by [11]. The pseudo function is defined everywhere and also has a continuous first and second derivative. This important feature allows the application of second order methods, if needed, for the unconstrained minimization of the pseudo function. The QUA method also provides a sequence of improving feasible designs. In theory, this approach tends to be numerically better conditioned when compared to its predecessors [4].

Mathematically the penalty function is defined by

$$P(p) = \sum_{j=1}^{l} \tilde{g}_j(p) \qquad (25)$$

where

$$\tilde{g}_j(p) = \begin{cases} \dfrac{-1}{g_j(p)} & \text{if} \quad g_j(p) \le -\varepsilon \\[4mm] \dfrac{1}{\varepsilon}\left[\left[\dfrac{g_j(p)}{\varepsilon}\right]^2 + \dfrac{3g_j(p)}{\varepsilon} + 3\right] & \text{if} \quad g_j(p) > -\varepsilon \end{cases}$$

$$(26)$$

in which ε is in this case the transition parameter

defined by $\varepsilon = -C\left(r_p\right)^a$; $1/3 \le a \le 1/2$ and C is a constant. It is clear that due to its quadratic form the penalty function (26) may become highly nonlinear. This is often seen as the disadvantage of this approach. Highly nonlinear functions may converge slowly or not converge at all. In addition, it has also been noticed [4] that the QUA method is sensitive to the value of the penalty multiplier r_p, a feature that may lead to overflow. This may be avoided by selecting a small r_p, say 1 and a soft γ, say 0.7.

Augmented Lagrange Multiplier Method (ALM)

The augmented Lagrange multiplier method (ALM) is an approach which incorporates the advantages of the penalty methods. In particular the ALM method includes information concerning the constraint functions in the process which updates the Lagrange multipliers. This feature enhances the efficiency and reliability of this approach. In fact, it has been argued by [12] that the use of SUMT which do not include Lagrange multipliers is obsolete as a practical optimization tool.

In mathematical form the ALM method may be defined by a pseudo function expressed as

$$L\left(p,\lambda,r_p\right) = F(p) + \sum_{j=1}^{l}\left[\lambda_j\psi_j + r_p\psi_j^2\right]$$
$$+ \sum_{k=1}^{m}\left\{\lambda_{k+m}h_k(p) + r_p\left[h_k(p)\right]^2\right\} \quad (27)$$

where

$$\psi_j = \max\left[g_j(p),-\frac{\lambda_j}{2r_p}\right] \quad (28)$$

in which λ stands for the Lagrange multipliers. The update formulas for the Lagrange multipliers are

$$\lambda_j^{q+1} = \lambda_j^q + 2r_p\left\{\max\left[g_j(p),\frac{-\lambda_j^q}{2r_p}\right]\right\} \quad j=1,l \quad (29)$$

$$\lambda_{k+l}^{q+1} = \lambda_{k+l}^q + 2r_p h_k\left(p^q\right) \quad k=1,m \quad (30)$$

In summary, the following important advantages can be highlighted concerning the ALM approach. First, the method is relatively insensitive to the values of r_p. Second, it is not necessary to increase $r_p \to \infty$ to get the optimum solution since the process of updating the Lagrange multipliers requires information concerning the constraint functions, a feature which speeds up the convergence process. Third, in theory it is possible to obtain precise

$g_j(p) \le 0$ and $h_k(p) = 0$. Fourth, the starting point may be either feasible or infeasible.

Constrained Quasi-Newton Method (PLBA-CR)

In the PLBA-CR approach the search direction is found by solving a subproblem with quadratic objective and linear constraint. The objective function is augmented using Lagrange multipliers and an exterior penalty so that the resulting one dimensional search is unconstrained. In mathematical terms the subproblem to be solved, i.e. the search direction vector S, may be expressed by

Minimize $\quad f = \mathbf{c}^{\mathrm{T}}S + 0.5S^{\mathrm{T}}\mathrm{H}S \quad (31)$

Subject to $\quad \mathrm{A}^{\mathrm{T}}S \le \mathbf{b}$, $\mathrm{N}^{\mathrm{T}}S = \mathbf{e}$, $S \le 0 \quad (32)$

where

$$\mathbf{c}^{\mathrm{T}} = \left[\frac{\partial F[p,\varphi(p)]}{\partial p_1} \cdots \frac{\partial F[p,\varphi(p)]}{\partial p_i}\right] \quad (33)$$

A is an $n \times l$ matrix of the gradient of the inequality constraint ($a_{ij} = \partial g_j(p)/\partial p_i$), N is an $n \times m$ matrix of the gradient of the equality constraint ($n_{ik} = \partial h_k(p)/\partial p_i$), H is an $n \times n$ approximate Hessian matrix of the Lagrange function, $b_j = -\left[g_j(p)\right]$ and $e_k = -\left[h_k(p)\right]$.

The QP subproblem that gives constraint correction can be developed by neglecting the first term of (31) and subject to the same constraints as (32). The solution to this subproblem gives a direction with the shortest distance to the constraint boundary from infeasible point. The subproblem for the objective reduction algorithm can be defined by setting the right-hand side vector e in (32) to be zero. The step size (α) can be calculated with the required reduction in objective which is based on a fractional reduction (γ) as $\alpha = \left|\gamma f\right|/\left|\mathbf{c} \cdot S\right|$ [4].

IV. RESULTS

Magnetostatic Problem

The problem consists in determining the optimum shape of the poles of an electromagnet in order to maintain the magnetic flux density B constant in its air gap. Half of the electromagnet is shown in Fig.2a. The 2D model used in the analysis is given in Fig.2b. The 2D domain is made up of three main regions defined by $\Omega = \Omega_F + \Omega_C + \Omega_A$, where Ω_F, Ω_C and Ω_A represent the ferromagnetic, coil and air region, respectively. Dirichlet and Neumann boundary

conditions are imposed on Γ_0 and on Γ_1 respectively. The mesh used in the simulations consisting of 156 nodes and 263 elements is illustrated in Fig.3a. A zoom in the pole face showing the moving nodes is given in Fig.3b. The data used in the simulations are given as follows: $\mu = 1000\mu_0$ in Ω_F and $J = 1000$ A / cm^2 in Ω_C.

(a)   (b)
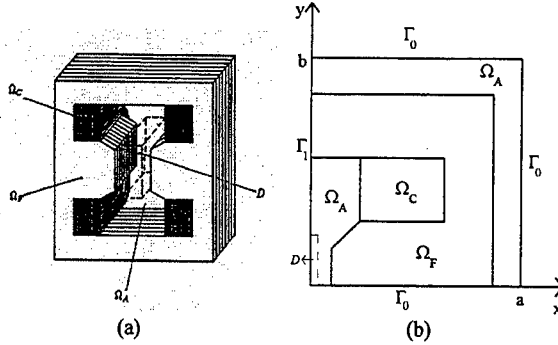
Fig. 2. Electromagnet

(a)   (b)
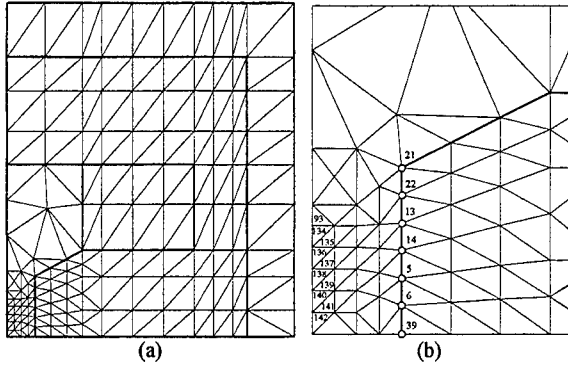
Fig.3 FE mesh used in the simulations

The aim of this problem is to find the optimum position of the moving nodes indicated in Fig.3b, the design variables p_i, which set up a shape in the pole of the electromagnet that insure a given constant flux density B_d over D (which includes 9 elements, also indicated in Fig.3b). Mathematically the problem can be defined as

$$\text{Minimize} \quad F = \sum_{q=1}^{9} \left| B_{c_q} - B_d \right|^2 \quad (34)$$

Subject to

$$g_j(p) \equiv \frac{p_j^2 - \left(p_j^U + p_j^L\right)p_j + p_j^U p_j^L}{\left(p_j^U - p_j^L\right)^2} \le 0 \quad (35)$$

$$0.012 \le p_j \le 0.017 \text{ m} ; \quad j = 1,...,6 \quad (36)$$

This problem was also used to validate the sensitivity analysis. The comparison for the calculation of $\{\partial B/\partial p\}$ using the differentiation of the FE matrices and the FD method for node 5 is given in Table I.

Each component of the gradient vector ∇F is obtained as a summation of terms of the form

$$\frac{dF}{dp_j} = \frac{\partial F}{\partial p_j} + \frac{\partial F}{\partial |B_c|}\frac{\partial |B_c|}{\partial p_j} = 2|B_c - B_d|\frac{\partial |B_c|}{\partial p_j} \quad (37)$$

The term $\partial |B_c|/\partial p_j$ in (37) is calculated using the formulation presented in section II.

TABLE I
RESULTS CONCERNING THE CALCULATION OF $\{\partial B/\partial p\}$

	Node 5 $\{\partial B/\partial p\}$	
Element	FE	FD
93	-3.1506	-3.1437
134	-7.4744	-7.4641
135	-5.0445	-5.0147
136	-6.6736	-6.6680
137	-5.1984	-5.1649
138	-7.5811	-7.5815
139	-7.2837	-7.2755
140	-7.6979	-7.6616
141	-8.2650	-8.2737
142	-7.9274	-7.8926

The final result for $B_d = 0.35$T is given in Table II. The number of function evaluations corresponds to the number of field solutions required in which FE stands for the direct differentiation of the FE matrices and FD for the finite difference method. The final shape obtained for the pole of the electromagnet is shown in Fig.4.

TABLE II
FINAL RESULT FOR $B_d = 0.35$T

Element	QUA $\|B_c\|$ (T)	ALM $\|B_c\|$ (T)	PLBA-CR $\|B_c\|$ (T)
134	0.3498	0.3510	0.3493
135	0.3479	0.3472	0.3483
136	0.3499	0.3492	0.3496
137	0.3518	0.3505	0.3522
138	0.3502	0.3501	0.3495
139	0.3514	0.3501	0.3507
140	0.3499	0.3507	0.3493
141	0.3507	0.3503	0.3495
142	0.3499	0.3509	0.3492
No.of function evaluations (FE)	742	642	151
No. of function evaluations (FD)	2474	2388	755
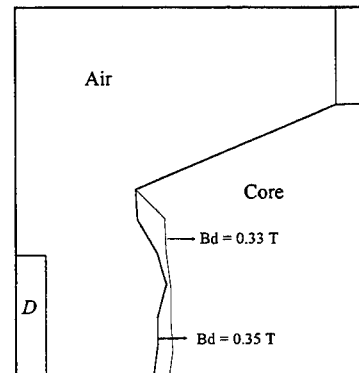
Fig.4 - Final shape obtained using the PLBA-CR method

122

Electrostatic Problem

The objective in this idealised problem is to reduce the E tangential at the top surface of an insulator to values lower than 16 KV/m (this is just an example). The two dimensional model investigated is given in Fig.5. The mesh used in the simulations consisting of 261 nodes and 494 elements is given in Fig.6. The insulator is made of porcelain ($\varepsilon_r = 7$) and is surrounded by air. Neumann boundary condition was imposed on Γ_1. The problem was reduced to find the optimum values of L_1 and the three arcs defined by R_1, R_2 and R_3 and their respective angles, θ_1, θ_2 and θ_3. The initial values for these variables are $R_1 = 4.0\text{mm}$, $R_2 = R_3 = 5.0\text{mm}$ and $\theta_1 = \theta_2 = \theta_3 = 90$.
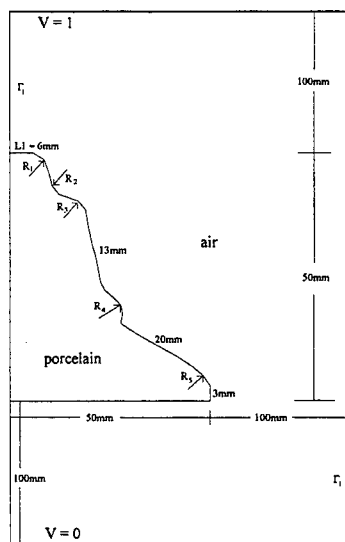
Fig.5 - Idealised insulator
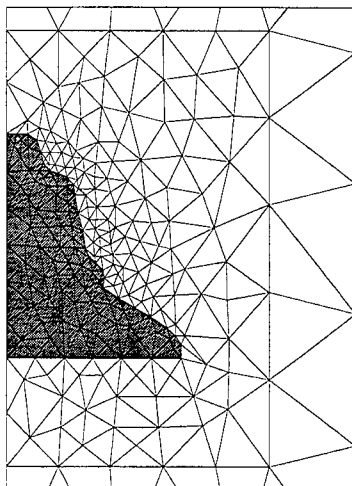
Fig.6 - Mesh used in the simulations

The objective function in this case is given by

Minimize $\quad F = \sum_{i=1}^{n} \left| E_{c_i} - E_{d_i} \right|^2 \quad$ (38)

in which n is the number of test points where E will be calculated. Four points were considered, one in the middle of L_1 and the other three situated in the middle of the surface of the arcs 1,2 and 3. The design variables were subject to the following constraints $3 \le p \le 10mm$ for L_1; $3 \le p \le 10mm$ for R_1, R_2 and R_3; $0 \le p \le 90$ degrees for θ_1, θ_2 and θ_3. The initial and final shape of the insulator for the target defined are given in Fig.7. Table III gives the information concerning the optimization process.
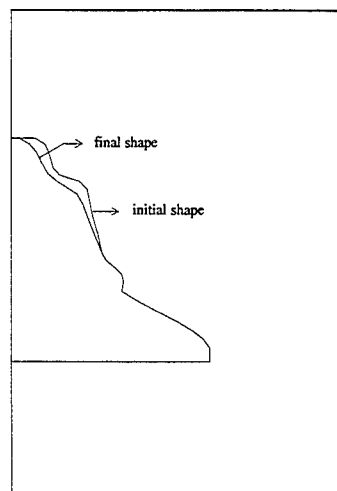
Fig.7 - Initial and final shape for the insulator

TABLE III
RESULTS CONCERNING THE ELECTROSTATIC PROBLEM

Variables	ALM	PLBA-CR
L_1 (mm)	3.0	3.25
R_1 (mm)	8.25	8.0
θ_1 (degrees)	61.94	64.12
R_2 (mm)	6.32	6.14
θ_2 (degrees)	53.10	55.10
R_3 (mm)	7.62	7.48
θ_3 (degrees)	43.63	45.74
No. of function evaluations (FE)	496	164

Time Harmonic Problem

The idealised problem considered here consisted in the determination of the optimum shape of a conducting cylinder of copper placed under the influence of a transverse time harmonic field. The objective is to obtain the magnetic flux density in the interior region of the cylinder at certain prescribed values, whilst keeping its area constant. The cylinder is assumed to be infinitely long in the z direction. One quarter of the 2D model is shown in Fig.8 (not to scale). The detail of the mesh used consisting of 264 nodes and 472 elements is shown in Fig.9.

123
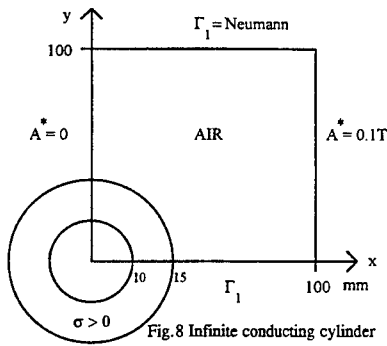
Fig.8 Infinite conducting cylinder

Mathematically this problem may be expressed by

Minimize $\quad F = \sum_{i=1}^{n} \left| B_{c_i}^* - B_{d_i}^* \right|^2 \qquad$ (39)

which was subject to the following constraints, ±5% variation allowed in the area of the cylinder, $13 \leq p \leq 18mm$ and $8 \leq p \leq 12mm$ for the moving nodes of the outer and inner radius respectively. The objective function (39) was evaluated over all elements included in a 4mm² centered on the origin, see Fig.9. The final shape achieved for $B^* < 1.0T$, $f = 50Hz$ is shown in Fig.10. In this case the ALM method took 633 functions evaluations to converge whereas the PLBA-CR took 178.
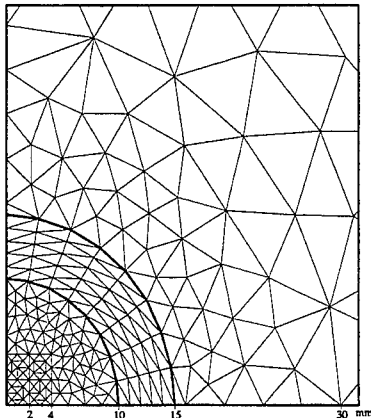
Fig.9 - Mesh used in the simulations
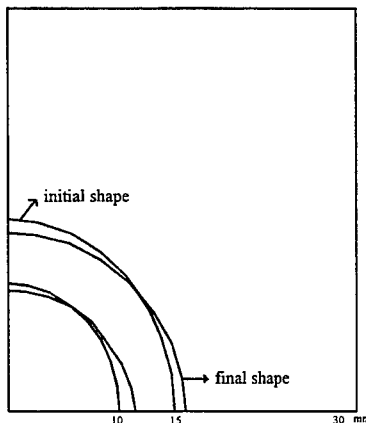
Fig.10 - Final shape for the conducting cylinder

V. CONCLUSIONS

This paper shows how the shape optimization of electromagnetic devices may be solved using deterministic methods combined with the FE approach. In particular it has been shown how to obtain the equations concerning the search direction S, which are essential for deterministic methods, for 2D time harmonic systems by direct differentiation of the FE matrices. In addition it has also been indicated how to obtain the corresponding equations for 2D magnetostatic and electrostatic systems. It has been observed that the direct differentiation of the FE matrices requires less field calculations than the FD method. Three deterministic approaches were investigated. In particular, it has been noticed that the ALM method is in general more efficient and reliable than the QUA method. In terms of field calculations, it has been found that the PLBA-CR is the most efficient amongst the approaches studied. In general, it converged to an acceptable solution requiring five to ten time less computing CPU time than the QUA and ALM methods, see Tables II and III. The three problems solved indicate the power and applicability of the theory. Finally, the authors believe that the theory is of sufficient generality to be extended to 3D problems.

REFERENCES

[1] P.P. Silvester and R.L. Ferrari, Finite Elements for Electrical Engineers. CUP, Cambridge, UK, 2nd ed., 1990.

[2] S.R.H. Hoole, Computer Aided Analysis and Design of Electromagnetic Devices. Elsevier, New York, 1989.

[3] N. Ida and J.P.A. Bastos, Electromagnetics and Calculation of Fields. Spring Verlag, New York, 1992.

[4] G.N. Vanderplaats, Numerical Optimization Techniques for Engineering Design: with Applications. McGraw-Hill, 1984.

[5] K. Preis, C. Magele, O. Biro, FEM and evolution strategies in the optimal design of EM devices. IEEE Trans. on Mag., vol.26, no.5, pp.2181-2183, September 1990.

[6] J. Simkin and C.W. Trowbridge, Optimizing electromagnetic devices combining direct search methods with simulated annealing. IEEE Trans. on Mag., vol.28, no.2, pp.1545-1548, March 1992.

[7] J.A. Vasconcelos, L. Krähenbühl, L. Nicolas, A. Nicolas, Design optimization using BEM coupled with genetic algorithm. Proc. of the 2nd IEE Int. Conf. on Computational Electromagnetics. Nottingham, UK: 12-14 April, 1994.

[8] S. Gitosusastro, J.L. Coulomb, J.C. Sabonnadiere, Performance Derivative Calculations and Optimization Process. IEEE Trans. on Mag., vol.25, no.4, pp.2834-2839, July 1989.

[9] S.R.H. Hoole, Optimal design, inverse problems and parallel computers. IEEE Trans. on Mag., vol.27, no.5, pp.4146-4149, September, 1991.

[10] S. Russenschuck, Application of Lagrange multiplier estimation to the design optimization of permanent magnet synchronous machines. IEEE Trans. on Mag., vol.28, no.2, pp.1525-1528, March, 1992.

[11] R.T. Haftka and J.H. Starnes Jr., Applications of a quadratic extended interior penalty function for structural optimization. AIAA Journal. vol.14, no.6, pp.718-724, June, 1976.

[12] M.J.D. Powell, Optimization Algorithms in 1979. Committe on Algorithms Newsletter, no.5, Mathemathical Programming Society, pp.2-16, February, 1981.

Determination and Analysis of Causes of Induction Motor Magnetic Noise

Sebastião Lauro Nau and Solon Brum Silveira
WEG Motores Ltda.
C.P. 420
89256-900 Jaraguá do Sul - SC - Brazil

Abstract - This paper presents the causes of the acoustic noise magnetically generated by three-phase induction electric motors and some results of tests and calculation are discussed. The influence of the rotor slots skewing on the reduction of the magnetic noise is also analysed through calculated values. The paper gives a general view about how the magnetic noise in induction motors is generated and how much its prevision is important during the design stage.

INTRODUCTION

Basically, the rotating electric machines have three noise sources:
a) due to the ventilating system;
b) due to the bearings;
c) magnetic origin.

The segregation of the noise in these three categories permits the evaluation of each source individually. So, it is possible to determine the higher intensity source which must be reduced.

The noise due to the ventilating system is particularly important in the 2 and 4 poles motors. In these motors it is the highest noise source. By the other hand, in the 6 and greater poles motors the main noise source is the electromagnetic circuit. There are two reasons for that: first, as the velocity of the fan decreases with the increase of the numbers of poles, the noise generated by it also decreases. Second, in opposition, if the number of poles is higher, the stator yoke height is smaller. So, as it is easier to deform a stator core with a thin yoke than with a thick one, the generated noise due to electromagnetic origins is higher.

The noise due to the bearings is not significant in comparison with the other causes when the bearings have no failures. Otherwise, if the bearings are damaged, the noise can be increased very much. In such case, the solution is to change those bearings.

Many researchers have investigated and written about magnetic noise in electric motors. Kako et alli [1] considered the magnetic noise only due to slot harmonics and they determined the noise emitted by a motor for a skewed and non-skewed rotor, but they did not mention how much the rotor was skewed. Brauer [2] described a digital computer program which predicts the total magnetic noise of induction motors. But, for pratical results, it is very important to make evident each cause of the magnetic noise in order to reduce the biggest one. This is the aim of this paper.

The references were selected taking into account the objective of the paper. We suppose to be more appropriate to consider pioneer but still current works about the basics of this subject [3, 4, 5, 6, 7], including doctorate dissertation [6, 7] in order to clarify some aspects about the generation of the magnetic noise. Nevertheless, other avaliable recent books and papers were also analysed just to give us more information and knowledge about magnetic noise, but they were not used as reference.

The originality of this paper is to present the causes of the magnetic noise separately for three-phase induction motors as well as the results calculated for 24 different motors from 1 hp to 550 hp for 2, 4, 6 and 8 poles. The influence of the rotor slots skewing is also analysed for several values of skewing.

MAGNETIC NOISE GENERATION

The noise of magnetic origin in electric machines is generated by the interaction of the induction waves (fundamental and harmonics) present in the airgap. These waves are variable in space and time and exist because of the winding distribution and variation of the airgap permeance due to the stator and rotor slots, saturation and eccentricity. These induction harmonics, combined themselves according to Maxwell's tensor expression, generate periodic force waves in the airgap deforming the stator core and exciting the surrounding air. This way, the acoustic noise is generated. The Fig. 1 shows this situation.

The induction harmonic calculation as well as the determination method of magnetic noise were early presented by Jordan [3] in 1950. Nevertheless, the magnetic noise calculation requires thousands of combinations of the harmonics. Therefore, a reliable and fast determination of magnetic noise became

possible only after the computers appearance.

It is not easy to determine accurately the magnetic noise. The accuracy of the results is reduced by the simplificative hypothesis which are necessary to eliminate some randomic influences of the motor manufacturing process. In fact, the magnetic noise determination is accurate in relation to the frequencies involved. Nevertheless, the results of the sound pressure level or sound power level do not have a good accuracy in all cases. In some cases they provide us only a good idea about the magnetic noise.

mmf linear density
$$a(x,t) = \sum_{\mu} A_{\mu} \cdot sen(\mu x - \omega_{\mu}t - \phi_{\mu})$$
airgap permeance
$$\Lambda(x,t) = \Lambda_0 + \sum_{\lambda} \Lambda_{\lambda} cos(\lambda x - \omega_{\lambda}t - \phi_{\lambda})$$

airgap induction
$$b(x,t) = \sum_{\nu} B_{\nu} \cdot cos(\nu x - \omega_{\nu}t - \phi_{\nu})$$

radial pressure waves
$$P_r(x,t) = P_r \cdot cos(rx - \omega_r t - \phi_r)$$

stator deformation
$$y_r(x,t) = y_r \cdot cos(rx - \omega_r t - \phi_r)$$

sound pressure level
$$L_r = 20 \log(9,05.10^7.f_r.y_r) + 10 \log P_{rel}$$
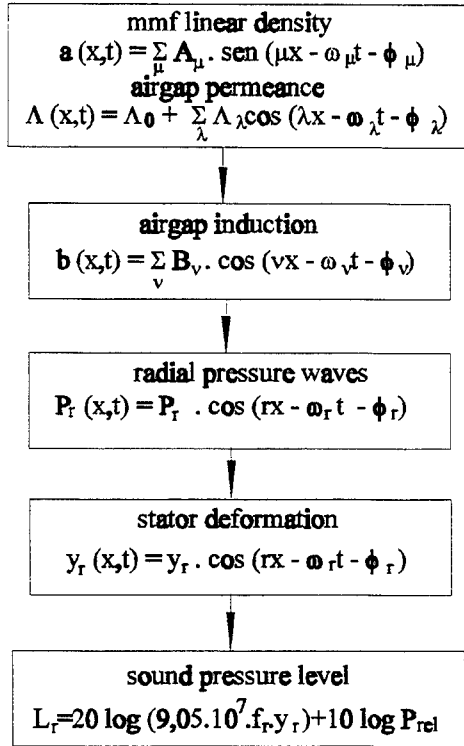
Fig. 1: Magnetic noise generation scheme

In Fig.1, Prel is a correction in sound pressure level that considers the cylindrical surface of the motor and fr is the frequency of the force wave.

RADIAL FORCE WAVES

On the stator surface in contact with the airgap, i. e., in the boundary between two regions with different permeabilities - in this case iron and air - radial forces act. Such forces are proportional to the squared airgap induction b(x,t). The Maxwell's tensor expression

gives the magnetic pressure P(x,t) [4,5,6]:

$$P(x,t) = \frac{b(x,t)^2}{2\mu_0} \qquad (1)$$

Where μ_0 is the air permeability.

The airgap induction b(x,t) is, actually, the sum of the fundamental induction wave with all harmonics due to winding distribution, stator and rotor slots, saturation and eccentricity [3]. Generally, b(x,t) is expressed by [4,5]:

$$b(x,t) = \sum_{n=1}^{p} B_n \; cos \; (\nu_n x - \omega_n t - \varphi_n) \qquad (2)$$

Where:
B_n = amplitude of the induction harmonic
ν_n = pair of poles of the induction harmonic
x = space coordinate
ω_n = angular frequency of the induction harmonic
ϕ_n = phase angle of the induction harmonic
p = integer number as high as possible to
    consider the most of the induction harmonics.

So, developing the equation (1), it results:

$$P(x,t) = \frac{1}{2\mu_0}\sum_{n=1}^{p}\frac{Bn^2}{2}[1 + cos(2\nu_n x - 2\omega_n t - 2\varphi_n)] +$$

$$+ \frac{1}{2\mu_0}\sum_{n=1}^{p-1}\sum_{m=n+1}^{p} B_n \cdot B_m \cdot$$

$$\cdot cos \; [(\nu_n \pm \nu_m)x - (\omega_n \pm \omega_m)t - (\varphi_n \pm \varphi_m)] \qquad (3)$$

It can be noted that the magnetic pressure is formed by a constant term, a double frequency term and one third term where induction harmonic frequency and pair of poles are given by adding and subtracting each individual component.

The waves of the induction harmonics are given according to [4] by:

$$b(x,t) = \mu_0 R \Lambda(x,t). \sum_{v=1}^{n} \frac{A_v}{v}.\cos\ (vx - \omega v.t - \varphi_v) -$$

$$- \frac{1}{2\pi\Lambda_0} \sum_{v=1}^{n} \sum_{\lambda=1}^{n} \frac{A_v . \Lambda_\lambda}{2v} \int_{0}^{2\pi} f(x,t)dx \qquad (4)$$

Where f(x,t) is given by:

$$f(x,t) = \left[\cos\ (v \pm \lambda)x - (\omega_v \pm \omega_\lambda)t - (\varphi_v \pm \varphi_\lambda)\right] \qquad (5)$$

The permeance $\Lambda(x,t)$ is given by a constant permeance of the airgap $\Lambda_0(t)$ and a sum of periodic permeances due to slots, saturation and eccentricity generically shown as follows:

$$\Lambda(x,t) = \Lambda_0(t) + \sum_{\lambda=1}^{n} \Lambda x . \cos\ (\lambda x - \omega_\lambda . t - \varphi_\lambda) \qquad (6)$$

and the mmf linear density a(x,t) is given by:

$$a(x,t) = -\sum_{v=1}^{n} A_v sen\ (vx - \omega_v t - \varphi_v) \qquad (7)$$

The equations to calculate the permeances and mmf linear density are not shown in this paper. They are easily found in the literature [4].

Solving the equation (4), the fundamental and the induction harmonics waves are determined. In this survey, each induction harmonic component is separated in groups according to its origin as follows :

1. **Fundamental induction wave.** It is determined by multiplying the fundamental magnet-motive force (mmf) by the constant permeance of the airgap.

2. **Harmonics due to stator and rotor windings.** These harmonics exist due to the variation of the mmf caused by the winding distribution combined with the constant permeance of the airgap.

3. **Harmonics due to stator and rotor slots.** They occur due to the combination of stator and rotor slots permeance with the mmf.

4. **Harmonics due to the interaction between stator and rotor slots.** They occur due to the mutual permeance between stator and rotor slots combined with the mmf.

5. **Fundamental saturation wave.** It is determined from the fundamental mmf combined with the saturation permeance waves.

6. **Harmonics due to stator and rotor slots saturation.** These harmonics are caused by the mutual permeance due to the saturation and stator and rotor slots combined with the mmf.

7. **Harmonics due to stator and rotor winding saturation.** These harmonics are caused by the saturation mmf waves combined with the constant permeance of the airgap.

8. **Fundamental eccentricity wave.** It is determined from the fundamental mmf combined with the eccentricity permeance waves.

9. **Harmonics due to stator and rotor slots eccentricity.** These harmonics are caused by the mutual permeance due to the eccentricity and stator and rotor slots combined with the mmf.

10. **Harmonics due to stator and rotor winding eccentricity.** These harmonics are caused by the eccentricity mmf waves combined with the constant permeance of the airgap.

These induction harmonics, combined according to (1) give as result force density waves which deform the stator core periodically in time and space, generating the noise. Nevertheless, only few combinations can provide a high level of sound power [5]. In order to limit the number of possible combinations of the induction harmonics, it is enough to consider the following combinations:

- **stator harmonics with themselves**

$$r = v_1 + v_2 \qquad (8)$$
$$f_r = 2 f_v \qquad (9)$$

- **stator harmonics with rotor harmonics**

$$r = \lambda \pm v \qquad (10)$$
$$f_r = f_\lambda \pm f_v \qquad (11)$$

127

- **stator harmonics with rotor saturation harmonics**

$$r = \lambda_s \pm v \qquad (12)$$

$$fr = f_{\lambda s} \pm f_v \qquad (13)$$

- **stator harmonics with rotor eccentricity harmonics**

$$r = \lambda_\varepsilon \pm v \qquad (14)$$

$$fr = f_{\lambda \varepsilon} \pm f_v \qquad (15)$$

- **rotor harmonics with stator saturation harmonics**

$$r = v_s \pm \lambda \qquad (16)$$

$$fr = f_{vs} \pm f_\lambda \qquad (17)$$

- **rotor harmonics with stator eccentricity harmonics.**

$$r = v_\varepsilon \pm \lambda \qquad (18)$$

$$fr = f_{v\varepsilon} \pm f_\lambda \qquad (19)$$

The parameters used to determine the vibration modes r and the noise frequencies fr are listed below for three phase squirrel cage induction motors:

$$v = p\,(1 + 6g_1) \qquad g_1 = 0, \pm 1, \pm 2, \pm 3, \ldots$$

$$\lambda = v + g_2 N_2 \qquad g_2 = \pm 1, \pm 2, \pm 3, \ldots$$

$$v_s = 3\,p + g_s N_1 \qquad g_s = 0, \pm 1, \pm 2, \pm 3, \ldots$$

$$\lambda_s = v_s + g_s\,N_2$$

$$v_\varepsilon = p \pm 1 + g_\varepsilon\,N_1 \qquad g_\varepsilon = 0, \pm 1, \pm 2, \pm 3, \ldots$$

$$\lambda_\varepsilon = v_\varepsilon + g_\varepsilon\,N_2$$

$$f_v = f$$

$$f_\lambda = f + \frac{g_2\,N_2}{p}\,(1 - s)\,f$$

$$f_{vs} = 3f$$

$$f_{\lambda s} = 3f + \frac{g_2\,N_2}{p}\,(1 - s)\,f$$

$$f_{v\varepsilon} = f$$

$$f_{\lambda \varepsilon} = f + \frac{g_\varepsilon\,N_2}{p}\,(1 - s)\,f \qquad \text{for static eccentricity}$$

$$f_{\lambda \varepsilon} = f + \frac{g_\varepsilon\,N_2 \pm 1}{p}\,(1 - s)\,f \qquad \text{for dynamic eccentricity}$$

Where:

v/f_v: pairs of poles/frequency of stator harmonics

λ/f_λ: pair of poles/frequency of rotor harmonics

v_s/f_{vs}: pair of poles/frequency of stator saturation harmonics

$\lambda_s/f_{\lambda s}$: pair of poles/frequency of rotor saturation harmonics

$v_\varepsilon/f_{v\varepsilon}$: pair of poles/frequency of stator eccentricity harmonics

$\lambda_\varepsilon/f_{\lambda \varepsilon}$: pair of poles/frequency of rotor eccentricity harmonics

Actually, the most important source of magnetic noise in induction motors is the combination of the stator induction harmonics with the rotor induction harmonics. Sometimes the fundamental induction wave combined with itself can also produce a high level of noise and vibration with double line frequency.

NOISE DETERMINATION

For each force wave generated by interaction of the induction harmonics, it is calculated the deformation y_r on the stator surface, the vibration mode r, the excitation frequency of this force f_r and the natural frequency of stator f_n for each vibration mode [3]. The expressions used to calculate the vibration mode r and the excitation frequency fr are given in the equations (8) to (19). The expressions for deformation Yr and natural stator frequency fs are well known from literature [4, 6]. The rotor deformation can be neglected, because it is very much easier to deform the stator than the rotor.

After that, the sound pressure level in dB or dB(A) on the stator surface is determined, considering it as a vibrating free body. In the determination of magnetic noise are considered only the radial forces acting in the motor airgap. The proximity between natural frequencies and excitation frequency are considered through a ressonance factor [5] that can increase significantly the noise. In practice, it is not easy to find good results for this factor, because the algebric expressions do not take into account the influence of the frame. So, as suggestion, perhaps better results would be acquired through the use of an finite element method to determine the natural frequencies of the motor.

Vibration Mode

The vibration mode r, that results from the combination of the induction harmonic pole pairs is important until, at maximum, r=20 for large machines. Normally, it is enough to consider r=12. The natural frequency of the stator is determined for each vibration mode. The force waves deform the stator according to the vibration mode. Fig. 2 shows these deformations. For r = 0, the force has a uniform distribution along stator bore, varying in time. For r = 1, there is a rotating radial force over the stator or rotor. The stator deformations are not considered, only the rotor

bending. For r=2 or more there are rotating radial forces applied on 2r points of stator that deform it periodically in time and space. The most critical case for deformation and consequently noise generation is when r=2 because, in this case, the stator is eliptically deformed. This is the easiest way to deform it.
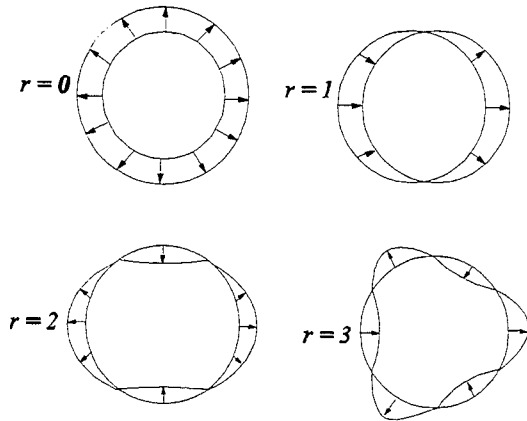
Fig. 2: Vibration modes

Results

The results of the magnetic noise calculation on the stator surface are shown in the Table 1 for several motors on load from 1 hp (0.75 kW) to 550 hp (400 kW) for 2, 4, 6 and 8 poles. These results were obtained using a software developed for FORTRAN 77 (Microsoft FORTRAN Powerstation 32 bits) with the presentation of the results for WINDOWS. This software calculates and shows the noise separated by causes and it runs together with WEG's motor design and calculation softwares in order to give to our engineers a fast analysis tool. In the Table 1 are shown only the most significant values for each vibration mode and cause. There are three separated columns, according to the causes of the magnetic noise: **winding/slots, saturation** and **eccentricity based on 10%**. For each column there are still two other columns indicating what combinations of flux density harmonics were considered according to equations (8) to (19).

In order to condense the results presentation, the frequency and the vibration mode are shown only for the higher sound pressure level calculated. In the Table 1 the sound pressure level Lr is shown for 1 meter far from the motor surface and it is given in dB(A). N1 is the number of stator slots and N2 is the

number of rotor slots. The sound pressure levels below zero are not shown in the Table 1.

Some values of sound pressure level are higher than those obtained from the tests. This indicates that it is important to consider the influence of the motor frame in the stator natural frequencies. In this simulation the influence of the motor frame was neglected. If the resonance factor is too high when only the stator dimensions are considered in the natural frequency determination, the simulation results are higher than those obtained from the tests. Otherwise, if the resonance factor is low, the calculation can indicate a low value and the tests can indicate a high one.

INFLUENCE OF THE ROTOR SLOTS SKEWING ON THE MAGNETIC NOISE

Rotor slots skewing is a very useful way to reduce the rotor slot harmonics. As the rotor slots harmonics are an important cause in the generation of the magnetic noise, their reduction or elimination can decrease the magnetic noise as a whole. The magnetic noise for a 1 hp, 6 poles motor with rated load is shown in the fig. 3 in relation to rotor slots skewing. The rotor slots skewing is indicated in relation to the stator slot pitch.

This graphic shows the dependence of the noise with respect to the rotor slots skewing. The curve shown can be significantly different from one motor to another. It is important to perceive, however, the great dependence of the noise with respect to the rotor slot skewing.

Fig. 3: Influency of the rotor slots skewing on the magnetic noise

129

TABLE 1 - RESULTS OF MAGNETIC NOISE CALCULATION SEPARATED BY CAUSES FOR ON LOAD (RATED) THREE-PHASE MOTORS

Power [hp]	Poles	N_1/N_2	STATOR WITH STATOR r	f_r [Hz]	L_r [dB(A)]	STATOR WITH ROTOR r	f_r [Hz]	L_r [dB(A)]	STATOR WITH ROTOR SATURATION r	f_r [Hz]	L_r [dB(A)]	ROTOR WITH STATOR SATURATION r	f_r [Hz]	L_r [dB(A)]	STATOR WITH ROTOR ECCENTRICITY r	f_r [Hz]	L_r [dB(A)]	ROTOR WITH STATOR ECCENTRICITY r	f_r [Hz]	L_r [dB(A)]
1	2	24/18	2	120	29.5	2	2046.3	64.8	2	2826.3	43.9	2	2826.3	28.8	3	2946.3	14.4	3	2889.5	20.2
10	2	36/28	2	100	32.8	2	1345.3	65.9	2	1545.3	5.2	4	1545.3	3.7	3	4183.8	-	9	3887.7	14.7
50	2	36/28	2	120	51.3	6	8185.4	60.1	2	1541.1	-	4	1901.1	21.6	-	-	-	7	1720.4	22.2
100	2	48/40	2	120	50.2	8	11850.3	56.7	-	-	-	4	2610.1	10.2	3	2370.1	-	5	2549.3	19.5
200	2	48/40	2	120	55	0	2499.6	53.1	-	-	-	4	2019.6	14.5	-	-	-	5	2559.1	22.9
550	2	60/44	2	120	65	0	2500.1	62.1	14	7980.3	0.3	12	2860.1	24.3	13	7919.9	9.2	13	7919.9	35.5
1	4	36/44	4	120	9.6	4	6288.6	61.3	4	4013.2	9.7	0	1017.7	-	3	3653.2	17.7	3	1137.7	12.2
10	4	48/40	4	120	14.2	4	1271.1	60.5	0	1397.1	-	0	1397.1	16.3	3	1306.0	25.5	3	1306	31.9
50	4	48/54	4	120	26.0	2	1473.0	78.1	2	1353	15.5	2	1353	25.2	3	1473	42.6	3	1502.5	54.0
100	4	72/58	4	100	24.3	4	2757.2	61.3	-	-	-	6	1628.6	16.0	3	1528.6	29.4	9	1553.2	17.4
200	4	72/58	4	120	31.7	2	1841.9	56.3	-	-	-	6	1961.9	19.6	9	1871.6	1.8	9	1871.6	31.4
550	4	72/58	4	120	34.1	10	1839.8	51.7	6	1959.8	5.8	6	1959.8	24.5	9	1839.8	19.8	9	1859.5	35.3
1	6	36/44	6	120	-	2	708.2	61.9	2	708.2	13.3	2	708.2	12.3	3	723.0	9.3	3	727	8.1
10	6	36/28	2	120	1.1	2	1626.8	88.6	2	1866.8	30.9	4	1866.8	34.3	3	4702.2	51.9	5	1804.9	44.3
50	6	72/56	6	120	2.6	0	3186.5	76.2	4	1342.2	18.5	4	1342.2	32.4	3	1102.2	22.6	9	1241.9	22.1
100	6	72/58	6	120	18.1	4	1142.7	82.8	2	1382.7	-	2	1382.7	25.1	7	3327.8	14.8	7	1282.4	33.9
200	6	72/58	6	120	16.7	4	1142.0	71.2	2	1382.0	-	2	1382.0	19.4	7	1281.6	5.7	7	1281.6	36.8
550	6	72/58	6	120	24.5	4	1153.0	70.8	2	1393	20.5	2	1393.0	43.6	7	1292.9	9.3	7	1273.0	41.5
1	8	36/44	4	120	-	0	479.8	21.9	4	1439.5		-	-	-	3	1932.9	-	1	493.4	-
10	8	48/54	8	120	-	2	667.7	81.4	2	667.7	32.1	2	667.7	37.4	3	1455.3	30.9	3	653.1	25.0
50	8	72/56	8	120	5.6	0	3171.8	79.9	0	1062.9	5.4	0	1062.9	30.2	1	717.7	-	7	957.7	27.2
100	8	72/56	8	120	11.3	8	4157.2	77.6	0	1071.5	14.4	0	1071.5	42.9	7	966.3	-	7	966.3	34.4
200	8	72/82	8	120	1.5	2	1099.6	76.3	4	2199.6	21.0	4	2199.6	19.1	3	1114.7	40.0	3	1114.7	46.2
550	8	72/82	8	120	23.5	2	1100.3	78.9	4	2200.6	21.5	4	2200.6	20.2	3	1100.3	42.5	1	1085.4	52.2

CONCLUSION

As expected, from the Table 1, the highest magnetic noise level occurred several times for the vibration mode equal 2. Actually, when the vibration mode r=2 exists, the highest magnetic noise occurs likely for this mode, except when there is a strong ressonance in a frequency related to other vibration mode. It can be noted that the influence of the saturation and eccentricity is very small for an usual design of a motor. In this simulation, the eccentricity was limited in 10% of the airgap lenght.

According to the segregation of the magnetic noise causes it is possible to improve the performance of the electric motor. The calculation method provides very useful result to the magnetic noise evaluation of three-phase induction motors. The calculation of the force and deformation waves frequencies is accurate. If, through the calculation, the maximum noise occurs for a determined frequency, this situation certainly will happen during the test, but the measured value can be different in amplitude from the calculated value.

In relation to rotor slots skewing, the Fig. 3 shows clearly the dependence of the magnetic noise with respect to the rotor slots skewing. It can be noted for that specific case a minimum point, indicating that small skewing variations can produce large variations in the noise. This condition is critical because it is very difficult to assure a good precision in the rotor slots skewing during manufacturing process.

The determination of the magnetic origin sound noise is important during the motor design stage, when the characteristics of the motor can be changed with a relatively low cost. After the motor is assembled, there is nothing to do to reduce the noise level without a high cost. That is a reason for the electric motor manufacturers to use this calculation and analysis tool.

REFERENCES

[1] **F. Kako, T. Nagaishi, H. Kohmo**, *Experimental study on magnetic noise of large induction motors.* IEEE Transactions on Power Apparatus and Systems, Vol. PAS-102, No. 8, August 1983.

[2] **J. R. Brauer**, *Magnetic noise of induction motors.* IEEE Transactions on Power Apparatus and Systems, Vol. PAS-95, No. 1, January/February 1976.

[3] **H. Jordan**, *Low noise electric motors (German).* Essen: W. Girardet, 1950.

[4] **R. Gerlach**, *Generation of magnetic noise in synchronous and asynchronous machines (German).* VDE Seminar about Noise and Vibration in Electrical Machines, Aachen, 1969.

[5] **S.L. Nau**, *Magnetic noise of rotating electrical machines (Portuguese).* II International Seminar about Electric Motors and Regulated Drives, p. 51-64, São Paulo, 1991.

[6] **Z. Üner**, *About the determination of the magnetic noise sound intensity of squirrel-cage three phase induction motors (German).* Doktor - Ingenieur Dissertation - Technische Hochschule Hannover, Hannover, 1964.

[7] **H. Frohne**, *About the primary parameters to determine sound intensity in asynchronous machines (German).* Doktor - Ingenieur Dissertation - Technische Hochschule Hannover, Hannover, 1959.

GROUND-3D LINKED TO LINE PARAMETERS: A METHOD TO FAULT CURRENT DISTRIBUTION AND EARTH POTENTIAL DETERMINATION

Brodskyn, H. O.; Costa, M. C.; Cardoso. J. R.; Abe, N. M.; Passaro, A.*;
Nabeta, S. I.; Giarolla, M. H.

Escola Politécnica da USP
Depto. de Engenharia de Energia e Automação Elétrica
Av. Prof. Luciano Gualberto, Trav. 3, 158
05508-900 - São Paulo - SP

*Instituto de Estudos Avançados - IEAv/CTA
São José dos Campos

Abstract - **In previous work [1,2] the author presents a methodology, based on finite elements method (FEM), to calculate the potential distribution influence on the grounding area. At that time the input of the solver admits as known the split of the system. The aim of this article is to demonstrate the advantages of finite element method (FEM) associated with power systems equations with lumped parameters to intrinsically obtain the distribution of fault current in several offered conductor ways and the potential distribution on the ground, simultaneously. To solve the complex equations system, the methodology adopted was that described by Mesquita [3].**

INTRODUCTION

This work describes a method to calculate the distribution of currents between ground and over head ground wires when a line ground fault occurs in a transmission line as well as the potential grades that had been developed in the earth.

The method described on references [4], [6] is based on:

- Calculation of lumped parameters and use of traditional network studies, with simplifications mainly on the representation of the ground resistance and their mutual;

- Analyses based on empirical graphics.

This kind of phenomena on the last years started to be solved using FEM techniques [1], but even in this case this solution assumes known fault current distribution.

Our proposal is to combine both FEM techniques on the ground and lumped parameters of the over ground network as well the mutual between line

and ground cables in the same solution using a global complex matrix.

The computation in the frequencies domain brings a new contribution to the study.

The application of the Incomplete Cholesky Complex-Bi-Conjugate Gradients method (ICCBCG) was identified as the most appropriate, in the face of encouraging results obtained until the moment, as well as existing symmetry in the resultant matrix.

In the developed methodology, the domain is subdivided in two parts:

1. soil and buried elements;
2. electric network, as shown on fig. 1.
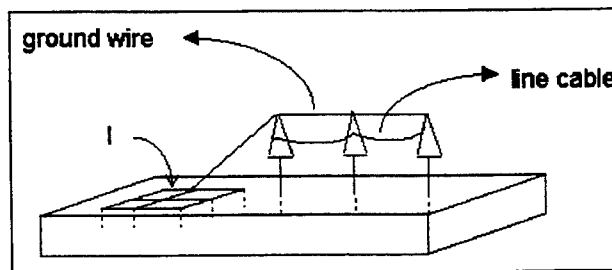
Fig. 1 - Schematic Model of the Study Domain

The matrix that simulates the system will be the composition of the global matrix arising from mathematics formulation for the FEM to the ground system, with the insertion of the network lumped parameters, resulting in a system of equation like:

$$Ax = b \qquad (1)$$

where A is the complex matrix, result of the global matrix composition of the FEM with insertion of lumped parameters of the fault current dispersal system, x is the potential of all domain nodes, and b it is the impress current vector.

This method helps to get more accuracy on results of potential distribution on soil minimising investment on ground grid. As by-product, the used methodology allows the study of transference potentials in metallic elements not directly linked up with the electric system, but which are situated in their influence area (problem domain) like: plumbing, metallic structures, armours, which have contact or which are buried in the soil, in the moment of incident of the line to ground fault.

CONSTRUCTION OF THE COMPLEX MATRIX

Following [4] we can simplify the network model, to the following fig. 2:
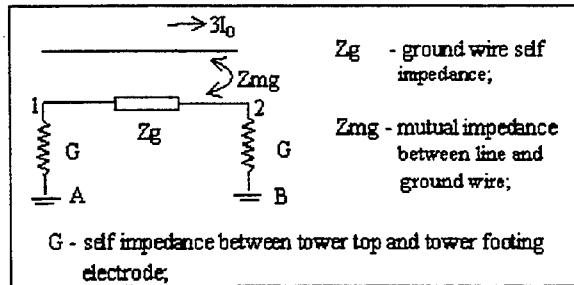
Fig. 2 - Impedance model of lumped parameters.

The points A and B are examples of interface between model with lumped parameter and ground (FEM).

If we change in the above model the Zmg impedance by current generator:

$$Ig = \frac{Zmg}{Zg}(3Io) \qquad (2)$$

the interconnection of two substations can be shown in fig. 3:
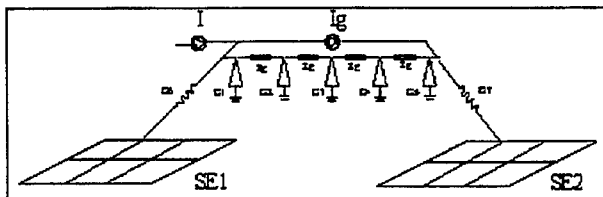
Fig. 3- Interlink of two ground networks of substations.

The construction of the Matrix is done including in the FEM matrix [G] the nodes introduced by the links with the lumped parameters. To do that the impedance of the interconnections between the tower top and the ground electrode, and the self impedance of

the over ground wire will be treated as one dimension elements to be included in the main matrix as shown bellow:
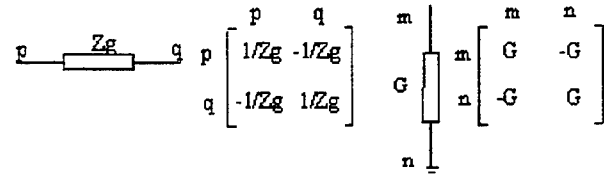
Tower interconnections series impedances.

Elements of parallel impedance.

[G] after lumped elements included.

The tower connections with the over ground wires will be considered as resistive so the final matrix will be symmetric with complex elements. This algorithm is the inclusion of an element in an already built Y matrix [5]:

SOLUTION METHODOLOGY

As described by Mesquita when the matrix A is symmetric and complex, we can use Incomplete Choleski method before applying the CBCG, making the ICCBCG (Incomplete Choleski Complex Bi-Conjugate Gradients). These solutions introduce reductions compared to direct inversion of the matrix using usual technics with lumped parameters and network studies.

EXAMPLE AND RESULTS

In the first approach we will use the simplified example of figure 4, with DC current of 1500 A on point 2.

Fig. 4 - Example Scheme

Fig. 5 - Equivalent Model

The solver had considered the elements between the points 2-13, 13-14, and 14-5 as lumped values, and the rest of domain had been simulated with FEM and ICCG (Incomplete Cholesky Conjugate Gradients) solution because with DC current, the matrix becomes real. The results are shown below:

$V_1 = 226.48$ V	$V_2 = 226.53$ V
$V_3 = 226.45$ V	$V_4 = 226.47$ V
$V_5 = 124.99$ V	$V_6 = 124.97$ V
$V_7 = 124.97$ V	$V_8 = 124.98$ V
$V_9 = 0$ V	$V_{10} = 0$ V
$V_{11} = 0$ V	$V_{12} = 0$ V
$V_{13} = 218.07$ V	$V_{14} = 133.45$ V

For verification lets take an equivalent system where the FEM domain will be simulated by lumped parameters too.

Considerations:
- Distance between two points: 1m
- Soil Resistivity: $r_{solo} = 1/12$ Ω.m
- Resistances: element between points 2-13: 0,03 Ω
  element between points 13-14: 0,3 Ω
  element between points 14-5: 0,03 Ω
Then,
$$R_{solo} = \rho/s = 1/12 * 1 = 0,08334$$

The current is uniformly distributed in the 1-2-3-4 area.
So, we have the solution of the equivalent model of figure 5:

	Traditional Method	ICCBCG
V1	226.5 V	226.48 V
V5	125.0 V	124.99 V
V9	0.0 V	0.0 V

To the other result we will use the example of the fig. 6:

Fig. 6 - Example domain

The ground rods located on the four corners of the mesh and of the towers (one rod per tower) are 6.0 m long, the mesh is buried at 0 m level, and the soil is stratified in three layers as follows:

0m -3m: 100 Ω.m
-3m -9m: 400 Ω.m
-9m -15m: 1300 Ω.m

Fig. 7 shows the equipotential lines due to a total ground fault (I= 40 A) imposed to the left-side mesh.

Fig. 7 - Equipotential lines

Fig. 8 shows the potential profile in the direction (A-A') as shown in fig. 6, and the fig. 9 shows the potential surface at 0m level.

Fig. 8 - Potential profile

134

Fig. 9 - Potential Surface

First tests on ICCBCG using the example of fig. 4, changing the connection impedance to:

- Impedances: element between points 2-13: 0,03 Ω
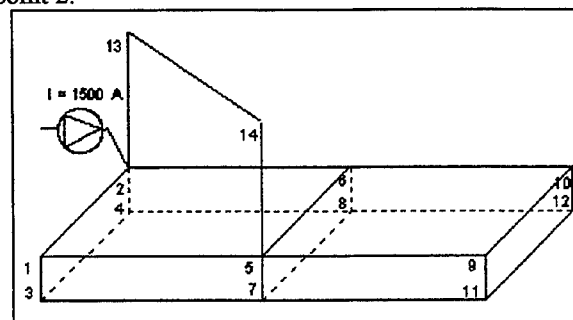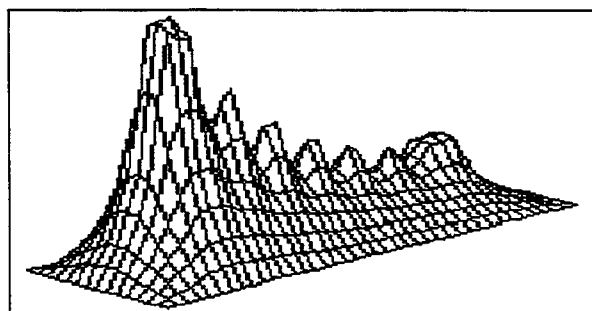element between points 13-14: 0,3j Ω
element between points 14-5: 0,03 Ω

The results are:

$V_1 = 236.47 + 28.25j$ V	$V_2 = 236.52 + 28.27j$ V
$V_3 = 236.44 + 28.25j$ V	$V_4 = 236.46 + 28.25j$ V
$V_5 = 124.98 - 0.02j$ V	$V_6 = 124.96 - 0.01j$ V
$V_7 = 124.96 - 0.01j$ V	$V_8 = 124.97 + 0.01j$ V
$V_9 = 0.0 + 0.0j$ V	$V_{10} = 0.0 + 0.0j$ V
$V_{11} = 0.0 + 0.0j$ V	$V_{12} = 0.0 + 0.0j$ V
$V_{13} = 231.66 + 38.44j$ V	$V_{14} = 129.84 - 10.19j$ V

For verification, we use an equivalent model, using normal circuit technics and the results are:

	Traditional Method	ICCBCG
V1	236.50 + 28.27j V	236.47 + 28.25j V
V5	125.0 + 0.0j V	124.98 - 0.02j V
V9	0.0 + 0.0j V	0.0 + 0.0j V

CONCLUSION

The results show that the implementation of the global matrix gives results in an acceptable precision compared with direct methods of circuit calculation. This way of calculation doesn't come to substitute other methods, but to look more carefully the locations where problems are detected.

The great advantage is to obtain the division of currents between over-ground-cable and soil intrinsically resulting a more easy iterative analyses to the elements on ground.

REFERENCES

[1]   Cardoso, J.R.; GROUND-3D Versão 2.0 - Um software CAD/CAE para análise de sistemas de aterramento em baixa frequência. In: XII SNPTEE - Seminário Nacional de Produção e Transmissão de Energia Elétrica, Recife, Out. 93.

[2]   Cardoso, J.R; FEM Modeling of Grounded Systems with Unbounded Approach. In: CONFERENCE ON THE COMPUTATIONAL ON ELETROMAGNETIC FIELDS, 9. Miami, 1993. COMPUMAG: proceedings. Miami,1993.

[3] Mesquita, R.C.;'Cálculo de campos eletromagnéticos tridimensionais utilizando elementos finitos: Magnetostática, Quase-estática e Aquecimento Indutivo.', Tese de Doutorado - Universidade Federal de Santa Catarina, Dez. 90.

[4]   Senger, E.C.; Anniochimo, M.W.,'Método numérico para cálculo de distribuição em sistemas de aterramento multiconectado',In: XIV Congresso Ibero Latino Americano de Métodos Computacionais em Engenharia, Dez. 93.

[5]   Stagg, G.W.;El-Abiad, A.H.;Computer Methods in Power System Analysis, McGraw-HIll, 1968.

[6] Sobral; Dewabili; "Decoupled Method" for studying large interconnected grounding systems using microcomputer. Part 1 - Fundamentals IEEE/PES 1986, Summer Meeting, Mexico City, July, 1986.

An Investigation of the Scattering of Surface Waves at Dielectric Slab Waveguide with Axial Discontinuity

CRESO S. DA ROCHA [1]

Abstract— This paper introduces a technique for studying the radiation due to an abrupt axial discontinuity in the geometry of a planar dielectric waveguide (slab waveguide) when an even *TM* surface wave strikes the discontinuity. The mode matching technique is applied at the discontinuity giving rise to formally exact integral equations which are solved by the Method of Moments.
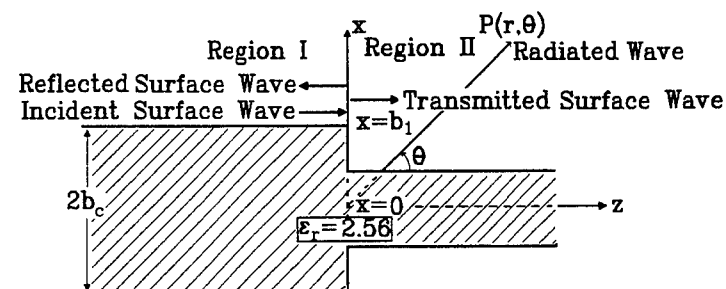
I. INTRODUCTION

ELECTROMAGNETIC scattering due to a discontinuity in the geometry of a surface waveguide has occupied attention of several investigators in the past few decades [1]-[7]. These authors, in one way or another, make approximations that turn solution of the problem unavailable for large range of discontinuity. On the other hand, in all cases, the back radiation is considered very small and neglected. In our work there is no restriction values for the discontinuity, but we can observe that the solution becomes unstable as the structure in the right side approaches the air, Fig. 1, (by making $b_2 = 0$).

In this paper a method for investigating the scattering of an incident surface wave at the axial discontinuity of a dielectric slab with a step in the geometry is introduced. In our approach we formulate the field equations in an exact way by using the mode matching technique of the tangential fields, represented by a complete set of eigenfunctions that are solved by the Method of Moments. In the integral equations, both back and forward scattered radiation spectral densities are considered, initially without approximations.

II. MODE MATCHING AT THE INTERFACE

With reference to Fig. 1, consider a TM surface wave with even symmetry $[H_y(x) = H_y(-x)]$ striking the discontinuity at $z = 0$ from the left and giving rise to a transmitted and a reflected surface wave as well as scattered radiation. The single mode is guaranteed by taking the slab of thickness not larger than $2b_c$ in the region I, where b_c is given by $2b_c = \lambda_0/\sqrt{\epsilon_r - 1}$ (dominant mode). At the discontinuity the boundary conditions cannot be satisfied by the surface waves alone; an additional field

[1] The author is with the Department of Electrical Engineering, Federal University of Paraíba, P.O. Box 10053 - 58100 Campina Grande, PB - Brazil, e-mail: creso@dee.ufpb.br

with radiation characteristics must be introduced, that is, the total field must be given as

$$\psi_1 = \psi_{incident} + \psi_{reflected} + \psi_{radiated}, \quad [z \leq 0]$$

and

$$\psi_2 = \psi_{transmitted} + \psi_{radiated}, \quad [z \geq 0]$$

(a) The slab waveguide with abrupt step in the geometry
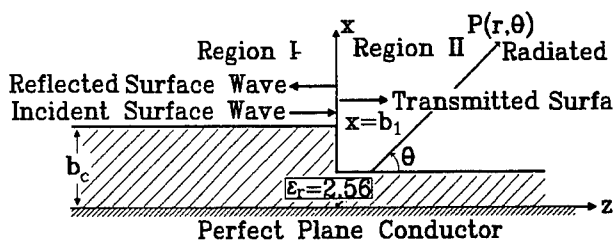
(b) Equivalent Structure for even TM_0 mode

Figure 1: The Dielectric Slab with Axial Discontinuity.

The radiation is accounted for by the continuous spectrum of pseudo-surface waves. Because $h(s)$, the wave number in the z-direction for the continuous spectrum, is a double-valued function of s, the wave number in the x-direction, it is necessary to define its branches to uniquely define the pseudo-mode solutions, that is

$$h(s) = + \sqrt{k_0^2 - s^2}, \quad [0 \leq s \leq k_0] \tag{1}$$

$$h(s) = -j\sqrt{s^2 - k_0^2}, \quad [k_0 \leq s \leq \infty] \tag{2}$$

Equation (1) corresponds to the spectrum of radiation modes (visible range) while equation (2) is for the evanescent modes (invisible range).

Let the incident surface wave have amplitude I and the reflected and transmitted surface waves have amplitude R and T, respectively. Taking $\psi = H_y(x, z)$ for the TM_0 mode. Matching the total fields at $z = 0$ gives [8]

$$(I + R)h_{y1} + \int_0^\infty [B_1(s)/h(s)]h_{y1}(s)ds =$$

$$Th_{y2} + \int_0^\infty [B_2(s)/h(s)]h_{y2}(s)ds \quad (3)$$

$$(h_1/\epsilon_{r1})(I - R)h_{y1} - \int_0^\infty (1/\epsilon_{r1})B_1(s)h_{y1}(s)ds =$$

$$(h_2/\epsilon_{r2})Th_{y2} + \int_0^\infty (1/\epsilon_{r2})B_2(s)h_{y2}(s)ds \quad (4)$$

where h_y and $h_y(s)$ are the transverse function for the discrete and continuous TM field, respectively. B_1 and B_2 are the unknown spectral densities for the left and right region, respectively. In the expressions above, including the dielectric constant, the x–dependence is understood.

III. TRANSFORMATION TO THE SPECTRAL DOMAIN

In order to apply the Moment Method one must first eliminate the x–dependence, so that (3) and (4) will be in a form suitable for computation. To do so and to take advantage of the orthogonality properties, (3) is multiplied by $h_{y1}(\tilde{s})/\epsilon_1(x)$ and by $h_{y1}/\epsilon_1(x)$ separately and integrated over x from 0 to ∞ [8]. Similarly (4) is multiplied by $h_{y1}(s)$ and h_{y1} separately and integrated over x from 0 to ∞.

Noting the orthogonality properties, the following set of equations is obtained:

$$\frac{B_1(\tilde{s})}{h(\tilde{s})}N_1^2(\tilde{s}) = TF_{12}(\tilde{s}) + \int_0^\infty B_2(s)H_{12}(s, \tilde{s})ds/h(s) \quad (5)$$

$$-B_1(\tilde{s})N_1^2(\tilde{s}) = h_2TG_{12}(\tilde{s}) + \int_0^\infty B_2(s)I_{12}(s, \tilde{s})ds \quad (6)$$

$$(I + R)N_1^2 = TH_{12} + \int_0^\infty B_2(s)G_{21}(s)ds/h(s) \quad (7)$$

$$(I - R)h_1N_1^2 = h_2TI_{12} + \int_0^\infty B_2(s)F_{21}(s)ds \quad (8)$$

where the integrals $F_{12}(\tilde{s})$, $G_{12}(\tilde{s})$, $H_{12}(s, \tilde{s})$, $I_{12}(s, \tilde{s})$, $F_{21}(s)$, $G_{21}(s)$, H_{12} and I_{12} and the normalization factors N_1 and $N_1(s)$ are defined as follows, for i and j mutually exclusive and equal to 1 or 2 according to the region considered (left or right region):

$$F_{ij}(\tilde{s}) = \int_0^\infty \frac{1}{\epsilon_i(x)}h_{yi}(\tilde{s})h_{yj}dx \quad (9)$$

$$H_{ij}(s, \tilde{s}) = \int_0^\infty \frac{1}{\epsilon_i(x)}h_{yi}(\tilde{s})h_{yj}(s)dx \quad (10)$$

$$H_{ij} = \int_0^\infty \frac{1}{\epsilon_i(x)}h_{yi}h_{yj}dx \quad (11)$$

$$N_i^2 = \frac{1}{2}\left[\frac{b_i}{\epsilon_i} + \frac{\sin(2g_ib_i)}{2\epsilon_ig_i} + \frac{\cos^2(g_ib_i)}{\alpha_i}\right] \quad (12)$$

and

$$N_i^2(s) = \frac{\pi}{2}\left[v_i^2(s) + w_i^2(s)\right] \quad (13)$$

where $v_i(s)$ and $w_i(s)$ are defined as follows ([8], Cap. 2):

$$v_i(s) = \cos[g_i(s)b_i] \quad (14)$$

$$w_i(s) = \frac{g_i(s)}{\epsilon_{ri}s}\sin[g_i(s)b_i] \quad (15)$$

g_i is the discrete wavenumber inside the guide and α_i is an attenuating factor outside the guide in x–direction. Note the g_i and α_i are solutions of the characteristic equation system

$$g_i\tan(g_ib_i) = \alpha_i\epsilon_{ri}$$

$$g_i^2 + \alpha_i^2 = k_0^2(\epsilon_{ri} - 1)$$

$g_i(s)$ and s are related by ([8], Cap. 2)

$$g_i^2(s) - s^2 = k_0^2(\epsilon_{ri} - 1)$$

$$h^2(s) = k_0^2 - s^2$$

The integrals $G_{ij}(\tilde{s})$, $I_{ij}(s, \tilde{s})$ and I_{ij} follow from $F_{ij}(\tilde{s})$, $H_{ij}(s, \tilde{s})$ and H_{ij}, respectively by replacing $\epsilon_i(x)$ by $\epsilon_j(x)$.

The system of four equations (5-8) is a set of integral equations in R, T, $B_1(s)$ and $B_2(s)$ that can be solved by a suitable numerical method.

IV. MOMENT METHOD SOLUTION

To put the system to be solved in an appropriate form for the Method of Moments, let the unknown spectral density $B_i(s)$ be represented by the following series,

$$B_i(s) = \sum_{n=1}^N b_n^{(i)}f_n(s), \quad i = 1, 2 \quad (16)$$

where $f_n(s)$ are pulse functions, chosen as testing functions, and defined as follows:

$$f_n(s) = P(s - s_n) = \begin{cases} 1, & \text{for } |s - s_n| < \Delta s/2 \\ 0, & \text{for } |s - s_n| > \Delta s/2 \end{cases} \quad (17)$$

where Δs is the width of the pulse functions and s_n is the nth pulse function's midpoint:

$$s_n = (n - 1/2)\Delta s$$

$$\Delta s = k_0/N_0$$

and

$$K = s_N + \Delta s/2$$

where N is a suitable number of points, usually larger than N_0, the last value of n in which $h(s_{n-1})$ is still real. K is a large number that replaces infinity in the integrals of (5-8). The optimal values of N and N_0 are dictated by the convergence of the solution. For $n \geq N_0$, $h(s_n)$ is pure imaginary, giving rise to the evanescent modes.

By using the expansion (16) the equations (5-8) become,

$$\sum_{n=1}^{N} b_n^{(1)} P(\tilde{s} - s_n)/h(\tilde{s}) =$$

$$TF_{12}(\tilde{s}) + \sum_{n=1}^{N} b_n^{(2)} \int_0^K P(s - s_n)H_{12}(s, \tilde{s})ds/h(\tilde{s}) \quad (18)$$

$$-\sum_{n=1}^{N} b_n^{(1)} P(\tilde{s} - s_n)N_1^2(\tilde{s}) =$$

$$Th_2 G_{12}(\tilde{s}) + \sum_{n=1}^{N} b_n^{(2)} \int_0^K P(s - s_n)I_{12}(s, \tilde{s})ds \quad (19)$$

$$(I + R)N_1^2 = TH_{12} + \sum_{n=1}^{N} b_n^{(2)} \int_0^K P(s - s_n)G_{21}(s)ds/h(s) \quad (20)$$

$$(I - R)N_1^2 = Th_2 I_{12} + \sum_{n=1}^{N} b_n^{(2)} \int_0^K P(s - s_n)F_{21}(s)ds \quad (21)$$

If one uses the *point-matching method*, a suitable inner product is defined as follows,

$$< w_m, L(f_n) > = \int_0^K \delta(\tilde{s} - s_m)L(f_n)d\tilde{s}$$

where w_m, the weighting function, is given by $w_m = \delta(\tilde{s} - s_m)$, $L(f_n)$ is a linear operator, and f_n is the *unknown response* to be determined.

Thus, multiplying (21) by $\delta(\tilde{s} - s)$ and integrating over $\tilde{s}$ from 0 to K gives

$$b_m^{(1)} N_1^2(s_m) = TF_{12}(s_m)h(s_m) + h(s_m)\sum_{n=1}^{N} b_n^{(2)} l_{mn} \quad (22)$$

$$-b_m^{(1)} N_1^2(s_m) = TG_{12}(s_m)h_2 + \sum_{n=1}^{N} b_n^{(2)} m_{mn} \quad (23)$$

$$(I + R)N_1^2 h_1 = TH_{12}h_1 + \sum_{n=1}^{N} b_n^{(2)} l_{0n} \quad (24)$$

$$(I - R)N_1^2 h_1 = TI_{12}h_2 + \sum_{n=1}^{N} b_n^{(2)} m_{0n} \quad (25)$$

where l_{mn}, m_{mn}, l_{0n}, m_{0n} are defined as

$$l_{mn} = \int_{\Delta s_n} H_{12}(s, s_m)ds/h(s) \quad (26)$$

$$m_{mn} = \int_{\Delta s_n} I_{12}(s, s_m)ds \quad (27)$$

$$m_{0n} = \int_{\Delta s_n} G_{12}(s)ds/h(s) \quad (28)$$

$$m_{0n} = \int_{\Delta s_n} F_{21}(s)ds \quad (29)$$

where $\Delta s_n = (s_n - \frac{1}{2}\Delta s, s_n + \frac{1}{2}\Delta s)$.

Because of the properties of the pulse functions the range of these integrals were changed to 'local' range where each integral is performed over each pulse alone, Fig. 2. The above integrals cannot be solved in closed form. An approximate procedure is to expand part of the integrand that does not contain a function of the type $1/(s^2 - f^2)$ in a Taylor series about $s = s_n$, the midpoint of the range of integration. It is sufficient to consider only two terms of the expansion because the range of integration is or can be made small. This approximation is valid only for points where $h(s)$ does not vanish. Points very close to $s = k_0$ would give poor approximations.
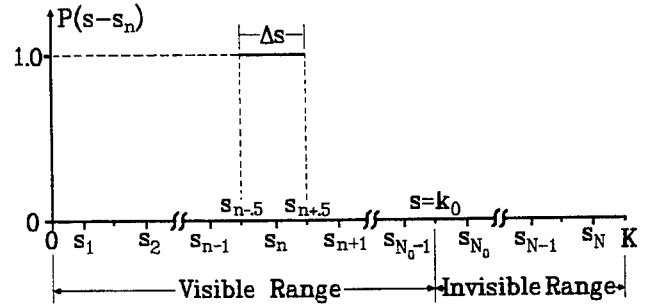
Figure 2: Pulse Function for N Points.

V. POWER CONSIDERATIONS

Power in the Surface Wave

The power carried by the dominant mode surface wave (per unit length in the y-direction) for the upper half of the slab waveguide is

$$P_s = \frac{1}{2} \text{Re} \int_0^\infty E_x H_y^* dx \quad (30)$$

where 'Re' means 'Real part of'. For TM modes the surface wave H field is given by

$$H_y(x, z) = Ah_y(x)e^{-jh_{\pm}z} \quad (31)$$

where A is the mode amplitude. The '±' suffix for the wave number h has the following meaning

$$h_+ = h \quad \text{(forward wave)}$$

$$h_- = h \quad \text{(reflected wave)}$$

Moreover from Maxwell Equations,

$$E_x = \frac{1}{\omega\epsilon(x)}\frac{\partial}{\partial z}H_y = \frac{h_\pm}{\omega\epsilon_0\epsilon(x)}H_y(x,z) \qquad (32)$$

Putting (31) and (32) into (30) gives

$$P_s = \frac{h_\pm}{2\omega\epsilon_0}|A|^2\int_0^\infty\frac{1}{\epsilon(x)}|h_y(x)|^2 dx \qquad (33)$$

Therefore the total power carried by the even TM_0 mode is

$$P_s = \frac{Z_0 h_\pm}{4k_0}|A|^2 N^2 \qquad (34)$$

where N is the discrete normalization factor given in (12), $Z_0 = \sqrt{\mu_0/\epsilon_0} \cong 120\pi\Omega$.

The Radiated Power

The total power of the radiating field for the upper half region is defined as

$$P_{\text{rad}} = \frac{1}{2}\int_0^\infty P(\theta)d\theta \qquad (35)$$

where $P(\theta)$, the angular power density per unit width in the y−direction, is defined by

$$P(\theta)d\theta = Z_0|H_y(\rho,\theta)|^2, \quad [\rho\rightarrow\infty] \qquad (36)$$

where ρ is the distance to the far field observation point from the origin and θ is the angle between the direction of and the z−axis, measured from the latter (Fig. 1).

For TM pseudo-modes the pseudo-surface wave H field is given by

$$H_y(x,z) = \frac{1}{2}\int_0^\infty\frac{B(s)}{h_\pm(s)}h_y(x,s)\,e^{-jh_\pm(s)z}\,ds \quad \text{(cf.(31))} \qquad (37)$$

where $B(s)$ is the unknown spectral density and $h_y(x,s)$, the transverse function for the continuous TM mode field is given by

$$h_y(x,s) = [v(s)-jw(s)]e^{-js(x-b)}, \quad [x\geq b] \qquad (38)$$

where $v(s)$ and $w(s)$ are given by (14) and (15), respectively. Notice that in writing (37) one considered only the outgoing term of the pseudo-mode solution because the incoming one makes no contribution in the upper half region. It is possible to show that the incoming term leads to an expression for the radiated power in the lower half

region, which, by symmetry can be deduced from that for the upper half region.

The integral above - (37), cannot be evaluated in closed form. Fortunately, for radiation problems, the primary interest is with the far field and so one can apply asymptotic integration techniques such as the saddle-point method. It is convenient to make the following changes of variables,

$$x - b = \rho\sin(\theta), \quad z = \rho\cos(\theta) \qquad (39)$$

$$s = k_0\sin\gamma, \quad h(s) = k_0\cos(\gamma) \qquad (40)$$

since

$$\rho^2 = x^2 + z^2 \qquad (41)$$

$$k_0^2 = s^2 + h^2(s) \qquad (42)$$

In terms of the new variables, (37) can be written, for $(0 < \theta < \pi)$

$$H_y(\rho,\theta) = \frac{1}{2}\int_C B(k_0\sin\gamma, \pm k_0\cos\gamma)$$
$$[v(k_0\sin\gamma) - jw(k_0\sin\gamma)]\,e^{\mp jk_0\rho\cos(\gamma\mp\theta)}\,d\gamma \qquad (43)$$

where the upper and lower signs in the exponential term and in the function B stand for $z \geq 0$ and $z \leq 0$, respectively. C is the integral path for the saddle-point method of integration.

For $z > 0$ $(\pi/2 \leq \theta < \pi)$ the saddle point is $\tilde{\theta} = \theta$ and for $z < 0$ $(\pi/2 \leq \theta < \pi)$ the saddle point is $\tilde{\theta} = \pi - \theta$ ([9],p.108,9).

For very large $k_0\rho$, that is, for points far from the discontinuity, the following asymptotic expression is obtained

$$H_y(\rho,\tilde{\theta}) \cong \sqrt{\frac{\pi}{2k_0\rho}}B(k_0\sin\theta, \pm k_0\cos\theta)$$
$$[v(k_0\sin\theta) - jw(k_0\sin\theta)]\,e^{-j(k_0\rho-\pi/4)} \qquad (44)$$

Thus the far field of (44) is a diverging cylindrical wave satisfying the radiation condition, with pattern given by

$$Q(\tilde{\theta}) = B(\tilde{\theta})[v(\tilde{\theta}) - jw(\tilde{\theta})] \qquad (45)$$

In view of (44) one writes

$$\left|H_y(\rho,\tilde{\theta})\right|^2 \cong \frac{\pi}{2k_0\rho}|B(\theta)|^2[v^2(\theta) + w^2(\theta)] \qquad (46)$$

and consequently, with reference to (36),

$$P(\tilde{\theta}) = \frac{Z_0}{4k_0}|B(\tilde{\theta})|^2 N^2(\tilde{\theta}) \qquad (47)$$

where $N^2(\tilde{\theta})$ is given by

$$N^2(\tilde{\theta}) = \frac{\pi}{2}[v^2(\tilde{\theta}) + w^2(\tilde{\theta})] \qquad (48)$$

Substituting (47) into (35) gives

$$P_{\text{rad}} = \frac{Z_0}{4k_0} \int_0^\infty |B(\tilde{\theta})|^2 N^2(\tilde{\theta}) d\tilde{\theta} \qquad (49)$$

More explicitly, in terms of s

$$P_{\text{rad}} = \frac{Z_0}{4k_0} \int_0^\infty |B(s)|^2 N^2(s) ds/h(s) \qquad (50)$$

Notice that $ds/h(s) = \tilde{\theta}$, due to the change of variable.

The forward and backward radiation powers are included in (49) when $\tilde{\theta}$ is properly replaced; thus when $\tilde{\theta}$ runs from 0 to π, é has two stationary values and consequently the integrand is split into two terms, corresponding to the forward and back scattered radiation each associated with the same value of s.

The power pattern is then

$$Q(\tilde{\theta}) = |B(\tilde{\theta})|^2 N^2(\tilde{\theta}), \quad [0 < \tilde{\theta} < \pi] \qquad (51)$$

VI. NUMERICAL RESULTS AND DISCUSSION

For numerical calculation purposes the incident power is set to unity. Consequently, the transmitted, reflected, and radiated powers are normalized with respect to the incident power. They are in the convenient forms given as follows :

$$P_{\text{trans}} = T^2 \left(\frac{h_2 N_2^2}{h_1 N_1^2} \right) \qquad (52)$$

$$P_{\text{ref}} = R^2 \qquad (53)$$

$$P_{\text{rad}} = \frac{1}{h_1 N_1^2} \sum_{n=1}^{N_0} \left[\left| b_n^{(1)} \right|^2 N_1^2(s_n) + \left| b_n^{(2)} \right|^2 N_2^2(s_n) \right] \frac{\Delta s}{h(s_n)} \qquad (54)$$

The superscript upon b_n and the subscript in the other variables refer to the medium on the left '1' and on the right '2'.

The actual total power (incident plus scattered) for the slab waveguide is double the value obtained here because one is considering only half the slab.

The backward and forward power patterns are written as functions of θ_n and $b_n^{(1)}$ and $b_n^{(2)}$ as

$$Q_1(\theta_n) = |b_n^{(1)}|^2 N_1^2(\theta_n), \quad [\pi/2 < \theta_n \leq \pi] \qquad (55)$$

$$Q_2(\theta_n) = |b_n^{(2)}|^2 N_2^2(\theta_n), \quad [0 < \theta_n \leq \pi/2] \qquad (56)$$

where

$$\theta_n = \begin{cases} \sin^{-1}(s_n/k_0), & [0 < \theta_n \leq \pi/2] \\ \pi - \sin^{-1}(s_n/k_0), & [\pi/2 \leq \theta_n < \pi] \end{cases} \qquad (57)$$

Notice that, in principle, the total scattered power equals 1 and that the following relation must hold

$$P_{\text{trans}} + P_{\text{ref}} + P_{\text{rad}} = 1 \qquad (58)$$

The expression above is useful to indicate whether the calculations performed are or are not accurate. Of course this relation is not a sufficient condition for the solution of the problem.

In the following subsection the solutions of the system of equations (22-25) are presented for several selected cases.

Convergence

Curves showing the variation of the transmitted, reflected, and radiated power with changes of the slab thickness in the right region are shown in Fig. 3. These plots were obtained by varying $2b_2/\lambda_0$ from .001 to 0.40. The conservation of energy was verified in all cases with $N = 48$ points and $N_0 = 24$ points. These results show that there are no problems of convergence for changes in b_2, even for very small values. It is worth remarking that the radiated energy is very small, unless large steps are considered (small values of b_2). For example, when $2b_2/\lambda_0 = 0.001$ almost all energy is radiated and the reflected energy is very small.

Power Patterns

The main concern here is the radiation characteristics due to the step in the geometry. Several cases were considered in order to show these properties. Curves of Fig. 4 and 5 show the pattern characterists for some particular cases. One can notice that the smaller the dimension of the slab at the right side the closer to $\theta = 0°$ is the peak of the radiated field. The error with respect to the total power involved in the calculations above is less then 1% for all cases with $N = 48$ and $N_0 = 24$.

V. CONCLUSION

The Moment Method applied throughout this work has been shown to be accurate, efficient, and the results are very convincing for many practical cases of axial discontinuities in dielectric waveguide structures. The formulation of the field equations are exact and straightforward. On the other hand one concludes that the truncated number of equations N and the number of equations in the visible range N_0 play a very important role in the convergence of the solution. For most specific cases the number of points in the invisible range need not be large.

The technique applied in this work can also be used for the slab and rod (TM_{01}) waveguide with ascending steps in the geometry. Steps in the dielectric medium are also possible and the formulation is slightly simpler. Mixed cases can also be treated with some increase in complexity of mathematical handling.

The method has to be changed in the case of free-end structures ($b_2 = 0$) since one gets more equations than needed because T becomes zero (see set of equations (22-25)). That is the reason the system gets unstable as b_2 approaches the air.

REFERENCES

[1] H. M. Barlow and J. Brown. *Radio Surface Waves.* Oxford University Press, Amen House, London, 1962.

[2] Alan F. Kay. "Scattering of a Surface Wave by a Discontinuity in Reactance" *IRE Trans. Antennas and Prop.*, AP-7:22-31, (Jan) 1959.

[3] Elmer L. Johansen. "Surface Wave Scattering by a Step". *IEEE Transactions on Antennas and Propagation*, AP-15:442+6, May 1967.

[4] Dietrich Marcuse. "Radiation Losses of Tapered Dielectric Slab Waveguides". *Bell System Technical Journal*, 49:273+17, February 1963.

[5] S. Nemoto and T. Makimoto. "Radiation Loss Caused by Discontinuities in a Dielectric Slab Waveguide". *Wave Electronics*, 3:249+13, March 1978.

[6] A. Ittipiboon and M. Hamid. "Scattering of Surface Waves at a Slab Waveguide Discontinuity" *Proc. IEEE*, 126-#9:798-804,(Sep) 1979.

[7] Koichi Hirayama and Manasori Koshiba. "Numerical analysis of arbitrarily shaped discontinuities between planar dielectric waveguides with different thicknesses" *IEEE Trans. Microwave Theory Tech.*, MTT-38:260-264, (Mar) 1990.

[8] Creso S. da Rocha. **An Investigation of the Scattering of Surface Waves at Dielectric Waveguide Discontinuities by the Moment Method**, Ph.D. Thesis, Dept. of Elect. Eng'g, The University of Waterloo, Waterloo, Ontario, Canada (1980).

[9] V. V. Shevchenko **Continuous Transitions in Open Waveguides**, The Golem Press, Boulder, Colorado, 1971.
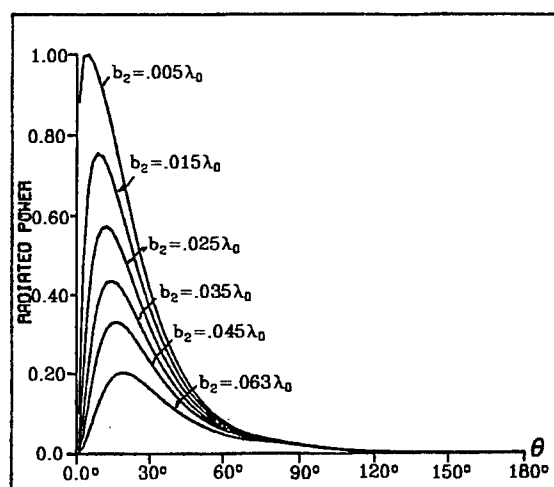
Figure 4: The Power Pattern for $b_2/\lambda_0 = 0.005...0.063$ with $\epsilon_{r1} = \epsilon_{r2} = 2.56$.
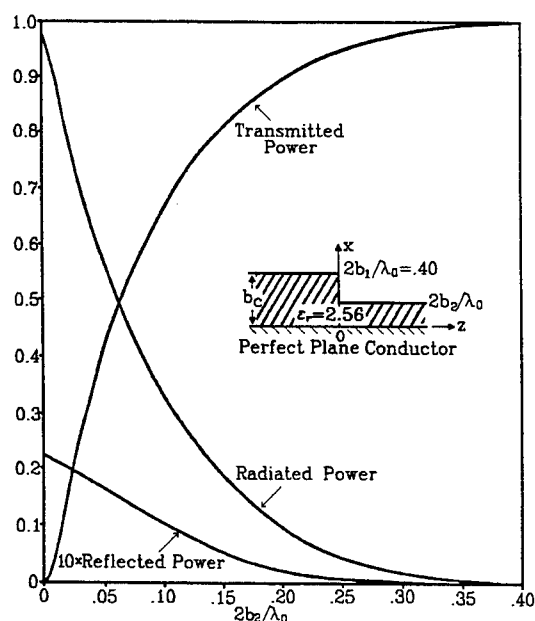

Figure 3: Power vs. the Slab Thickness in the Right Region for $2b_1 = .4\lambda_0$ and $\epsilon_{r1} = \epsilon_{r2} = 2.56$.
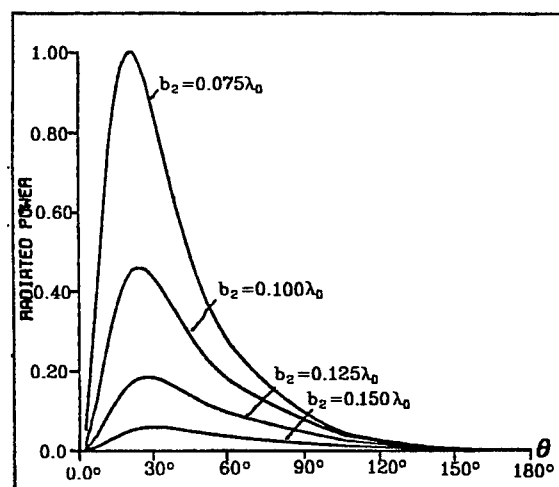

Figure 5: The Power Pattern for $b_2/\lambda_0 = 0.075...0.150$ with $\epsilon_{r1} = \epsilon_{r2} = 2.56$.

Adaptive Meshing in Two-Variable Static Problems with Field Based Error Estimators Using Edge and Facet Elements

P. Girdinio, P. Molfino, G. Molinari, M. Nervi

Dipartimento di Ingegneria Elettrica, Universita' di Genova
11a, Via Opera Pia - I-16145 Genova, Italy

Abstract— In this paper a family of field-based error estimators for Finite Element analysis of electrostatic and magnetostatic problems in plane and axisymmetric geometries is presented. For the error estimation in magnetostatics, each element is divided in three sub-elements using an edge element approach, whereas for electrostatic problems a subdivision using facet elements is used. The methods and the numerical techniques are described, comparisons with known solutions are performed, some examples of application in cases of practical interest are reported and the obtained results are briefly discussed.

I. INTRODUCTION

Techniques for error estimation in Finite Element solutions of field problems and for automatic mesh modification to guarantee a user-defined error level have been proposed for many years, in all areas of engineering analysis [1]. Today they are becoming more and more interesting, particularly in Electromagnetic Analysis, because of their strategic importance in allowing reliable Finite Element solutions without specific user skills, in turn essential for automation of design environment, device optimization and inverse problem applications, increasingly required in designing advanced electromagnetic devices [2]. Many techniques for the estimation of errors have been proposed, but it has also been shown that the efficiency of each technique is significantly dependent on the specific problem to be solved [3-6].

In this paper a family of error estimators, resulting among the most efficient for electrostatic and magnetostatic problems in the range developed and tested by the authors, is presented. All error estimators are developed for first order, triangular meshes, operate on a single element at a time, and are available both for plane and axisymmetric geometries. The estimators present some analogies with the "Local Error Problem" approach, developed by the authors, that has been found very efficient with respect to other approaches [5]. The error estimators have been developed casting the errors directly in terms of fields, the quantity of more direct physical interest, defining a "Local Field Error Problem" [7].

The distinctive feature of the family of error estimators presented in the paper is the representation of the field over the element, that is related to the type of potential, scalar or vector, used to derive the field. This ensures the ability to capture effectively the biggest error contribution, connected to the normal derivative of the potential from which the field is derived. The representation of the error variables is then in terms of "edge" or "facet" elements for solutions derived from vector or scalar potentials, respectively [8]. To ensure a practical representation of these variables, a "Whitney forms" description has been used [9].

The error estimators defined in this way have then been used to build up an adaptive meshing strategy, based on the subdivision of elements with high errors, usually termed "h refinement" [10,11]. All algorithms have been implemented in the two-dimensional Finite Element development environment CEDEF, also used for other error estimation and adaption procedures developed in the authors' group [12].

In the paper the structure of error estimators is described, the adaptive meshing strategy used is outlined, the validation of their performance in cases with known solutions is performed, and results of usage in cases of practical industrial interest are reported and briefly discussed.

II THE LOCAL FIELD ERROR APPROACH

The "Local Field Error Problem" for the electrostatic and magnetostatic cases is derived from the proper subset of Maxwell equations, defining a governing set in terms of curl and divergence of the numerical error [6,7,13]. The estimation is based on the solution of a differential problem over each element using as "error sources" the jump in normal derivatives of potential along element edges. In a similar way, it is possible to derive a formulation defining again a local problem over each element; this will assume as unknowns the errors in the evaluation of field quantities, with "error sources" derived from the jumps in the normal derivatives of potential applying Ampere's and Gauss' laws.

The development of an "a posteriori" error estimate based on a "Local Field Error" approach requires the definition of the error estimate unknown in term of fields, the use of Maxwell equations in differential form and the definition of a closed domain where Dirichlet-like boundary conditions are applied. This implies that the unknown vector entity is uniquely defined by Helmholtz's theorem.

A. Electrostatic Problems

The evaluation of the estimate of numerical errors in FEM solutions of electrostatic problems can be carried out by defining an adjoint problem, in terms of errors in electric field evaluation, where the unknowns are the components of the error vector $\bar{e}$, defined as difference between the "true" electric field $\bar{E}_t$ and the computed one $\bar{E}_c$, that is:

$$\bar{e} = \bar{E}_t - \bar{E}_c \tag{1}$$

The error equations are derived from the electrostatic subset of Maxwell equations applied to the "true" electric field $\bar{E}_t$. This leads to the set of vector equations in terms of the error $\bar{e}$:

$$\nabla \cdot \bar{D} = \delta \Rightarrow \nabla \cdot (\varepsilon \bar{e}) = \delta - \nabla \cdot \left(\varepsilon \bar{E}_c\right) \tag{2}$$

$$\nabla \times \bar{E} = 0 \Rightarrow \nabla \times \bar{e} = -\nabla \times \bar{E}_c \tag{3}$$

where ε is the permittivity of materials and δ is the free charge density. The RHS term of (2) can be expressed in terms of a fictitious charge density δ_f by applying Gauss' law as:

$$\nabla \cdot \bar{D}_c - \delta = \nabla \cdot \left(\varepsilon \bar{E}_c\right) - \delta = \delta_f \tag{4}$$

The fictitious charge density δ_f is the volume source of the problem in terms of error and must be derived from the numerical solution in terms of the electric potential V.

B. Magnetostatic Problems

For magnetostatic problems, the evaluation of the estimate of numerical errors in Finite Element solutions can be carried out defining an adjoint problem where the unknowns are the components of the error vector $\bar{e}$, defined as the difference between the "true" magnetic induction $\bar{B}_t$ and the computed one $\bar{B}_c$, that is:

$$\bar{e} = \bar{B}_t - \bar{B}_c \tag{5}$$

The governing equations of the error problem are derived from the magnetostatic subset of Maxwell equations applied to the "true" magnetic induction $\bar{B}_t$. This leads to the set of vector equations for the numerical vector error $\bar{e}$:

$$\nabla \cdot \bar{B}_t = 0 \Rightarrow \nabla \cdot (\bar{e}) = -\nabla \cdot \left(\bar{B}_c\right) \tag{6}$$

$$\nabla \times \bar{H} = \bar{J} \Rightarrow \nabla \times (\nu \bar{e}) = \bar{J} - \nabla \times \left(\nu \bar{B}_c\right) \tag{7}$$

where ν is the reluctivity of materials and J is the applied current density. The RHS term of (7) can be expressed in terms of a fictitious current density J_f by applying Ampere's law as:

$$\nabla \times \bar{H}_c - \bar{J} = \nabla \times \left(\nu \bar{B}_c\right) - \bar{J} = \bar{J}_f \tag{8}$$

Those fictitious current densities are the volume sources of the problem in terms of error and must be derived from the numerical solution in terms of magnetic vector potential.

C. Solution Strategy

Equations (2) plus (3) and (6) plus (7) define the sets of vector equations for the error problems over a generic open domain, in the electrostatic and magnetostatic cases, respectively. This general form could be applied, in principle, to the whole domain of a problem discretized and solved with FEM, defining an adjoint problem where the unknowns are the error vectors: this problem would be of the same size, in term of unknowns, as the original FEM solution. However, this solution is in general considered too expensive, since it requires at each iteration the solution of two problems roughly of the same size. The solution strategy generally used to overcome this problem is based on the definition of the error problem on "patches" of a limited number of elements, considering the FEM discretized domain as a set of subdomains in each of which, if appropriate boundary conditions are applied, equations (2) and (3) or (6) and (7) can be defined [1,3,4].

In order to cope better with complex geometries with many interfaces, very likely to be of interest in industrial electromagnetic design, the authors have always chosen to restrict the "patch" to a single element [5-7].

III. ERROR SOURCES

As previously pointed out, the problem is restricted to the solution of a "local problem", over each element, consisting of a set of two equations: one in terms of "divergence" (eq. 2 or 6) and one in terms of "curl" (eq. 3 or 7). In order to obtain a unique solution, the definition of appropriate boundary conditions on each element is required. As it is well known, the derivatives computed by a FEM solution in terms of scalar potential, or of vector potential with a single component, are continuous in the tangential component at each inter element boundary, and are discontinuous on the normal component at the same boundaries. This leads to the assumption that the information relevant to the numerical error associated with the discrete solution are contained in those discontinuities [3-7].

In the standard approach proposed in [3,4], the continuity of the tangential component of the derivatives of the potential leads to the assumption that the error in the node is by definition set to zero, implying that it can

be considered negligible with respect to the error along the sides of the element. Similarly, in the "Field Based" approach proposed by the authors it is assumed that the error related to one of the components of the field (the tangential component of electric field or the normal component of magnetic induction) is negligible with respect to the error related to the other component. The consequence is that one of the two equations (the "curl" equation (3) for the electric field and the "divergence" equation (6) for the magnetic field) can be assumed as identically satisfied and can then be neglected in the error problem. With this assumption, the sources for the error problem can be identified only for the "meaningful" component of the error (the normal component for the electric field and the tangential component for the magnetic field) and the governing set of equations is restricted to one equation only.

On each element of the discretized domain the boundary conditions are given on the surface of the element in term of the jump of the normal derivatives of the potential at inter-element boundaries. The computed jump, expressed in terms of field, is split between the two neighbouring elements, i and j, for the electric and magnetic field, respectively, as:

$$e_{i(j)} = \omega_{i(j)}\left(\vec{E}_c^i - \vec{E}_c^j\right)\cdot\vec{n} \tag{9}$$

$$e_{i(j)} = \omega_{i(j)}\left(\vec{B}_c^i - \vec{B}_c^j\right)\times\vec{n} \tag{10}$$

The weight factors $\omega i(j)$ take into account the ratio between the absolute values of the field in the two adjoining elements. At exterior boundaries and interfaces, the conditions on the error are derived by the residual in the evaluation of the relevant condition with respect to the normal (electric field) or tangential (magnetic field) component of the field.

The fictitious charge density δ_f and current densitiy J_f defined by (4) and (8), assumed to be constant over each element, can be evaluated applying Gauss' law, or Ampere's law, respectively, to the exterior boundary $\partial\Delta$ of each element Δ:

$$\oint_{\partial\Delta} \vec{D}_c \cdot \vec{n}\,ds - \int_\Delta \delta\,d\Omega = \int_\Delta \delta_f d\Omega \tag{11}$$

$$\oint_{\partial\Delta} \vec{H}_c \cdot d\vec{\ell} - \int_\Delta \vec{J}\cdot d\vec{\Omega} = \int_\Delta \vec{J}_f \cdot d\vec{\Omega} \tag{12}$$

IV. NUMERICAL SOLUTION

The adjoint problem in terms of error, defined by (2) for the electrostatic problem or by (7) for the magnetostatic problem over each element of the discretized mesh, with boundary conditions like (9) or (10) and internal sources like (11) or (12), can be

numerically solved by discretizing the domain (that is, each generic element) into three sub-elements, by adding a node at the centroid of the element.

On each sub-element the unknown error (the normal component of the error in the evaluation of the electric field, or the tangential component of the error in the evaluation of magnetic field) is represented using a vector interpolation representation expressed using a "Whitney forms" description [8,9] in terms of the nodal basic interpolation functions of first order (N_1, N_2, N_3).

A. Electrostatic problem

In electrostatic Finite Element solutions, the vector interpolation form for the definition of the error problem that has been found more suitable to represent the error in terms of electric field is the "Facet Element" interpolation technique. This technique is particularly useful for this case since it represents very well quantities related to a flux [8], that is the normal component of fields, which is the one more directly linked to the error in this case, as previously outlined. The boundary conditions and the unknowns for the error problem over each element are shown in Fig. 1.

The three normal components applied to the outer sides are the known jumps, given by (9), that are derived from the numerical solution, while the three normal component applied to the inner sides are the unknown values.

Fig. 1: Discretized "local domain" for the error problem and error unknowns in the electrostatic case.

The error vector on a single sub-element can be defined as:

$$\vec{e} = \sum_k \vec{W}_k e_k \quad \text{where} \quad \vec{W}_k = N_i\nabla\times\vec{N}_j - N_j\nabla\times\vec{N}_i \tag{13}$$

Using a weighted residual approach, the discretized equation is then derived by the integral relation:

$$\int_\Omega \left(\nabla\cdot\vec{W}_k\right)\left(\varepsilon\nabla\cdot\vec{e} - \delta_f\right)d\Omega = 0 \tag{14}$$

In this way, on each element a set of three equations is defined, having as three unknowns the normal components of the error vector in the three inner sides of the discretized "local domain", as described in Fig. 1.

144

B. Magnetostatic problem

In the magnetic case, the vector interpolation form for the definition of the error problem that appears more suitable to represent the vector error in terms of magnetic induction is the "Edge Element" interpolation technique.

This technique is particularly useful for this case since it represents very well quantities related to a circulation [8].

The boundary conditions and the unknowns for the numerical problem are shown in Fig. 2, where the three tangential components applied to the outer sides are the known jumps, given by (10), derived from the numerical solution, while the three tangential components applied to the inner sides are the unknown values.
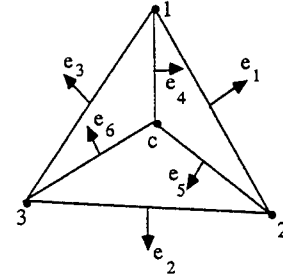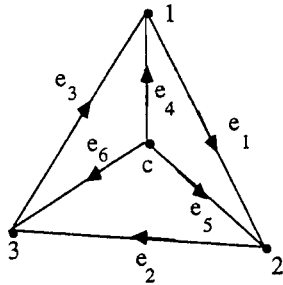

Fig. 2: Discretized "local domain" for the error problem and error unknowns in the magnetostatic case.

The error vector on a single sub-element can be derived as:

$$\bar{e} = \sum_k \bar{W}_k e_k \quad \text{where} \quad \bar{W}_k = N_i \nabla N_j - N_j \nabla N_i \qquad (15)$$

Using a weighted residual approach, the discretized equation is then described by the integral relation:

$$\int_\Omega \left(\nabla \times \bar{W}_k \right) \cdot \left(\nu \nabla \times \bar{e} - \bar{J}_f \right) d\Omega = 0 \qquad (16)$$

defining on each element a system of three equations in three unknowns, the tangential components of the error vector, defined on the three inner sides of the discretized "local domain", as detailed in Fig. 2.

V. MESH REFINEMENT

The use of the error estimates previously presented in an automatic procedure for mesh refinement requires the identification of an adaption strategy. After a series of initial tests, the authors have identified a procedure that has proven reliable and robust for electromagnetic analysis applications, also in the case of complex geometries of practical industrial interest [10,11].

As defined in a previous paper [11], the procedure is based on the definition of a refinement indicator to guide the subdivision of elements, of a convergence parameter to stop the iterative process of mesh

refinement and also provides a final estimate of the local relative error on each element of the final refined mesh. All quantities are computed on the basis of evaluation of quadratic norms over each element of local values. The quadratic norm of a scalar or vector quantity is defined as:

$$\|u\| = \sqrt{\int_\Omega |u|^2 \, d\Omega} \qquad (17)$$

The refinement indicator is defined as :

$$\eta_i = \sqrt{\frac{\|\bar{e}_i\|^2}{\sum_j \|\bar{F}_j\|^2}} \qquad (18)$$

where the vector F is the electric field in electrostatic cases or the magnetic induction in magnetostatic problems. The refinement indicator is used to identify the elements to be subdivided. The convergence parameter and the final error estimator are defined by:

$$c = \sqrt{\sum_i \eta_i^2} \quad ; \quad \varepsilon_i = \frac{\|\bar{e}_i\|}{\|\bar{F}\|_{max}} \qquad (19)$$

The convergence indicator is used to terminate the iterative procedure, that is stopped when its value falls below a user defined value of "average desired error", in relative or percentual terms. The final error estimate is then evaluated with respect to the maximum field value F (electric or magnetic) computed over the domain. Mesh refinement is realized using the h-refinement procedure detailed in [11].

VI. IMPLEMENTATION AND TEST CASES

The proposed method has been implemented in the two-dimensional Finite Element development environment CEDEF, in the interactive module developed for the comparison of adaptive meshing and error estimation techniques [12]. Each solution is obtained with first order triangular elements.

In order to validate the approach and to evaluate the performance of the proposed method, a set of analytically known problems has been analysed. The comparisons between estimated errors and real ones have been realized using in both cases the formula given in (20), but substituting, for the real errors, the exact solution.

All tests performed have indicated a good performance of the method, that has generally provided consistent meshes and a final error estimate close to the real error. To allow a direct evaluation of results, some of the comparisons performed are reported in the following subsections.

145

A. Dielectric cylinder in uniform field

This model problem is particularly useful to test the performance of the method in the presence of an interface between two materials with different permittivity. An analytical solution for this problem is given in [14].

In Fig. 3 the initial and the refined meshes, with a convergence level set to 1%, are reported. The results obtained, in terms of error estimate and real error on the refined mesh, are plotted in Fig. 4 with reference to the behaviour of errors along a line at y=0 across the interface.

As can be observed from Fig. 4, the procedure shows a good agreement with real errors, as also found in other test cases of similar type, not reported here for the sake of brevity.
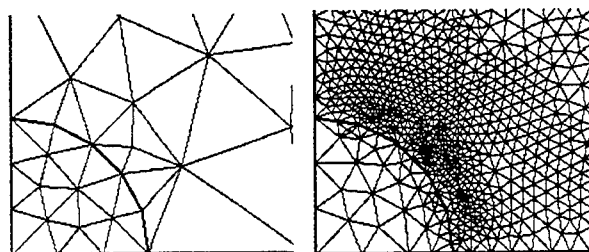

Fig. 3: Initial and refined meshes for the dielectric cylinder problem, showing only a detail of the mesh.
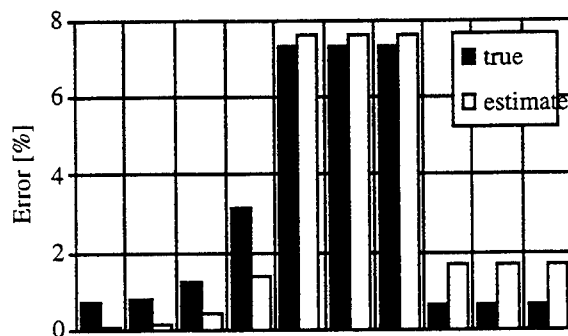

Fig. 4: Plot of the comparisons between true and estimated errors. for the Dielectric cylinder problems along a line at y=0 across the interface.

B. Conductor Bar

Another reference problem that has been used as a test is the evaluation of magnetic induction distribution generated by a conductor bar of infinite length in an ironless domain. The analytic solution is obtained by the integration of Biot-Savart's law [14]. The model for the numerical solution has been obtained using a Dirichlet boundary condition at a sufficient distance from the conductor, computed by means of analytical formulae. In Fig. 5 the initial and the refined mesh, with a convergence level set to 1% are shown. In Fig. 6 the behaviour of the real and estimated errors along a line on the symmetry axis (y=0) crossing the conductor is reported.
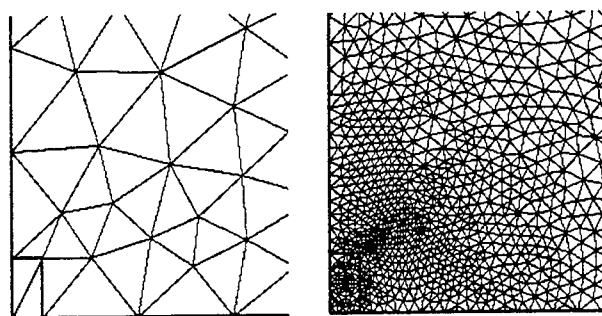
Fig. 5: Initial and refined meshes for the "Conductor Bar" problem, showing only a detail of the mesh.
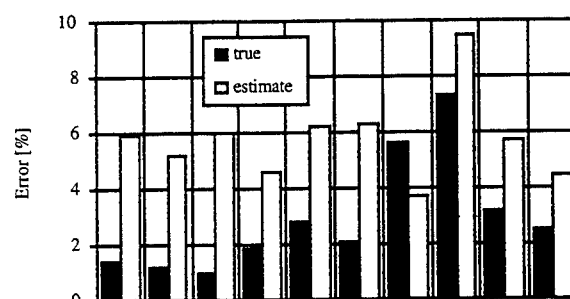
Fig. 6: Behaviour of the real and estimated errors along a line on the symmetry axis of the conductor bar problem.

VII. ROTATIONAL SYMMETRY PROBLEMS

Since the error problems are cast in terms of fields, the error estimates with the "Local Field Error Problem" approach can be also extended to rotational symmetry problems with a limited amount of conceptual changes with respect to the formulation presented above.

This extension has been performed and validated in the CEDEF development environment previously mentioned, and has provided also for this type of geometries very good results. Some examples of this kind are given in the next section.

VIII. INDUSTRIAL DESIGN EXAMPLES

The adaptive procedures realized on the basis of the "Local Field Error" formulation have been also used in real, industrial level test problems, to evaluate the robustness of the procedure for practical applications.

Fig. 7: Initial and final mesh for the evaluation of electrostatic fields in an SF$_6$ switchgear.

Fig. 8: Initial and final mesh for the evaluation of magnetic induction in a permanent magnet loudspeaker.

In Fig. 7 the initial and final meshes for the evaluation of electrostatic fields in the axial section of an axisymmetric 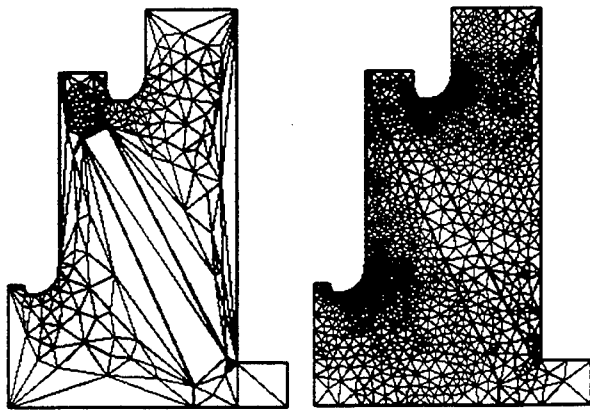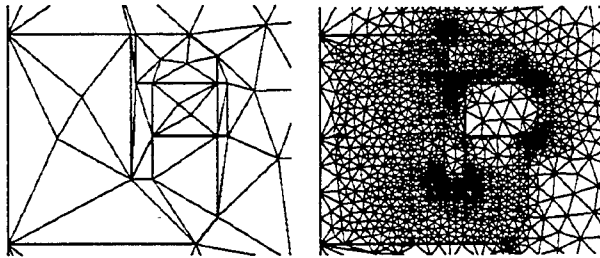SF$_6$ switchgear, comprising high voltage electrodes and an insulating cone are given, while in Fig. 8 the initial and final meshes for the evaluation of magnetic fields in a permanent magnet loudspeaker are displayed .

In both cases the initial and final meshes have been produced in complete automation by the procedure, with the user required to define the average accuracy level only, set to one percent for each solution, and the results have proven consistent with those obtained with other codes, run with fine meshes without using an adaptive technique.

IX. CONCLUSIONS

The family of error estimators and adaptive algorithms presented in this paper has proven very effective and reliable in the cases tested. They also covered geometries of interest in industrial design, and helped to obtain FEM solutions of practical electrostatic and magnetostatic problems without any effort in the definition of the mesh. The solution quality is under the control of users but independent of their skills.

The algorithms devised appear rather robust and flexible and the authors are carrying on further activity to extend the coverage to other subclasses of electromagnetic analysis.

REFERENCES

[1] I Babuska, O.C. Zienkiewicz, J. Gago, E.R. de Oliveira, Eds: *Accuracy estimates and adaptive refinement in Finite Element Computation*, Wiley, New York, 1986.

[2] C. Emson, C.W. Trowbridge, P. Girdinio, G. Molinari, M. Repetto: "Towards an environment for the integration of analysis and design" *Comp. Integrated Manuf. Systems*, Vol. 3, n. 4, Nov. 1990, pp. 216-222.

[3] I. Babuska, W. C. Rheinboldt: "A-posteriori error estimates for the finite element method", *Int. J. for Numerical Methods in Engineering*, Vol. 12, 1978, pp. 1597-1615.

[4] R.E. Bank, A. Weiser: "Some a-posteriori error estimators for elliptic partial differential equations", *Mathematics of Computation* , Vol. 44, Apr. 1985, pp. 283-381.

[5] P. Fernandes, P. Girdinio, P. Molfino, M. Repetto: "Local error estimates for adaptive mesh refinement" *IEEE Trans on Magnetics*, Vol. 24, n. 1, Jan. 1988, pp. 299-302.

[6] P. Barabaschi, G. Drago, P. Girdinio, P. Molfino, M. Repetto, G. Secondo: "A local error 'field based' method for error estimation and adaptive meshing for finite element analysis", *Proc. of 4th IGTE Symposium*, Graz (Austria), Oct. 1990, pp. 47-51.

[7] G. Drago, P. Molfino, M. Nervi, M. Repetto, "A 'Local Field Error Problem' Approach for Error Estimation in Finite Element Analysis", *IEEE Trans. on Magnetics*, vol. 28, n. 2, March 1992, pp. 1743-1746,

[8] A. Bossavit: "A rationale for 'Edge Elements' in 3-D fields computations", *IEEE Trans. on Magnetics*, Vol. 24, n. 1, Jan. 1988, pp. 74-79.

[9] A. Bossavit: "Whitney forms: a class of finite elements for three-dimensional computations in electromagnetism" *IEE Proceedings*, Vol. 135, Pt. A, n. 8, Nov. 1988, pp.493-500.

[10] P. Fernandes, P. Girdinio, P. Molfino, G. Molinari, M. Repetto: " A Comparison of Adaptive Strategies for Mesh Refinement Based on 'A Posteriori' Local Error Estimation Procedure" *IEEE Trans. on Magnetics*, Vol. 26, n. 2, March 1990, pp. 795-798.

[11] P. Fernandes, P. Girdinio, M. Repetto, G. Secondo: "Refinement Strategies in Adaptive Meshing" *IEEE Trans. on Magnetics*, Vol. 28, n. 2, March 1992, pp. 1739-1742.

[12] G. Molinari *et al.* : "A modular Finite Element package for research in electromagnetic analysis developed in a group of italian universities" *Proc. of Int. Conf. BISEF 88*, Beijing, China, Sept. 1988, pp. 625-628.

[13] P. Girdinio, A. Manella, P. Molfino, M. Nervi, "A 'Facet Element' Error Estimate for Adaptive Meshing in Electrostatic FEM Solutions", *Proc. of 6th. IGTE Symposium*, Graz (Austria), Sept. 1994, pp. 138-143.

[14] E. Durand, *Electrostatique et magnetostatique*, Paris: Masson et C.ie, 1953.

Finite element modelling schemes for the design and analysis of electrical machines

D.Rodger, P.J.Leonard, H.C.Lai and N.Allen

University of Bath, Bath Avon BA2 7AY, U.K.

Abstract— Electrical machines are complex objects. We have found that a variety of numerical techniques are required in order to model them using finite elements. We concentrate here on the different formulations which are useful in modelling such devices. Examples of modelling some of these machines using the MEGA package are described.

INTRODUCTION

Many electrical machines and other electromagnetic devices can be difficult to model using finite elements. They can contain features such as magnetic nonlinearity, movement, geometric complexity and connection to an external circuit. Here we describe some features of a general purpose finite element package MEGA which allows some of the less pathological problems to be treated. First we review the formulations used in the finite element models.

FINITE ELEMENT FORMULATIONS

The non conducting and conducting regions are modelled using the magnetic scalar potential, ψ, and the magnetic vector potential, $\mathbf{A}$, respectively. This approach leads to an economic description of the field problem.

Non Conducting Regions

Non conducting regions are modelled using magnetic scalar potentials, either the total scalar ψ ,defined as $\mathbf{H}_T = -\nabla\psi$, or the reduced scalar ϕ, defined as $\mathbf{H}_T = -\nabla\phi + \mathbf{H}_S$. Here $\mathbf{H}_T$ is the total magnetic field intensity and $\mathbf{H}_S$ is the field defined as $\nabla\times\mathbf{H}_S = \mathbf{J}_S$, where $\mathbf{J}_S$ is the source current density. The basic method outlined in [1] has been extended to allow voltage forced conditions [2], and to produce cuts for solving multiply connected problems. Both scalars give rise to a Laplacian type equation which has to be solved:

$$\nabla\cdot\mu\nabla\psi = 0 \qquad (1)$$

Conducting Regions Including the Minkowski Transformation

Fields in conductors can be modelled using $\mathbf{A}$, the magnetic vector potential, and V, the electric scalar potential.

Using $\mathbf{B} = \nabla\times\mathbf{A}$ and $\mathbf{E} = -\frac{\partial\mathbf{A}}{\partial t} - \nabla V + \mathbf{u}\times\nabla\times\mathbf{A}$, where $\mathbf{u}$ is the material velocity, we obtain:

$$\nabla\times\frac{1}{\mu}\nabla\times\mathbf{A} = \sigma\left(-\frac{\partial\mathbf{A}}{\partial t} + \mathbf{u}\times\nabla\times\mathbf{A} - \nabla V\right) \qquad (2)$$

$$\nabla\cdot\sigma\left(\frac{\partial\mathbf{A}}{\partial t} - \mathbf{u}\times\nabla\times\mathbf{A} + \nabla V\right) = 0 \qquad (3)$$

The term involving $\mathbf{u}\times\nabla\times\mathbf{A}$ in the above arises from the Minkowski transformation and is only valid if the moving media cross section normal to the direction of motion is invariant. Where appropriate [3], it is economical to dispense with V from the above set of equations. If we substitute $V = \mathbf{A}\cdot\mathbf{u}$ in the above formulation we have:

$$\nabla\times\frac{1}{\mu}\nabla\times\mathbf{A} =$$
$$\sigma\left(-\frac{\partial\mathbf{A}}{\partial t} - (\mathbf{u}\cdot\nabla)\mathbf{A} - (\mathbf{A}\cdot\nabla)\mathbf{u} - \mathbf{A}\times(\nabla\times\mathbf{u})\right) \qquad (4)$$

Now a solution of (4) involving only $\mathbf{A}$ is required.

The uniqueness of $\mathbf{A}$ is fixed by using a penalty term to specify the divergence of $\mathbf{A}$ and forcing the normal component of $\mathbf{A}$ to be zero on the inside surface of conductors. The last two terms in (4) are non zero in the case of rotational velocity [4] but are zero in the case of translational velocity [5]. Equations (1) and (4) are solved using a Galerkin finite element scheme [6]. If nonlinear, the equations are solved using a Newton-Raphson scheme. This scheme can be very unstable if used directly. A modified scheme which uses line searches has been found to be necessary in the general case [7]. The terms involving $\mathbf{u}$ in (4) lead to numerical instability. This is alleviated by using an upwinding scheme [8]. The scheme here allows for a conductor moving at a velocity $\mathbf{u}$, and leads to an asymmetric global matrix which has to be solved. The non moving case is of course symmetric.

Electrostatic Problems

Electrostatics problems may sometimes be formulated in terms of the electric scalar potential V, so that

$$\mathbf{E} = -\nabla V \qquad (5)$$

Since

$$\nabla \cdot D = \rho, \qquad (6)$$

we obtain the Laplacian in V:

$$-\nabla \cdot \epsilon \nabla V = \rho \qquad (7)$$

As usual this may be solved using a Galerkin technique and either 2D or 3D finite elements. After some manipulation, this results in, for a 3D system:

$$\int_\Omega \nabla N \cdot \epsilon \nabla V \, d\Omega - \int N \epsilon \frac{\partial V}{\partial n} \, dS = \int_\Omega N \rho \, d\Omega \qquad (8)$$

Note that this formulation results in an exact enforcement of the $\mathbf{E} \times \mathbf{n}$ continuous condition and that the $\mathbf{D} \cdot \mathbf{n}$ condition is weakly correct.

COMBINING THE FIELD AND CIRCUIT EQUATIONS

Electrical machines are almost always connected to a fixed voltage supply or an electrical circuit such as an inverter. Unfortunately many finite element packages only allow constant current sources. Often a finite element model is used to derive a simpler equivalent circuit which may be connected to the external circuit.

In some situations it is not possible to use the finite element field model to derive an equivalent circuit. For example if the field equations are nonlinear then the equivalent circuit would have to be identified for all possible field states, which is not practical. It is possible in some circumstances to use a separate field and circuit model and iterate until the interface conditions are met. This may work if the field and circuit are loosely coupled but for the tightly coupled case a combined solution is attractive. Another advantage of the tightly coupled finite element/circuit model is that the user interface is easier to deal with, as the complexity of the situation is handled in the software. This means that as far as the designer is concerned, the computer model is conceptually very easy to visualise and hopefully very similar to just wiring up an experiment in the laboratory.

The general problem is to combine the field equations in terms of potentials with circuit node equations. In our scheme we use various field formulations for 2D and 3D. In the circuit problem we solve for nodal voltages using Kirchoff's current equations at each node. To couple the two models we must identify the voltage and current within the field equations. These can then be used directly in Kirchoff's circuit equations.

The field equations fall into two forms depending on the formulation,

- Current is the source term:

$$\begin{bmatrix} K & Q \\ Q^T & R \end{bmatrix} \begin{pmatrix} X_{field} \\ V \end{pmatrix} = \begin{pmatrix} 0 \\ I \end{pmatrix} \qquad (9)$$

- Voltage is the source term:

$$\begin{bmatrix} K & W \\ W^T & L \end{bmatrix} \begin{pmatrix} X_{field} \\ I \end{pmatrix} = \begin{pmatrix} 0 \\ V \end{pmatrix} \qquad (10)$$

EXAMPLE OF A 2D MOTOR

Consider a 2D model with coils of a given turns density.

- Each wound coil has a known current distribution (but unknown value I_c).

- The *turns density* tdefines the distribution of current.

- Then current density is

$$\mathbf{J} = I_{coil} \mathbf{t} \qquad (11)$$

- The voltage across the terminals is found by integrating the back e.m.f.

$$V = l \int \mathbf{t} \cdot \dot{\mathbf{A}} \, dS \qquad (12)$$

The equations to be solved are,

$$-\nabla \cdot \frac{1}{\mu} \nabla A_z + \sigma \frac{\partial A_z}{\partial t} - \mathbf{t} I_{coil} = 0 \qquad (13)$$

$$\int \sigma \mathbf{t} \frac{\partial A_z}{\partial t} \, dS - V = 0 \qquad (14)$$

After applying the usual Galerkin procedure we get a set of equations that can be expressed in matrix form,

$$\begin{bmatrix} K & W \\ W^T & 0 \end{bmatrix} \begin{pmatrix} \mathbf{A} \\ I_c \end{pmatrix} = \begin{pmatrix} 0 \\ V \end{pmatrix} = 0 \qquad (15)$$

If this is connected to ports A and B, we have:

$$\begin{bmatrix} K & W & 0 & 0 \\ W^T & 0 & -1 & 1 \\ 0 & -1 & 0 & 0 \\ 0 & 1 & 0 & 0 \end{bmatrix} \begin{pmatrix} \mathbf{A} \\ I_c \\ V_A \\ V_B \end{pmatrix} = \begin{pmatrix} 0 \\ 0 \\ I_A \\ I_B \end{pmatrix} = 0 \qquad (16)$$

3D MODEL OF A CAR ALTERNATOR

The car alternator can be difficult to model because of its complex shape. Figure 1 shows a 3D finite element model of a typical claw-pole type car alternator. It has 12 rotor poles and 36 stator slots. It is difficult to model because the features of its rotor and stator are so different both circumferentially and axially that the finite element meshes at the interface between these objects will be totally incompatible. As a result, creating a sensible mesh in the air gap will be difficult.

149

To overcome this meshing difficulty, we create separate meshes for the stator and rotor and then bring them together to touch in the middle of the air gap. The two meshes are then coupled together by linking their potential variables on the interface using Lagrange multipliers. The main advantage of this approach is that the nodes of the two meshes do not need to be 'matched' on the interface. As a result, the individual meshes can be made to be as well-formed as possible.

This method is used to solve the FE model shown in Fig. 1. Due to symmetry, only one-twelveth of the whole alternator is modelled. The resulting vector plot of **B** near the tip of one of the rotor pole is shown in Fig. 2.
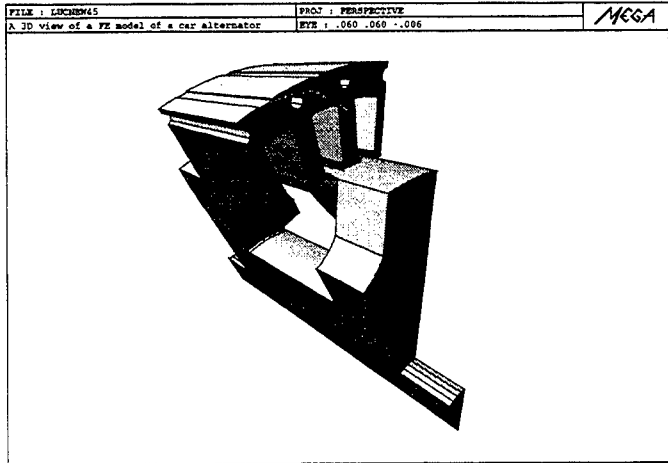

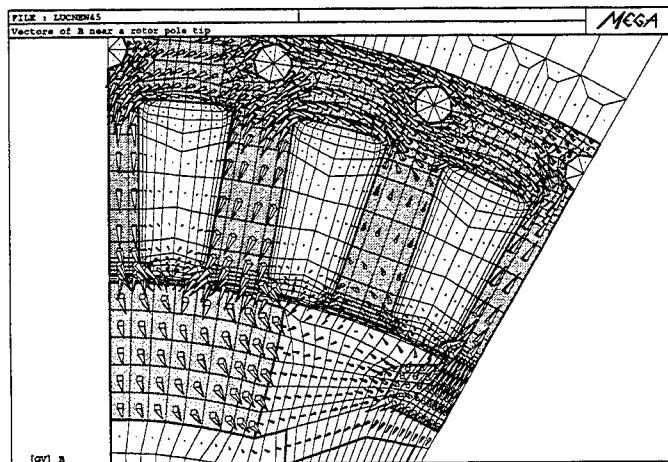Fig. 1. A 3D view of a FE model of a car alternator

Fig. 2. Field vectors near the rotor pole tip

An Electrostatic Micro Machine

Often electrostatic devices move or rotate and finite element solutions would be required at many positions. This may be achieved using Lagrange multipliers in much the same way as for magnetics formulations [9]. If a region is split up into two meshes which have some common interface which will allow relative movement, such as a cylinder or a flat plane, equations such as (8) may be used in each mesh. These meshes would still be disconnected and the natural boundary condition would prevail on the common interface. The meshes can be joined using Lagrange multipliers. The condition that V is continuous may be enforced at the common interface using Lagrange multipliers. The Lagrange multipliers may be identified with $\frac{\partial V}{\partial n}$ so that, as before, the $\mathbf{D} \cdot \mathbf{n}$ continuous condition is weakly satisfied and the continuity of V and therefore $\mathbf{E} \times \mathbf{n}$ is correct in an average sense. The two meshes need not have the same mesh at the common interface, nor the same number of nodes.

Figure 3 shows a small electrostatic machine, diameter $15 \times 10^{-5} m$. The torque versus position curve is of some interest to designers of such machines. The Lagrange sliding interface method is used to solve the problem with the rotor in 12 different positions, as shown in Fig. 4. This is achieved with very little user effort.
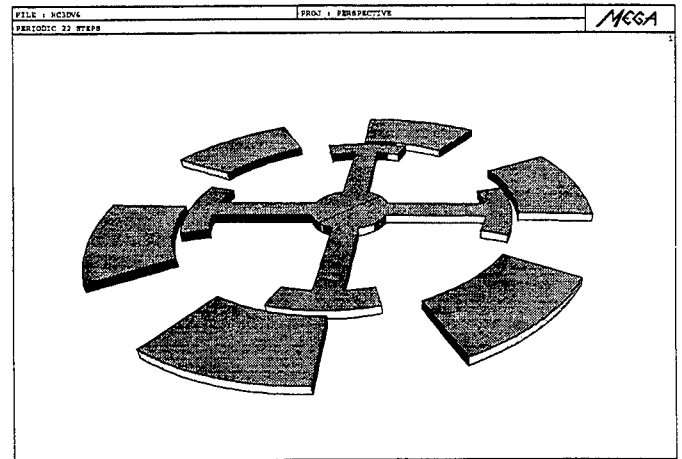
Fig. 3. A micro machine

Periodic boundary conditions

Often symmetry may be used to reduce the size of a finite element model. This section deals with another type of feature, periodicity. This is a function of the shape of the device and the state of the fields within it.

One of the earliest references to periodic boundary conditions may be found in [10], so the concept is well established. However, all of the published work up to now (as far as the authors know) deals with scalar variables. When solving 3D eddy current problems, vector variables are required, at least in conducting regions. These are slightly more complex and are described here.

If periodic boundary conditions exist on some parts of a device, a relationship between some potentials on boundaries is implied, of the following form:

150

Fig. 4. Torque versus rotor angle for a micro machine

$$slavevariable = P * mastervariable \qquad (17)$$

In this case the slave variables depend on the master variables. Only the master variables appear as degrees of freedom in the final set of equations. In the general case, for a vector variable at a periodic node, we can relate the slave variable to the master variable using a transformation matrix and a periodic parameter.

$$\begin{bmatrix} A_x \\ A_y \\ A_z \end{bmatrix}_{slave} = P \begin{bmatrix} l_{xx} & l_{xy} & l_{xz} \\ l_{yx} & l_{yy} & l_{yz} \\ l_{zx} & l_{zy} & l_{zz} \end{bmatrix} \begin{bmatrix} A_x \\ A_y \\ A_z \end{bmatrix}_{master} \qquad (18)$$
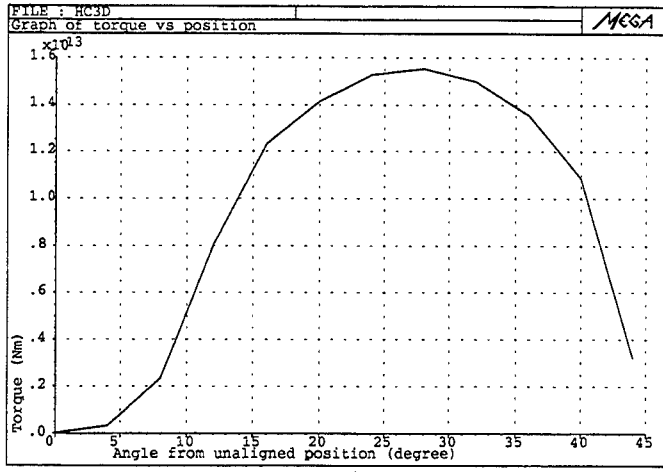
$$\psi_{slave} = P\psi_{master} \qquad (19)$$

The transformation matrix shown in (18) 'rotates' the slave vector so that the components of slave and master are aligned. This is more fully explained in [11]. The P in the above is the periodic parameter.

In general, the information required for establishing the periodic constraints in a typical electrical machine model are the location of the axis of rotational symmetry, a defined master-slave boundary, and the degrees of mechanical (M) and electrical (E) rotation. In the case of time transient or magnetostatic problems (P) the periodic parameter would normally be equal to cos E, where E would be 0 or 180 degrees. For linear time harmonic problems where complex numbers are used, P could be complex.

If the axis of mechanical symmetry is, for example, the z-axis, the potentials at the slave nodes are related to those of the master nodes in the following way:

$$\begin{bmatrix} A_x \\ A_y \\ A_z \end{bmatrix}_{slave} = \cos E \begin{bmatrix} \cos M & -\sin M & 0 \\ \sin M & \cos M & 0 \\ 0 & 0 & 1 \end{bmatrix} \begin{bmatrix} A_x \\ A_y \\ A_z \end{bmatrix}_{master} \qquad (20)$$

$$\psi_{slave} = (\cos E)\psi_{master} \qquad (21)$$

A PERIODIC TEST PROBLEM

The device to be modelled is a purpose built test rig, having the basic configuration of a switched reluctance machine. All iron parts are solid so that we have a 3D nonlinear eddy current problem. A full model of the test rig is shown in Fig. 5. A detailed description is presented in [7]. The purpose of the experiment is to use the finite element method to simulate the behaviour of the time-transient torque when a step voltage is applied to the system, and to validate these predicted results against measurement.
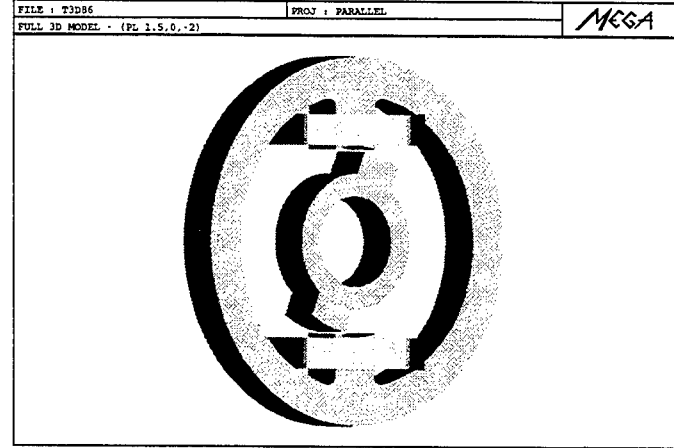
Fig. 5. Full model of the test rig

When using a full model of the test rig, which does not take advantage of the periodic boundary conditions, satisfactory correlation can be obtained between predicted and measured results. The discrepancy is less than 2% at a near-stabilized current. However, this problem is computationally expensive to solve, in both time and space. The file containing the results at each time step requires approximately 1.5 GBytes of disk space. In order to reduce the computational demands, periodicity constraints are implemented in the finite element software package, MEGA, and a new model, half the size, is constructed.

Only one half of the device width need be modelled for reason of symmetry. Further symmetry simplification is not possible because of the unaligned position of the rotor with respect to the stator pole. However a periodic model, shown in Fig. 6, can be constructed, containing only one of the coils and a periodic boundary.

The rig is excited from a constant voltage supply. A step voltage of 23.14V is applied to the coils which have a total resistance of 3.09Ω [7]. The coil currents are therefore unknowns in the system and must be calculated. This is carried out using the techniques described in the first section.

151

FILE : T3D86SLPERV6XC
3D SLICE, PERIODIC, VERSION 6, AUTOMATIC CUTS

Fig. 6. A view of the periodic model mesh

Results

A preliminary validation of the periodic model is carried out using a 1mm-thick slice of the original model. The periodic and non periodic 3D slice models yield identical torque curves, as may be observed in Fig. 7. However, since the periodic model contains only half the number o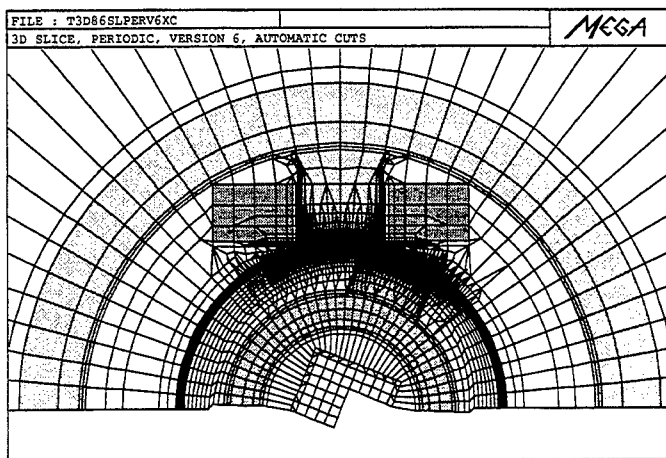f nodes compared to the non periodic one, the answer file containing all the time-step results is also decreased by the same factor (35 MBytes vs 70MBytes). The solving time on a DEC ALPHA model 3000 workstation has reduced from 6 hours to 2.4 hours, a saving of approximately 60%.

FILE : T3DPERV6
TORQUE RESULTS

△ PER. FULL 3D FORCE
▽ PER. 3D SLICE TORQUE
--- NON PER. 3D SLICE TORQUE
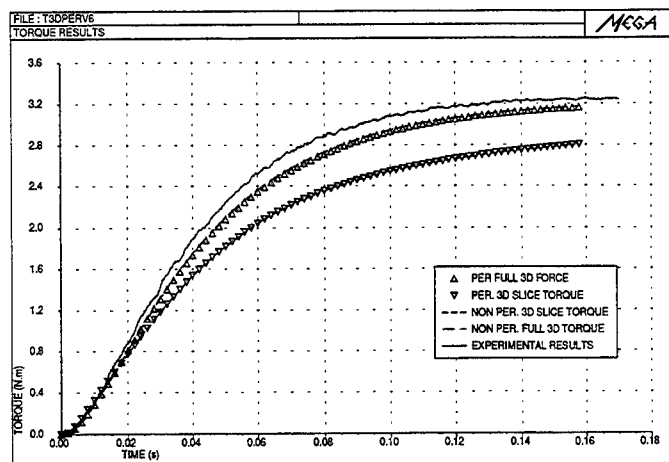— - NON PER. FULL 3D TORQUE
— EXPERIMENTAL RESULTS

Fig. 7. Comparison of measured and calculated torque

Full periodic and nonperiodic models were then constructed. Both of these torque curves agree very well with each other, as is shown in Fig. 7. The agreement with experimental results is also quite good. At 0.16s, the last computed time shown on the curve, the full 3D model predictions agree with experimental results to within 3%. Results from the slice models, which are essentially 2D, are of course less accurate. Here the agreement with measurement is approximately 14% at 0.16s.

CONCLUSIONS

Some of the techniques which can help in modelling electrical machines using finite elements have been presented. The sliding interface technique allows a machine to rotate in a realistic manner, while connected to an external circuit. The use of periodic boundary conditions can sometimes yield a more economic solution. Despite many recent developments around the world, electrical machines still present some difficult challenges for the modeller.

REFERENCES

[1] J.Simkin and C.W.Trowbridge. "On the use of the total scalar potential in the numerical solution of three dimensional magnetostatic problems". *IJNME*, 14:423–440, 1979.

[2] P.J.Leonard and D.Rodger. "Modelling voltage forced coils using the reduced scalar potential method". *IEEE Trans. Magn.*, MAG 28(2):1615–1617, March 1992.

[3] D.Rodger. "Finite-element method for calculating power frequency 3-dimensional electromagnetic field distributions". *IEE Proceedings Part A*, 130(5):233–238, July 1983.

[4] D.Rodger, N.Allen, P.C.Coles, S.Street, P.J.Leonard, and J.F. Eastham. "Finite element calculation of forces on a DC magnet moving over an iron rail". *IEEE Trans. Magn.*, 30(6):pp4680–4682, November 1994.

[5] D.Rodger, T.Karaguler, and P.J.Leonard. "A formulation for 3D moving eddy current problems". *IEEE Trans. Magn.*, 25(5):4147–4149, September 1989.

[6] O.C.Zienkiewicz. *"The Finite Element Method"*. McGraw-Hill Book Company Limited, 3rd edition, 1986.

[7] D.Rodger, N.Allen, H.C.Lai, and P.J.Leonard. " Calculation of transient 3D eddy currents in non linear media - Verification using a rotational test rig". *IEEE Trans. Magn.*, 30(5):2988–2991, September 1994.

[8] T.J.R.Hughes. "A simple scheme for developing "upwind" finite elements". *IJNME*, 12:pp 1359–1365, 1978.

[9] H.C.Lai, D.Rodger, and P.J.Leonard. "Coupling meshes in 3D problems involving movement". *IEEE Trans. Magn.*, MAG 28(2):1732–1734, March 1992.

[10] P.Silvester, H.Cabayan, and B.T.Browne. "Efficient techniques for finite element analysis of electric machines". *IEEE Trans. Power App. and Syst.*, pages pp1274–1281, 1973.

[11] D.Rodger and J.F.Eastham. "The use of transformations in applying boundary conditions to 3D vector field problems". *IEE Proceedings Part A*, 132(4):165–170, July 1985.

Three dimensional magnetostatics using the magnetic vector potential with nodal and edge finite elements

E. J. Silva, R. C. Mesquita

Departamento de Engenharia Elétrica - Universidade Federal de Minas Gerais
Av. Antônio Carlos, 6627, Belo Horizonte, MG, Caixa Postal 209, 30161-970, Brazil

Abstract — **In this paper, the three dimensional vector potential magnetostatic problem is solved using nodal and edge finite elements. The influence of the gauge condition A.w=0 in the characteristics of the edge-element generated matrix is analyzed. Three gauge conditions are studied: no gauge, the complete A.w=0 gauge and the incomplete A.w=0 gauge condition.**

I. INTRODUCTION

The 3D nodal finite-element magnetostatic formulations are usually based on scalar potentials. However, these formulations present some problems such as the cancellation errors in highly permeable regions and difficulties to treat multiply connected regions [4]. These problems do not appear when the magnetic vector potential is used. However, there are also some computational drawbacks in this case, due to the use of three unknowns per node and due to the necessity of imposing a gauge condition.

A new kind of finite-element that is being nowadays used is the edge element [1]. This element is very interesting from the computational point of view. Its degrees of freedom are line integrals of the vector potential along the edges. These elements automatically impose the tangential continuity of the interpolated variable between elements and let the normal component free. These elements are also adequate to impose the gauge A.w=0, where w is an arbitrary vector field that does not possess closed lines.

The main objective of this paper is to compare the use of the edge and nodal finite elements in the solution of 3D magnetic vector potential static problems. The number of unknowns, the number of non zero elements in the matrix and the number of ICCG iterations are analyzed. The influence of the gauge A.w=0, for edge elements is also analyzed.

II. MATHEMATICAL FORMULATION

The magnetic vector potential **A**, defined by

$$\vec{B} = \vec{\nabla} \times \vec{A}$$ (1)

satisfies the following differential equation:

$$\vec{\nabla} \times (v\vec{\nabla} \times \vec{A}) = \vec{J}$$ (2)

where **B** is the flux density, v is the magnetic reluctivity and **J** is the current density vector.

This problem is not completely defined yet. The interface conditions between regions of different material characteristics, the boundary and gauge conditions must be specified. The interface conditions are based on the tangential continuity of the magnetic field **H** and on the continuity of the normal component of the magnetic induction **B** on the interface between regions of different characteristics, that is:

$$\hat{n} \times (v(\vec{\nabla} \times \vec{A})_1) = \hat{n} \times (v(\vec{\nabla} \times \vec{A})_2)$$
$$(\vec{\nabla} \times \vec{A})_1 \cdot \hat{n} = (\vec{\nabla} \times \vec{A})_2 \cdot \hat{n}$$ (3)

Here **n** is a unit vector normal to the interface.
The boundary conditions can be specified as:

$$v\vec{\nabla} \times \vec{A} \times \hat{n} = 0 \qquad where \qquad \vec{H} \times \hat{n} = 0$$
$$\vec{A} \times \hat{n} = 0 \qquad where \qquad \vec{B} \cdot \hat{n} = 0$$ (4)

where **n** is a unit vector normal to the boundary.
Using the Galerkin method and considering the interface and boundary conditions, the following weak form can be obtained [4]:

$$\int_\Omega v\vec{\nabla} \times \vec{A} \cdot \vec{\nabla} \times \vec{W} \, d\Omega = \int_\Omega \vec{W} \cdot \vec{J} \, d\Omega \qquad \forall \vec{W}$$ (5)

where **W** is a vector weighting function.
Equation (2) associated with conditions (3) and (4) does not assure the uniqueness of the solution **A**. If **A₁** is one solution, other solutions can be generated adding an arbitrary gradient function, that is:

$$\vec{B} = \vec{\nabla} \times \vec{A}_1 = \vec{\nabla} \times (\vec{A}_2 + \vec{\nabla}\phi) = \vec{\nabla} \times \vec{A}_2$$ (6)

A gauge condition must be imposed so that the magnetic vector potential is uniquely determined. The strategy to apply this gauge is different if we consider

153

nodal or edge elements. This is discussed in the following section:

A. Nodal finite-elements

The Coulomb gauge is imposed to guarantee the solution uniqueness, that is:

$$\vec{\nabla} \cdot \vec{A} = 0 \qquad (7)$$

Now, the weak form becomes [4]:

$$\int_{\Omega} \nu(\vec{\nabla} \times \vec{A} \cdot \vec{\nabla} \times \vec{W} + \vec{\nabla} \cdot \vec{A}\, \vec{\nabla} \cdot \vec{W})\, d\Omega = \int_{\Omega} \vec{W} \cdot \vec{J}\, d\Omega \qquad (8)$$

The magnetic vector potential is approximated by nodal finite elements, that is:

$$\vec{A}^h = \sum_{i=1}^{NNOS} (A_{xi}\hat{i} + A_{yi}\hat{j} + A_{zi}\hat{k}) N_i \qquad (9)$$

where NNOS is the number of nodes of the element, (A_{xi}, A_{yi}, A_{zi}) are the components of $\mathbf{A}$ at the node i, and N_i is the nodal shape function associated with the node i.

B. Edge finite elements

The magnetic vector potential is now approximated by vector shape functions, defined over the element edges, that is:

$$\vec{A}^h = \sum_{i=1}^{NAR} A_i \vec{W}_i \qquad (10)$$

where NAR is the number of edges of the element. The A_i's are the line integrals of $\mathbf{A}$ along the edges and the $\mathbf{W}_i$'s are the vector shape functions. The line integral of $\mathbf{W}_i$ along the edge where it is defined is equal to one and along the other edges it is equal to zero[7].

As already mentioned, a gauge condition must be imposed to guarantee the solution uniqueness. The adopted gauge for edge elements is $\mathbf{A}\cdot\mathbf{w} = 0$ where $\mathbf{w}$ is an arbitrary vector field without closed lines. In [2] it is proved that this gauge guarantees the solution uniqueness.

If the finite element mesh is seen as a connected graph, there exists a very interesting way to apply this gauge. The discretized version of $\mathbf{A}\cdot\mathbf{w} = 0$ is obtained choosing the direction $\mathbf{w}$ as an arbitrary tree of the mesh graph [2]. Then, the degrees of freedom

associated with the tree are zeroed and only the edges corresponding to the co-tree must be evaluated.

As the tree is arbitrary, there are some cases where it can generate an ill conditioned matrix and this can result in a big number of ICCG iterations [5]. To avoid this problem, an incomplete gauge condition has been investigated. In this case, the edges that are zeroed form an incomplete tree, that is, a path connecting two arbitrary nodes cannot exist. In this work, the construction of this incomplete tree is based on the idea that the edges where $\mathbf{A}$ is significant should not be zeroed [3].

III. NUMERICAL RESULTS

The problem shown in Fig. 1 has been solved to compare the two finite element types. The problem consists of a cube with relative permeability equal to 1000. A magnetic induction of 1 T is applied in the z direction. Hexahedral elements are used to discretize the geometry. The solution of the generated matrix system is obtained by the ICCG method. The convergence criterion for the ICCG is reached when the Euclidean norm of the residual is less than 1E-7. The problem does not present an analytic solution. So, $\mathbf{B}$ is evaluated at the point x=y=z=10mm so that the calculated values can be compared with the values presented in [5].

Different meshes are used. The discretization characteristics are presented in Table I. Table II shows the results obtained using nodal elements. Tables III, IV and V show the results obtained with edge elements without using any gauge, using the $\mathbf{A}.\mathbf{w}=0$ gauge and the incomplete $\mathbf{A}.\mathbf{w}=0$ gauge, respectively. In this case, the incomplete gauge was applied zeroing all the edge unknowns in the z direction.
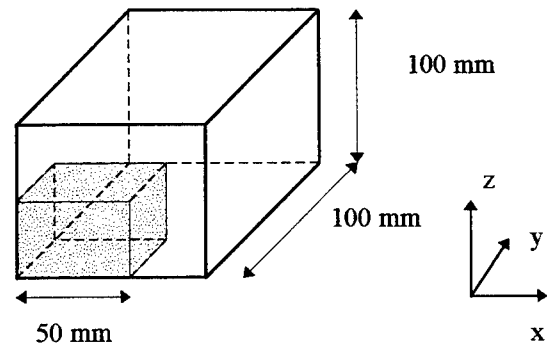

100 mm

z

100 mm

y

50 mm

x

Fig. 1:A magnetic cube in an uniform field

154

Table I.
Discretization Characteristics

Divisions	Number of Elements	Number of Nodes	Number of Edges
4x4x4	64	125	300
6x6x6	216	343	882
8x8x8	512	729	1944

Table II.
Nodal Elements

Divisions	Matrix coeffic.	Equations	ICCG iterations	B |T|
4x4x4	3630	177	2	2.5860
6x6x6	16224	615	3	2.6114
8x8x8	43826	1477	3	2.6288

Table III.
Edge Elements without gauge

Divisions	Matrix coeffic.	Equations	ICCG iterations	B |T|
4x4x4	1680	156	8	2.6007
6x6x6	7294	570	10	2.5912
8x8x8	19356	1400	13	2.5963

Table IV.
Edge Elements with the A·w =0 gauge.

Divisions	Matrix coeffic.	Equations	ICCG iterations	B |T|
4x4x4	851	111	31	2.6009
6x6x6	3475	395	80	2.6040
8x8x8	8971	959	131	2.6116

Table V.
Edge elements with the incomplete A·w =0 gauge

Divisions	Matrix coeffic.	Equations	ICCG iterations	B |T|
4x4x4	892	120	10	2.6007
6x6x6	3592	420	16	2.5914
8x8x8	9204	1008	21	2.5964

The results were obtained through an Object Oriented Program written in the C++ language [6] using a 486, 50 MHz, PC.

When no gauge is applied, edge elements generate a matrix system with dimension approximately equal to the dimension of the nodal elements generated matrix. However, the first matrix is much more sparse.

The nodal elements' system has a very fast ICCG convergence, as compared to the edge elements. It can be seen in Table III that the formulation without

gauge presents the lowest number of ICCG iterations for the edge element formulations. However, the number of equations and non zero elements is much bigger than the ones presented in Tables IV and V. Comparing the data in Tables IV and V, it can be seen that the incomplete gauge formulation reduces significantly the number of ICCG iterations, as compared to the complete gauge formulation. It can also be seen that the number of unknowns and of non zero coefficients is only a little greater than in the complete gauge formulation.

The number of ICCG iterations can be reduced if the "Shifted Incomplete Cholesky Factorization" [8] is used. In this method the standard Incomplete Cholesky Factorization is modified including a shift factor γ to scale the diagonal elements. The case of $\gamma=1$ corresponds to the Standard Incomplete Cholesky Factorization. The effectiveness of the preconditioning method changes with γ. Fig. 2 shows the influence of this factor in the number of ICCG iterations for all the edge element formulations.
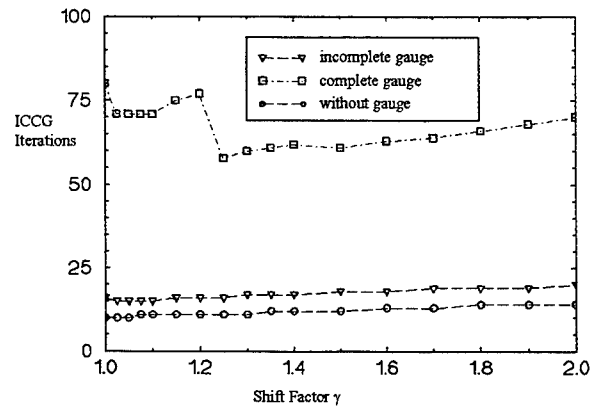
Fig. 2: Number of ICCG iterations as influenced by the Incomplete Cholesky Factorization Shift Factor

It can be seen in Fig. 2 that for the no gauge and the Incomplete Gauge formulations the shift factor does not have a big influence on the ICCG convergence and the standard ICCG can be used. However, for the complete gauge formulation, we must use a shift factor greater than one.

The flux density **B** is almost the same for the four different formulations and converges to the value presented in [5]. Fig. 3 confirms this, showing the values of **B** along the z direction evaluated with nodal and edge elements with the complete gauge.
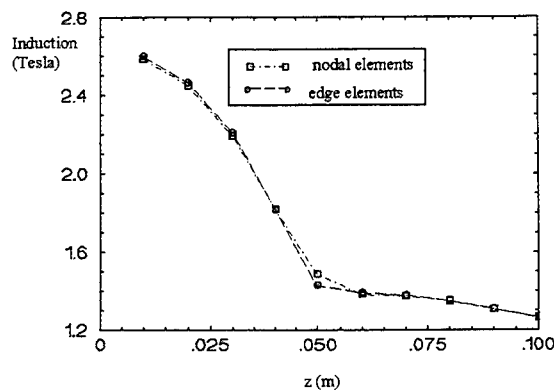
Fig. 3: |B| in the z direction (x=y=0.01)

IV. CONCLUSIONS

In this paper we presented a comparison between nodal and edge finite elements for 3D vector potential magnetostatic formulations. From the results presented in the previous sections, the following conclusions can be obtained:

- Nodal elements present better convergence for the ICCG method;
- The edge elements matrix is more sparse than the matrix generated by the nodal elements matrix;
- The application of the complete gauge condition reduces considerably the number of equations and the number of non-zero elements in the system matrix. However, it increases a lot the number of ICCG iterations;
- The complete gauge formulation is very sensitive to the value of the shift factor in the Incomplete Cholesky Factorization. The standard factorization ($\gamma = 1$) must be avoided in this case, because the number of ICCG iterations is very high;

- The incomplete gauge seems to be the best of the edge element formulations if we consider the analyzed aspects of memory requirements and the number of ICCG iterations. However, it must be emphasized that this conclusion is limited to the simple structure treated in this paper. For more complicated structures additional work must be done to guarantee that this is still valid.

V. REFERENCES

[1] A. Bossavit, "A rationale for edge-elements in 3-D fields computations", *IEEE Trans. Magn.*, Vol. 24, No. 1, pp. 74-79, 1988.

[2] Albanese, R., Rubinacci, G. "Magnetostatic Field Computation in Terms of Two-Component Vector Potential", *Int. Journal for Numerical Methods in Engineering*, Vol. 29, pp. 515-532.

[3] Golias, N.A., Tsiboukis, T.D., "Magnetostatics With Edge Elements: A Numerical Investigation in the Choice of the Tree", *IEEE Trans. Mag*, Vol. 30, No. 05, pp. 2877-2880:, Sep.,1994.

[4] Mesquita, R. C. *"3D Electromagnetic Field Computation using the finite element method: Magnetostatics, eddy-currents and induction heating"*, Ph.D. Thesis, Federal University of Santa Catarina, Florianópolis, Brazil, 1990 (in Portuguese).

[5] K.Fujiwara, T. Nakata, N.Takahashi and T.Imai "Effects of Gauge Condition on Accuracy and CPU time for 3D Finite Element method using Edge Element" *Proc. 4th CEFC Conf.*, Toronto, CA-10,1990.

[6] Silva, E.J., Mesquita, R.C., Saldanha, R.R, Palmeira, P.F.M. "An Object-Oriented Finite Element Program for Electromagnetic Field Computation", *IEEE Trans. Magn.*, Vol. 30, No. 05, pp. 3618-3621, Sep. 1994.

[7] Welij, J. S. Van "Calculation of Eddy Currents in Terms of H on Hexahedra", *IEEE Trans. Magn.*, Vol. 21, No. 6, pp. 2239-2241.

[8] Manteuffel, T. A. *The Shifted Incomplete Cholesky Factorization*, Sandia Laboratories, SAND 78-8226, 1978.

1997 INSTITUTIONAL MEMBERS

THE AEROSPACE CORPORATION
PO Box 92957
Los Angeles, CA 90009-2957

ANDREW CORPORATION
10500 W. 153rd Street
Orland Park, IL 60462

ATOMIC WEAPON ESTAB.
Bldg. E3, Awe Aldermaston
Reading, BERKS, UK RG7 4PR

BRITISH AEROSPACE
FPC 267 PO Box 5
Filton, BRISTOL, UK BS12 7QW

BRITISH AEROSPACE
Warton Aerodrome, NR Warton
Preston, LANCS, UK PR14 1AX

BRITISH BROADCASTING CO R&D
Kingswood Warren
Tadworth, SURREY, UK KT20 6NP

CAMBRIDGE CONSULTANTS, LTD.
Milton Road, Science Park
Cambridge, CAMBS, UK CB5 4DW

CHALMERS UNIV. OF TECH.
Microwave Technology
Gothenburg, SWEDEN S 412 96

CSC PROFESSIONAL SERVICE.
10101 Senate Drive
Lanham, MD 20706-4368

CSELT/RADIO
Via Gugliemo Reiss Romoli 274
Turin, ITALY 10148

CSIRO, CTR FOR ADV. TECH.
PO Box 883
Kenmore, QLD, AUSTRALIA 4069

CUBIC CUMMUNICATIONS
PO Box 85587
San Diego, CA 92186-5587

CULHAM LAB
UK Atomic Energy Authority
Abingdon, OXFORD, UK OX14 3DB

DARTMOUTH COLLEGE
Feldberg Library
Hanover, NH 03755-1809

DEFENCE TECH & PROCUREMENT
NEMP Lab, AC-Zentrum
Spiez, SWITZERLAND CH 3700

DEFENSE RESEARCH ESTAB. LIB.
3701 Carling Avenue
Ottowa, ON, CANADA K1A 0Z4

DLR OBERPFAFFENHOFEN
Zentralbibliothek
Wessling, OBB, GERMANY 8031

DSTO LIBRARY
Box 1500
Salisbury, SA AUSTRALIA 5108

ELECTRICAL COMM. LAB,
1-1 Hikarinooka Yokusuka Shi
Kanagawa, KEN, MZ, JAPAN 239

ERA TECHNOLOGY LTD.
Cleve Road
Leatherhead, SURREY, UK KT22 7SA

ESCUELA TRANSMISS. EJERCITO
Ctr. Extremadura, KM, 10,200
Madrid, SPAIN 28024

FANFIELD LTD.
Braxted Park
Witham, ESSEX, UK CM8 3XB

FELDBERG LIBRARY
Dartmouth College
Hanover, NH 03755-1809

FGAN/FHP/AUS
Neuenahrer Strasse 20
Wachtbert, Werth, GERMANY 53343

GEC MARCONI RES. CTR. LIB.
W. Hanningfield Road,
Chelmsford, ESSEX, UK CM2 8HN

HKUST, UNIVERSITY LIBRARY
Clear Water Bay Road
Kowloon, HONG KONG

HOKKAIDO DAIGAKU
Nishi 8, Kita 13
Sapporo, JAPAN 060

HUGHES RESEARCH LIBRARY
3011 Malibu Canyon Road
Malibu, CA 90265-4737

HUNTING ENGINEERING LTD.
Reddings Wood, Ampthill
Bedford, UK MK45 2HD

IABG MBH, TRM
Einsteinstrasse 20
Ottobrunn, GERMANY D 85521

IIT RESEARCH INSTITUTE
185 Admiral Cochrane Drive
Annapolis, MD 21401-7396

IMAGINEERING LTD.
95 Barber Greene Road, Ste. 112
Toronto, ON, CANADA M3C 3E9

INFORMATION CENTRE
A4 Bldg. Ively Road
Farnsborough, HAMPS. UK GU14 0LK

IPS RADIO & SPACE SVC/LIBRARY
PO Box 5606
W. Chatswood, AUSTRALIA 2057

KERSHNER, WRIGHT & HAGAMAN
5730 Gen. Washington Drive
Alexandria, VA 22312

LARDALENS UNIVERSITY
Box 883
Vasteras, SWEDEN S 721-23

LIBRARY, IREQ
1800 Montee Ste. Julie
Varennes, QC, CANADA J3K 1S1

LICOSA LIB COMM SANSONI
Via Duca Di Calabria 1/1
Florence, ITALY 50125

LINDA HALL LIBRARY
5109 Cherry Street
Kansas City, MO 64110-2498

MATRA DEFENSE
37 Av. Louis Breguet Bp 1
Velizy Cedex, FRANCE 78590

METAWAVE COMMUNICATIONS
8700 148th Avenue, N.E.
Redmond, WA 98052

MISSISSIPPI STATE UNIV LIBRARY
PO Box 9570
Mississippi State, MS 39762

MITRE CORPORATION LIBRARY
202 Burlington Road
Bedford, MA 01730-1407

MOD(PE) DGSS
Abbey Wood #54, PO Box 702
Bristol, UK BS12 7DU

MONASH UNIVERSITY
900 Dandenong Rd, Caulfield East
Melbourne, VIC, AUSTRALIA 3145

MOTOROLA CSGR.
600 N. US Hwy 45
Libertyville, IL 60048

MPB TECHNOLOGIES, INC.
151 Hymus Blvd.
Pointe-Claire, QC, CANADA H9R 1E9

NATIONAL AEROSPACE LAB, NLR.
Anthony Fokkerweg 2, PO Box 153
Emmeloord, NETHERLANDS 1059

NATL RADIOLOGICAL PROT. BD.
Chilton
Didcot, OXON, UK OX11 0RG

NAVITALIA
5301 Wisconsin Ave. NW
Washington, DC 20015

NGIC
220 7th Street, NE
Charlottesville, VA 22902-5396

NIKSAR
35/45 Gilbey Road
Mt. Waverley, VIC, AUSTRALIA 3149

NORTEL TECHNOLOGY
London Road
Harlow, ESSEX, UK CM17 9NA

OXFORD INSTRUMENTS
Osney Mead
Oxford, OXON., UK OX 0DX

PENN STATE UNIV LIBRARY
Pattee Library
University Park, PA 16802

QUEEN MARY & WESTFIELD COLL
Mile End Road
London, UK E1 4NS

RADIO FREQUENCY SYS. PTY. LTD.
36 Garden Street
Kilsyth, VIC, AUSTRALIA 3137

RADIO FREQUENCY SYS. P/L
12 Waddikee Road
Lonsdale, SA, AUSTRALIA 5600

RES. INST. OF IND. SCI LIB.
17 Haengdang-Dong
Sungdond-Ku, S. KOREA 133-791

ROYAL MILIT COLL OF SCI/CIT.
Cranfield University
Swindon, WILTS, UK SN6 8LA

SERCO SERVICES
Funtingdon North, Common Road
Chichester, W. SUSSEX, UK PO18
9PD

SONY CORPORATION
174 Fujitsukacho, Hodogaya Ku
Yokohama MZ, JAPAN 240

SOUTHWEST RESEARCH INST.
6220 Culebra Road
San Antonio, TX 78238

SWETS SUBSCRIPTION SERVICE
440 Creamery Way, Suite A
Exton, PA 19341

TASC - LIBRARY
55 Walkers Brook Drive
Reading, MA 01867-3297

TECHNISCHE UNIV. DELFT
Mekelweg 4, Delft
HOLLAND,NETHERLANDS 2628 CD

TECHNON-FOR-ON-TIME
DCN International
Jamaica, NY 11434-5410

TELEBRAS - CPQD, LIB.
Rod. Campinas
Campinas, SP BRAZIL 13088-061

TELESTRA LIBRARY
Private Bag 37
Clayton, VIC, AUSTRALIA 3168

TELSTRA RES. LABS, EMC.
770 Blackburn Road
Clayton, VIC, AUSTRALIA 3168

UNIV OF CENTRAL FLORIDA LIB.
PO Box 162440
Orlando, FL 32816-2440

UNIV OF COLORADO LIB.
Campus Box 184
Boulder, CO 80309-0184

UNIV OF MISSOURI-ROLLA LIB.
1870 Miner Circle
Rolla, MO 65409-0001

UNIV OF SURREY
Ctr for Satellite Res.
Guildford, SURREY, UK GU2 5XH

UNIVERSITAT DER BUNDESWEHR
Werner Heisenberg Weg 39
Neubiberg, GERMANY D-85577

US COAST GUARD ACADEMY
15 Mohegan Avenue
New London, CT 06320-4195

VECTOR FIELDS LTD.
24 Bankside Kidlington
Oxford, UK OX5 1JE

VIT, TECHNICAL RESEARCH. CTR.
PO Box 1202
Espoo, FINLAND FIN-02044

WATKINS-JOHNSON CO. LIB.
700 Quince Orchard Road
Gaithersburg, MD 20878-1794

YORK ELECTRONICS CENTRE
University of York
Heslington, YORK, UK Y01 5DD

ACES COPYRIGHT FORM

This form is intended for original, previously unpublished manuscripts submitted to ACES periodicals and conference publications. The signed form, appropriately completed, MUST ACCOMPANY any paper in order to be published by ACES. PLEASE READ REVERSE SIDE OF THIS FORM FOR FURTHER DETAILS.

TITLE OF PAPER:

AUTHORS(S)

PUBLICATION TITLE/DATE:

RETURN FORM TO:
Dr. Richard W. Adler
Naval Postgraduate School
Code EC/AB
833 Dyer Road, Room 437
Monterey, CA 93943-5121 USA

PART A - COPYRIGHT TRANSFER FORM

(NOTE: Company or other forms may not be substituted for this form. U.S. Government employees whose work is not subject to copyright may so certify by signing Part B below. Authors whose work is subject to Crown Copyright may sign Part C overleaf).

The undersigned, desiring to publish the above paper in a publication of ACES, hereby transfer their copyrights in the above paper to The Applied Computational Electromagnetics Society (ACES). The undersigned hereby represents and warrants that the paper is original and that he/she is the author of the paper or otherwise has the power and authority to make and execute this assignment.

Returned Rights: In return for these rights, ACES hereby grants to the above authors, and the employers for whom the work was performed, royalty-free permission to:
1. Retain all proprietary rights other than copyright, such as patent rights.
2. Reuse all or portions of the above paper in other works.
3. Reproduce, or have reproduced, the above paper for the author's personal use or for internal company use provided that (a) the source and ACES copyright are indicated, (b) the copies are not used in a way that implies ACES endorsement of a product or service of an employer, and (c) the copies per se are not offered for sale.
4. Make limited distribution of all or portions of the above paper prior to publication.
5. In the case of work performed under U.S. Government contract, ACES grants the U.S. Government royalty-free permission to reproduce all or portions of the above paper, and to authorize others to do so, for U.S. Government purposes only.

ACES Obligations: In exercising its rights under copyright, ACES will make all reasonable efforts to act in the interests of the authors and employers as well as in its own interest. In particular, ACES REQUIRES that:
1. The consent of the first-named author be sought as a condition in granting re-publication permission to others.
2. The consent of the undersigned employer be obtained as a condition in granting permission to others to reuse all or portions of the paper for promotion or marketing purposes.

In the event the above paper is not accepted and published by ACES or is withdrawn by the author(s) before acceptance by ACES, this agreement becomes null and void.

AUTHORIZED SIGNATURE   TITLE (IF NOT AUTHOR)

EMPLOYER FOR WHOM WORK WAS PERFORMED   DATE FORM SIGNED

PART B - U.S. GOVERNMENT EMPLOYEE CERTIFICATION

(NOTE: If your work was performed under Government contract but you are not a Government employee, sign transfer form above and see item 5 under Returned Rights).

This certifies that all authors of the above paper are employees of the U.S. Government and performed this work as part of their employment and that the paper is therefore not subject to U.S. copyright protection.

AUTHORIZED SIGNATURE   TITLE (IF NOT AUTHOR)

NAME OF GOVERNMENT ORGANIZATION   DATE FORM SIGNED

PART C - CROWN COPYRIGHT

(Note: ACES recognizes and will honor Crown Copyright as it does U.S. Copyright. It is understood that, in asserting Crown Copyright, ACES in no way diminishes its rights as publisher. Sign only if *ALL* authors are subject to Crown Copyright.

This certifies that all authors of the above Paper are subject to Crown Copyright. (Appropriate documentation and instructions regarding form of Crown Copyright notice may be attached).

AUTHORIZED SIGNATURE   TITLE OF SIGNEE

NAME OF GOVERNMENT BRANCH   DATE FORM SIGNED

Information to Authors

ACES POLICY

ACES distributes its technical publications throughout the world, and it may be necessary to translate and abstract its publications, and articles contained therein, for inclusion in various compendiums and similar publications, etc. When an article is submitted for publication by ACES, acceptance of the article implies that ACES has the rights to do all of the things it normally does with such an article.

In connection with its publishing activities, it is the policy of ACES to own the copyrights in its technical publications, and to the contributions contained therein, in order to protect the interests of ACES, its authors and their employers, and at the same time to facilitate the appropriate re-use of this material by others.

The new United States copyright law requires that the transfer of copyrights in each contribution from the author to ACES be confirmed in writing. It is therefore necessary that you execute either Part A-Copyright Transfer Form or Part B-U.S. Government Employee Certification or Part C-Crown Copyright on this sheet and return it to the Managing Editor (or person who supplied this sheet) as promptly as possible.

CLEARANCE OF PAPERS

ACES must of necessity assume that materials presented at its meetings or submitted to its publications is properly available for general dissemination to the audiences these activities are organized to serve. It is the responsibility of the authors, not ACES, to determine whether disclosure of their material requires the prior consent of other parties and if so, to obtain it. Furthermore, ACES must assume that, if an author uses within his/her article previously published and/or copyrighted material that permission has been obtained for such use and that any required credit lines, copyright notices, etc. are duly noted.

AUTHOR/COMPANY RIGHTS

If you are employed and you prepared your paper as a part of your job, the rights to your paper initially rest with your employer. In that case, when you sign the copyright form, we assume you are authorized to do so by your employer and that your employer has consented to all of the terms and conditions of this form. If not, it should be signed by someone so authorized.

     NOTE RE RETURNED RIGHTS: Just as ACES now requires a signed copyright transfer form in order to do "business as usual", it is the intent of this form to return rights to the author and employer so that they too may do "business as usual". If further clarification is required, please contact: The Managing Editor, R.W. Adler, Naval Postgraduate School, Code EC/AB, Monterey, CA, 93943, USA (408)656-2352.

Please note that, although authors are permitted to re-use all or portions of their ACES copyrighted material in other works, this does not include granting third party requests for reprinting, republishing, or other types of re-use.

JOINT AUTHORSHIP

For jointly authored papers, only one signature is required, but we assume all authors have been advised and have consented to the terms of this form.

U.S. GOVERNMENT EMPLOYEES

Authors who are U.S. Government employees are not required to sign the Copyright Transfer Form (Part A), but any co-authors outside the Government are.

Part B of the form is to be used instead of Part A only if all authors are U.S. Government employees and prepared the paper as part of their job.

     NOTE RE GOVERNMENT CONTRACT WORK: Authors whose work was performed under a U.S Government contract but who are not Government employees are required to sign Part A-Copyright Transfer Form. However, item 5 of the form returns reproduction rights to the U.S. Government when required, even though ACES copyright policy is in effect with respect to the reuse of material by the general public.

July 1996

ACES MEMBERSHIP - NEWSLETTER & JOURNAL SUBSCRIPTION FORM

please print

LAST NAME _____ FIRST NAME _____ MIDDLE INITIAL _____

COMPANY/ORGANIZATION/UNIVERSITY _____ DEPARTMENT/MAIL STATION _____

PLEASE LIST THE ADDRESS YOU WANT USED FOR PUBLICATIONS

MAILING ADDRESS _____

CITY _____ PROVINCE/STATE _____ COUNTRY _____ ZIP/POSTAL CODE _____

TELEPHONE _____ FAX _____ AMATEUR RADIO CALL SIGN _____

E-MAIL ADDRESS _____ E-MAIL ADDRESS CAN BE INCLUDED IN ACES DATABASE ☐ YES ☐ NO

PERMISSIONIS GRANTED TO HAVE MY NAME PLACED ON MAILING LISTS WHICH MAY BE SOLD ☐ YES ☐ NO

CURRENT SUBSCRIPTION PRICES

AREA	INDIVIDUAL SURFACE MAIL	INDIVIDUAL AIRMAIL	ORGANIZATIONAL (AIRMAIL ONLY)
U.S. & CANADA	( ) $65	( ) $65	( ) $115
MEXICO,CENTRAL & SOUTH AMERICA	( ) $68	( ) $70	( ) $115
EUROPE, FORMER USSR, TURKEY, SCANDINAVIA	( ) $68	( ) $78	( ) $115
ASIA, AFRICA, MIDDLE EAST & PACIFIC RIM	( ) $68	( ) $85	( ) $115

FULL-TIME STUDENT/RETIRED/UNEMPLOYED RATE IS $25 FOR ALL COUNTRIES

Non-USA participants: Prices are in U.S. dollars. All currencies must be converted to U.S. dollars payable by banks with U.S. affiliates. (1) Bank Checks, must have U.S. address of bank; (2) Traveler's Checks (in U.S. $$); (3) U.S./International Money Order drawn in U.S. funds, payable in U.S., (4) Credit Cards: Visa, MasterCard, Amex and Discover.

PAYMENT METHOD: ALL CHECKS/TRAVELER'S CHECKS/MONEY ORDERS ARE PAYABLE TO "ACES"

☐ CHECK (PAYABLE TO ACES)   ☐ TRAVELER'S CHECKS   ☐ INTERNATIONAL MONEY ORDER

☐ CREDIT CARD   ☐ VISA   ☐ MASTERCARD   ☐ AMEX   ☐ DISCOVER

CREDIT CARD USERS

SIGNATURE AND ADDRESS OF CARD HOLDER IS MANDATORY.

IF YOU ARE PAYING VIA ANOTHER PERSONS CARD, HE/SHE MUST PRINT AND SIGN NAME AND ADDRESS.

PRINT CARD HOLDER NAME: _____

CREDIT CARD HOLDER SIGNATURE: _____

CREDIT CARD EXPIRATION DATE: _____/_____

CREDIT CARD HOLDER ADDRESS, IF CARD IS NOT YOUR OWN. _____

CREDIT CARD ACCOUNT # ☐☐☐☐☐☐☐☐☐☐☐☐☐☐☐☐☐   January 1997

ACES NEWSLETTER AND JOURNAL COPY INFORMATION

Issue	Copy Deadline
March	January 13
July	May 25
November	September 25

APPLIED COMPUTATIONAL ELECTROMAGNETICS SOCIETY JOURNAL

INFORMATION FOR AUTHORS

STYLE FOR CAMERA READY COPY

The ACES Journal is flexible, within reason, in regard to style. However, certain requirements are in effect:

1. The paper title should NOT be placed on a separate page. The title, author(s), abstract, and (space permitting) beginning of the paper itself should all be on the first page. The title, author(s), and author affiliations should be centered (center-justified) on the first page.

2. An abstract is REQUIRED. The abstract should state the computer codes, computational techniques, and applications discussed in the paper (as applicable) and should otherwise be usable by technical abstracting and indexing services.

3. Either British English or American English spellings may be used, provided that each word is spelled consistently throughout the paper.

4. Any commonly-accepted format for referencing is permitted, provided that internal consistency of format is maintained. As a guideline for authors who have no other preference, we recommend that references be given by author(s) name and year in the body of the paper (with alphabetical listing of all references at the end of the paper). Titles of Journals, monographs, and similar publications should be in boldface or italic font or should be underlined. Titles of papers or articles should be in quotation marks.

5. Internal consistency shall also be maintained for other elements of style, such as equation numbering. As a guideline for authors who have no other preference, we suggest that equation numbers be placed in parentheses at the right column margin.

6. The intent and meaning of all text must be clear. For authors who are NOT masters of the English language, the ACES Editorial Staff will provide assistance with grammar (subject to clarity of intent and meaning).

7. Unused space should be minimized. Sections and subsections should not normally begin on a new page.

MATERIAL, SUBMITTAL FORMAT AND PROCEDURE

The preferred format for submission and subsequent review, is 12 point font or 12 cpi, double line spacing and single column per page. Four copies of all submissions should be sent to the Editor-in-Chief. Each submission must be accompanied by a covering letter. The letter should include the name, address, and telephone and/or fax number and/or e-mail address of at least one of the authors.

Only camera-ready original copies are accepted for publication. The term "camera-ready" means that the material is neat, legible, and reproducible. The preferred font style is Times Roman 10 point (or equivalent) such as that used in this text. A double column format similar to that used here is preferred. No author's work will be turned down once it has been accepted because of an inability to meet the requirements concerning fonts and format. Full details are sent to the author(s) with the letter of acceptance.

There is NO requirement for India ink or for special paper; any plain white paper may be used. However, faded lines on figures and white streaks along fold lines should be avoided. Original figures - even paste-ups - are preferred over "nth-generation" photocopies. These original figures will be returned if you so request.

While ACES reserves the right to re-type any submitted material, this is not generally done.

PUBLICATION CHARGES

ACES members are allowed 12 pages per paper without charge; non-members are allowed 8 pages per paper without charge. Mandatory page charges of $75 a page apply to all pages in excess of 12 for members or 8 for non-members. Voluntary page charges are requested for the free (12 or 8) pages, but are NOT mandatory or required for publication. A priority courtesy guideline, which favors members, applies to paper backlogs. Full details are available from the Editor-in-Chief.

COPYRIGHTS AND RELEASES

Each primary author must sign a copyright form and obtain a release from his/her organization vesting the copyright with ACES. Forms wlll be provided by ACES. Both the author and his/her organization are allowed to use the copyrighted material freely for their own private purposes.

Permission is granted to quote short passages and reproduce figures and tables from an ACES Journal issue provided the source is cited. Copies of ACES Journal articles may be made in accordance with usage permitted by Sections 107 or 108 of the U.S. Copyright Law. This consent does not extend to other kinds of copying, such as for general distribution, for advertising or promotional purposes, for creating new collective works, or for resale. The reproduction of multiple copies and the use of articles or extracts for commercial purposes require the consent of the author and specific permission from ACES. Institutional members are allowed to copy any ACES Journal issue for their internal distribution only.

APPLIED COMPUTATIONAL ELECTROMAGNETICS SOCIETY JOURNAL

INFORMATION FOR AUTHORS

PUBLICATION CRITERIA

Each paper is required to manifest some relation to applied computational electromagnetics. **Papers may address general issues in applied computational electromagnetics, or they may focus on specific applications, techniques, codes, or computational issues.** While the following list is not exhaustive, each paper will generally relate to at least one of these areas:

1. Code validation. This is done using internal checks or experimental, analytical or other computational data. Measured data of potential utility to code validation efforts will also be considered for publication.

2. Code performance analysis. This usually involves identification of numerical accuracy or other limitations, solution convergence, numerical and physical modeling error, and parameter tradeoffs. However, it is also permissible to address issues such as ease-of-use, set-up time, run time, special outputs, or other special features.

3. Computational studies of basic physics. This involves using a code, algorithm, or computational technique to simulate reality in such a way that better or new physical insight or understanding is achieved.

4. New computational techniques, or new applications for existing computational techniques or codes.

5. "Tricks of the trade" in selecting and applying codes and techniques.

6. New codes, algorithms, code enhancement, and code fixes. This category is self-explanatory but includes significant changes to existing codes, such as applicability extensions, algorithm optimization, problem correction, limitation removal, or other performance improvement. **Note: Code (or algorithm) capability descriptions are not acceptable, unless they contain sufficient technical material to justify consideration.**

7. Code input/output issues. This normally involves innovations in input (such as input geometry standardization, automatic mesh generation, or computer-aided design) or in output (whether it be tabular, graphical, statistical, Fourier-transformed, or otherwise signal-processed). Material dealing with input/output database management, output interpretation, or other input/output issues will also be considered for publication.

8. Computer hardware issues. This is the category for analysis of hardware capabilities and limitations in meeting

various types of electromagnetics computational requirements. Vector and parallel computational techniques and implementation are of particular interest.

Applications of interest include, but are not limited to, antennas (and their electromagnetic environments), networks, static fields, radar cross section, shielding, radiation hazards, biological effects, electromagnetic pulse (EMP), electromagnetic interference (EMI), electromagnetic compatibility (EMC), power transmission, charge transport, dielectric and magnetic materials, microwave components, MMIC technology, remote sensing and geophysics, communications systems, fiber optics, plasmas, particle accelerators, generators and motors, electromagnetic wave propagation, non-destructive evaluation, eddy currents, and inverse scattering.

Techniques of interest include frequency-domain and time-domain techniques, integral equation and differential equation techniques, diffraction theories, physical optics, moment methods, finite differences and finite element techniques, modal expansions, perturbation methods, and hybrid methods. This list is not exhaustive.

A unique feature of the Journal is the publication of unsuccessful efforts in applied computational electromagnetics. Publication of such material provides a means to discuss problem areas in electromagnetic modeling. Material representing an unsuccessful application or negative results in computational electromagnetics will be considered for publication only if a reasonable expectation of success (and a reasonable effort) are reflected. Moreover, such material must represent a problem area of potential interest to the ACES membership.

Where possible and appropriate, authors are required to provide statements of quantitative accuracy for measured and/or computed data. This issue is discussed in "Accuracy & Publication: Requiring quantitative accuracy statements to accompany data", by E.K. Miller, *ACES Newsletter*, Vol. 9, No. 3, pp. 23-29, 1994, ISBN 1056-9170.

EDITORIAL REVIEW

In order to ensure an appropriate level of quality control, papers are refereed. They are reviewed both for technical correctness and for adherence to the listed guidelines regarding information content. Authors should submit the initial manuscript in draft form so that any suggested changes can be made before the photo-ready copy is prepared for publication.